The Hashemite Kingdom of Jordan
Scientific Research Support Fund
The Hashemite University

JJEES

Jordan Journal of Earth and Environmental Sciences

Indexed by Scopus
ELSEVIER

Volume (16) Number (2)

Cover photo © Hani Al Amoush

JJEES is an International Peer-Reviewed Research Journal

ISSN 1995-6681 jjees.hu.edu.jo June 2025

Jordan Journal of Earth and Environmental Sciences (JJEES)

JJEES is an International Peer-Reviewed Research Journal, Issued by Deanship of Scientific Research, The Hashemite University, in corporation with, the Jordanian Scientific Research Support Fund, the Ministry of Higher Education and Scientific Research.

Editorial Board:

Associate Editorial Board: (Arranged Alphabetically)

International Advisory Board: (Arranged Alphabetically)

Editorial Board Support Team:

Submission address:

Manuscripts should be submitted electronically to the following e-mail:

jjees@hu.edu.jo

For more information and previous issues:

www.jjees.hu.edu.jo

Hashemite Kingdom of Jordan

Scientific Research Support Fund

Hashemite University

Jordan Journal of Earth and Environmental Sciences

JJEES

An International Peer-Reviewed Scientific Journal

Financed by the Scientific Research Support Fund

Volume 16 Number (2)

http:// jjees.hu.edu.jo/

ISSN 1995-6681

Ecosystem in Wadi Araba, Photo by Hani Al Amoush

JJEES
Jordan Journal of Earth and Environmental Sciences

JJEES

JJEES (2025) 16 (2): 108-116
ISSN 1995-6681

Jordan Journal of Earth and Environmental Sciences

Heavy Metals Accumulation in the Agricultural Soils around the Limestone-MiningArea of Gunungkidul Regency, Indonesia

Andrea Sumarah Asih[1], Akhmad Zamroni[2*], Haris Nur Eka Prasetya[3], Ronnel C. Nolos[4], Hill Gendoet Hartono[2], Alan Prahutama[5], and Roel F. Ceballos[6]

[1]*Department of Civil Engineering, Institut Teknologi Nasional Yogyakarta, Indonesia*
[2]*Department of Geological Engineering, Institut Teknologi Nasional Yogyakarta, Indonesia*
[3]*Department of Mining Engineering, Institut Teknologi Bandung, Indonesia*
[4]*College of Environmental Studies, Marinduque State University, Boac 4900, Philippines*
[5]*Department of Statistics, Diponegoro University, Indonesia*
[6]*Department of Mathematics and Statistics, University of Southeastern Philippines, Philippines*

Received on January 19, 2024, Accepted on December 31, 2024

Abstract

The study area, situated in an agricultural zone near limestone mining activities, faces significant threats from heavy metal pollution. The study aims to assess the concentrations of heavy metals (Pb, Zn, Cu, Cd, Mg, and Cr) in agricultural soils surrounding limestone-mining areas and evaluate the extent of heavy metal pollution based on World Health Organization (WHO) guidelines. Ten soil samples were collected from agricultural fields, with an additional three taken from limestone-mining sites to compare heavy metal accumulation using opportunistic sampling techniques. Heavy metal concentrations in the limestone formation influenced the levels found in soil samples from MOS-01, MOS-02, MOS-03, MOS-04, MOS-06, MOS-09, MOS-10, MOS-11, MOS-12, and MOS-13. At MOS-05, MOS-07, and MOS-08 sampling sites, heavy metals in agricultural soil were impacted by concentrations from clastic rock formations. Mining activities and agricultural fertilizers collectively influenced heavy metal content in agricultural soil at MOS-01, MOS-02, and MOS-10 sampling sites. Meanwhile, agricultural fertilizers alone impacted heavy metal concentrations at MOS-03, MOS-04, MOS-05, MOS-06, MOS-07, MOS-08, and MOS-09 sampling sites. Several sampling locations showed heavy metal concentrations that exceeded WHO standards, particularly Zn at all sites except MOS-09 and MOS-13, and Cu at all sites except MOS-10 and MOS-13. These findings highlight significant environmental concerns and underscore the urgent need for mitigation strategies to safeguard agricultural productivity and human health in the affected areas.

Keywords: *Soil pollution; agriculture; heavy metals; limestone mining*

1. Introduction

Environmental contamination due to the direct disposal of heavy metals has become a serious issue in recent years (Tarawneh et al., 2021; Fang et al., 2022). Since various forms and amounts of heavy metals can be found in soil, it is important to monitor their levels. The types, concentrations, and relationships of heavy metals in soil have been investigated through field sampling and indoor chemical analysis techniques (Fu et al., 2019). Heavy metal accumulation is often associated with mining activities (Agarin et al., 2021; Senoro et al., 2023). A study by Nolos et al. (2022) revealed that the high concentration of heavy metals in the soil of an island province in the Philippines was attributed to nearby mine sites. A significant amount of waste material rich in metals is generated during mineral exploration. These materials remain in the environment and pose a threat to human health, often leading to severe physical and chemical degradation of soils. Contamination with hazardous elements such as Cd, Pb, and Zn is a serious concern (Yang et al., 2009), as they can accumulate in soils and waterways, posing environmental and public health risks. According to Penido et al. (2019), high levels of heavy metals in soils can degrade the soil ecosystem, affecting parameters such as pH, electrical conductivity, soil mineralogy, cation exchange capacity, and microbial and biological activities.

Gunungkidul is a regency in Daerah Istimewa Yogyakarta (DIY) Province, Indonesia. Located in the eastern part of the province, Gunungsewu Geopark is one of the oldest tropical karst landscapes, spanning over 120 kilometers and featuring diverse geographical features, from coastal areas to highland locales (Zamroni et al., 2022; Zamroni et al., 2023). Large-and-small-scale limestone-mining activities pose the greatest threat to preserving karst areas in this region, evident in the destruction of hillsides due to mining operations (Sari et al., 2020). The potential ecological hazards associated with heavy metal contamination from limestone-mining operations have been extensively documented globally (Ali et al., 2022; Luo et al., 2021; Sarireh et al., 2021; Xie et al., 2022). Following the mining and crushing of limestone, significant quantities of mine waste materials are dispersed near the mining sites (Mohd Isha et al., 2021). One of the most active limestone-mining areas is Semin District, Gunungkidul Regency, where

* Corresponding author e-mail: akhmadzamroni@itny.ac.id

sedimentary limestone mine wastes are prevalent.

In agricultural areas, soil heavy metal pollution is increasingly becoming a serious environmental hazard. Over the past 50 years, more than 0.8 million tons of Pb and 0.03 million tons of Cr have been released into the environment, primarily accumulating in soils and causing severe heavy metal contamination (Xiang et al., 2021). Due to their non-biodegradable nature, toxic heavy metals pose a significant concern. Moreover, crops can absorb these elements, potentially affecting food safety and quality (Yaseen and Al-Hawari, 2019). The persistence and toxicity of heavy metals make them particularly harmful. Soil acts as a reservoir for heavy metals through processes such as sorption, precipitation, and complexation. The accumulation of hazardous substances in agricultural soils, located close to human populations, is worrisome. Heavy metals can enter the human body through the food chain, inhalation, ingestion, and skin contact (Khudhur et al., 2018).

In Indonesia, rice cultivation plays a crucial role in ensuring food security. To enhance soil quality, ensure the safety and quality of agricultural products, and safeguard human health, it is essential to establish a plan for controlling soil pollution (Kang et al., 2020). This study follows up on research by Zamroni et al. (2022), which investigated the geochemical characteristics of surface water in the study area. According to Indonesian government regulations, the quality of surface water in the research area was deemed suitable for irrigation. In this context, understanding the accumulation of soil heavy metals, including contamination levels and associated hazards in agricultural areas, is crucial. The present study aims to determine the concentrations of heavy metals (Pb, Zn, Cu, Cd, Mg, and Cr) in agricultural soils surrounding limestone-mining areas in Gunungkidul Regency. Additionally, it seeks to evaluate the extent of heavy metal pollution in agricultural soils in Gunungkidul Regency using guidelines established by the World Health Organization (WHO).

2. Geology of the Study Area

The study area is located within the Surakarta-Giritontro Quadrangle of Java's regional geological map (Figure 1). The predominant structural trends in the area are northeast-southwest and northwest-southeast (Sutarto et al., 2020). Several faults have been identified based on their northwest-southeast orientation, intersecting the Semilir Formation volcanic rock unit and the Wonosari Formation limestone unit. Recent studies have characterized these faults as thrust faults extending continuously to the southeast (Prasetyadi et al., 2011). The exposed formations in the study area, arranged from oldest to youngest, include the Mandalika Formation, Semilir Formation, Wonosari-Punung Formation, and Alluvium Formation (Surono et al., 1992). The Mandalika Formation, formed from late Oligocene to early Miocene magmatic activity, consists of tuff, basalt, andesite, and andesite breccias. Extensive areas are covered with breccia and lava deposits (Idrus et al., 2021; Susilo et al., 2021). The lithology of the Semilir Formation comprises tufaceous sandstone, lapilli tuff, sandstone, tuff, claystone, siltstone, and shale. This formation, dating to the Early Miocene, was deposited by turbidite currents in a deepwater environment influenced by gravity flows (Rahmad et al., 2017). The abundance of tuff and pumice in the Semilir Formation suggests it was formed during a significant volcanic eruption (Ardine et al., 2022). The Wonosari-Punung Formation, described by Fawzy Ismullah M. and Altin Massinai (2018), includes limestone, conglomerate limestone, marble-tuff limestone, siltstone, tuff, and sandstone. The geochemical composition of the Wonosari-Punung limestones indicates influence from hydrothermal fluid activity, post-depositional diagenetic processes, and a minor contribution of terrigenous material (Atmoko et al., 2018). Lastly, the Alluvium Formation consists of clay, silt, sand, and gravel, formed along rivers due to denudation processes on steep and extremely steep terrain (Saputra et al., 2016).

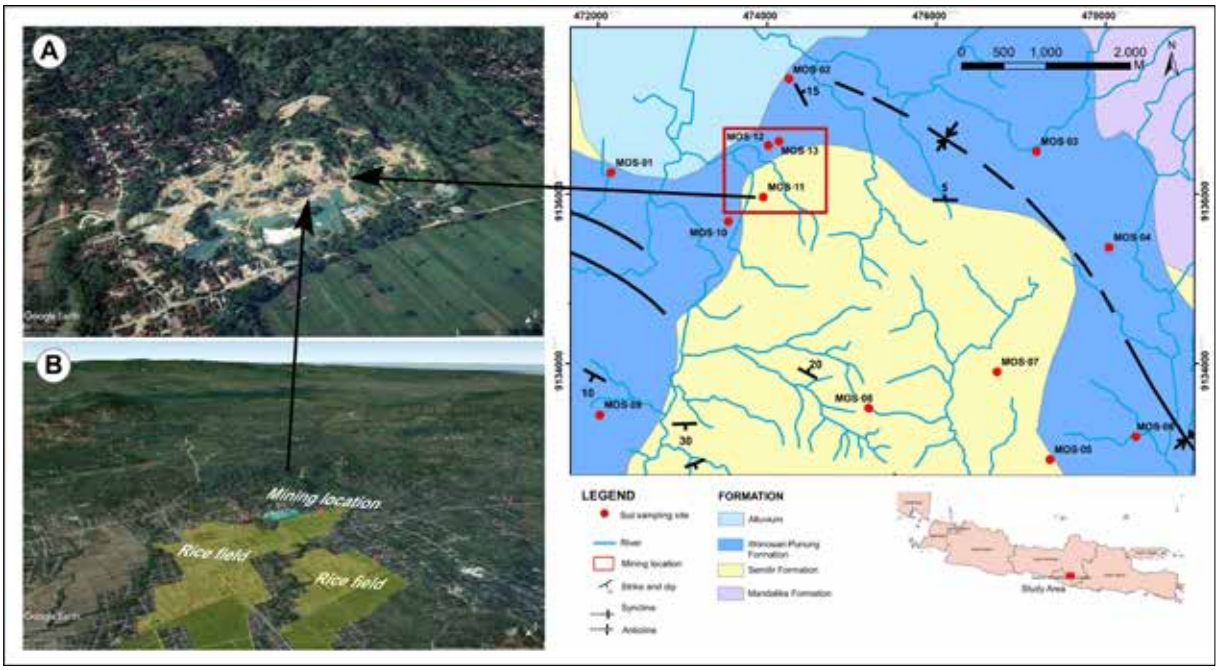

Figure 1. Geological map of the study area (A) Mining location, and (B) Mining location and rice fields around the study site (Modified from Surono et al., 1992).

3. Materials & Methods

In July 2023 (dry season), sampling was conducted in Semin District, Gunungkidul Regency, Daerah Istimewa Yogyakarta Province, Indonesia (Figure 1). The study area is characterized by limestone mining activities where locals use rudimentary mining equipment. Mining operations have been ongoing in the area since the 1990s, covering approximately 1.5 square kilometers of land dedicated to limestone extraction. Sampling points in this study were categorized into two zones: agricultural fields and mining sites. Ten soil samples were collected from agricultural fields near the limestone mining area, while three samples were taken directly from the limestone mining site to compare levels of heavy metal accumulation. An opportunistic sampling approach was employed based on accessibility, with proper consent obtained from relevant authorities or property owners (Bora et al., 2023). At each sampling location, soil samples were collected from the top 0–50 cm layer and placed into brand-new plastic zipper bags. The samples were kept chilled before analysis (Prartono et al., 2016).

Each sample's pH was measured using a pH meter. Concentrations of lead (Pb), zinc (Zn), copper (Cu), cadmium (Cd), magnesium (Mg), and chromium (Cr) were determined using an atomic absorption spectrophotometer (AAS) at the Balai Besar Teknik Kesehatan Lingkungan dan Pengendalian Penyakit (BBTKLPP), also known as the Center for Environmental Health and Disease Control Engineering, in Yogyakarta, Indonesia. The analysis followed the US EPA SW-846 7000B method for flame atomic absorption spectroscopy, utilizing a Varian SpectraAA atomic absorption spectrophotometer (United States Environmental Protection Agency, 2007). The World Health Organization (WHO, 1996) has established maximum permissible levels for heavy metals in soil, as indicated in Table 1. To assess potential risks, a risk assessment was conducted by comparing the measured concentrations of heavy metals in the soil (mg/kg) with these maximum permissible limits.

Table 1. The maximum permissible levels for heavy metals in soil (WHO, 1996)

Element	Maximum permissible levels in soil (mg/kg)
Pb	85
Zn	50
Cu	36
Cd	0.8
Mg	No guideline value set
Cr	100

4. Results and Discussion

4.1 Possible Source of Heavy Metals Accumulation

Table 2 presents the results of the analysis of heavy metal concentrations in agricultural soils within the study area. The elevation of each sampling site in the limestone-mining region (MOS-11, MOS-12, and MOS-13) was determined using a Shuttle Radar Topography Mission (SRTM) image. Figure 2 shows the SRTM image of the study area, categorizing sampling sites into two groups based on elevation relative to the limestone-mining area: those with elevations lower than or equal to the mining area (MOS-01, MOS-02, and MOS-10), and those with elevations higher than the mining area (MOS-03, MOS-04, MOS-05, MOS-06, MOS-07, MOS-08, and MOS-09). The elevation plays a significant role in determining the origin of heavy metal pollution. Areas with elevations equal to or lower than the limestone-mining area are influenced by pollution originating from mining activities, geological conditions, and human activities such as the use of chemical fertilizers. Conversely, areas with elevations higher than the limestone-mining area are primarily affected by geological factors and chemical fertilizers, without direct exposure to sediment from the mining area through rainwater runoff and airborne soil transport.

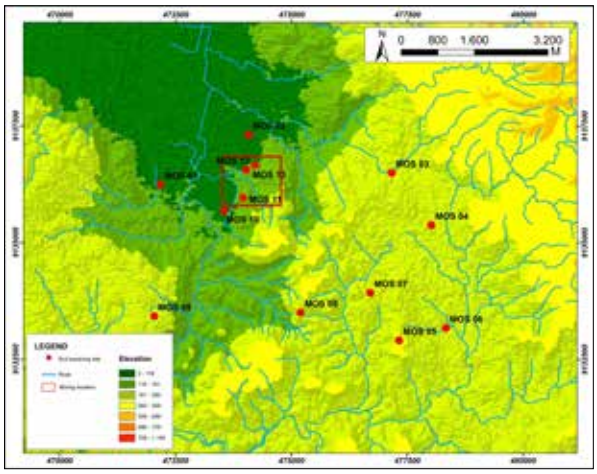

Figure 2. The Shuttle Radar Topography Mission (SRTM) of the study area.

4.2 The Relationship between pH and Heavy Metal Concentrations

In the study area, the pH values range from 5.26 to 6.72. Typically, pH in limestone-mining areas tends to be alkaline (Akande and Ifelola, 2011), but the measured values in this study are acidic to close to neutral. This acidity or near-neutrality is likely influenced by leaching processes involving other materials, including heavy metal concentrations in top soils and shales. Studies conducted across various contexts (agricultural, urban, and transitional land-use zones) have shown that heavy metals are more mobile in acidic soils compared to alkaline soils. The solubility of heavy metals decreases as pH increases, leading to more common heavy metal accumulation in alkaline environments. Conversely, heavy metal contamination can elevate soil pH levels (Kazlauskaitė-Jadzevičė et al., 2014; Sintorini et al., 2021).

In Microsoft Excel, a simple linear regression was performed to examine the relationship between pH and heavy metals (Zn, Mg, Cu, and Cr). Notably, Pb and Cd were excluded from the analysis as their values were below the detection limit. Figure 3 displays the results of the regression analysis between pH and the aforementioned heavy metals. A negative correlation was observed between pH and the concentrations of Zn, Mg, Cu, and Cr, with corresponding R-squared (R^2) values of 0.1327, 0.0179, 0.0021, and 0.2465, respectively. While previous studies have often reported significant associations between pH and heavy metal levels in soils, the findings of this analysis suggest otherwise due to limited supporting data. The lack of a substantial relationship between pH and heavy metals could be attributed to variations in pollution sources, soil types, and fertilizer applications across the sampled area (Ma et al., 2015).

Table 2. Heavy metal concentrations in agricultural soils in the study area.

Location	Coordinate		Land use type*	pH	Pb (mg/kg)	Zn (mg/kg)	Cu (mg/kg)	Cd (mg/kg)	Mg (mg/kg)	Cr (mg/kg)
	Easting	Northing								
MOS-01	472173.00	9136244.00	AA	6.62	<3.251	55.401	44.151	<0.848	4,826.87	29.505
MOS-02	474077.00	9137311.00	AA	6.48	<3.251	57.505	55.795	<0.848	5,703.45	19.667
MOS-03	477162.00	9136494.00	AA	6.72	5.510	53.403	69.297	<0.848	2,002.62	20.344
MOS-04	478016.00	9135375.00	AA	6.67	<3.251	54.994	52.896	<0.848	2,813.77	16.163
MOS-05	477325.00	9132905.00	AA	5.26	<3.251	82.949	52.653	<0.848	2,588.77	22.566
MOS-06	478332.00	9133172.00	AA	5.5	3.373	55.238	54.184	<0.848	1,935.44	14.547
MOS-07	476703.00	9133926.00	AA	5.71	<3.251	52.208	50.489	<0.848	3,130.32	9.668
MOS-08	475198.00	9133502.00	AA	5.63	<3.251	68.501	60.865	<0.848	3,237.43	7.635
MOS-09	472042.00	9133422.00	AA	5.78	<3.251	43.077	39.132	<0.848	1,583.46	11.730
MOS-10	473550.00	9135676.00	AA	5.57	<3.251	59.788	33.455	<0.848	3,753.49	13.598
MOS-11	473959.00	9135959.00	MA	5.97	<3.251	73.265	110.238	<0.848	4,103.30	21.775
MOS-12	474018.00	9136562.00	MA	6.54	<3.251	67.106	52.433	<0.848	397.67	21.577
MOS-13	474018.00	9136562.00	MA	6.37	<3.251	42.662	32.257	<0.848	4,145.52	18.105

**AA: Agricultural Area, MA: Mining Area*

Higher pH values are typically observed in sampling sites near mining areas, likely influenced by contact with alkaline limestone and the accumulation of heavy metals from anthropogenic activities, thereby increasing heavy metal concentrations in soils. Alkaline soils also tend to contain clay minerals with high cation exchange capacity (CEC), enabling them to adsorb and retain metal ions, contributing to their accumulation in the soil (Anjolaiya, 2015).

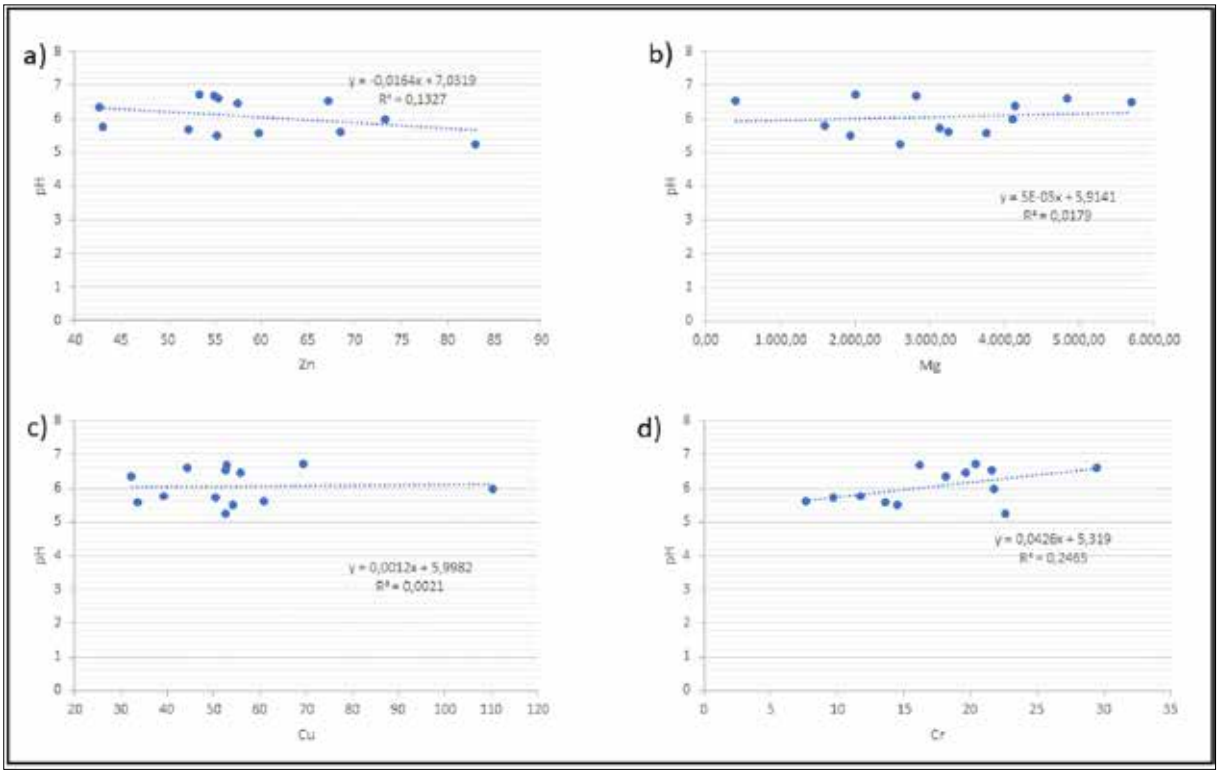

Figure 3. The regression analysis between pH and heavy metals; **a)** pH vs Zn, **b)** pH vs Mg, **c)** pH vs Cu, and **d)** pH vs Cr.

4.3 Heavy Metal Concentrations in Agricultural Soils

In the geological setting of the study area, sampling sites are situated within two formations: the Wonosari-Punung Formation (MOS-01, MOS-02, MOS-03, MOS-04, MOS-06, MOS-09, MOS-10, MOS-12, and MOS-13) and the Semilir Formation (MOS-05, MOS-07, and MOS-08). Given MOS-11's location in the Semilir Formation but near the Wonosari-Punung Formation, the assumption is that this specific location is considered part of the Wonosari-Punung Formation due to its association with soil sampling at a limestone mining site. The geological setting discussion focuses on the relationship between the lithology of these formations and the concentrations of heavy metals in the study area. The Wonosari-Punung Formation consists of limestone, conglomerate limestone, marble-tuff limestone, tuff, siltstone, and sandstone. On the other hand, the Semilir Formation is composed of tufaceous sandstone, lapilli tuff, sandstone, tuff, claystone, siltstone, and shale.

The sampling sites MOS-01, MOS-02, MOS-03, MOS-04, MOS-06, MOS-09, MOS-10, MOS-11, MOS-12, and MOS-13 are situated within the limestone formation, where weathering processes of the limestone lithology predominantly influence heavy metal concentrations. Regarding soil metals, Pb is known for its stability and low mobility in non-acidic soils (Elnazer et al., 2015). This stability is reflected in the consistently low Pb values observed across all sampling sites. In nature, Pb is commonly found in the form of galena, a compound containing sulfur. The paragenetic stages during formation influence the Pb isotope ratios found in galena, which typically reflect the original Pb isotope composition of hydrothermal fluids (Hu et al., 2022). In the parent limestones, Zn exists in three forms: Zn associated with pyrite and calcite sphalerite grains, Zn bound to goethite within inherited phosphate nodules, and Zn attached to phyllosilicates. During pedogenesis (soil formation), processes such as eluviation, two stages of redox reactions, and carbonate dissolution contribute to the redistribution of Zn. The breakdown of carbonates in limestones releases Zn previously bound to calcite into the soil solution. As a result, Zn concentrations in soil often exceed those in the parent limestones due to residual enrichment (Laveuf et al., 2009). At most sampling sites, Zn concentrations are high; this enrichment contribution is likely attributed to hydrothermal inputs, which are considered the primary source of elevated Zn concentrations in limestone at these sites (Jacquat et al., 2011). The geochemical composition of the Wonosari-Punung limestones indicates that hydrothermal fluid activity, a minor contribution of terrigenous material, and post-depositional diagenetic processes played significant roles in the deposition of rare earth elements. Additionally, hydrothermal fluids have influenced the enrichment of Cr concentrations in this formation (Atmoko et al., 2018). The Wonosari-Punung Formation also contains mineralized porphyry with lower-grade Cu adjacent to ore-grade primary Cu within the limestone. During the Miocene epoch, numerous dioritic rocks intruded into the Wonosari-Punung Formation. This formation predominantly comprises Quaternary sediments and volcanic products from nearby active volcanoes (Idrus et al., 2023).

The concentrations of Cd in soils are primarily determined by factors such as soil type, geological age, rock type, and geomorphic characteristics. Specifically, in karst areas like the Wonosari-Punung Formation within the Wonosari karst, carbonatite weathering, and deposition processes contribute significantly to Cd concentrations (Zhao et al., 2020). The Wonosari karst is a vital component of the Gunungsewu karst megasystem in Gunungkidul Regency (Damayantia et al., 2021). The levels of Mg observed can be attributed to the presence of high-Mg lava during the formation of limestones, rather than diagenesis processes (Cutillas-Barreiro et al., 2016). This is supported by the occurrence of volcanic rocks such as tuff, marble tuff, and conglomerate, which are in contact with limestone within the Wonosari-Punung Formation.

The explanation above pertains to the heavy metals contained in the parent limestone. However, several sampling sites in the study area have heavy metal contents that exceed WHO standard limits (Table 1), specifically Zn at all sampling sites except MOS-09 and MOS-13, and Cu at all sampling sites except MOS-10 and MOS-13. This indicates that anthropogenic factors have contributed to the increase in heavy metal concentrations at those sampling sites. Natural weathering of parent materials contributes to the presence of heavy metals in soils, human activities have significantly augmented metal reservoirs in the soil system since the early 1900s. The intensity of human activity can disrupt the biogeochemical cycles of heavy metals in terrestrial ecosystems (Asih et al., 2022; Putra et al., 2023). Excavation activities in the limestone-mining disturb the natural soil layers, bringing heavy metals closer to the surface, particularly Zn and Cu, the soil surrounding limestone quarries often exhibits severe pollution levels (Mulwa et al., 2012; Wang et al., 2021). Run-off from rainwater, erosion, and airborne transport contribute to spreading these contaminants, affecting nearby areas, especially those at or below the elevation of the limestone mining sites, such as MOS-01, MOS-02, and MOS-10. Agricultural activities, notably in rice fields within the study area, also contribute to the high concentrations of heavy metals observed at various sampling sites, regardless of their elevation relative to the limestone mining areas. The primary sources of heavy metals in agriculture are fertilizers and pesticides. Both organic and inorganic fertilizers contribute to the accumulation of heavy metals in soil. Prolonged use of fertilizers increases the potential for accumulation of metals such as copper Cu, Zn, and Cd in agricultural soils. Synthetic magnesium sulfate, often used in fertilizers, contributes to the elevated Mg levels observed in the study area (Azzouzi et al., 2016). Inorganic fertilizers such as phosphate fertilizers, liming materials, and biofertilizers are major contributors to heavy metal release into agricultural soils, where they can be absorbed by plants and subsequently enter the food chain, affecting humans and animals (Alengebawy et al., 2021).

Compared to clastic rocks, soils derived from carbonate rocks exhibit significantly higher levels of heavy metals. This phenomenon can be attributed to several factors: the formation of clay minerals, high initial concentrations of heavy metals in carbonate rocks, and secondary enrichment processes during weathering and soil formation. Background concentrations of heavy metals in carbonate rocks often exceed crustal abundance estimates, particularly noticeable for Cd in limestone. As carbonate rocks weather, they release heavy metals into the soil, resulting in parent materials with higher concentrations of heavy metals than the original bedrock (Zhang et al., 2020). The accumulation of heavy metals in topsoils primarily depends on ongoing weathering of the soil's parent material, regardless of external inputs. However, sampling sites such as MOS-05, MOS-07, and MOS-08 also exhibit elevated heavy metal concentrations comparable to those found in limestone formations. This indicates that high concentrations are not solely due to the weathering of clastic rocks in the Semilir Formation but are exacerbated by agricultural practices, particularly the use of fertilizers, at sites higher in elevation than the mining areas. Figure 4 illustrates a schematic representation of the study's findings.

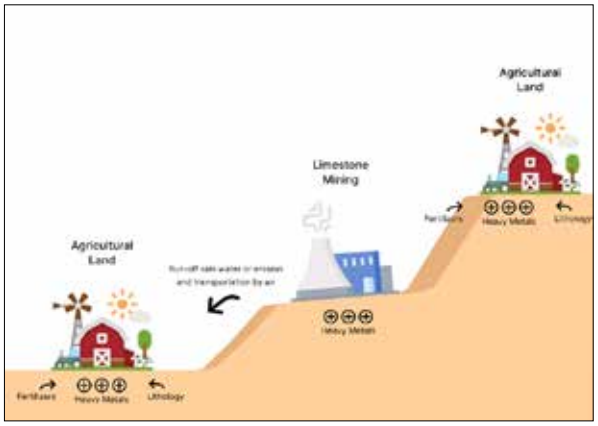

Figure 4. The sketch of heavy metal contamination in the agricultural soil in the study area (Icon made by www.flaticon.com).

4.4 Comparison with Sediment Quality Standard

The sediment quality standards in the study area are based on the maximum permissible levels of heavy metals in the soil as defined by the WHO (Table 1). According to the heavy metal concentrations observed in agricultural soils within the study area, several sampling sites have heavy metal contents that exceed WHO standard limits (Table 1), specifically Zn at all sampling sites except MOS-09 and MOS-13, and Cu at all sampling sites except MOS-10 and MOS-13. Zn plays crucial roles as a catalytic, structural, and regulatory cofactor in numerous enzyme processes in plants. It is essential for glucose metabolism, protein synthesis, and growth hormone production such as indoleacetic acid, maintaining cell membrane integrity. Plants experiencing acute Zn deficiency exhibit symptoms like stunted growth, leaf chlorosis, shortened internodes and petioles, and clustering of small, deformed leaves at the top (a typical dicotyledon rosette symptom). Even without apparent deficiency symptoms, moderately Zn-deficient soils can lower crop yields and quality (Montalvo et al., 2016). Water-soluble Zn in soils can contaminate groundwater, posing risks due to its accumulation in plants beyond their physiological needs. While Zn is essential, excessive amounts can be phytotoxic, adversely affecting crop yields and soil fertility. Soil concentrations of total Zn ranging from 70 to 400 mg/kg are considered critical, with toxicity observed at higher levels. Excessive Zn can also pose health risks to humans, potentially causing poisoning (Bentum et al., 2011). Cu is another essential micronutrient for plants, but its excessive presence in soil can lead to detrimental effects. Cu toxicity disrupts cellular processes, causing protein denaturation and membrane damage in bacteria, and inhibits the growth and function of microbial communities, even at low concentrations like 1% CuO (Alengebawy et al., 2021). Additionally, Cu toxicity can affect gene expression, neuronal activity, and lipid metabolism, and potentially influence tumor cell resistance to chemotherapy (Cai et al., 2019). Given these implications, the elevated concentrations of Zn and Cu highlight a significant environmental concern that necessitates mitigation strategies to prevent further contamination of agricultural soils and safeguard water sources used by the community.

Mitigation is key to addressing environmental issues caused by heavy metal contamination from mining activities and associated health risks linked to industrial expansion (Prasetya et al., 2021; Zamroni et al., 2020). Government regulators and mining companies must take decisive action. Strict enforcement of environmental regulations, particularly regarding waste discharge, and effective control of pollution sources are essential strategies to mitigate soil heavy metal pollution. Many small-scale mining operations significantly harm the environment due to inefficient mining practices and outdated technology. Therefore, supporting sustainable integrated approaches—such as legislation, education, and financial incentives for adopting appropriate pollution control technologies—is crucial for communities affected by small-scale mining. In Indonesia, the enforcement of environmental rules is often lax, leading to relatively low rates of environmental restoration, despite legal requirements for all mining companies to participate in such efforts. Furthermore, cleaning up heavy metal-contaminated soils is costly and technically challenging. Phytoremediation presents a more affordable and efficient alternative to soil replacement and leaching techniques. Instead of solely focusing on agriculture and forestry for economic gain, diversifying restoration efforts to include wildlife habitats and nurseries is essential. Priority should be given to controlling key pollutants that pose significant risks to human health. Special attention must also be paid to protecting vulnerable groups, particularly children living near mining areas. Specific measures, such as restricting outdoor activities, can help reduce soil ingestion rates among children in proximity to mining zones (Li et al., 2014; Rachmawati and Zamroni, 2020; Kurniati et al., 2023; Nolos et al., 2023).

5. Conclusions

Heavy metal concentrations (Pb, Zn, Cu, Cd, Mg, and Cr) in the study area were influenced by geological factors and anthropogenic activities. Geological factors refer to the weathered rock lithology, the parent materials for agricultural soil, while anthropogenic activities are dominated by farm fertilizer and limestone mining. Heavy metal concentrations in the limestone formation influenced the heavy metal content in soil at sampling sites of MOS-01, MOS-02, MOS-03, MOS-04, MOS-06, MOS-09, MOS-10, MOS-11, MOS 12, and MOS-13. In contrast, heavy metal concentrations in the clastic rock formation influenced the heavy metal content in agricultural soil at MOS-05, MOS-07, and MOS-08 sampling sites. Heavy metals from mining activities and agricultural fertilizers influenced the heavy metal content in agricultural soil at sampling sites of MOS-01, MOS-02, and MOS-10, while the concentration of heavy metals at sampling sites of MOS-03, MOS-04, MOS-05, MOS06, MOS-07, MOS-08, and MOS-09 was only influenced by agricultural fertilizers. Several sampling sites have heavy metal contents that exceed WHO standard limits, specifically Zn at all sampling sites except MOS-09 and MOS-13, and Cu at all sampling sites except MOS-10 and MOS-13. Government authorities and mining firms must take significant action to address the heavy metal pollution caused by mining operations and the attendant health concerns connected with industrial development.

Acknowledgments

We are grateful to "Institut Teknologi Nasional Yogyakarta" for financing this research. We would also like to express our gratitude to Ayu Atikha Reinaty for creating the best research sketch and to Arman, Dicky, and Aldam, the field assistants who helped us gather soil samples.

References

Agarin, C. J. M., Mascareñas, D. R., Nolos, R., Chan, E., & Senoro, D. B. (2021). Transition metals in freshwater crustaceans, tilapia, and inland water: Hazardous to the population of the small island province. Toxics, 9(4), 71.

Akande, J. M., & Ifelola, E. O. (2011). Analysis of soil, water and dust during limestone mining and processing. Miner Wealth, 157, 14-24.

Alengebawy, A., Abdelkhalek, S. T., Qureshi, S. R., & Wang, M. Q. (2021). Heavy metals and pesticides toxicity in agricultural soil and plants: Ecological risks and human health implications. Toxics, 9(3), 42.

Ali, M. M., Rahman, S., Islam, M. S., Rakib, M. R. J., Hossen, S., Rahman, M. Z., ... & Phoungthong, K. (2022). Distribution of heavy metals in water and sediment of an urban river in a developing country: a probabilistic risk assessment. International journal of sediment research, 37(2), 173-187.

Anjolaiya, O. (2015). Sorption behaviour of metal contaminants in clay minerals, soils and matrices: understanding the influence of organic matter, pH, ionic strength and mineralogy (Doctoral dissertation, Loughborough University).

Ardine, J. E., Nugroho, M. O. B., Maulana, M. I., Nugroho, A. N. K., & Hisan, N. K. (2022). Deep Marine Reservoir Analog From Semilir Formation Outcrop Data in Ngoro-Oro Area, Gunungkidul, Indonesia.

Asih, A.S., Zamroni, A., Alwi, W., Sagala, S.T., & Putra, A.S. (2022). Assessment of Heavy Metal Concentrations in Seawater in the Coastal Areas around Daerah Istimewa Yogyakarta Province, Indonesia. The Iraqi Geological Journal, 55 (1B), 14-22.

Atmoko, D. D., Titisari, A. D., & Idrus, A. (2018). Geochemical Characteristics of Limestone of Wonosari-Punung Formation, Gunungkidul Regency, Yogyakarta, Indonesia. Indonesian Journal on Geoscience, 5(2).

Azzouzi, H., Ouzaouit, K., Aboulaich, A., Dali, Y., Kaddami, A., & Akalay, I. (2016). Managem products potentially used in fertilizers industry. Procedia Engineering, 138, 302-307.

Bentum, J. K., Adotey, J. P. K., Koka, J., Koranteng-Addo, E. J., Yeboah, A., & Boamponsem, L. K. (2011). Assessment of lead, copper and zinc contamination of soil from University of Cape Coast School of Agricultural farmland, Ghana. International journal of biological and chemical sciences, 5(4), 1703-1711.

Bora, F. D., Babeș, A. C., Călugăr, A., Jitea, M. I., Hoble, A., Filimon, R. V., ... & Bunea, C. I. (2023). Unravelling Heavy Metal Dynamics in Soil and Honey: A Case Study from Maramureș Region, Romania. Foods, 12(19), 3577.

Cai, L. M., Wang, Q. S., Luo, J., Chen, L. G., Zhu, R. L., Wang, S., & Tang, C. H. (2019). Heavy metal contamination and health risk assessment for children near a large Cu-smelter in central China. Science of the Total Environment, 650, 725-733.

Cutillas-Barreiro, L., Pérez-Rodríguez, P., Gómez-Armesto, A., Fernández-Sanjurjo, M. J., Álvarez-Rodríguez, E., Núñez-Delgado, A., ... & Nóvoa-Muñoz, J. C. (2016). Lithological and land-use based assessment of heavy metal pollution in soils surrounding a cement plant in SW Europe. Science of the total environment, 562, 179-190.

Damayantia, A., Riadinia, F., & Pamungkasa, F. D. (2021). Potential Areas of Land Subsidence in Karst Landscape: Case Study in Ponjong and Semanu District, Gunungkidul Regency, Yogyakarta, Indonesia. International Journal on Advanced Science, Engineering and Information Technology, 11(2), 712-719.

Elnazer, A. A., Salman, S. A., Seleem, E. M., & Abu El Ella, E. M. (2015). Assessment of some heavy metals pollution and bioavailability in roadside soil of Alexandria-Marsa Matruh Highway, Egypt. International Journal of Ecology, 2015.

Fang, H., Wang, X., Xia, D., Zhu, J., Yu, W., Su, Y., ... & Qiu, J. (2022). Improvement of Ecological Risk Considering Heavy Metal in Soil and Groundwater Surrounding Electroplating Factories. Processes, 10(7), 1267.

Fawzy Ismullah M, M., & Altin Massinai, M. (2018, March). Shallow Depth Study Using Gravity & Magnetics Data in Central Java-Yogyakarta. In Journal of Physics Conference Series (Vol. 979, No. 1, p. 012046).

Fu, P., Yang, K., & Feng, F. (2019). Study on heavy metal in soil based on spectral second-order differential Gabor transform. Journal of the Indian Society of Remote Sensing, 47, 629-638.

Hu, Y., Ye, L., Huang, Z., Wei, C., Wu, T., Xiang, Z., ... & Li, Z. (2022). Genetic model for early Cambrian reef limestone-hosted Pb-Zn deposits in the world-class Huayuan orefield, South China: New insights from mineralogy, fluorite geochemistry and sulfides in situ S-Pb isotopes. Ore Geology Reviews, 141, 104682.

Idrus, A., Dana, C.D., Setijadji, L.D., Sutarto, Ernowo, Sakellaris, G.A., & van Leeuwen, T. (2023). Nature of magma and ore-forming conditions at the Randu Kuning porphyry Cu-Au deposit, Indonesia: a comparative study with other Cu-Au deposits in the region. International Geology Review, pp.1-19.

Idrus, A., Masti, S. D., & Azizi, R. R. (2021, March). Determination of slope susceptibility in hydrothermally altered rocks region with a case study in wonotirto district, blitar regency, east java province, indonesia. In IOP Conference Series: Earth and Environmental Science (Vol. 683, No. 1, p. 012058). IOP Publishing.

Jacquat, O., Rambeau, C., Voegelin, A., Efimenko, N., Villard, A., Föllmi, K. B., & Kretzschmar, R. (2011). Origin of high Zn contents in Jurassic limestone of the Jura mountain range and the Burgundy: evidence from Zn speciation and distribution. Swiss Journal of Geosciences, 104(3), 409-424.

Kang, Z., Wang, S., Qin, J., Wu, R., & Li, H. (2020). Pollution characteristics and ecological risk assessment of heavy metals in paddy fields of Fujian province, China. Scientific reports, 10(1), 12244.

Kazlauskaitė-Jadzevičė, A., Volungevičius, J., Gregorauskienė, V., & Marcinkonis, S. (2014). The role of pH in heavy metal contamination of urban soil. Journal of Environmental Engineering and Landscape Management, 22(4), 311-318.

Khudhur, N. S., Khudhur, S. M., & Ahmad, I. N. (2018). An Assessment of heavy metal soil contamination in a Steel Factory and the surrounding area in Erbil City. Jordan Journal of Earth and Environmental Sciences, 9(1), 1-11.

Kurniati, A.C., Putri, W.E.C., Zamroni, A., Sagala, S.T., & Rachmawati, Y. (2023, June). How to educate children in the mining areas: A concept to implement environmental education for elementary students in Indonesia. In AIP Conference Proceedings (Vol. 2598, No. 1). AIP Publishing.

Laveuf, C., Cornu, S., Baize, D., Hardy, M., Josière, O., Drouin, S., ... & Juillot, F. (2009). Zinc redistribution in a soil developed from limestone during pedogenesis. Pedosphere, 19(3), 292-304.

Li, Z., Ma, Z., van der Kuijp, T. J., Yuan, Z., & Huang, L. (2014). A review of soil heavy metal pollution from mines in China: pollution and health risk assessment. Science of the total environment, 468, 843-853.

Luo, P., Xu, C., Kang, S., Huo, A., Lyu, J., Zhou, M., & Nover, D. (2021). Heavy metals in water and surface sediments of the Fenghe River Basin, China: Assessment and source analysis. Water Science and Technology, 84(10-11), 3072-3090.

Ma, L., Sun, J., Yang, Z., & Wang, L. (2015). Heavy metal contamination of agricultural soils affected by mining activities around the Ganxi River in Chenzhou, Southern

China. Environmental monitoring and assessment, 187, 1-9.

Mohd Isha, N. S., Mohd Kusin, F., Ahmad Kamal, N. M., Syed Hasan, S. N. M., & Molahid, V. L. M. (2021). Geochemical and mineralogical assessment of sedimentary limestone mine waste and potential for mineral carbonation. Environmental Geochemistry and Health, 43, 2065-2080.

Montalvo, D., Degryse, F., Da Silva, R. C., Baird, R., & McLaughlin, M. J. (2016). Agronomic effectiveness of zinc sources as micronutrient fertilizer. Advances in agronomy, 139, 215-267.

Mulwa, B. M., Maina, D. M., & Patel, J. P. (2012). Multielemental analysis of limestone and soil samples of Kitui South (Kenya) limestone deposits. International Journal of Fundamental Physical Sciences (IJFPS), 2(4), 48-51.

Nolos, R. C., Agarin, C. J. M., Domino, M. Y. R., Bonifacio, P. B., Chan, E. B., Mascareñas, D. R., & Senoro, D. B. (2022). Health Risks due to metal concentrations in soil and vegetables from the six municipalities of the Island Province in the Philippines. International Journal of Environmental Research and Public Health, 19(3), 1587.

Nolos, R. C., Zamroni, A., & Evina, K. F. P. (2023). Drivers of Deforestation And Forest Degradation In Palawan, Philippines: An Analysis Using Social-Ecological Systems (SES) And Institutional Analysis And Development (IAD) Approaches. GEOGRAPHY, ENVIRONMENT, SUSTAINABILITY, 15(4), 44-56.

Penido, E. S., Martins, G. C., Mendes, T. B. M., Melo, L. C. A., do Rosário Guimarães, I., & Guilherme, L. R. G. (2019). Combining biochar and sewage sludge for immobilization of heavy metals in mining soils. Ecotoxicology and Environmental Safety, 172, 326-333.

Prartono, T., Sanusi, H. S., & Nurjaya, I. W. (2016). Seasonal distribution and geochemical fractionation of heavy metals from surface sediment in a tropical estuary of Jeneberang River, Indonesia. Marine pollution bulletin, 111(1-2), 456-462.

Prasetya, H. N. E., Aditama, T., Sastrawiguna, G. I., Rizqi, A. F., & Zamroni, A. (2021, June). Analytical landslides prone area by using Sentinel-2 Satellite Imagery and geological data in Google Earth Engine (a case study of Cinomati Street, Bantul Regency, Daerah Istimewa Yogyakarta Province, Indonesia). In IOP Conference Series: Earth and Environmental Science (Vol. 782, No. 2, p. 022025). IOP Publishing.

Prasetyadi, C., Sudarno, I., Indranadi, V. B., & Surono, S. (2011). Pola dan Genesa Struktur Geologi Pegunungan Selatan, Provinsi Daerah Istimewa Yogyakarta dan Provinsi Jawa Tengah. Jurnal Geologi dan Sumberdaya Mineral, 21(2), 91-107.

Putra, A. S., Zamroni, A., Asih, A. S., Sagala, S. T., & Tingson, K. N. (2023). Heavy Metals in Surface Sediments of the Coastal Area Around Daerah Istimewa Yogyakarta, Indonesia: Their Relations to Land-Use Types. The Iraqi Geological Journal, 156-168.

Rachmawati, Y., & Zamroni, A. (2020). How Indonesian Governments Care for Local People's Education in the Mining Area: Experiences from other Countries. Psychology and Education Journal, 57(9), 5924-5934.

Rahmad, B., Hananto, H., Nugroho, T., Pramono, S. H., & Sumantri, A. Shale Hydrocarbon Potential of Semilir Formation in Buyutan, Klaten, Central Java, Indonesia.

Saputra, A., Gomez, C., Hadmoko, D. S., & Sartohadi, J. (2016). Coseismic landslide susceptibility assessment using geographic information system. Geoenvironmental Disasters, 3, 1-16.

Sari, A.S., Bahagiarti, S., Suharsono, S., & Prasetyadi, C. (2020). Groundwater quality in Ponjong Karst, Gunungkidul Regency, Special Region of Yogyakarta. Journal of Earth and Marine Technology (JEMT), 1(1), pp.7-11.

Sarireh, M., Ghrair, A. M., Alsaqoor, S., & Alahmer, A. (2021). Evaluation of the Use of Volcanic Tuff in concrete block production. Jordan Journal of Earth and Environmental Sciences (JJEES), 16.

Senoro, D. B., Plasus, M. M. G., Gorospe, A. F. B., Nolos, R. C., Baaco, A. T., & Lin, C. (2023). Metals and Metalloid Concentrations in Fish, Its Spatial Distribution in PPC, Philippines and the Attributable Risks. Toxics, 11(7), 621.

Sintorini, M. M., Widyatmoko, H., Sinaga, E., & Aliyah, N. (2021, April). Effect of pH on metal mobility in the soil. In IOP Conference Series: Earth and Environmental Science (Vol. 737, No. 1, p. 012071). IOP Publishing.

Surono, Toha, B, & Sudarno, I. (1992). Peta Geologi Lembar Surakarta Giritontro, Jawa, Skala 1:100.000 (Bandung: Pusat Penelitian dan Pengembangan Geologi).

Susilo, A., Haji, A. T. S., Suharto, B., Suyadnya, I. W., Pramais, C. W., & Rahman, A. H. (2021, February). Inventory and identification of geodiversity to support geotourism in the Lenggoksono bay area of South Malang, Indonesia. In Journal of Physics: Conference Series (Vol. 1816, No. 1, p. 012111). IOP Publishing.

Sutarto, S., Idrus, A., Harjoko, A., Setijadji, L. D., Meyer, F. M., & Sindern, S. (2020, July). Mineralization style of the Randu Kuning porphyry Cu-Au and intermediate sulphidation epithermal Au-base metals deposits at Selogiri area, Central Java Indonesia. In AIP Conference Proceedings (Vol. 2245, No. 1). AIP Publishing.

Tarawneh, K., Eleyan, I., Alalwan, R., Sallam, S., & Hammad, S. (2021). Assessment of heavy metals contamination levels in surfaces soil in Baqa'a area, Jordan. Jordan Journal of Earth & Environmental Sciences, 12(4).

United States Environmental Protection Agency – US EPA. (2007). Method 7000B (SW-846): Flame Atomic Absorption Spectrophotometry, Revision 2. Washington: US EPA.

Wang, Z., Bao, J., Wang, T., Moryani, H. T., Kang, W., Zheng, J., ... & Xiao, W. (2021). Hazardous heavy metals accumulation and health risk assessment of different vegetable species in contaminated soils from a typical mining city, central China. International Journal of Environmental Research and Public Health, 18(5), 2617.

World Health Organization (WHO). (1996). Permissible limits of heavy metals in soil and plants. Geneva, Switzerland.

Xiang, M., Li, Y., Yang, J., Lei, K., Li, Y., Li, F., ... & Cao, Y. (2021). Heavy metal contamination risk assessment and correlation analysis of heavy metal contents in soil and crops. Environmental Pollution, 278, 116911.

Xie, F., Yu, M., Yuan, Q., Meng, Y., Qie, Y., Shang, Z., ... & Zhang, D. (2022). Spatial distribution, pollution assessment, and source identification of heavy metals in the Yellow River. Journal of Hazardous Materials, 436, 129309.

Yang, P., Mao, R., Shao, H., & Gao, Y. (2009). An investigation on the distribution of eight hazardous heavy metals in the suburban farmland of China. Journal of hazardous materials, 167(1-3), 1246-1251.

Yaseen, I. B., & Al-Hawari, Z. (2019). Assessment of Metal Pollution of the Surface Sediments along the Wadi Al Rayyan area, Jordan. Jordan Journal of Earth & Environmental Sciences, 75.

Zamroni, A., Kurniati, A. C., & Prasetya, H. N. E. (2020). The assessment of landslides disaster mitigation in Java Island, Indonesia: a review. Journal of Geoscience, Engineering, Environment, and Technology, 5(3), 124-128.

Zamroni, A., Trisnaning, P. T., Prasetya, H. N. E., Sagala, S. T., & Putra, A. S. (2022). Geochemical Characteristics and Evaluation of the Groundwater and Surface Water in Limestone Mining Area around Gunungkidul Regency, Indonesia. The Iraqi Geological Journal, 189-198.

Zamroni, A., Trisnaning, P. T., & Widiatmoko, F. R. (2023, February). Karst landscapes in Indonesia: Potential disaster and mitigation. In AIP Conference Proceedings (Vol. 2482, No. 1). AIP Publishing.

Zhang, J., Yang, R., Li, Y. C., Peng, Y., Wen, X., & Ni, X. (2020). Distribution, accumulation, and potential risks of

heavy metals in soil and tea leaves from geologically different plantations. Ecotoxicology and Environmental Safety, 195, 110475.

Zhao, Y., Deng, Q., Lin, Q., Zeng, C., & Zhong, C. (2020). Cadmium source identification in soils and high-risk regions predicted by geographical detector method. Environmental Pollution, 263, 114338.

JJEES

JJEES (2025) 16 (2): 117-135
ISSN 1995-6681

Jordan Journal of Earth and Environmental Sciences

Age, Geochemistry, and Petrogenetic Constraints on Ediacaran Granitoids, Southwest Jordan.

Reema Moshtaha[1], Rolf Romer[2], and Ghaleb H. Jarrar[3*]

[1]Ministry of Education, Amman, Jordan
[2]GeoForschungszentrum-Potsdam, Germany
[3]Geology Department, The University of Jordan, P.O.Box 13633, 11942-Amman, Jordan

Received on March 6, 2024, Accepted on January 2, 2025

Abstract

The final stages of the terminal collision between East and West Gondwana at 600 ± 50 Ma ago are characterized by post-collisional calc-alkaline and A-type alkaline granitoids intruding the Neoproterozoic basement in southern Jordan. Available U-Pb zircon, Rb-Sr and Sm-Nd mineral and whole-rock age data on these granitoids are inconsistent. To improve constrain the geological relevance and timing of the change in the chemical character of magmatism in the Jordanian basement, the geochemical, mineralogical, isotopic characteristics and dating of representative calc-alkaline (Sabil granodiorite) and A-type alkaline (Feinan, Humrat and Mubarak) granitoids were reevaluated by several geochemical, mineralogical and dating methods. Sabil is a high-K calc-alkaline intermediate intrusion. It shows enrichments of LILE relative to HFSE as well as Sr, Ba, P, Zr, Ti, Cr, Co, and Ni. Further, a well-developed depletion in K, Rb, Th, Ta, Nb, and Y; and a weak E-anomaly (Eu/Eu* = 0.7 - 1.0). The alkaline granitoids display higher SiO2, Na2O+K2O, Fe/Mg, enrichment in Zr, Nb, Y, Rb, Ta, K, and REE contents, with corresponding depletion in CaO, Ba, Sr, Ti, and P along with a pronounced Eu anomaly (Eu/Eu* = 0.06 – 0.85). They show close similarity to within-plate A-type granites. Both of them have LREE-enriched and flat HREE patterns. Nevertheless, the alkaline granites are characterized by higher LREE enrichment and lower MREE and HREE contents, except for the Mubarak unit, which displays a concave upward REE pattern. They also follow a gently sloping LREE and almost flat HREE chondrite-normalized patterns in general, while the calc-alkaline Sabil unit shows a smooth flat to steep chondrite-normalized REE pattern. The U-Pb zircon ages for the Sabil granodiorite unit are about 616 Ma, and 603, 601, and 586 Ma for the Feinan, Mubarak, and Humrat units, respectively. The εNd values of the alkali rocks ranged from + 2.9 to + 5.4 with (0.70146 to 0.715080) initial $^{87}Sr/^{86}Sr$. They overlap with the εNd values of the calc-alkaline rocks (+ 3.7 to + 4.6) with low initial $^{87}Sr/^{86}Sr$ (~ 0.70374). Mineralogical and geochemical characteristics suggest that both rocks were not products of the same magma source. The investigated granitoid could have been produced through decompressional partial melting of the subcontinental lithosphere and lower continental crust, following slab failure and mantle delamination, with fractional crystallization and minor crustal assimilation. The transitional magmatism (Feinan and Mubarak units) coincides or slightly post-dates with the Araba Unconformity and the extensive dike swarms.

Keywords: Arabian-Nubian Shield, Jordan, U-Pb zircon geochronology, granitoids, geochemistry.

1. Introduction

The continental crust, which is mainly made of granitoids, cannot be directly derived from the mantle through partial melting due to disequilibrium between the felsic melts and the ultramafic mineral assemblage of the mantle (e.g., Johannes and Holtz, 1996). Hence, two principal mechanisms and derivatives, thereof, are invoked for the generation of the granitoid magmas: differentiation by fractional crystallization with or without crustal contamination of mantle-derived mafic magmas and water, or hydrous minerals, assisted by partial melting of felsic, meta-igneous and metasedimentary rocks (Moyen et al., 2017). The first mechanism contributes to crustal growth, while the second just recycles pre-existing crustal rocks (e.g., Tang et al., 2020).

The Arabian-Nubian Shield (ANS) is the northern segment of East African Orogen (EAO, ~ 900 to 530 Ma, Stern, 1994) that extends from south to north for about 6000 km and represents one of the largest juvenile continental crust exposures on Earth. The EAO combines two types of mobile orogenic belts: juvenile volcanic arc terranes of the ANS and the lower crustal associated remnants of the Mozambique belt. The former, according to Kröner and Stern (2004), comprises Neoproterozoic supracrustal and magmatic assemblages including ophiolites, subduction or collision-related granitoids, while the latter is made of poly-metamorphosed high-grade metamorphic assemblages, with protoliths predominantly of Mesoproterozoic to Archean continental crust as well as the reworked Neoproterozoic crust (e.g. Boyd et al., 2010).

The juvenile island and volcanic arc terranes of the ANS witnessed, during the EAO, a series of repeated deformational and metamorphic events ranging from greenschist to upper amphibolite facies (e.g. Abu El-Enen and Whitehouse 2013; Habboush and Jarrar 2009; Jarrar et al., 2013a). The above authors and Elisha et al., 2017; 2019 constrained the age of

* Corresponding author e-mail: jarrargh@ju.edu.jo

the peak of metamorphism at ~ 620 ± 5 Ma. These processes were associated with and followed by voluminous intrusive and volcanic activities that culminated in the cratonization of the ANS (e.g., Jarrar et al., 2003; Eyal et al., 2010; Johnson et al., 2013).

During the final stages of the amalgamation of the ANS terranes (630-540 Ma), the chemical affinity of the magmatism changed from calc-alkaline to alkaline with a contemporaneous change in tectonic style from collision through post-collision to within plate extension and finally to stable platform setting (Garfunkel, 1999; Kröner and Stern, 2004). El-Bialy and Hassen (2012) documented the onset of anorogenic alkaline magmatism in Sinai at St. Katherina at 590-580 Ma. The wealth of geochronologic data in the last two decades documents intensive and continuous magmatic activity including the gradual transition from calc-alkaline to alkaline magmatism (Eyal et al. 2019). Beyth et al. (1994) suggested that the transition has occurred at ca. 610 Ma. Ibrahim and McCourt (1995), based on field observations and limited geochronological and geochemical data, divided the basement complex of South Jordan into two complexes: the Aqaba and Araba complexes, which are separated by intra Neoproterozoic unconformity that is marked by the deposition of the Saramuj conglomerate. Powell et al. (2015) coined the name Araba Unconformity for this unconformity and placed it at about 605 Ma. It should, however, be noted that the age data for both complexes are scarce and mainly comprise Rb-Sr whole rock data (Brook et al., 1990), Ibrahim and McCourt, 1995; Jarrar et al., 2008). Brook et al. (1990), reported whole-rock Rb-Sr isochrons of 589 ± 36, 538 ± 30, 567± 5, and 560 ± 10 Ma for the Sabil, Feinan, Humrat, and Mubarark units, respectively. Jarrar et al. (2008) reported a whole-rock Rb-Sr age of 558 ± 13 Ma for the Feinan granite. These ages generally overlap and quite often contradict the field observation. Furthermore, there is a scarce U-Pb zircon age for the granitoid of the Neoproterozoic of Jordan, in particular the Araba Complex.

Accordingly, this study presents U-Pb conventional age determinations on zircons and titanite as well as detailed geochemical, petrologic, and Sr-Nd-Pd isotope investigations for three granitic units, Feinan, Humrat, and Mubarak, and on the Sabil granodioritic unit from the calc-alkaline batholiths of the Aqaba Complex (Ibrahim and McCourt, 1995).

2. Geologic Setting

The northernmost outcrops of the ANS in South Jordan (Figures. 1 A and B) cover about 1400 sq. km and are dominated by granitoids that intrude into the two principal metamorphic complexes, the Abu-Barqa metasedimentary suite and the Janub Metamorphic Complex in addition to megaxenoliths of amphibolites and biotite-hornblende schists i.e. Abu-Saqa schist (Ibrahim and McCourt, 1995, Jarrar, 1995). The U-Pb ages of the protoliths of the Abu-Barqa metasedimentary suite have been constrained at 680-900 Ma, while the age of the peak of metamorphism was constrained at about 620±5 Ma (Jarrar et al., 2013a; Elisha et al., 2019). Field relationships with cross-cutting granitoids in addition to SIMS U-Pb ages on zircon constrained the age of Janub Metamorphic Complex and the associated magmatic activity between 645-615 ± 5 Ma. The lower limit of 615 Ma coincides with the age of Abu-Barqa Metamorphic Suite (Ghanem et al., 2022).

The Aqaba Complex includes metamorphic and calc-alkaline igneous rocks below the regional peneplain (Ibrahim, 1991,1993). The complex comprises metamorphic rocks, preserved as narrow belts and megaxenoliths, ranging in age from 800-620 Ma, hornblendite and hornblende gabbro, and amphibolites (Jarrar, 1995, 1998), a foliated granitic suite (Rahma Foliated Suite), and four 625-600 Ma old post-orogenic granitoid suites (Darba Tonalitic, Rumman Granodiorite, Urf Porphyritic, and Yutum Granitic Suites). The whole complex is extensively cut by dike swarms of variable compositions and nature i.e. simple, composite, and hybrid (Ghanem et al., 2020; Jarrar et al., 2004, Jarrar et al., 2013b; Wachendorf et al., 1985).

The Araba Complex is bounded by two major unconformities, the Ediacaran Araba Unconformity (~ 605 Ma, as set by Powell et al., 2015) at its base, which truncates the Aqaba Complex lithologies, and the regional lower Cambrian Ram Unconformity (set at ~ 530 Ma; Powell et al, 2014). The latter is marked by the extensive deposition of the lowest member of the Ram siliciclastic sedimentary Group (Ibrahim and McCourt, 1995; Jarrar et al., 2003). The Araba Complex comprises the Safi Group (Saramuj Conglomerate Formation and the Hiayala Volcani-clastic Formation), the magmatic rocks of the Humrat-Feinan Suite, the Araba Mafic to Intermediate Suite, and the Aheimir alkaline to peralkaline rhyolitic Suite. The first two magmatic suites were lumped together as the Araba Alkaline Bimodal Plutonic Suite (Jarrar, et al., 2003). Furthermore, the Araba Complex commences by the deposition of the Safi Group, which comprises the Saramuj Conglomerate, the Haiyala Volcaniclastic, and the Um Gaddah Formations (Powell et al., 2015). Generally speaking, rocks of this complex are exposed along the eastern margin of Wadi Araba in addition to sporadic exposures throughout the basement, east and northeast of Aqaba (Figs. 2 and 3)

This study focuses on the Humrat-Feinan Suite (Mubarak, Feinan, and Humrat alkali-feldspar granites and syenogranites units) and the calc-alkaline Sabil granodiorite unit as a part of the Rumman Granodiorite Suite from the Aqaba complex. The Humrat-Feinan Suite is exposed mainly in a horst block in the Dana area (Feinan, Figure. 2), an area of very rugged terrane, and in places to the east and northeast of Aqaba, e.g., Jabal Humrat, Wadi Yutum, Jabal Mubarak, and Wadi Sabil (Sabit) (Figure. 3). This suite, in particular the Humrat unit, is rarely cut by dikes and presumably represents the felsic end member of the Araba Alkaline Plutonic Bimodal Suite (Jarrar, et al., 2003).

The Humrat alkali-feldspar granites are the youngest among the investigated granitoids (Jarrar, et al., 2003). Jarrar, et al. (2008) suggested that the Feinan granite could have been derived from the Ghuweir mantle-derived mafics via fractional crystallization depending on their Rb-Sr ages for Araba granites (Humrat 568 Ma; and Feinan 559 Ma), while the mafic rocks cluster at 595 Ma using U-Pb

zircon Concordia of the complex suites (Ghanem and Jarrar, 2013; Jarrar and Ghanem, 2021)

The Rumman Granodiorite Suite occurs dominantly in the southeastern part of the granitoid outcrops extending to the south and west from Wadi Rumman to Wadi Sabil down to the Jordan-Saudi Arabia border (Figure. 3). According to McCourt and Ibrahim (1990), the suite comprises four units ranging in composition from diorite to monzogranite.

In the field, these grayish-green units generally have a low relief and are extensively cut by NE-SW trending dike swarms. The age of the suite was determined to be 583 ± 3 Ma with an initial $^{87}Sr/^{86}Sr$ ratio of 0.7035 ± 0.0001 using Rb-Sr whole dating (Brook et al., 1990). Regional petrological correlation with the Midyan area indicates that this Rb-Sr age is too young in comparison to the younger granites exposed in the Eastern Desert of Egypt (McCourt and Ibrahim, 1990).

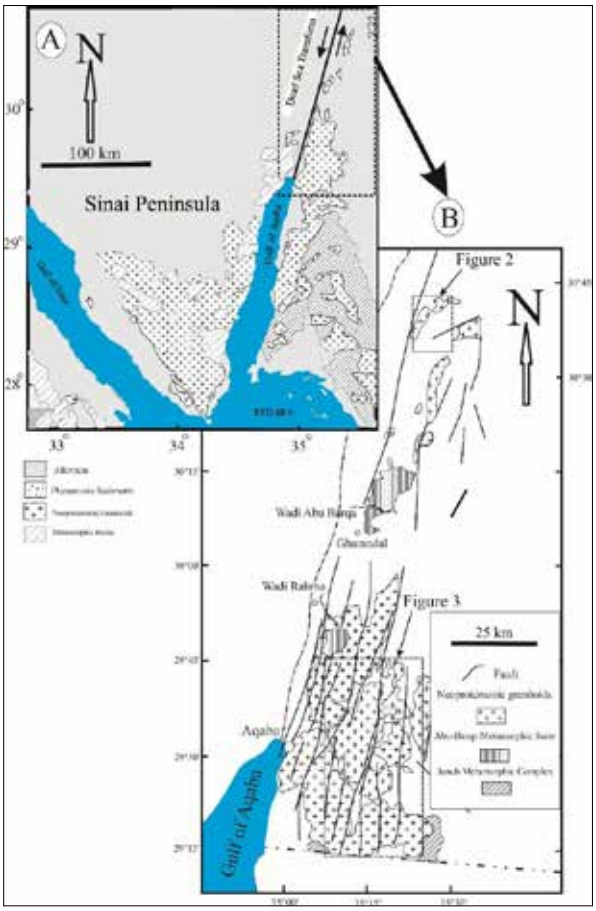

Figure 1. A. The northernmost exposures of the Arabian-Nubian Shield in Sinai, Jordan, and surrounding areas; **B.** The outcrops of the Neoproterozoic basement in southern Jordan and along the eastern shoulder of Wadi Araba, insets for Figures. 2 and 3 are shown on the map. Slightly modified after Ibrahim and McCourt (1995).

3. Field and petrographic aspects

In Wadi Marsad in the Quweira area, the Humrat granite carries the Marsad granite of the older Urf suite as roof pendants (Figure. 4A). Further to the south in Wadi Sabil, the Humrat granite intrudes the Sabil granodiorite with a vertical contact, that is typical of shallow intrusions (Figure. 4B). In this area and elsewhere, this granite is rich in miarolitic vugs filled with euhedral quartz and other secondary minerals. The Feinan granites show great similarity to the Humrat granite in hand-specimen, but quite often are white reddish in contrast to the Humrat which is always brick red in color. The reddish colored, simply twinned microperthite dominates over albite plagioclase.

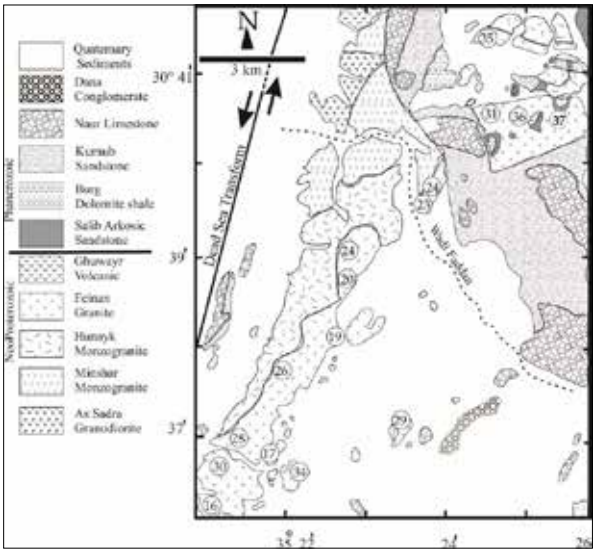

Figure 2. The outcrops and sample locations of Feinan unit granites in Central Wadi Araba. Other Neoproterozoic basement and Phanerozoic rocks are shown. Modified from Figure 5.2 (Jarrar and Ghanem, 2021)

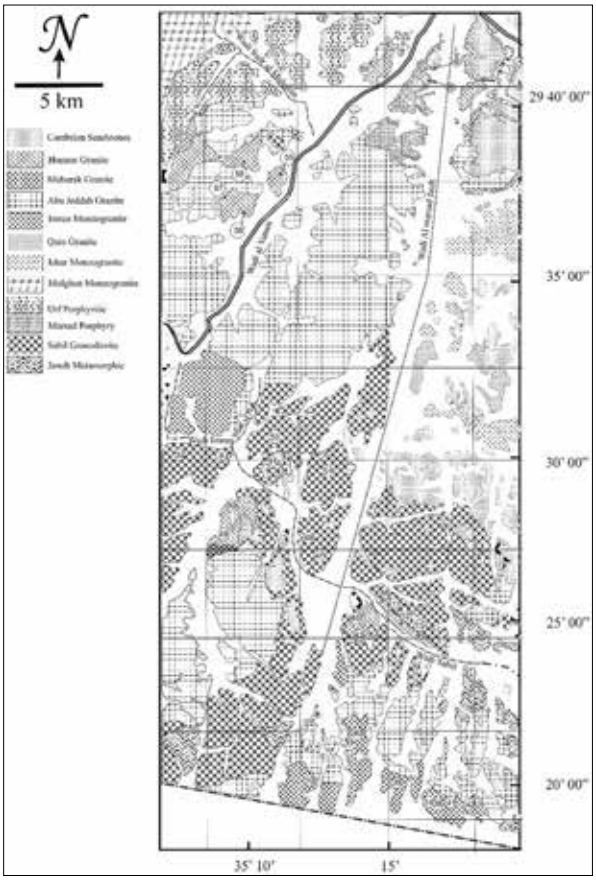

Figure 3. Distribution and sample locations of Sabil granodiorite, Humrat and Mubarak granites east and northeast of Aqaba. Other units of the Aqaba complex are shown as well. Modified from Figure 5.2 (Jarrar and Ghanem, 2021).

The Humrat unit is alkali feldspar granites to syenogranites that are reddish in color, aphyric, medium to coarse-grained and comprises principally microperthite,

albite plagioclase and quartz with occasional biotite and accessories of apatite, zircon, titatnite and fluorite. Micrographic texture is occasionally present between microperthite and quartz (Figure. 5 A&B).

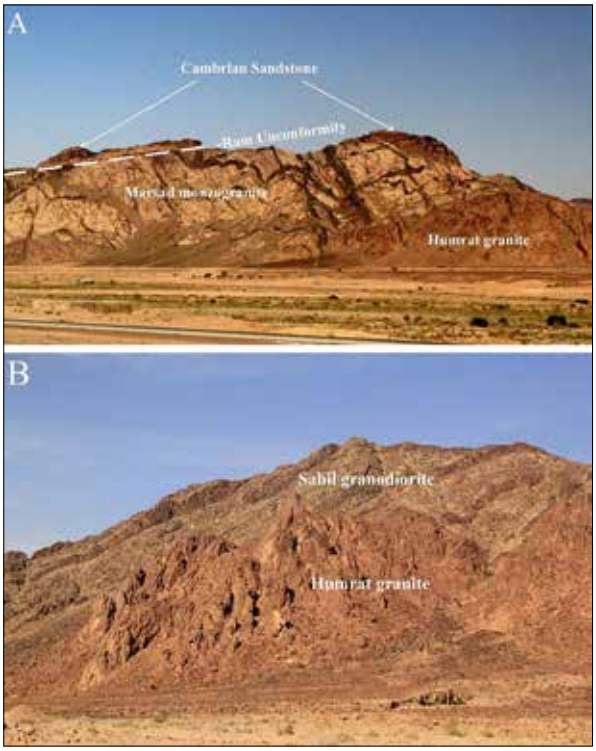

Figure 4. A. The Humrat granite is carrying Marsad granite as roof pendants, and both are truncated by the Ram Unconformity. Note the abundance of dykes in the Marsad granite compared to the dolerite cutting both types of granites. **B.** Humrat granites intruding the Sabil granodiorite with vertical contacts. Note the rhyolite dykes crossing the Sabil granodiorite in the background.

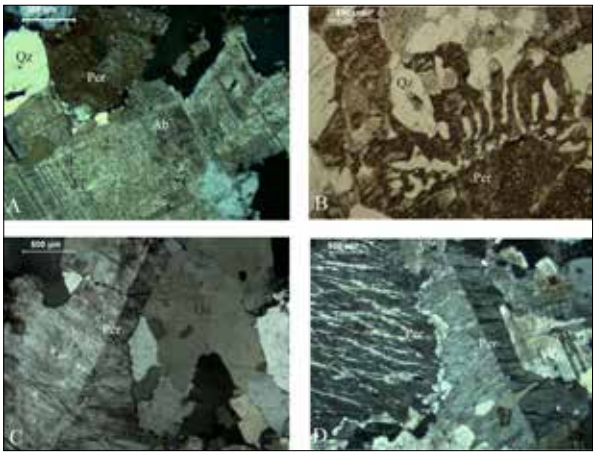

Figure 5. A sericitized albite (Ab) and perthite (Per) in Humrat granite (X-Nicols); **B.** micrographic texture of quartz intergrowth with perthite in Humrat granite (PPL, Sample NF-43); **C.** Slightly weathered perthite with simple twin in Feinan Granite (X-Nicols, Sample NF-31) ; Herringbone structure in perthite in Mubarak granite (X-Nicols, Sample NF-39).

Feinan granite is massive medium to coarse grained and locally pegmatitic. It consists of micro to mesoperthite, albite plagioclase, and quartz as major constituents. Accessories of chloritized biotite, fluorite, zircon, apatite, titanite and opaques. Feinan granite consists of brownish to cloudy microperthite and quartz, with scarce albite (Figure. 5C).

Mubarak granite consists of albite (An ~5%), perthite, and quartz. Scarce biotite and opaque. The Mubarak Monzogranite is coarse-grained to sub-pegmatitic granite with rare aggregates of biotite. The perthite displays the Manebach twin with a typical herringbone pattern of exsolved albite (Figure. 5D).

The Sabil granodiorite is greenish grey weathered medium to coarse-grained granular hypidiomorphic rock with a high color index due to the abundance of hornblende, biotite, and titanite. In the field, it forms low-lying hills relative to the intruding, brick-red alkali feldspar granite of the Humrat unit. Oligoclase is the principal mineral that occurs as subhedral tabular to prismatic grains, complexly twinned, and often with weathered cores. A flow texture is obvious from the arrangement of the plagioclase (Figure. 6 A) Quartz is dull grey and occurs with K-feldspar and interstitial milky white plagioclase.

Hornblende is euhedral, brownish green, and strongly pleochroic (Figure. 6B).

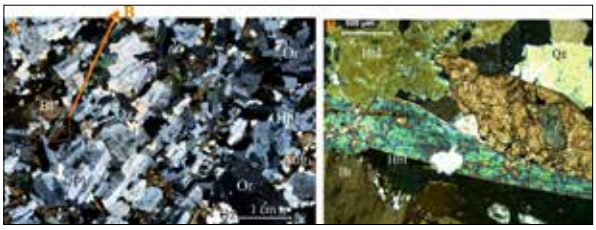

Figure 6. A. whole thin section microphotograph of Sabil granodiorite (X-Nicols, Sample NF-8). Flow texture is well demonstrated by the twinned prismatic oligoclase (PL). Hornblende (Hbl., bioitite (Bt.), and titanite (Tn) form clusters. Some hornblende is rimming augite (Aug). Orthoclase (Or) and quartz (Qz) are interstitial phases. **B.** Enlarged part of A, indicated by the arrow, showing hornblende, titanite quartz, and biotite.

4. Analytical Techniques

Fifty-nine samples were collected from the investigated granitoids for the purpose of petrographic, geochemical, isotopic characterization, and age determination. Zircon concentrates were separated from six samples, about 20 kg each. Standard polished thin-sections were prepared for petrographic study at the Department of Geology, the University of Jordan; and for microprobe analysis at Helmholtz-Zentrum Potsam, Deutsches GeoForschungsZentrum (GFZ) laboratories in Potsdam and at the Institute for Mineralogy and Crystallography, Stuttgart University, Germany. Sample powder preparation for chemical analysis was also carried out at the University of Jordan and GFZ.

Bulk chemistry was determined at the GFZ, namely H_2O and CO_2 on elementary analyzer (Vario EL); major oxides and selected trace elements (Ba, Cr, Ga, Ni, Nb, Rb, Sr, V, Zn, and Zr) on Axios advanced spectrometer system from Panalytical; the REE and Ba, Y, Li, Co, Cu, Zn, Rb, Sr, Cs, Nb, Hf, Ta, Pb, Th, and U for 24 samples on Inductively coupled plasma-atomic emission spectrometer ICP-AES(VISTA MPX); and the concentrations of Li, Be, Nb, Mo, Cd, Cu, Tl, Bi, Co, Sb, and Sn were determined on the VG Plasma Quad PG2 ICP-MS following the procedure outlined by Romer and Hanhe (2010). Details on the procedure of REE concentration and analysis can be found in Zugeler and Erzinger (1988) and Dulski (2001).

A total of 52 zircon, 12 titanite, and 6 feldspar fractions were separated from six whole rock samples at the GFZ geochronology lab in Potsdam. Jaw and roller crusher were utilized for grinding the samples to less than 400-micron size. The concentration of zircons, titanite, and feldspar was achieved using shaking table, heavy liquids: bromoform and di-iodomethane, and a Frantz magnetic Barrier separator (LB-1). Additional purification was performed by hand-picking under a binocular microscope. The zircons of Feinan and Mubarak granites were further abraded by pyrite in a small metallic instrument that uses air pressure to remove coated and weathered rims. Purified zircons and titanites were cleaned by washing successively with 7N HNO3, distilled water, and acetone. Thereafter, ca. 0.1 mg fractions were prepared, spiked with ^{205}Pb-^{235}U tracer, and dissolved in concentrated HF in a Parr autoclave for four days at 200 °C; dried and redissolved in 6N HCl for one day at 200 °C. Three to 4 mg of feldspar from each sample were ground in a mortar and leached with a mixture of 0.8N HBr and HF to get rid of non-structural lead. The cleaned feldspar was then dissolved in HF on a hotplate at ca. 160 °C overnight.

For whole rock Rb-Sr and Sm-Nd isotopic analysis, ca 140 mg of powdered rock were dissolved in HF for four days at 160 ◦C and redissolved in 6N HCl for one day (Pfaff et al., 2009). Extraction of U, Pb, Sr, and Nd from zircons, titanite, feldspar, and whole rock samples was performed using ion exchange chromatography described by Schmidt et al., 2003; Pfaff et al., 2009; and Romer and Hahne, 2010. Lead and uranium were loaded together with HNO3 and silica gel on single rhenium filaments and their isotopic composition was measured at 1210-1240 and 1320-1420 ◦C, respectively on Finnigan MAT262 multicollector mass spectrometer in static multicollection mode. Mass fractionation was corrected with 0.1% / amu.(Pfaff et al., 2009). Strontium was loaded on a single Ta-filament and its isotopic composition was measured on a TRITON multicollector mass spectrometer in a dynamic multi-collection setup; while neodymium was loaded on a double Re-filament and its isotopic composition was measured on a Finnigan MAT262 multicollector mass spectrometer.

5. Geochemistry

The chemical data, including CIPW norms for the studies rocks, are listed in Table 1 (supplementary data, available upon request from the third author). The investigated granitoids have average silica contents of 76.3, 74.5, 76.7, and 65.3 wt. % for the Humrat, Feinan, Mubarak, and Sabil, respectively. On the Harker variation plots (Figure. 7) of selected major and trace elements versus silica, the four units define a smooth liquid line of descent starting with the Sabil granodiorite and ending with Humrat granite. Nevertheless, the Humrat, Mubarak, and Feinan lithologies do show cluster of data points rather than a scatter and this is due to their narrow range of silica content.

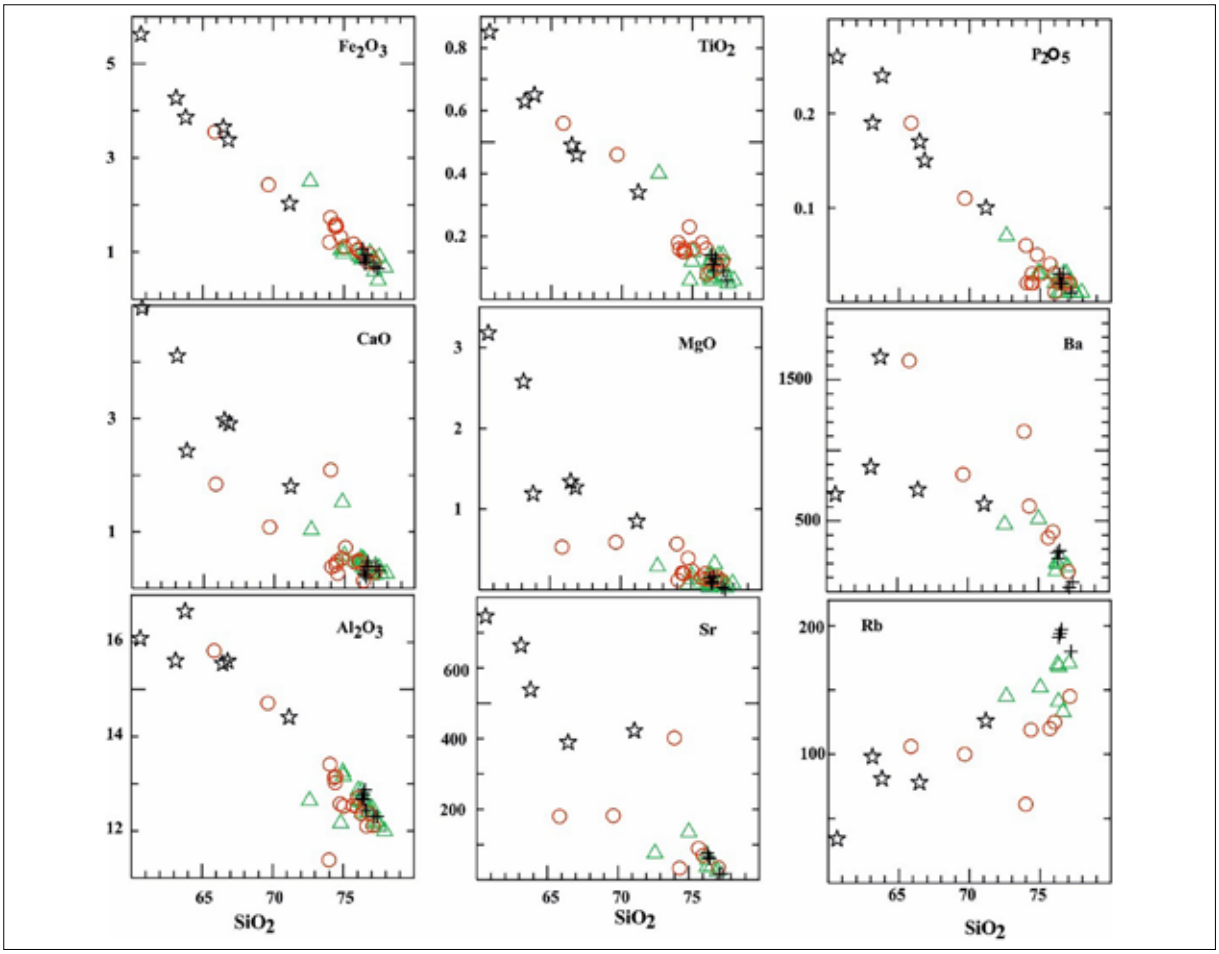

Figure 7. Harker variation diagrams of major elements (wt.%), Rb, and Sr (ppm) versus silica (wt.%) of the investigated rock units. Symbols: Stars = Sabil granodiorite, circles = Feinan granite, triangles = Humrat granite, crosses = Mubarak granite

The normative mineralogy places the first three rock units (HFM) into the syeno- to alkali-feldspar granite fields and the Sabil unit into and quartz monzodiorite and granodiorite fields (Figure. 8A). Furthermore, the Humrat-Feinan-Mubarak (HFM) alkali feldspar granite cluster close to the granite minimum on the normative AB-Q-OR triangle while Sabil samples plot further down from this point together with two samples from the Feinan granite (Figure no shown). Most of the samples of the HFM samples plot in the field of A-type granite except for few samples that straddle the border to the I and S-type granites (Figures 8 Band C). On the same plot the Sabil samples fall into the I and S-type granites or close to the border to the A-type field. The investigated two suites belong to the high-K alkali-calcic to alkali granitoids (Figure 8D & E). The HFM granites have a ferroan affinity while the Sabil unit granodiorites is magnesian in the sense of Frost et al. 2001 (Figure. 8F). Furthermore, the majority of the samples plot in the peraluminous field (Figure. 8G).

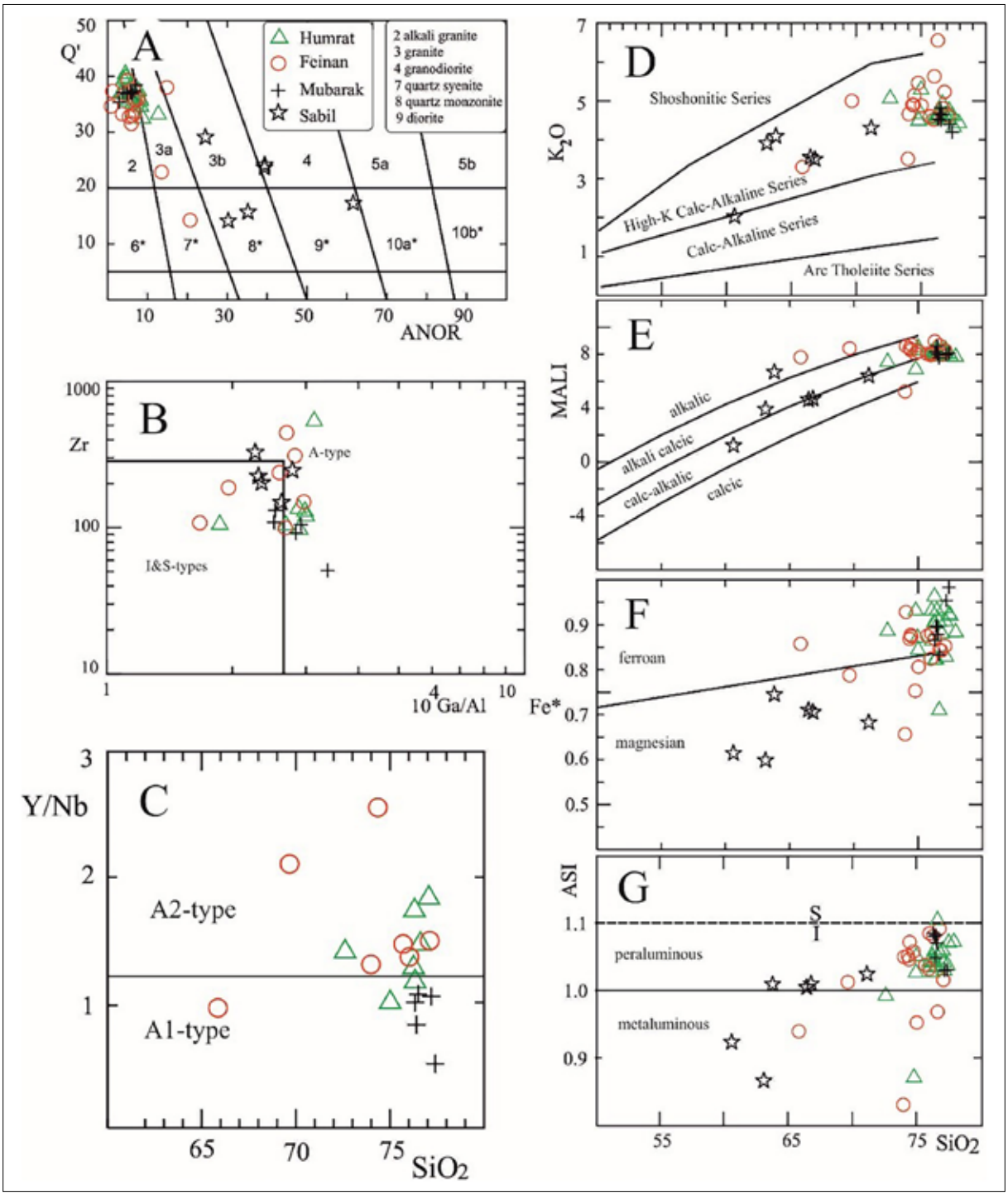

Figure 8. Chemical classification diagrams of the investigated rocks. **A.** Q'-ANOR normative classification of igneous rocks (Streckeisen and Le Maitre, 1979), **B.** Zr (ppm)-(10000*Ga/Al) classification of granitoids (Whalen et al., 1987).
C. Y/Nb vs. SiO2 (wt. %) discrimination diagram of A-type granites (Eby, 1992), **D.** K2O (wt.%) vs. SiO2 (wt. %) plot with lines after LeMaitre 1989 and Rickwood 1989, **E.** MALLI Index vs. SiO2 (wt.%) (Frost and Frost, 2008), **F.** Fe-index vs. SiO2 (wt. %) (Frost et al., 2001), **G.** ASI (Alumina saturation index) vs. SiO2 (wt. %) (Frost et al., 2008)

The investigated granitoids display three different chondrite-normalized patterns: The Humrat and Feinan have almost identical patterns with enriched LREE patterns and flat HREE and strong Eu anomaly (Figure. 9A & B); the Mubarak granites, on the other hand, shows a concave upward pattern with the lowest total REE content (Fig. 9C); To the contrary, the Sabil granodiorite (Figure. 9D) have a steep pattern (La/Lu)N = 8.4-25.5 with weak negative anomaly (Eu/Eu*=0.7-1.0) . The Dy/Dy* was calculated using the formula suggested by Davidson et al., 2013 and plotted versus Dy/Yb ratios. The well-defined trend on this diagram (Figure. 10) points to amphibole and clinopyroxene fractionation as controlling factor in the evolution of these granitoids where the Mubarak granites suffered the highest degree of differentiation

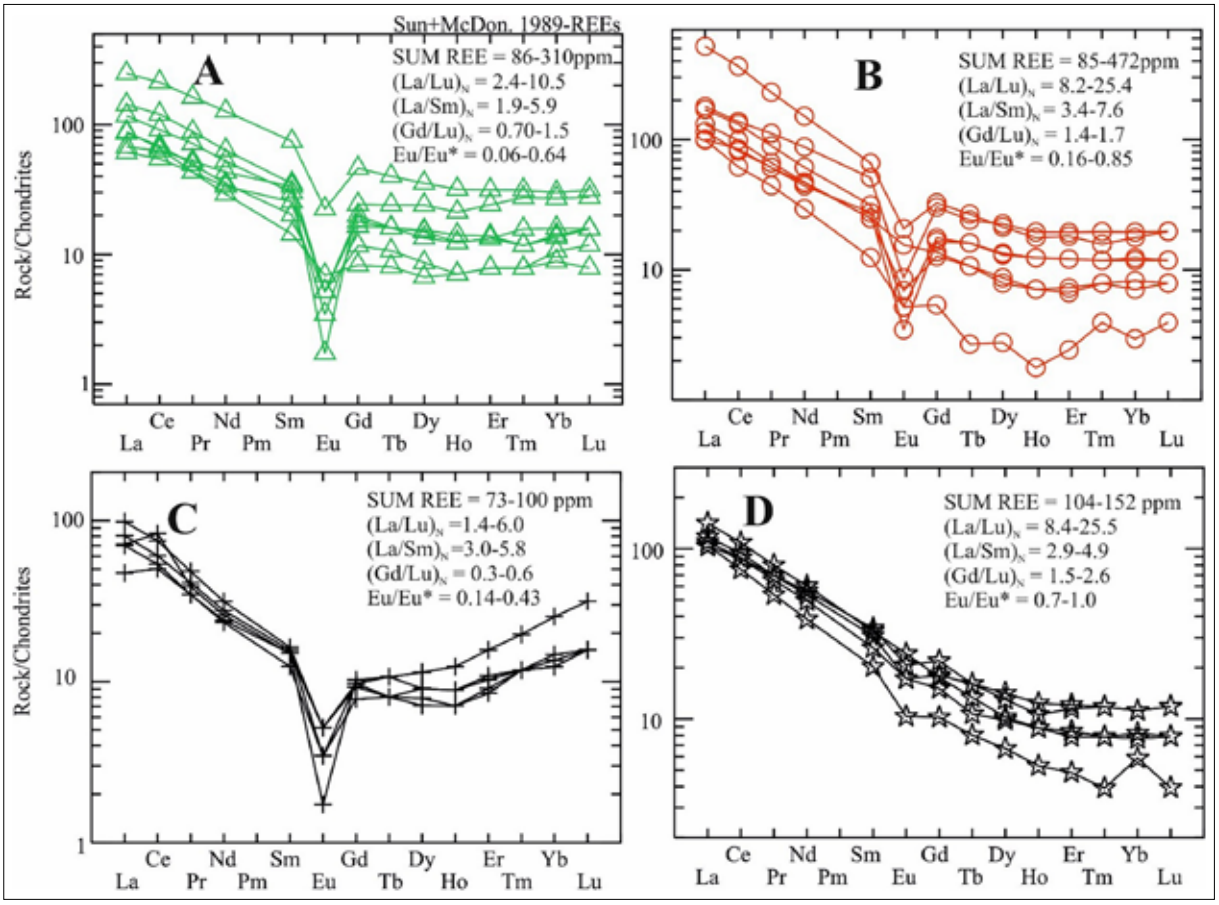

Figure 9. Chondrite-normalized pattern for the Humrat (**A**), Feinan (**B**), Mubarak (**C**), Sabil (**D**) units, respectively. Normalizing values are from Sun and McDonough, 1989.

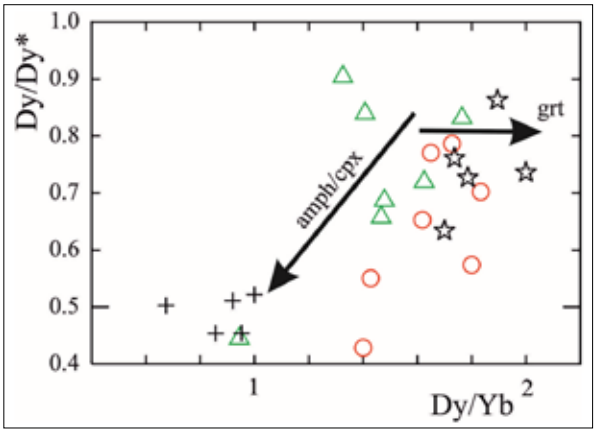

Figure 10. The Dy/Dy* vs. Dy/Yb plot (Davidson et al., 2013). The arrow indicated by the garnet might indicate the amount of residual garnet in the source area of Sabil granodiorite.

On the multi-element spider diagram, the HFM (Figure. 11A, B, and C) as well as the Sabil (Figure. 11D) units are variably enriched in Cs, Rb, Th, U, and Pb. On the other hand, the HFM units display variable degrees of Ba, Sr, and P depletions with Mubarak being the most prominent. The strongest Nb-Ta anomaly is shown by the Sabil unit and followed by Feinan, Humrat, and Mubarak in a decreasing order.

The trace element data is further used to make inferences regarding the tectonic setting of the investigated rocks and to discriminate the A-type granite. On the Nb-Y diagram (Figure 12A, Pearce et al. 1984) all samples plot in the VAG and syn-collisional granite except for 2 samples from Humrat and one from Mubarak units which fall in the within plate field. On the Rb versus Nb+Y diagram (Figure. 12 B, Pearce et al. 1984; Pearce et al. 1996) almost all samples plot in the post-collisional field. The post-collisional setting for the Humrat and Mubarak units is further confirmed by the Hf-Rb/30- Ta*3 and Hf-Rb/30-Nb/4 ternary plots (Figure. 12 C & D, Harris et al. 1986). On the other hand, the Feinan and Sabil units fall into the VAG field. The within-plate setting for the HFM units is confirmed by the Nb/Y vs. SiO2 diagram (Figure. 12 E, Pearce and Gale, 1977). Nonetheless, two samples from Feinan Unit plots together with the samples from the Sabil unit in the field of volcanic arc magmas.

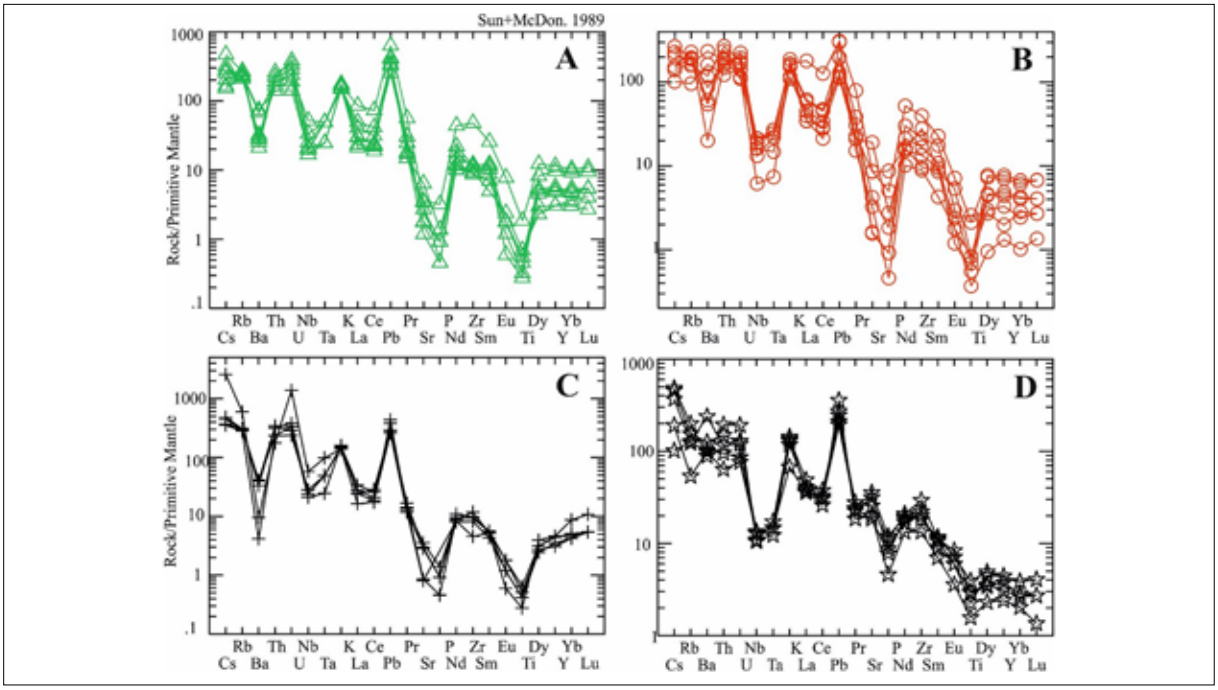

Figure 11. Multi-element spider diagrams for the Humrat (**A**), Feinan (**B**), Mubarak (**C**), and Sabil (**D**) units, respectively.

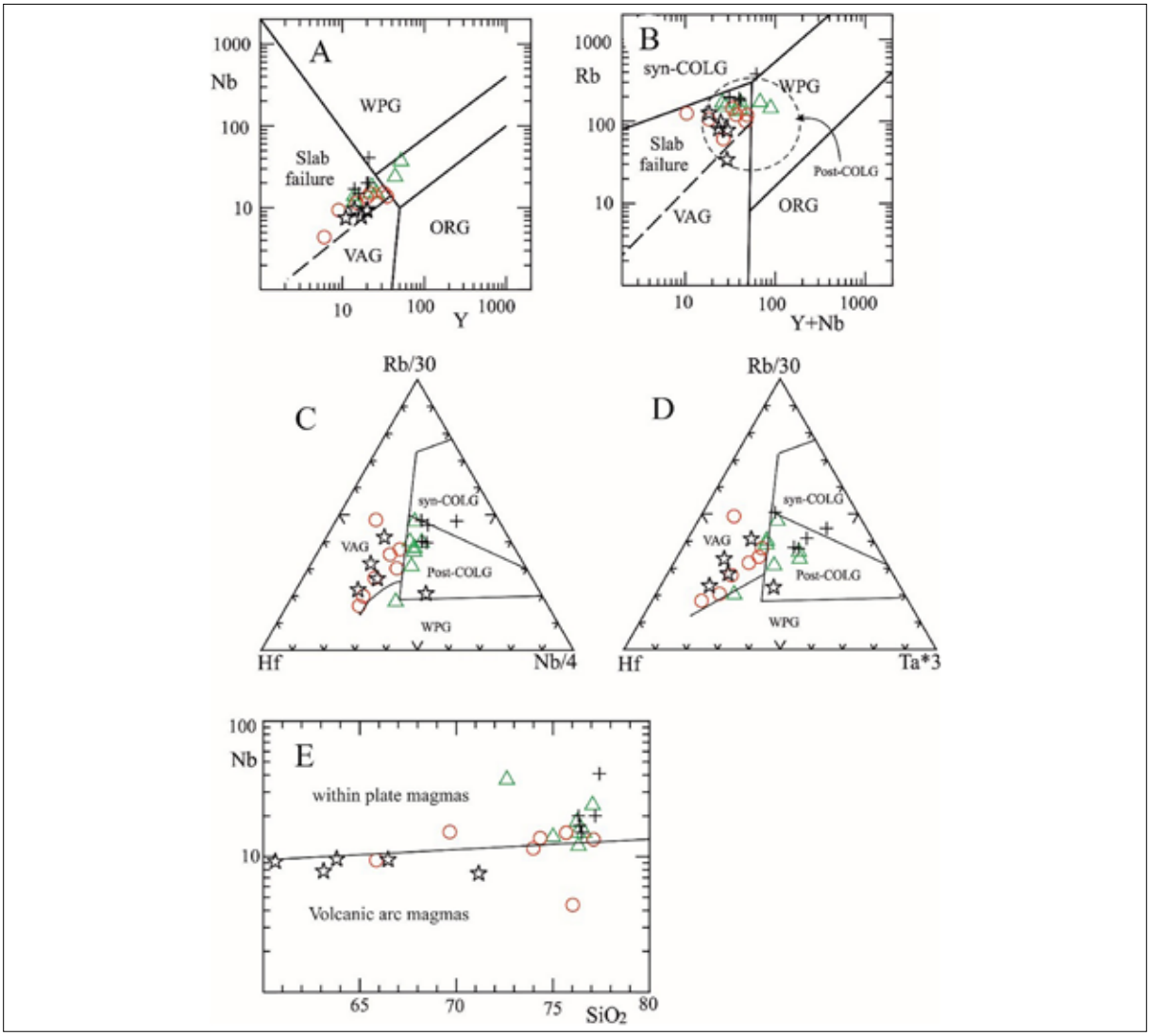

Figure 12. Tectonic discrimination diagrams. **A.** Nb (ppm) vs. Y (ppm) (Pearce et al. 1984), **B.** Rb (ppm) vs. Y+Nb (ppm)(Pearce et al. 1996), **C** & **D.** Hf-Rb-Ta (ppm) plots after Harris et al. 1986, **E.** Nb (ppm) vs SiO2 (wt. %) (Pearce and Gale, 1977). Symbols as in Figure. 7. The dashed line in **A** and **B** separates the volcanic arc granite (VAG) from Slab failure granites in the sense of Whalen and Hildebrandt (2019).

6. Mineral chemistry and thermo-barometric constraints.

Four representative polished thin sections (NF-8, NF-31, NF- 39, and NF-43) were made from the four investigated units and analyzed for plagioclase, alkali feldspar, amphibole, biotite, and opaques on Cameca electron microprobe (SX-100) at the Institute for Mineralogy and Crystallography, University of Stuttgart, Germany. Representative analyses with their respective chemical formulae are presented in Appendix 2. The feldspar chemical variation of the four units is shown in Figure 13A. In the granitic unit of Feinan, Humrat, and Mubarak, the alkali feldspars are either anorthoclase ($Or_{0\text{-}30\ \%}$) or orthoclase ($Or_{70\text{-}100\%}$). On the other hand, they are K-rich ($Or_{85\text{-}95\%}$) in the Sabil granodiorite unit.

The orthoclase of the Sabil (Sabit) granodiorite is in equilibrium with oligoclase ($An_{10\text{-}30\ \%}$). The amphiboles of the Sabil granodiorite are classified as Edenites of the calcic-amphiboles (Figure. 13B). We used the Zr content of the investigated rocks vs. their chemistry expressed by the parameter M = (Na+K+2Ca)/(Al*Si) to estimate the temperature of crystallization. The Sabil granodiorites cluster between the isotherms 800 -850 C. Humrat and Mubarak granite mostly around 800 while the Feinan granites show a larger scatter 800 – 850. Nevertheless, two samples from the granites fall around 950C. Furthermore, the crystallization of the Sabil granodiorite was modeled using the online MELTS-software (Ghiorso et al., 2015). All modal minerals of these rocks appeared in the model in a sequence starting with oligoclase, followed by titanomagnetite, biotite, orthoclase, quartz, hornblende and ending with apatite, and titanite. Equilibration and sub-solidus reactions seem to have continued up to 600 °C (Figure.13. D). The order of crystallization and the amount of modeled minerals fits well with thin section observations (Figure. 6A&B).

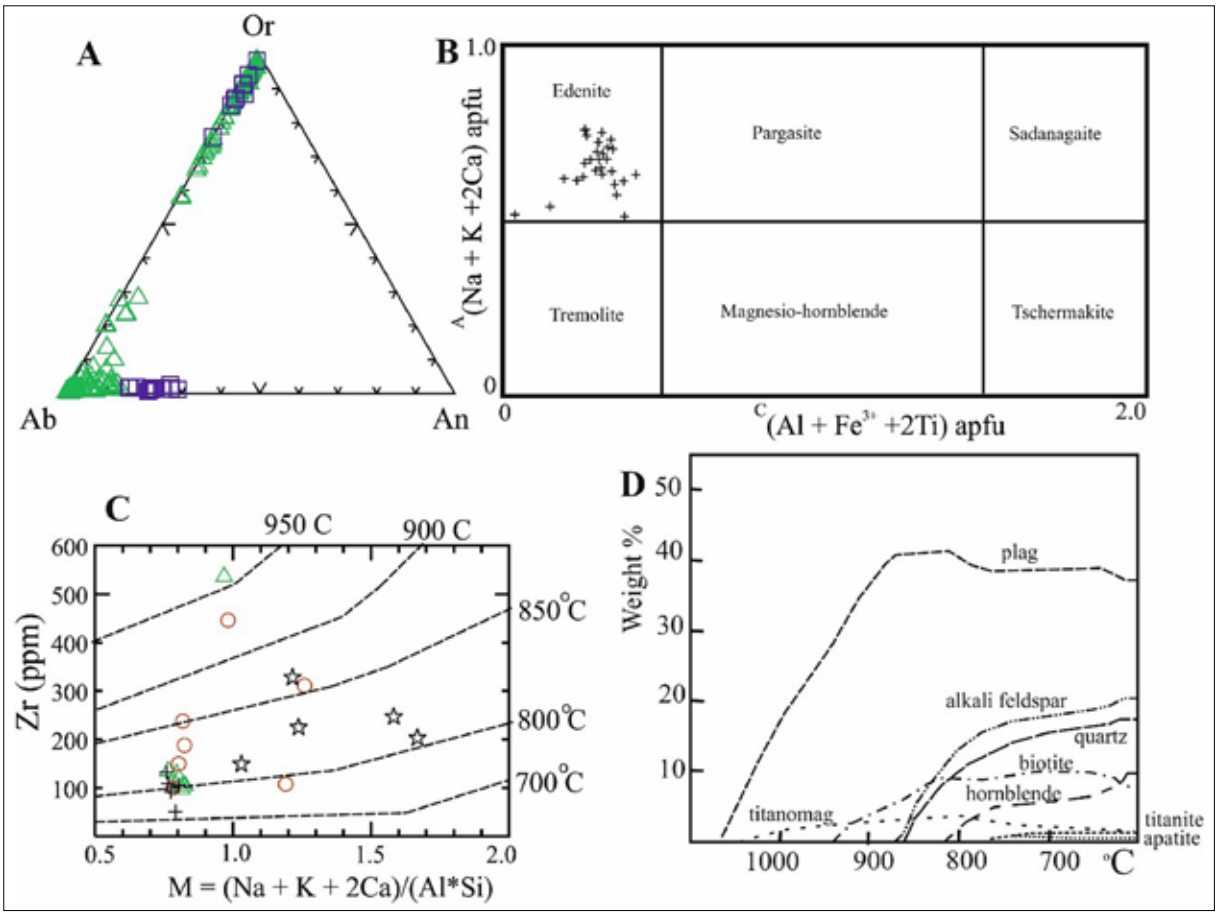

Figure 13. A. Compositional variation of feldspars in the investigated rocks. The blue squares for Sabil granodiorites, **B.** Amphibole chemistry plotted on the calcic-amphiboles diagram (Hawthorne et al. 2012), **C.** Zircon saturation thermometer (Watson & Harrison, 1983), **D.** Crystallization sequence and amounts of minerals in the Sabil granodiorite modeled by MELTS-Software (Ghiorso and Gualda, 2015).

7. Geochronology

A total of fifty two euhedral to subhedral inclusions and fractures—free zircon fractions and twelve titanites fractions— were separated from bulk samples of the four investigated rock units. Turbid and partially metamict zircons were abraded to get clear fresh cores. The isotopic data is presented in Table 2 while the concordia plots for the investigated units are shown in Figure 13. The $^{207}Pb/^{206}Pb$ ages were calculated (Table 2), as these are insensitive to recent lead loss. Potassium feldspar was separated from the same samples and leached before analysis following the procedure by Romer, et al. (1996) and used for the correction of common Pb (Table 3).

A summary of the robust zircon U–Pb ages for all samples is discussed below.

Table 2. The isotopic data of the investigated rocks.

Sample[a] (zircon fractions)		Weight (mg)	Concentration (ppm)		Measured ratios[b]	Radiogenic Pb (at.%)[c]				atomic ratios[c]			Apparent ages (Ma)[d]		
			U	Pb_{tot}	$^{206}Pb/^{204}Pb$	^{206}Pb	^{207}Pb	^{208}Pb	$^{238}U/^{204}Pb$	$^{206}Pb/^{238}U$	$^{207}Pb/^{235}U$	$^{207}Pb/^{206}Pb$	$^{206}Pb/^{238}U$	$^{207}Pb/^{235}U$	$^{207}Pb/^{206}Pb$
Humrat Alkali granite															
NF1 Zircon	1	0.048	480.4	34.06	534.792	6.120	0.35	0.68	8894	0.0636	0.4959	0.0565	398	409	474
	2	0.038	618.9	50.50	1115.58	7.260	0.44	1.19	17544	0.0741	0.6117	0.0599	461	485	599
	3	0.078	658.5	54.07	821.353	15.79	0.94	2.37	11504	0.0737	0.6049	0.0595	458	480	587
	4	0.120	923.4	65.69	657.905	29.02	1.73	4.27	10446	0.0628	0.5152	0.0595	393	422	586
	5	0.098	1084	85.34	979.601	31.97	1.89	4.36	13775	0.0721	0.5892	0.0593	449	470	576
	6	0.109	1093	81.39	471.150	31.65	1.88	4.50	7225	0.0637	0.5219	0.0594	398	426	583
	7	0.192	1057	79.87	603.624	55.90	3.35	8.28	8979	0.0660	0.5451	0.0599	412	442	600
NF11 Zircon	8	0.092	581.7	57.92	166.051	14.90	0.89	2.85	2243	0.0668	0.5481	0.0596	417	444	588
	9	0.084	550.8	46.15	531.101	13.54	0.80	2.61	7608	0.0702	0.5744	0.0594	437	461	581
	10	0.127	551.5	67.25	108.146	20.04	1.20	4.20	1323	0.0686	0.5660	0.0599	428	455	598
	11	0.096	506.0	48.98	194.460	13.72	0.81	2.71	2642	0.0677	0.5538	0.0593	422	448	578
	12	0.116	657.6	51.14	366.722	19.94	1.19	3.57	5671	0.0627	0.5126	0.0596	392	422	588
	13	0.134	549.2	51.12	298.805	22.16	1.32	4.11	3945	0.0722	0.5926	0.0596	449	473	587
Feinan Alkali granite															
NF21	14	0.085	335.4	31.36	1340.56	9.860	0.59	2.01	18496	0.0829	0.6859	0.0600	513	530	605
Abraded zircon	15	0.113	377.1	34.80	1677.92	14.78	0.89	2.83	22691	0.0831	0.6886	0.0601	515	532	606
	16	0.091	448.2	42.06	952.87	13.96	0.84	2.74	12235	0.0821	0.6800	0.0601	509	527	607
	17	0.106	319.5	32.30	1075.35	12.62	0.76	2.42	12946	0.0894	0.7396	0.0603	552	562	604
	18	0.098	480	51.9	193	14.8	0.89	2.89	2347	0.0756	0.6288	0.0603	470	495	616
	19	0.171	448	48.2	330	26.9	1.62	5.21	3746	0.0843	0.6971	0.0600	522	537	604
NF21	20	0.105	363	44.26	1813	17.65	1.06	3.19	18083	0.1111	0.9177	0.0599	679	661	601
Non abraded zircon	21	0.111	546	42.86	492	16.46	0.99	3.18	7518	0.0651	0.5370	0.0599	406	437	599
	22	0.099	388	37.5	650	13.11	0.79	2.67	8115	0.0819	0.6761	0.0599	509	524	600
Titanite	23	0.183	67.3	17.03	141.730	6.040	0.36	5.21	1074	0.1177	0.9742	0.0600	717	691	604

Continuing from Table 2 . The isotopic data of the investigated rocks.

Sample[a] (zircon fractions)		Weight (mg)	Concentration (ppm)		Measured ratios[b]	Radiogenic Pb (at.%)[c]				atomic ratios[c]			Apparent ages (Ma)[d]		
			U	Pb_{tot}	$^{206}Pb/^{204}Pb$	^{206}Pb	^{207}Pb	^{208}Pb	$^{238}U/^{204}Pb$	$^{206}Pb/^{238}U$	$^{207}Pb/^{235}U$	$^{207}Pb/^{206}Pb$	$^{206}Pb/^{238}U$	$^{207}Pb/^{235}U$	$^{207}Pb/^{206}Pb$
	24	0.201	73.3	16.24	110.500	5.730	0.34	5.31	1008	0.0934	0.7729	0.0600	576	581	605
	25	0.218	37.3	9.300	136.851	3.350	0.20	4.29	1248	0.0989	0.8201	0.0602	608	608	610
	26	0.284	92.4	18.39	146.938	11.11	0.67	7.35	1287	0.1015	0.8447	0.0604	623	622	616
	27	0.181	76.6	36.14	39.0540	6.060	0.36	4.72	203	0.1048	0.8498	0.0588	642	625	560
	28	0.249	60.6	13.52	143.412	6.430	0.38	5.84	1253	0.1022	0.8367	0.0594	627	617	581
NF31	29	0.094	1025.3	93.650	744.366	32.60	1.95	4.94	9170	0.0811	0.6703	0.0599	503	521	601
Abraded zircon	30	0.083	917.50	86.220	579.161	26.25	1.58	3.56	6944	0.0827	0.6851	0.0601	512	530	608
(1^{st} time)	31	0.076	1115.4	105.98	447.262	28.40	1.69	4.15	5408	0.0803	0.6593	0.0598	498	514	597
	32	0.130	1026.6	97.060	639.762	46.34	2.79	6.73	7582	0.0832	0.6919	0.0603	516	534	614
	33	0.243	1113.0	104.70	406.150	88.61	5.30	13.0	4968	0.0786	0.6476	0.0598	487	507	596
	34	0.121	1314.9	120.05	524.693	52.43	3.14	7.45	6483	0.0790	0.6530	0.0599	490	510	602
NF31	35	0.099	1858.5	186.11	2271.76	72.05	4.32	10.7	24820	0.0939	0.7767	0.0600	578	584	604
Abraded zircon	36	0.099	1581.1	159.82	1152.80	59.84	3.59	9.5	12629	0.0917	0.7582	0.0600	565	573	603
(2^{nd} time)	37	0.084	1747.3	179.99	1141.55	57.59	3.45	8.6	12191	0.0941	0.7780	0.5997	580	584	603
	38	0.106	1906.8	191.86	1445.04	78.28	4.70	11.7	15683	0.0928	0.7679	0.0600	572	579	603
	39	0.188	1636.5	163.17	1796.50	119.1	7.14	17.8	19503	0.0928	0.7673	0.0600	572	578	603
	40	0.199	1855.6	186.51	1301.10	140.8	8.45	22.8	14182	0.0914	0.7565	0.0600	564	572	604
NF31	41	0.099	1145.4	111.35	386.538	38.13	2.28	5.63	4619	0.0806	0.6633	0.0597	500	517	592
Non abraded zircon	42	0.085	1576.9	157.50	390.598	46.04	2.76	7.24	4564	0.0824	0.6805	0.0599	510	527	601
Mubarak Alkali granite															
NF38	43	0.076	557.4	59.67	713.435	16.76	1.01	2.55	7660	0.0949	0.7846	0.0600	584	588	603
Abraded zircon	44	0.121	570.3	68.28	278.435	27.01	1.62	4.01	2806	0.0938	0.7749	0.0599	578	583	600
	45	0.080	564.6	62.97	438.074	17.51	1.05	2.92	4635	0.0929	0.7680	0.0599	573	579	601
	46	0.071	637.4	71.93	403.645	17.64	1.06	2.82	4222	0.0935	0.7722	0.0599	576	581	600
	47	0.101	437.5	48.18	430.529	17.03	1.02	2.63	4580	0.0924	0.7634	0.0599	570	576	601

Continuing from Table 2 . The isotopic data of the investigated rocks.

Sample[a] (zircon fractions)		Weight (mg)	Concentration (ppm)		Measured ratios[b]	Radiogenic Pb (at.%)[c]				atomic ratios[c]			Apparent ages (Ma)[d]		
			U	Pb_{tot}	$^{206}Pb/^{204}Pb$	^{206}Pb	^{207}Pb	^{208}Pb	$^{238}U/^{204}Pb$	$^{206}Pb/^{238}U$	$^{207}Pb/^{235}U$	$^{207}Pb/^{206}Pb$	$^{206}Pb/^{238}U$	$^{207}Pb/^{235}U$	$^{207}Pb/^{206}Pb$
	48	0.186	597.5	67.75	367.443	43.28	2.61	6.33	3777	0.0934	0.7764	0.0603	575	583	615
	49	0.070	772	96.90	204.078	20.55	1.23	3.20	2062	0.0912	0.7548	0.0600	562	571	605
NF38	50	0.080	853.1	96.75	324.809	26.23	1.58	3.61	3372	0.0921	0.7653	0.0602	568	577	612
Non abraded zircon	51	0.160	827.4	96.66	262.988	49.41	2.98	8.09	2754	0.0895	0.7430	0.0602	553	564	611
	52	0.096	704.2	76.47	316.610	24.27	1.46	4.05	3515	0.0861	0.7150	0.0602	532	548	612
	53	0.105	712.7	84.75	234.954	27.66	1.67	4.67	2470	0.0886	0.7363	0.0603	547	560	613
Sabil granodiorite															
NF8 Zircon	54	0.099	236.4	25.91	2829.989	9.65	0.58	2.03	40628	0.0988	0.8205	0.0602	608	608	611
	55	0.130	252.2	26.65	3969.613	13.33	0.81	2.49	59367	0.0975	0.8112	0.0604	600	603	617
	56	0.104	255.1	27.66	4878.034	10.96	0.66	2.22	90078	0.0991	0.8263	0.0605	609	612	621
	57	0.089	268.7	28.74	2768.216	9.71	0.59	1.91	39789	0.0974	0.8093	0.0603	599	602	614
	58	0.105	230	24.31	4559.555	9.83	0.59	1.86	88324	0.0976	0.8123	0.0604	600	604	616
	59	0.153	183.2	19.58	1547.832	11.26	0.68	2.12	18644	0.0963	0.8014	0.0603	593	598	616
NF8 Titanite	60	0.168	229.2	42.77	545.914	17.66	1.09	13.65	4958	0.1099	0.9381	0.0619	672	672	671
	61	0.203	223.5	43.85	446.517	20.04	1.21	18.47	4139	0.1059	0.8790	0.0602	649	640	611
	62	0.253	213.7	41.64	538.095	23.72	1.43	22.54	5062	0.1051	0.8728	0.0602	645	637	611
	63	0.244	216.1	46	485.418	23.75	1.44	25.44	4419	0.1080	0.9007	0.0605	661	652	621
	64	0.236	173.5	40.18	591.450	19.96	1.21	22.19	5057	0.1169	0.9742	0.0605	713	691	620
	65	0.182	188.2	40.87	618.905	16.04	0.97	17.07	5566	0.1123	0.9335	0.0603	686	670	614

[a] Zircon concentrates were cleaned in warm 7N HNO_3 and H_2O before dissolution in concentrated HF in teflon-lined autoclaves at 210°C for 4 days. A mixed ^{205}Pb-^{235}U tracer was added before sample dissolution. Lead and U were separated using ion-exchange chromatographic procedures (e.g., Romer et al., 1996; Schmid et al., 2003). Lead and U were loaded together on single Re-filaments using a silica-gel emitter and H_3PO_4 (Gerstenberger & Haase, 1997) and measured at .1200°–1260°C and 1350–1400°C, respectively, on a Finnigan MAT262 multicollector mass-spectrometer (modified with an ion source by Spectromat) using Faraday collectors and ion counting

(.[b] Lead isotope ratios corrected for fractionation (0.1% / a.m.u

.[c] Lead corrected for fractionation, blank, tracer contribution, and initial lead ($^{206}Pb/^{204}Pb$ = 18.1±0.1, $^{207}Pb/^{204}Pb$ = 15.60±0.02, $^{208}Pb/^{204}Pb$ = 38.2±0.2). During the measurement period, total blanks were <15 pg for lead and <1 pg for uranium

([d] Apparent ages were calculated using the constants recommended by IUGS (Steiger & Jäger, 1977

7.1 Sabil granodiorite unit (NF8)

The uranium and lead contents of the zircons of this unit range between 183 – 269 ppm and 20 – 29 ppm, respectively. They have the highest measured $^{206}Pb/^{204}Pb$ ratios (Table 3) due to their very low common Pb content (0.16 – 0.61 ppm). The data points defined a cluster of concordant to sub-concordant data points on the Terra – Wasserburg Concordia diagram. Nevertheless, the clustering of the data does not constrain a discordia. The U-Pb zircon age is calculated in two ways: (i) A discordia is fitted through the origin of the diagram (0 ± 50 Ma). This yields an upper intercept of 615.8 ± 1.9 Ma (2σ; MSWD = 1.9) (Figure. 14 A). Although six zircon analyzed fractions have been used to calculate the discordia, this analysis essentially represents a two-point discordia (i.e., the data cluster and the origin of the diagram). It should be mentioned here that, without forcing the discordia to pass through zero, the age is 614.3 ± 4.2 M which agrees with the titanite age (614.1 ± 4.2 Ma). The major effect of forcing the discordia through the origin is to increase the age slightly and to reduce the error and the MSWD to more precise values (±1.9 Ma; MSWD = 1.9).

(ii) The weighted $^{207}Pb/^{206}$ Pb age is 615.8 ± 2.7 Ma (2σ, MSWD = 1.9). Both ways to calculate the age implicitly assume a recent disturbance of the U-Pb systems. This assumption has been used to interpret the Discordia diagrams obtained using conventional U-Pb zircon dating of the granitoids in the Arabian-Nubian Shield (e.g. Jarrar et al., 1983; Pallister et al., 1988). The titanite obtained from this sample has a high common lead content (2.1 -3.24 ppm) and, as a result, low to moderate $^{206}Pb/^{204}Pb$ ratios. The data points of these titanites are up to 30% discordant and fall above Concordia diagram; therefore, they are not discussed further. The age of 615 Ma has also been obtained for equivatlent granodiorite using single zircon dating (Ben Sireh, 2018, unpublished PhD thesis).

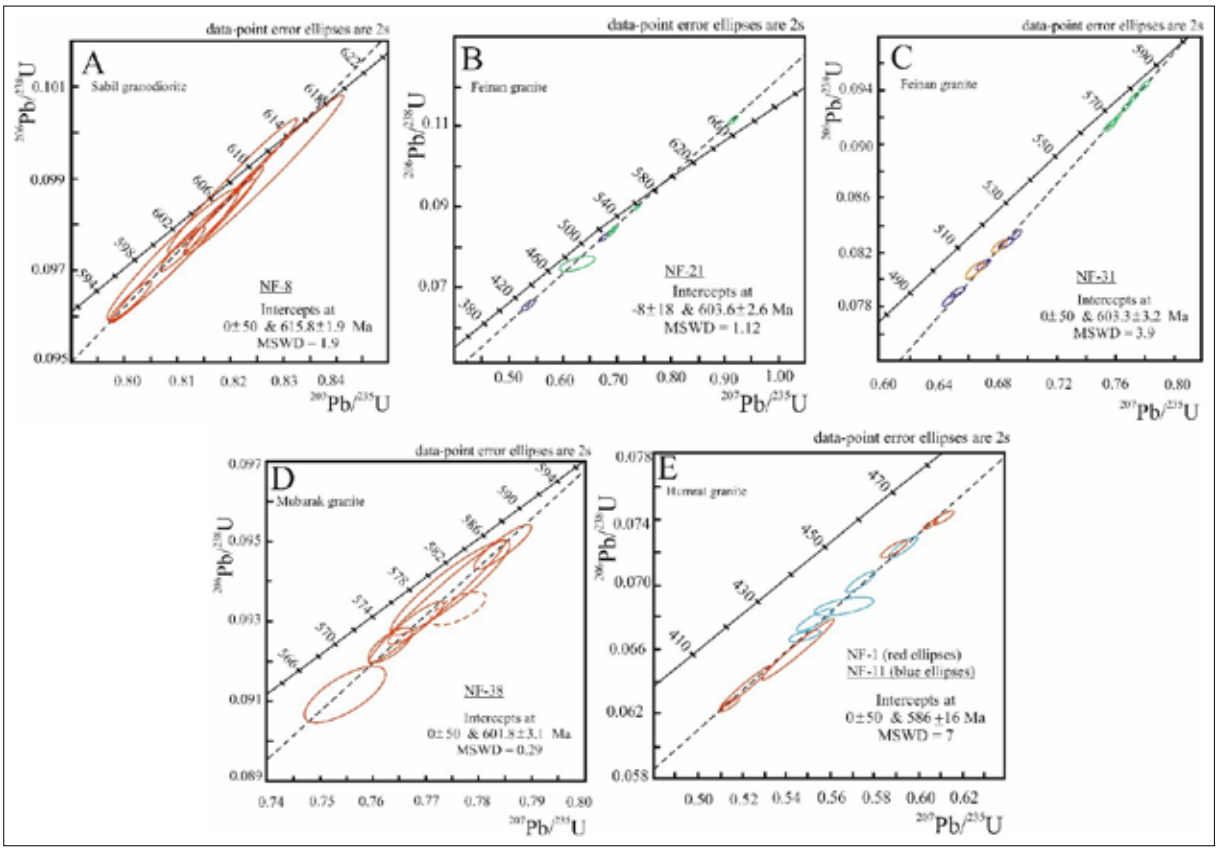

Figure 14. Zircon and titanite Concordia diagrams of the studied rocks.

7.2 Feinan alkali granite (NF21 & NF31)

A twenty-two zircon fractions and titanite grains were hand-picked from NF21 and NF31 samples from the Feinan Alkali granite.

7.2.1 NF21 Zircons

Two zircon fractions have 388 and 546 ppm of uranium and 38 and 43 ppm of total lead with low measured $^{206}Pb/^{204}Pb$ ratios (Table 3) and high common lead content of 3 and 4.5 ppm, respectively. Six more fractions of abraded zircon contain less uranium and total lead, about 320 – 448 ppm and 31–48 ppm, respectively, along with higher measured $^{206}Pb/^{204}Pb$ ratios (Table 3) compared to the non-abraded zircon fractions. The common Pb content is low; around one ppm for all samples except for fraction 18 that contains 7 ppm (Table 3). This indicates that abrasion preferentially removed metamict domains, which in addition to a disturbed U-Pb system also have higher contents of common Pb.

All the samples are discordant and close to the upper intercept, where the non -abraded samples are more discordant and scattered reflecting lead loss. Although few, they yield lower and upper intercepts of 6 ± 46 and 601 ± 11 Ma (2σ; MSWD = 0.0), whereas the abraded samples are less discordant and close to the intercept. They define a line with lower and upper intercepts of -20 ± 21 and 602.6 ± 2.8

Ma (2σ; MSWD = 0.25), consistent with the non-abraded ones. Thus, both abraded and non-abraded samples were plotted together and yielded a discordia line intercepting the Concordia at a more reliable and precise intercept of 603.6 ± 2.6 Ma (2σ; MSWD = 1.12) (Figure. 14B). Titanites are highly heterogeneous and produced intercepts with high uncertainty and therefore are not considered further.

Table 3. Initial Pb isotope data and preferred zircon ages of the investigated granitoids of south Jordan.

Sample	Preferred Zircon age (Ma)	$\frac{^{206}Pb}{^{204}Pb}$ a	$\frac{^{207}Pb}{^{204}Pb}$ a	$\frac{^{208}Pb}{^{204}Pb}$ a
Humrat Alkali granite				
NF1	587±17	17.807	15.570	37.534
NF11	584±16	17.860	15.572	37.581
NF1 & NF11	586±16			
Mubarak Alkali granite				
NF38	601.8±3.1	17.973	15.565	37.561
Feinan Alkali granite				
NF21	603.6±2.6	17.728	15.540	37.426
NF31	603.3±3.2	17.700	15.552	37.488
Sabil Granodiorite				
NF8	615.8±1.9	17.755	15.570	37.550
Average initial lead		17.804±0.3	15.562±0.05	37.523±0.5

a. 3-4 mg of feldspar grains from each sample were smashed in the hand agate mortar, washed with water and a mixture of 0.8N HBr and HF were added to the samples to remove all radiogenic lead. Finally, they were put on a 160 °C hotplate overnight after adding HF to them (Romer and Hanhe, 2010) and measured at 1200 - 1260 °C and 1350 - 1400 °C, respectively, on a Finnigan MAT262 multicollector mass-spectrometer (modified with an ion source by Spectromat) using Faraday collectors and ion counting. Lead isotope data corrected for mass discrimination with 0.1 % / A.M.U. Reproducibility at 2σ level is better than 0.1 %.

7.2.2 NF31-Zircons

The non-abraded zircon fractions have high uranium content (1145 and 1577 ppm) and high total lead amount (111 and 158 ppm) with low measured $^{206}Pb/^{204}Pb$ ratios due to the too-high common lead (15 and 22 ppm). After the first abrasion of six fractions, their U content remains high while the total Pb decreases to (86 – 120 ppm) and the common lead decreases to (7–14 ppm), which increases the measured $^{206}Pb/^{204}Pb$ ratios. More intense abrasion of zircon increased the uranium and the lead to about (1581 – 1907 ppm) and (160 – 192 ppm), respectively. The drop in common lead (5 – 9 ppm) resulted in the high measured $^{206}Pb/^{204}$ Pb ratios (1142 – 2272 ppm, Table 3). As a conclusion, abrasion removed the metamict domains. The increase of the U content is somewhat unexpected as normally domains with higher U content turn more metamict than domains with low contents and, thus, are preferentially removed during abrasion. As abrasion also reduced the common lead content, the measured $^{206}Pb/^{204}Pb$ ratios of the abraded samples were higher. The higher U contents in the abraded samples may indicate that the rims of zircon had lower U contents than the cores did.

Plotting all data of this unit on the Concordia diagram shows that the non-abraded and slightly abraded samples are highly discordant, while the strongly abraded fractions are less discordant. The data of both abraded groups fall along a discordia line that intercepts the concordia at 5 ± 46 and 604 ± 5.3 Ma (2σ; MSWD = 3.4). Forcing the discordia through the origin of the diagram (0±50 Ma) does not affect the upper intercept significantly (603.4 ± 3.1 Ma, 2σ; MSWD = 3.2).

The discordia, produced from all data forced through the origin of the diagram, yields an intercept of 603.3 ± 3.2 Ma (2σ; MSWD = 3.9; Figure. 14C). Using all the layers here offers large spread (scatters) and doesn't affect the intercept age, but makes the line better defined (Figure. 14C). The average weighted $^{207}Pb/^{206}Pb$ age, also yields an age of 603.2 ± 1.6 Ma (2σ; MSWD = 3.8) indicating the robustness of this crystallization age.

7.3 Mubarak alkali granite (NF38)

The abraded zircons from sample NF38 contain 438 to 772 ppm U and a total of 48 to 97 ppm lead, respectively (Table 3). They are characterized by low measured radiogenic $^{206}Pb/^{204}Pb$ ratios which reflect the relatively high common lead content which varies from 4.5 to 23.3 ppm. The non-abraded fractions have higher uranium contents (704 – 853 ppm), and higher common lead contents (12.5–18.7) and consequently lower measured $^{206}Pb/^{204}Pb$ ratios.

All the samples are normally discordant and close to the upper intercept, where the abraded samples are slightly less discordant. As the data cluster, the slope of discordia is not well defined, although there is no or only little excess scatters, e. g., all the data have MSWD of 2.1. Omission of one abraded sample even reduced the MSWD to 0.29 (Figure. 14D).

Because of the close clustering of the data, the slope of the discordia is not well constrained and the intercept with the Concordia is flat, which yields a large uncertainty. Forcing the discordia for the abraded samples through the origin reduces the intercept to 601.8 ± 3.1 Ma with (2σ; MSWD = 0.29; Figure. 13D), which is congruent with the average weighted $^{207}Pb/^{206}Pb$ age (601.8 ± 2.4 Ma, 2σ; MSWD = 0.3), and illustrates the robustness of the age for this unit.

7.4 Humrat alkali feldspar granite unit

NF1 & NF11 - Zircons

The zircon from sample NF1 has U contents ranging from 480 to 1093 ppm and a total lead from 34 to 85 ppm (Table 3) with relatively high common lead content varying from 2.2 to 9.4 ppm, which caused low measured radiogenic $^{206}Pb/^{204}Pb$ ratios. As shown in Figure (6-6), the samples are scattering largely along the discordia (MSWD = 14), where zircons from sample NF11 have perfect dispersion beside them (MSWD = 0.78) (Figure 6-7), and contain about 506 – 582 ppm of U and 46–67 ppm of total lead. The same as NF1, due to the rather high content of common lead of 4.5–26 ppm, the measured $^{206}Pb/^{204}Pb$ is not very radiogenic.

Forcing the discordia through the origin of the diagram (0 ± 50) yields upper intercept age of 587 ± 17 and 584 ± 16 Ma for samples NF1 and N11, respectively. The large uncertainty of the upper intercept age is due to the highly discordant nature of the analyzed zircons and the small spread of the data points along the Concordia. The obtained upper intercept ages, however, are mostly identical.

Since the two samples of the Humrat Alkali unit (NF1 and 11) are from the same pluton and the zircons of both samples are highly discordant and show a relatively small range of scatter along the discordia, their ratios were plotted together on the concordia diagram and gave an age of 586 ± 16 Ma with a relatively high MSWD value equals to 7 (Figure. 14E) consistent with the average weighted

$^{207}Pb/^{206}Pb$ age of 586.2 ± 5 Ma (2σ; MSWD = 7.1). A biotite rhyolite dike (600 ± 4 Ma, $^{40}Ar/^{39}Ar$ age of biotite), an andesite dike (594 ± 3, $^{40}Ar/^{39}Ar$ age of amphibole) and a dolerite dike (~579 Ma, 40Ar/39Ar whole rock total gas age) (Ghanem et al. 2020). The rhyolite and andesite dikes do not cut the Humrat granite, while the dolerite dikes are the only dikes cut through this granite elsewhere in the basement complex of south Jordan.

7.5 Rb-Sr and Sm-Nd data

Rb–Sr and Sm–Nd isotopic data are given in Table 4. Rb contents are higher than Sr contents in all samples except for the samples of the Sabil granodiorite Unit, with a maximum value of 22 in Mubarak Unit and a minimum value of 0.046 in the Sabil Unit (Table 1). This has great effects, in particular for weathered feldspars, on the $^{87}Sr/^{86}Sr$ ratios (Stoeser and Frost, 2006; Eyal et al., 2010). Therefore, only samples with $^{87}Rb/^{86}Sr$ ratios less than 4 were calculated for their initials because these should have experienced modest radiogenic growth for their $^{87}Rb/^{86}Sr$ (Stoeser and Frost, 2006). They yield initial $^{87}Sr/^{86}Sr$ ratios in the range from 0.70146 to 0.71508, with ascending averages of 0.70374, 0.70647, 0.70873, and 0.70947, for the Sabil, Feinan, Humrat and Mubarak samples, respectively.

In particular, the high values (note these samples also have high εNd values) indicate that the Rb/Sr ratio is disturbed, which results in over-and under-correction of in situ ^{87}Sr growth. These values are close to the contemporary depleted mantle, since they are below the ratio of the granitic rocks that have been derived from the crust (0.729), as well as within and above the ratio of the basaltic magma (undifferentiated reservoir) which is 0.7045 (Faure and Mensing, 2005).

Table 4. Rb-Sr and Sm-Nd data.

Sample [a]		$(^{87}Sr/^{86}Sr)^{b}$	Error	$(^{87}Sr/^{86}Sr)_{(T)}{}^{c}$	$(^{143}Nd/^{144}Nd)^{b}$	Error	$\varepsilon Nd_{(T)}{}^{c}$
Humrat alkali granite	NF1	0.783924	5	*0.71508*	0.512491	5	3.3
	NF7	0.731589	6	*0.70560*	0.512492	12	4.5
	NF11	0.808411	5	0.71909	0.512560	5	5.0
	NF12	0.751945	5	*0.70689*	0.512560	5	4.5
	NF45	0.800944	9	0.71734	0.512568	5	4.9
	NF54	0.902443	6	0.74084	0.512666	5	3.9
	NF59	0.762831	7	*0.70735*	0.512615	4	2.9
Mubarak alkali granite	NF10	1.011152	12	0.76418	0.512551	4	4.9
	NF14				0.512508	5	4.6
	NF39	0.769070	8	*0.70767*	0.512506	5	3.6
	NF40	0.785619	4	*0.71127*	0.512522	5	4.9
	NF41	1.270335	7	0.71058	0.512626	5	5.4
Feinan alkali granite	NF16				0.512543	5	3.8
	NF21	0.716882	9	*0.70373*	0.512427	5	4.4
	NF23	0.741231	6	*0.70894*	0.512480	5	4.2
	NF26	0.715448	9	*0.70146*	0.512483	5	4.0
	NF28	0.707734	6	*0.70411*	0.512481	5	4.1
	NF31	0.751308	7	*0.70789*	0.512426	4	4.5
	NF35	0.799512	8	*0.71264*	0.512484	3	3.3
Sabil granodiorite	NF8	0.707482	5	*0.70392*	0.512458	5	3.7
	NF47	0.704731	6	*0.70364*	0.512558	5	4.6
	NF48	0.709092	7	*0.70424*	0.512500	4	4.0
	NF52	0.706791	6	*0.70316*	0.512471	5	3.8
	NF53	0.711007	5	*0.70376*	0.512449	5	3.7

Samples were dissolved with concentrated HF for four days at 160 °C on the hot plate. Digested samples were dried and taken up in 6N HCl. Sr and Nd were separated and purified using ion-exchange chromatography as described in Romer et al. (2005).

$^{87}Sr/^{86}Sr$ and $^{143}Nd/^{144}Nd$, normalized to $^{86}Sr/^{88}Sr = 0.1194$ and $^{146}Nd/^{144}Nd = 0.7219$, respectively, Sr was analyzed on a VG54Sector, a Finnigan MAT262 or a Triton multi-collector mass-spectrometer commonly using dynamic multicollection. Nd isotope data were obtained on a Finnigan MAT262 multi-collector mass-spectrometer using dynamic multicollection. Analytical uncertainties are given at $2\sigma_m$ level.

$^{87}Sr/^{86}Sr$ (T) and εNd (T) were calculated for the stratigraphic age using $\lambda(^{87}Rb) = 1.42 \times 10^{-11}$ y^{-1} and λ (^{147}Sm) = 6.54 x10 $^{-12}$ y^{-1}, $(^{147}Sm/^{144}Nd)_0$ CHUR = 0.1967, and $(^{143}Nd/^{144}Nd)_0$ CHUR = 0.512638, respectively, and the concentration data given in tables 4-1, 2 and 3. The italic values are calculated for $^{87}Rb/^{86}Sr$ ratios less than 4(Stoeser and Frost, 2006)

8. Discussion

8.1. age constraints

The U–Pb age spectra obtained for the investigated granitiods are restricted to three periods: 615, 603-601, and 586 Ma, for Sabil, Feinan-Mubarak, and Humrat, respectively (Table 1 and Figure. 14). The Sabil granodiorite belongs to the post-collisional calc-alkaline magmatic stage and is clearly intruded by the Abu-Jadda granite (596 Ma, Jarrar et al. 2017), Mubarak and Humrat granites of this study. On the other hand, the ages of Feinan and Mubarak granites coincide within analytical errors with the ages of the composite, andesite, and rhyolitic dikes dated by Ghanem et al. (2020) at 607, 594, and 600 Ma, respectively. The ages of these granitoids and the dikes postdate the Araba Unconformity placed at ca. 605 Ma (Powell et al. 2015) and falls within the extension-related felsic plutonic magmatic activity of the Araba Complex (Jarrar et al. 2003). The Humrat granite dated 586 ± 16 Ma truncates all of the above mentioned granitoids and dikes and is itself cross-cut mainly by dolerites dated at 579 Ma (Ghanem et al. 2020) and rarely by andesite dikes not dated yet. There is no field evidence for plutonic unit younger than the Humrat granite (Jarrar, et al., 2003).

Generally, the zircon ages of the dated rocks in southwestern Jordan, in this study, are well correlated with their equivalent plutonic U-Pb range ages from the northern part of the Eastern Desert of Egypt, northern and southern part of Sinai. Possible equivalents of the Jordanian granites of the Araba Complex have been dated at 580 to 608 Ma in the Eastern Desert and on Sinai and elsewhere in the northern ANS using conventional and SHRIMP zircon methods (e.g., Be'eri-Shlevin, et al., 2009 b; Wilde and Youssef, 2000; Mousa, et al., 2008; Breitkreuz, et al., 2010 and Be'eri-Shlevin, et al., 2010; Eyal et al., 2019).

The previously reported Rb-Sr ages for the investigated rocks in Lenz, et al. (1972); Jarrar et al. (1983); Jarrar et al. (2008); Brook et al. (1990) and elsewhere in the ANS (e.g., Wilde and Youssef, 2000; and Be'eri-Shlevin, et al., 2009), are younger than the U-Pb ages by 20 to 30 Ma. This result could be attributed to many factors among which are the closure temperature of the Rb-Sr system and the sensitivity of the Rb-Sr system to weathering processes. Nevertheless, the reported age, e.g., 610 Ma of the Sabil granodiorite after Brook, et al. (1990), are younger than the uranium-lead age of the same rocks by 5 Ma.

8.2. Origin of intermediate and silicic magmas (Petrogenesis)

8.2.1. Evidence from Sr and Nd isotope ratios

The overlap in the $\varepsilon Nd_{(586-603\ Ma)}$ values for alkaline granites (+ 2.9 to + 5.4) and Sabil granodiorite $\varepsilon Nd_{(615\ Ma)}$ (+ 3.7 to + 4.6) (Table 4), suggest a genetic relation between the two magmas. It goes along with the low initial $^{87}Sr/^{86}Sr$ (~0.70374), as well as the high Nd content (~28ppm) of the post-collisional granitoids that could have been generated by small degree of partial melting of older island arc juvenile crust or by protracted fractional crystallization of mantle-derived parental mafic magma at about > 615 Ma (Smith, et al., 1999; and Jarrar, et al., 2003). The latter possibility should be abandoned due to the age difference of 15 to 30 Ma between the two suites.

The Nd model ages of the post-collisional and the extension-related Neoproterozoic rocks from south Jordan are similar, from 720 to 1060 Ma with an average of 800 Ma for all units (Table 4), suggesting little or no Archean or early to middle Proterozoic rocks contribution to the lower to middle crust of the northern ANS as has been documented by many investigators (Be'eri-Shlevin et al., 2009a; Liégeois and Stern, 2009; and Eyal, et al., 2010).

8.2.2. Geochemical evidence

8.2.2.1. Calc-alkaline suite

The calc-alkaline Sabil granodiorite is characterized by moderate to strong LREE enrichment but remain roughly parallel ((La/Lu)n = 8 - 26) and smooth without significant cross overs relative to the alkali granitoids among the three multi-elements patterns. The changes in the trace elements concentrations ratios are very small. The enrichments are obvious in Sr, Ba, P, Zr, Ti, Cr, Co, and Ni and show well-developed depletion in K, Rb, Th, Ta, Nb and Y. Furthermore, the Sabil granodiorites lack prominent Eu anomaly (Eu/Eu* = 0.7 - 1.0) that's typically observed in the alkali feldspar granites. Furthermore, these granodiorites are of Magnesian character in the sense of Frost et al. (2001) and display the strongest Ta-Nb anomaly.

These features are typical of subduction zone tectonic environment (Pearce, et al., 1984) and suggest a depleted lithospheric mantle source with some subducted crustal component (Whalen, et al., 1987; Eby, 1990; Smith, et al., 1999; and Auwera, et al., 2003). Nevertheless, the steep REE patterns of the granodiorite call for involvement of a garnet-bearing magma source like garnet-bearing mafic granulite of the lower crust. These garnet-granulites are documented as lower crustal xenoliths in Harrat Ash Sham Cenozoic basalts (Al-Zubi, 2015, unpubl. MSc Thesis).

8.2.2.2. Alkaline suite

The felsic end members in the Araba Complex, e.g. the Feinan-Mubarak and Humrat alkali feldspar granites suite rocks, share common features that hint to their origin. They are distinguished by high SiO_2 (~ 66 – 78 %), Na_2O +K_2O, Fe/Mg, and ΣREE (~ 86 – 472 ppm), enrichment in Zr, Nb, Y, Rb, Ta, and K, and low CaO, Ba, Sr, Ti, and P (Table 1), along with much lower Eu/Eu* values (0.06–0.85). Furthermore, they follow a gently sloping LREE ((La/Sm) n = ~ 2 - 8) and almost flat HREE ((Gd/Lu)n = ~ 0.3 – 1.7) chondrite-normalized patterns except the Mubarak which have a concave upwards HREE pattern. These geochemical features are very distinctive signature of the A-type granites (Whalen, et al., 1996; Landenberger and Collins, 1996).

On the other hand, the juxtaposition of both calc-alkaline and alkali granitoids in several locations in the Jordanian basement, e.g. Wadi ES-Sabil, overlap in their REE patterns and multi-elements plots (Figures. 9 and 11), and their relatively close U–Pb ages obtained from this study could be similar to the Sabil calc-alkaline granodiorite could fractionate to produce the alkaline granitoids. The REE pattern (Figure. 9 C) of the Mubarak granite and the The Dy/Dy* vs. Dy/Yb plot (Figure. 10) demonstrate that the

evolution of the magmas of rocks could have resulted from the fractionation of amphiboles and pyroxenes.

Experiments of Sisson, et al. (2005) demonstrated the possible formation of A-type granite magma by a partial melting of K-rich basalt rocks in the middle and lower crust. Eyal et al. 2010 advocated this for the formation of A-type granites in Sinai Peninsula.

All investigated granitoids fall mostly in the field of slab-failure (Whalen and Hildebrad, 2019) on the tectonic discrimination diagrams of granites of Pearce et al. (1984, 1995). Slab failure at the end of the East African Orogeny and a consequent asthenospheric upwelling could have triggered decompresion melting of the subcontinental lithosphere and the lower over-thickened continental crust. Fractionation of these magmas with possible minor assimilation of crustal material resulted in the formation of the different granitoidal units. Possible fractionated material of similar age, within analytical error, to the alkaline units (Feinan, Mubarak and Humrat) can be found in the gabbro-diorite intrusions in Wadi Qunaia (Ghanem and Jarrar, 2013) and the quartz diorite of Wadi Mureihil, Central Wadi Araba (Jarrar and Ghanem, 2021).

9. Summary and conclusions

The following conclusions, arranged in order of importance, can be drawn from this study:

1. The obtained conventional U-Pb zircon ages are ~ 616, ~ 603, ~601, and ~ 586 Ma for the Sabil granodiorite Feinan, Mubarak, and Humrat units, respectively.
2. The investigated rocks are divided into two groups: the alkaline group, which includes the Humrat, Mubarak and Feinan alkali granite units of the Araba Complex; and the high-K calc-alkaline Sabil granodiorite unit from the Aqaba Complex.
3. The calc-alkaline Sabil granodiorite unit is of Magnesian character and mostly metaluminous; while the alkaline group is mostly of ferroan affinity, A-type, and mostly slightly peraluminous.
4. The alkaline suite is characterized of high SiO_2, Na_2O +K_2O, Fe/Mg, enrichment in Zr, Nb, Y, Rb, Ta, K and REE contents, and low CaO, Ba, Sr, Ti and P along with prominent negative Europium anomaly. Furthermore, they follow a gently sloping LREE and almost flat HREE chondrites patterns, except for the concave pattern of the Mubarak unit. They bear a close resemblance to within plate A-type granites.
5. The calc-alkaline Sabil unit and to a lesser degree the Feinan units show a Nb-Ta anomaly that's characteristic for volcanic arc granites (VAG) while the Mubarak and Humrat are more within plate granites. However, all of the units fall in the field of slab-failure in the sense of Whalen and Hildebrand (2019).
6. The εNd values of the alkali units ranged (+ 2.9 to + 5.4) and overlap with the εNd values of the Sabil granodiorite (+ 3.7 to + 4.6) with low initial $^{87}Sr/^{86}Sr$ (~0.70374).
7. The Zr geothermometer constrains the temperatures of crystallization between 800 to 950◦C. This roughly close to temperatures obtained by modeled crystallization sequence of the investigated units. The modeled mineralogy is shown only for the Sabil granodiorite unit.
8. The investigated suite could have been produced through decompressional partial melting of the subcontinental lithosphere and lower continental crust with fractional crystallization and minor crustal assimilation.
9. The Sabil granodiorite belongs to the calc-alkaline phase of the Aqaba Complex; the Feinan and Mubarak units represent the transition to the alkaline within-plate magmatism, while the Humrat is a truly A-type within plate alkali-feldspar granite.
10. The transitional magmatism coincides or slightly post-dates with the Araba Unconformity and the extensive dike swarms.

Acknowledgements

This paper is a part of the PhD thesis of the senior author. The logistic and financial support provided to the lead author by the Deanship of the Scientific Research and the Department of Geology at The University of Jordan, is highly appreciated. The lab work including microprobe analysis, isotopic analysis and age determination, and bulk chemistry has been conducted at the Helmholtz Center Potsdam-German Research Center for Geosciences (GeoForschungsZentrum (GFZ) during a six-month research stay of the senior author that has been financially supported by the Deutscher Akademisher Austausch Dienst (DAAD). The support of both institutions is gratefully acknowledged. Dr. Hind Ghanem kindly carried out microprobe analyses for selected samples at the Institute for Mineralogy and Crystallography, University of Stuttgart, Germany.

References

Abu El-Enen, M.M., Whitehouse, M.J., 2013. The Feiran–Solaf metamorphic complex, Sinai, Egypt: Geochronological and geochemical constraints on its evolution. Precambrian Research 239, 106-125.

Al-Zubi, R. 2015. A suite of upper mantle and lower crustal xenoliths form Harrat Ash Shaam, NE Jordan: mineralogy, geochemistry, and petrogenesis. Unpubl. MSc Thesis, The University of Jordan. 178 pp.

Beyth M, Stern RJ, Altherr R, Kröner A (1994) The late Precambrian Timna igneous complex, Southern Israel: Evidence for comagmatic-type sanukitoid monzodiorite and alkali granite magma. Lithos, 31, 103 - 124.

Boyd, R., Nordgulen, Ø., Thomas, R.J., Bingen, B., Bjerkgard, T., Grenne, T., Henderson, I., Melezhik, V.A., Often, M., Sandstad, J.S., Solli, A., Tveten, E., Viola, G., Key, R.M., Smith, R.A., Gonzalez, E., Hollick, L.J., Jacobs, J., Jamal, D., Motuza, G., Bauer, W., Daudi, E., Feitio, P., Manhica, V., Moniz, A. and Rosse, D. (2010), The geology and geochemistry of the East African Orogen in the Northeastern Mozambique. South African Journal of Geology, 113 (1), 87-129.

Brook M, Ibrahim K, McCourt W (1990) New geochronological data from the Arabian Shield area of southwest Jordan. In: Proceedings of the 3rd Jordanian Geological. Conference, Amman, Jordan. pp 361-394

Davidson, J., Turner, S., and Plank, T. 2013. Dy/Dy*: variations arising from mantle sources and petrogenetic processes. Journal of Petrology 54, 525-537.

Dulski, P. (2001), Reference Materials for Geochemical studies: New Analytical Data by ICP-MS and critical discussion of reference values. Geostandard Newsletters25, 97-125.

Eby, GN. (1990) The A-type granitoids: A review of their occurrence and chemical characteristics and speculations on their petrogenesis. Lithos, 26, 115-134.

El-Bialy MZ , Hassen I (2012) The late Ediacaran (580-590 Ma) onset of anorogenic alkaline magmatism in the Arabian-Nubian Shield: Katherina A-type rhyolites of Gabal Ma'ain, Sinai, Egypt. Precambrian Research 2012-2016, 1-22.

Elisha B, Katzir, Y, Kylander-Clark, A (2017) Ediacaran (~620 Ma) high-grade regional metamorphism in the northern Arabian Nubian Shield: U-Th-Pb monazite ages of the Elat schist. Precambrian Research 295, 172-186.

Elisha B, Katzir Y, Kylander-Clark ARC, Golan T (2019) The timing of migmatization in the northern Arabian-Nubian Shield: Evidence for a juvenile sedimentary component in collision-related batholiths. Journal of Metamorphic Geology 37, 591-610.

Eyal, M., Litvinovsky, B., Jahn, B.M., Zanvilevich, A., Katzir, Y., 2010. Origin and evolution of post-collisional magmatism: Coeval Neoproterozoic calc-alkaline and alkaline suites of the Sinai Peninsula. Chemical Geology 269, 153-179.

Eyal Y, Eyal M, Litvinovsky B, Jahn Bm, Calvo R, Golan T (2019) The evolution of the Neoproterozoic Elat Metamorphic Complex, northernmost Arabian-Nubian Shield: Island arc to syncollisional stage and post-collisional magmatism. Precambrian Research 320:137-170

Faure, G. and Mensing, T. M. (2005), Isotopes: Principles and Applications. John Wiley & Sons.

Frost, B. R., Arculus, R. J., Barnes, C. G., Collins,W. J., Ellis, D. J. & Frost, C. D. (2001). A geochemical classification of granitic rocks. Journal of Petrology 42, 2033-2048

Frost, BR and Frost CD. (2008) A Geochemical Classification for Feldspathic Igneous Rocks. Journal of Petrology, 49, Issue 11, 1955–1969, https://doi.org/10.1093/petrology/egn054

Garfunkel Z (1999) History and paleogeography during the Pan-African orogen to stable platform transition: reappraisal of the evidence from the Elat area and the northern Arabian-Nubian Shield. Isr. J. Earth Sci. 48:135-157

Ghanem, H. & Jarrar., G. 2013. Geochemistry and Petrogenesis of the 595 Ma Qunai Monzogabbro, Jordan. Journal of African Earth Sciences 88, 1-14.

Ghanem H, McAleer RJ, Jarrar GH, Al Hseinat Ma, Whitehouse M (2020) 40Ar/39Ar and U-Pb SIMS zircon ages of Ediacaran dikes from the Arabian-Nubian Shield of south Jordan. Precambrian Res. 343:105714

Ghanem H, Jarrar GH, McAleer, RJ Passchier CW, Thomas, Whitehouse MJ, Wintsch, RP(2022): Drowned in granite - retrieving the tectono-metamorphic history of the Janub metamorphic complex, the northernmost part of the Arabian-Nubian Shield. Precambrian Research 106903, vol 383. https://doi.org/10.1016/j.precamres.2022

Ghiorso, M. S. and Gualda, G.A. R. (2015) An H2O-CO2 mixed fluid saturation model compatible with rhyolite-MELTS. Contributions to Mineralogy and Petrology, 169:53. DOI 10.1007/s00410-015-1141-8.

Habboush, M. A. and Jarrar, G. (2009). Petrology and geochemistry of the metasediments of the Janub metamorphic suite, southern Jordan: Implications for geothermobarometry and economic potential. Jordan Journal of Earth and Environmental Sciences. Vol 2, No.1, 7-17.

Harris, NBW, Pearce, JA, Tendle AG (1986). Geochemical characteristics of collision-zone magmatism. In: Coward MP, Ries AC, (eds) Collision tectonics, vol 19,Special publication of the Geological Society of London., pp 67-81. http://doi.org/10.1144.GSI. SP 1986 019.01.04.

Ibrahim KM and McCourt WJ (1995) Neoproterozoic granitic magmatism and tectonic evolution of the northern Arabian Shield: Evidence from Southwest Jordan. J Afr Earth Sci, 20, 103-118

Jarrar, GH., Baumann, A. and Wachendorf, H. (1983), Age determinations in the Precambrian basement of the Wadi Araba area southwest Jordan. Earth and planetary Science letters, 63: 292-304.

Jarrar GH (1995) Pan-African Amphibolites from SW-Jordan. Chemie Der Erde-Geochemistry 55(1):31-45

Jarrar GH (1998) Mineral chemistry in dioritic hornblendites from Wadi Araba, southwest Jordan. J. Afr. Earth Sci. 26(2):285-295

Jarrar, GH, Stern, R. J., Saffarini, G. and Al-Zubi, H. (2003), Late- and post-orogenic Neoproterozoic intrusions of Jordan: implications for crustal growth in the northmost segment of the East African Orogen. Precambrian Research, 123: 295-319.

Jarrar GH, Saffarini G, Baumann A, Wachendorf H (2004) Origin, age and petrogenesis of Neoproterozoic composite dikes from the Arabian-Nubian Shield, SW Jordan. Geol. J. 39(2):157-178

Jarrar, GH., Manton, W., Stern, R. and Zachmann, D. (2008), Late Neoproterozoic A-type granites in the Northernmost Arabian-Nubian Shield formed by fractionation of basaltic melts. Chemie der Erde-Geochemistry, 68: 295-312.

Jarrar, GH., Theye, T., Yaseen, N., Whitehouse, M., Pease, V., Passchier, C., 2013a. Geochemistry and P–T–t evolution of the Abu-Barqa Metamorphic Suite, SW Jordan, and implications for the tectonics of the northern Arabian–Nubian Shield. Precambrian Research 239, 56-78.

Jarrar GH, Yaseen N, Theye T (2013b) A hybrid composite dike suite from the northern Arabian Nubian Shield, southwest Jordan: Implications for magma mixing and partial melting of granite by mafic magma. J. Volcanol. Geotherm. Res. 254:80-93

Jarrar G.H., Stern R.J., Theye T., Yaseen N., Pease V., Miller N., Ibrahim K.M., Passchier C.W., Whitehouse M. 2017. Neoproterozoic Rosetta Gabbro from northernmost Arabian–Nubian Shield, south Jordan: Geochemistry and petrogenesis. Lithos. 284-285:545-559.

Jarrar, GH. and Ghanem, (2021) Neoproterozoic Crustal Evolution of the Northernmost Arabian-Nubian Shield, South Jordan. Chapter five in a book The Geology of the Arabian-Nubian Shield, Regional geology reviews, Springer Verlag. 109-137; https://doi.org/10.1007/978-3-03

Johannes W and Holtz 1996. Petrogenesis and experimental petrology of granitic rocks. Springer Verlag.

Johnson PR, Halverson GP, Kusky TM, Stern RJ, Pease V (2013) Volcanosedimentary Basins in the Arabian-Nubian Shield: Markers of Repeated Exhumation and Denudation in a Neoproterozoic Accretionary Orogen. Geosciences 3(3):389-445

Kröner A, Stern R (2004) Pan-African orogeny. In: Selley RC, Cocks LRM, Plimer IR (eds) Encyclopedia of Geology. Elsevier, Amsterdam., pp 1-12

Lenz, H., Bender, F., Besang, C., Harre, W., Kreuzer, H., Mueller, P. and Wendt, I. (1972), The age of early tectonic events in the zone of the Jordan Geosuture based on radiometric data. 24th International Geological Congress, 3: 371-379.

McCourt, W.J. and Ibrahim, K. (1990), The Geology, Geochemistry and Tectonic setting of the Granitic and Associated Rocks in the Aqaba and Araba Complexes of Southwest Jordan. Natural Resources Authority, Geological Directorate, Geological Mapping Division, Bulletin 10, Amman.

Mousa, E. M. M., Stern, R. J., Manton, W. I. and Kamal, A. (2008), SHRIMP zircon dating and Sm-Nd isotopic investigations of Neoproterozoic granitoids, Eastern Desert, Egypt. Precambrian Research, 160: 341-356.

Moyen, J.-F., Laurent O, Chelle-Michou, C., Couzini, S., Vanderhaege, O., Zeh, A., Villaros, Gardien, V. (2017) Collision vs. subduction-related magmatism: Two contrasting ways of granite formation and implications for crustal growth. Lihos, 277, 154-177.

Pallister, J.S. Stacey, J.S. , Fisher L.B. , PREMO, W. R. (1988). Precambrian ophiolites of Arabia: Geologic settings, U-Pb geochronology, Pb-isotope characteristics, and implications for continental accretion. Precambrian Research, 38, 1-54.

Pearce, J.A., Harris N.B.W., Tendle, A.G. (1984) Trace elements discrimination diagrams for the tectonic interpretation of granitic rocks. Journal of Petrology 25: 956-983.

Powell JH, Abed AM, Le Nindre Y-M (2014) Cambrian stratigraphy of Jordan. Geoarabia 19(3):81-134

Powell JH, Abed A, Jarrar GH (2015) Ediacaran Araba Complex of Jordan. Geoarabia 20(1):99-156

Romer, R. L., Schärer, U. and Steck, A. (1996), Alpine and pre-Alpine magmatism in the root-zone of the western central Alps. Contributions to Mineralogy and Petrology, 123, 138–158.

Romer, R. L., Heinrich, W., Schröder-Smeibidl, B., Meixner, A., Fischer, C. O. and Schulz, C. (2005), Elemental dispersion and stable isotope fractionation during reactive fluid-flow and fluid immiscibility in the Bufa del Diente aureole, NE-Mexico: Evidence from radiographies and Li, B, Sr, Nd, and Pb isotope systematics. Contributions to Mineralogy and Petrology, 149 (4), 400-429.

Romer, R. L. and Hahne, K. (2010), Life of the Rheic Ocean: scrolling through the shale record, Gondwana Research, 17 (2-3), 236-253.

Schmid, R., Romer, R. L., Franz, L., Oberhänsli, R. and Martinotti, G. (2003), Basement-Cover Sequences within the UHP unit of the Dabie Shan. Journal of Metamorphic Geology, 21 (6), 531-538.

Schmidt, C., Bruhn, D. and Wirth, R. (2003), Experimental evidence of transformation plasticity in silicates: minimum of creep strength in quartz. Earth and Planetary Science letters, 205, 273–280.

Steiger RH and Jager E (1977) Subcommission on geochronology: convention on the use of decay constants in geo- and cosmo-chronology. Earth Planet Sci Letters 36:359-362

Stern, R.J., 1994. Arc assembly and continental collision in the Neoproterozoic East African Orogen: implications for the consolidation of Gondwanaland. Annual Review of Earth and Planetary Sciences 22, 319-351.

Tang, Y-W, Chen, L, Zhao, Z-F, Zheng, Y-F. (2020) Geochemical evidence for the production of granitoids through reworking of the juvenile mafic crust in the Gangdese Orogen, southern Tibet. Geological Society of America Bulletin, 132, 1374-1364.

Wachendorf H, Zachmann D, Jarrar G (1985) The role of pressure in control of potassium, sodium, and copper concentration in hypabyssal intrusives as demonstrated in late Precambrian dikes in southwest Jordan. Precambrian Res. 30(3):221-248

Whalen, JB, Currie KL, Chappell, BW. (1987). A-type granites: geochemical characteristics, discrimination and petrogenesis. Contributions to Mineralogy and Petrology. 95: 407-419.

Whalen, JB, Jenner, GA, Longstaffe, FJ., Robert, F., Cartiepy, C. 1996. Geochemical and isotopic (O, Nd, Pb and Sr) constraints on A-type granite petrogenesis based on the Topsails igneous suite, Newfoundland Appalations. Journal of Petrology, 37, 1463-1489

Whalen JB, Hildebrand RS (2019) Trace elements discrimination of arc, slab failure, and A-type granitic rocks. Lithos, 348-349, 105 105179. https://doi.org/10.1016/j.lithos.2019.105179

JJEES

JJEES (2025) 16 (2): 136-143
ISSN 1995-6681

Jordan Journal of Earth and Environmental Sciences

Assessing the Land Use/Land Cover and Climatic Changes Impacts on Static Groundwater Level: A Case Study of Quetta, Pakistan

Malik Muhammad Akhtar[1*], Tanzeel khan[1], Abdul Rehman Khan[2], Rabia Akhtar[2], Danish Raza[3]

[1]*Department of Environmental Science, Faculty of Life Sciences & Informatics, Balochistan University of Information Technology, Engineering and Management Sciences, Quetta, 87300, Pakistan*
[2]*Balochistan University of Information Technology, Engineering and Management Sciences (BUITEMS), Quetta, Pakistan.*
[3]*The Urban Unit Lahore, the government of Punjab, Pakistan*

Received on March 9 2024, Accepted on December 31 2024

Abstract

Various natural and anthropogenic factors are affecting recharge processes in urban areas due to intense urban expansion; land-use/landcover change (LULC) and climate considerably influence the ecosystem functions. In Quetta, a terrible transformation of LULC has occurred due to an increase in human population and rapid urbanization over the past years. According to the Pakistan Bureau of Statistics, the population growth from 252,577 in 1972 to 2,275,699 in 2017 shows an abrupt rise which, in turn, has affected the aquifer recharge capability, vegetation, and precipitation at Quetta. This study focuses on the influence of population growth and LULC on groundwater table level by employing multi-temporal, multispectral satellite data during the selected years, i.e. 2014, 2017, and 2020. The results of land classification showed that barren land has shown a considerable decrease whereas the urban area has increased over time from 152.4 km^2 in 2014 to 195.5 km^2 in 2017 to 283.3 km^2 in 2020. In contrast, surface-water area coverage has increased since 2014 because of the construction of a few dams around the valley. The rapid urbanization stressed limited hydrology resources. This limitedness needs to be addressed to conserve/sustain the resources through educating the local community, awareness regarding water use and climate change, and supporting artificial recharge of the aquifers.

Keywords: *Climate changes, Urbanization, Geographic information system (GIS), Landcover changes, Watershed*

1. Introduction

The land use land cover (LULC) map has a major role in agricultural and water resources planning and management and in resources monitoring programs at local and national levels (Adham et al., 2018). Earth's surface or LULC change analysis is vital for understanding the relationship between natural phenomena of the environment and anthropogenic activities. LULC in a watershed can influence water quality as well as water supply (Rawat & Kumar, 2015). Geographical information system (GIS) is an important technology for the study of LULC and has been used widely to examine and assess large-scale land use changes (Khair et al., 2019). Land classification through GIS is a faster and more cost-effective method than traditional methods. With the advent of GIS, land use mapping provides a very effective and inclusive method for improving the selection of areas designed for agricultural, urban, and/or industrial areas of a region (Rawat et al., 2013).

In a watershed area urbanization, LCLU changes, and deforestation continuously affect the water availability as well as the nature and extent of surface water interactions thus affecting watershed ecosystems. Safer water conservation strategies can be made with an appropriate understanding of the spatial and temporal changes that take place in a watershed over time and the interaction of the hydrological components of a watershed with each other (Ashraf, 2013).

Some studies have shown that climate changes have substantial impacts on watershed hydrology (Earman, 2011). Some research has also indicated that even a slight variation in precipitation amount can significantly impact themean annual discharge. An urban watershed might experience severe weather incidents whether floods or droughts, with increased global warming and climate change (Zhang & Chang, 2013). Still, the hydrologic impacts of the alterations in climate and land use, particularly urbanization, may operate in cycles, and it is often hard to detect which factor will have a more dominant effect (Tomer & Schilling, 2009). A study concluded that climatic variables, such as precipitation and air temperature, might directly influence watershed hydrology although land use and land cover (LULC) can also have substantial impacts (Legesse et al., 2003). Another researcher also concluded that climate change has a significant relationship with peak discharge. Sultana and Hasan concluded in their research that the influence of climate sensitivity in a region could impact socioeconomic, demographic migration, and general community health (Sultana and Hasan, 2024). This change detection analysis requires utilizing multi-temporal and GIS tools to quantitatively examine the effects of an occurrence in the past and, thus, helps determining the changes associated with land cover and land use properties concerning the multi-temporal datasets (Butt et al., 2015).

Numerous research has been performed globally relating

* Corresponding author e-mail: drmalikma21@gmail.com

to the change analysis of watersheds through different methods, and these studies are important for developing efficient watershed management strategies (Bashir & Ahmad, 2017). Watershed management is immensely important because it's not just a hydrological unit (Singh et al., 2014), but it also has socio-ecological importance, which shows an essential role in determining economic, food, and social security and provision of life support services to residents (Wani & Garg, 2009). Understanding the aquifer's characteristics is extremely important to explore the water potential and groundwater development program for specific areas (Oluwatoyin, & Olatunji, 2022).

The study area is chosen for LULC change detection since it has been subjected to rapid urbanization, increased and unplanned human settlements, soil erosion, overgrazing, deforestation, lack of any cooperative communal structure, and overcrowding over the past 10 years. The rapid urban development that took placein Quetta has led to environmental challenges (Khan et al., 2013).

Hence, the main objective of this study is to apply GIS applications to determine the extent of changes that occurred in Quetta land use and watersheds over time in which future climate changes and urbanization can cause drastic consequences for water supply and demand. However, the objectives included (i) identification and delineation of different LULC categories and patterns of land use change in the watershed of the years 2014, 2017, and 2020 (ii) to examine the changes in the watershed (iii) to predict the hydrologic impact of land cover changes on groundwater table.

2. Methodology

2.1 Study Area

Quetta is a district of Balochistan, Pakistan, located in the northwest, on the border with Kandahar Province, Afghanistan. Area-wise Quetta is the 4th smallest district of Balochistan and has an area of 2,741(2653) km^2. It is situated at about 30° 10′N to 30° 25′ N and 66° 42′ E to 67° 18′ E, at an elevation level of 1,680 m above the sea level (Ahmad et al., 2020). Quetta district climate is considered as sub-tropical continental highland, that is, hot summers and extreme winters (Mahar et al., 2018).

2.2 Hydrology and Geology

Quetta is located on the border of the two Provinces of Balochistan (Pakistan) and Kandahar (Afghanistan). It is part of the Pishin Lora regional basin which is a landlocked watershed. Two aquifers have been identified: an unconsolidated alluvial aquifer and a bedrock aquifer. The main aquifer is an alluvial aquifer that consists of gravel, sand, and silt deposits. This aquifer is recharged from infiltration of precipitation, runoff, and inflow from the bedrock aquifer in the foothill areas. Water supply is largely dependent on groundwater, mainly derived from this alluvial aquifer. The bedrock aquifer consists of the limestone of the Shirinab and Chiltan formations and conglomerates of the Urak Formation. This aquifer is recharged in the surrounding mountain areas where these formations are exposed (Khan et al., 2013).

Balochistan is comprised of thirteen major river basins, and the flow of these rivers is characterized by spring runoff and occasional flash floods. Of the total water available per annum in Balochistan which is 27.73 billion m^3, 96% is contributed by surface water, and only about 4 percent is contributed by groundwater. The largest source of water, contributing 57% to the total available water, is floodwater. However, due to mountainous and variable terrain, the floodwater typically comes in the form of flash floods, and unfortunately, only 23% of this water resource is utilized. Indus Basin Irrigation System (IBIS) contributes around 39% to the total available water resource and is exploited by 60% in only 5% area of the province in the Kachhi Plain basin towards the east of Balochistan. The rest of the province benefits largely from the groundwater due to the absence of any other perennial source of water (Bhatti et al., 2008).

Figure 1. Location map of the study area

2.3 Temperature

Temperature data of the past years helps to analyze the temperature variation over time and helps to conclude future predictions. the temperature rise results from several factors. The only source for urban and rural water supply schemes for Quetta is the aquifers. Temperature varies in the valley, i.e., semi-arid climate with great deviations from summer to winter temperatures. The temperature usually rises to 38°C in summers and drops to 4°C to 6°C on average in winters (Durrani et al., 2018).

2.4 Precipitation

Quetta Valley does not have sustained rainfall in the monsoon season. From December till February, snow falls, and it very rarely occurs in March. The imbalance between precipitation and temperature is very important to note. The evaporation is usually higher than precipitation, and, thus, the sustainability and level of the groundwater table cannot be maintained. The highest rainfall of 113 mm was recorded on December 17, 2000 and the highest monthly rainfall of 232.4 mm was documented in March 1982 (Durrani et al., 2018).

2.5 Population

According to a census, the population of Quetta District in 1975 was reported to be 252,577. The population rapidly expanded in the late 1970s and 1980s because of migrations from a neighboring country, Afghanistan, due to wars. So, by 1981, the population had almost doubled and raised to 383,403. The population continued to increase at a constant rate, and according to 1998 census data, the population recorded was 773,936. In recent years, because of severe droughts in the surrounding areas of Quetta City, an increased migration from rural areas to Quetta occurred. In the recent census of 2017, the population of Quetta District increased to 2,275,699.

Table 1. Population census of Quetta city over the years

Name	Status	Population Census (1972)	Population Census (1981)	Population Census (1998)	Population Census (2017)
Quetta	District	252,577	383,403	773,936	2,275,699

Source: Pakistan Burau of Statistics

2.6 Data collection

This research is dependent on secondary data. To prepare the base maps for analysis purposes, satellite images have been downloaded from USGS Earth Explorer, and the study period is selected from the year 2014 to 2020 on an interval of 3 years. The second imagery source was Landsat 8 (05/05/2014), Landsat 8 (04/29/2017), and Landsat 8 (04/17/2020) satellites with 30 m resolution, from which we used the full set of spectral bands (USGS). We chose available cloud-free images from 2014, 2017, and 2020. The imagery georeferenced was 30 m to ensure proper alignment.

2.7 Data Pre-processing

In this stage, collected satellite images are processed through geo-referencing. At first, they are transformed into the World Transverse Mercator (WTM) map projection system, with datum WGS1984 (GCS) or UTM.

2.8 Land Classification

Among the two supervised and unsupervised classifications (Roy and Saha, 2016), the supervised classification method has been used in this study. In a supervised classification, an image is classified using polygons that represent separate sample areas of the different land use types to be classified. Four specific classes are taken for the classification: Urban Area, vegetation, Barren land, and Water body. The designation and covering features of each class are shown in Table 2.

2.9 Digital Elevation Model (DEM)

Water resources planning tools and hydrologic simulation models usually use hydrographic datasets, most significantly, stream network polylines, and watershed boundaries, which can be made from gridded (raster) digital elevation models (DEMs), using well-established terrain analysis techniques (Yang et al., 2014). The 30 m resolution SRTM DEM was downloaded from USGS Earth Explorer and was processed for the extraction of flow direction, flow accumulation, stream network generation, and finally the delineation of the watershed and sub-basins.

Table 2. Details of the land cover types

LAND USE	DESCRIPTION
Urban area	Commercial, residential, industrial, transportation, roads, housing schemes and other urban populations
Vegetation	Forest, vegetative lands, scrubs, and others crop fields
Barren land	Uncovered soils, sand fill, landfill sites
Water body	Permanent open water, dams, lakes, and reservoirs

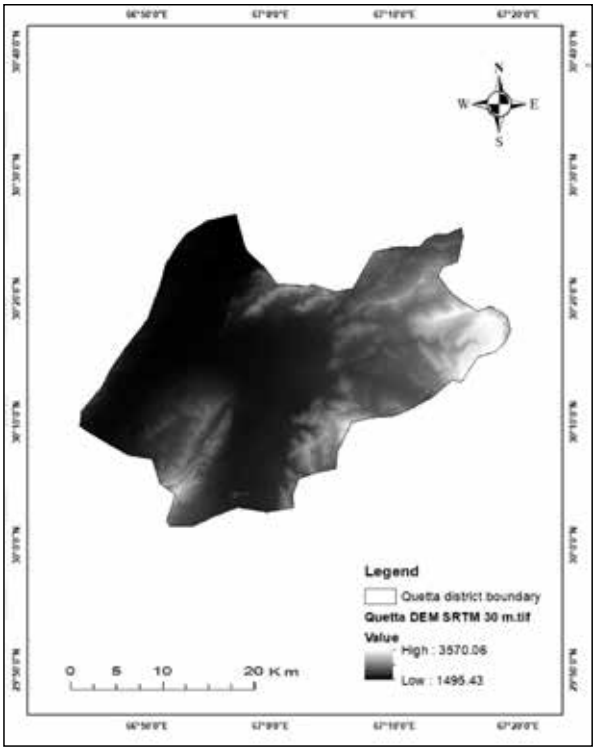

Figure 2. DEM with 30m resolution of the Study Area

3. Results And Discussions

3.1 Land classification

From the analysis of the geometry calculation on ArcGIS, it can be seen in Table 3 that urbanization is increasing at an alarming rate in Quetta District. The area covered by urbanization was 152.4 km^2 in 2014. It increased to 195.5 km^2, and further, it has increased to 283.3 km^2 in 2020. Vegetation seems to be lesser in 2017 as compared to 2014, but it has grown in 2020, covering an area of 242.5 km^2. According to a housing survey (Mahar et al., 2017), most of the houses were constructed during the last 40 years as shown in Fig 2. A major issue across the world faced by many countries is rapid urbanization. Pakistan is among the countries which are facing urbanization at the rate of 3% annually, reported at the fastest rate in South Asia. Urban expansion in Pakistan may be due to the natural increase in human population, or it might be due to external and internal migration of the people to metropolitan cities. The United Nations Population Division estimated that, by 2025, approximately half the country's population might be living in cities in comparison to one-third of the population at present. More recently, people of Pakistan's tribal areas and refugees from Afghanistan have triggered enormous pressure on urban areas, particularly, Peshawar, Quetta, and

Karachi. At the same time, many Pakistanis, particularly farmers and fishermen affected by rural water shortages and natural disasters including flooding and earthquakes, are moving to cities to seek better livelihoods (Jabeen et al., 2017). According to the results, the land cover with vegetation increased from 153.8 to 242.5 km2 over the last 10 years.

Table 3. Land use classification of the selected years

Year		2014	2017	2020
Sr. #	**Class name**	**Area (** km^2**)**	**Area (** km^2**)**	**Area (** km^2**)**
1	Barren land	1098.6	1134.3	878.5
2	Urban area	152.4	195.5	283.3
3	Vegetation	153.8	75.15	242.5
4	Water bodies	0.7406	0.4825	1.1498
Total Area		1405.5	1405.5	1405.5

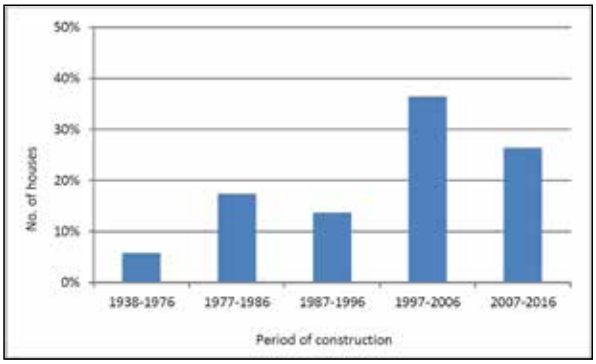

Figure 3. Rate of Construction in Quetta City (Mahar et al., 2017)

This proves a direct relationship between increased agriculture and water resource depletion. However, the major influence for these effects seems to be a rapid increase in population, which is creating a gap between water supply and demand. Deforestation in the mountain regions in 2017 may be contributing to the decrease in precipitation and rise in temperature. Water bodies covered an area of 0.7406 km^2 in 2014. It decreased to 0.4825 km^2 in 2017 due to droughts and lack of rainfall. In 2020, as a result of dam construction, the surface water body area increased to 1.1498 km^2. LULC can directly or indirectly impact infiltration, evapotranspiration, and surface runoff generation of water. LULC map was prepared (Fig. 4) from the satellite imagery of Landsat-8 OLI through a supervised classification technique (Samanta et al., 2018).

3.2 Climatology

According to data obtained from the weather stations installed by the meteorological department in Quetta. Figure 5 shows the annual rate of average temperature and precipitation in 2019. The highest average temperature has been recorded in July, i.e., 28.5 °C, whereas the lowest temperature recorded was in January, i.e., 4.6 °C. The highest average precipitation was recorded in March, i.e., 55.9 mm whereas the lowest average precipitation was recorded in September, i.e., 2.3 mm. The total precipitation in 2017 was 370.81 mm. In the highland Balochistan Province, rainfall decreases with altitude and each zone has differing climatic conditions, water availability, and cropping systems (Khair et al., 2015).

According to Durrani on July 10, 1998, the highest temperature recorded in Quetta was 42 °C. On January 8, 1970, the lowest temperature recorded was -18.3 °C. The summer season continues from May till September with an average temperature of 24-26 °C. The autumn duration is basically from September-November with a temperature range of 12-18 °C. The winter ranges from October to March with temperature variation of 4-5 °C. Spring ranges from April to May with an average temperature of 15 °C (Durrani et al., 2018).

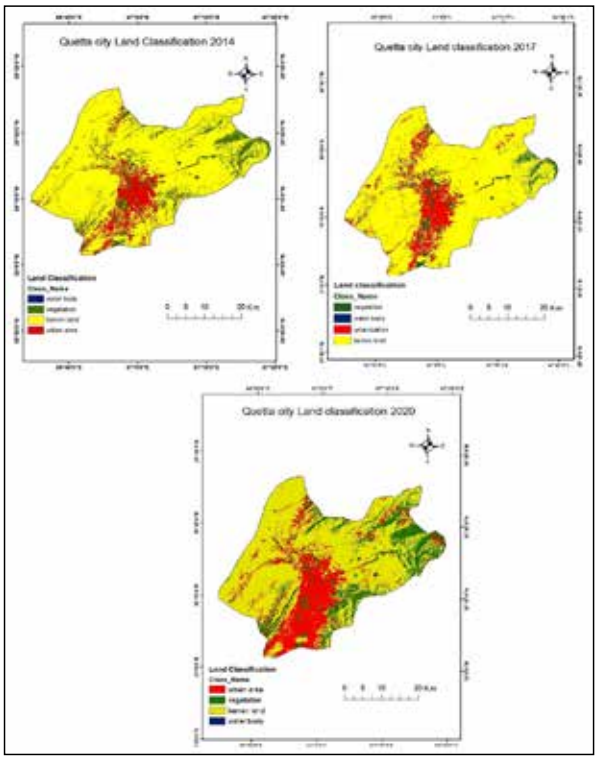

Figure 4. Land use classification comparison of different years

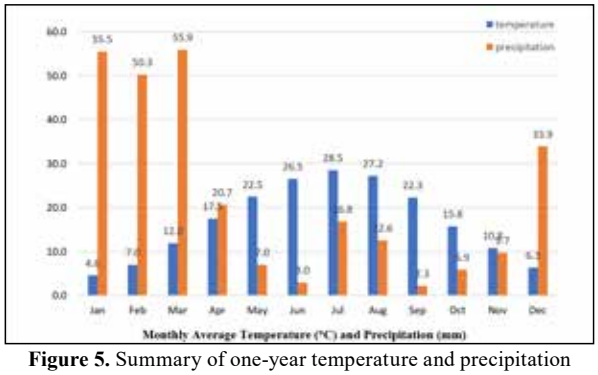

Figure 5. Summary of one-year temperature and precipitation

3.3 Watershed Model

Figure 6 shows the DEM of Quetta District on which the stream orders are also indicated with dark blue and light blue color lines. The colored parts on the map show the catchment areas. The blue lines show the path of the water streams that flow from the mountainous region in different directions in each catchment. The steeper slopes result in a low contact period with the land surface and reduce infiltration and groundwater recharge (Rukundo & Dogan, 2019), so the water running down the hilly terrain to the valley does not get enough time to get infiltrate. These streams, when reaching the ground surface and favorable soil quality, infiltrate into the groundwater aquifers.

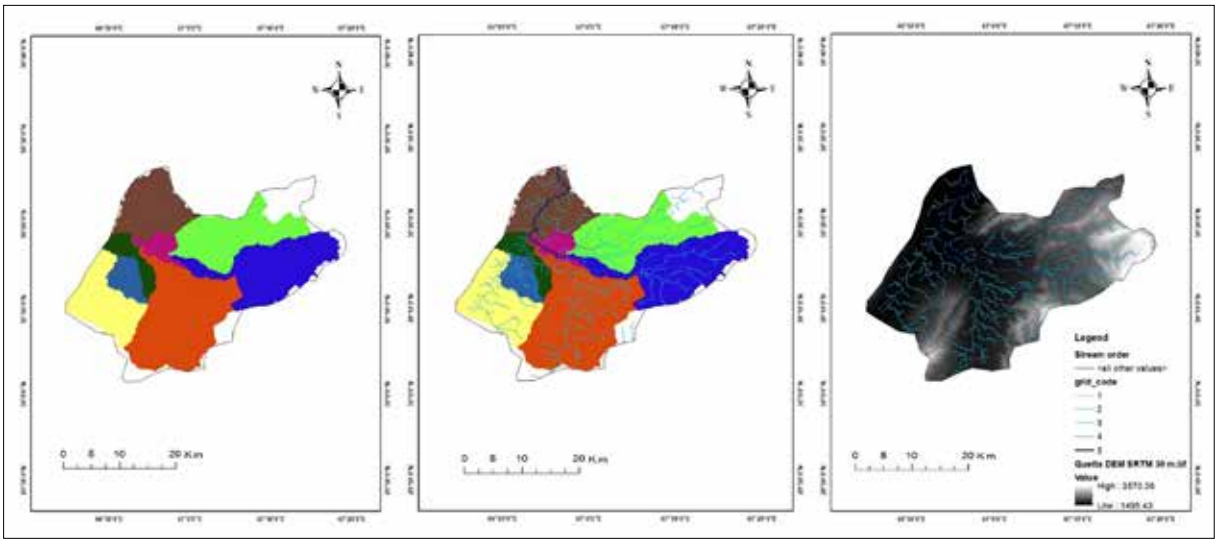

Figure 6. Watershed models of study area

slowly and gradually recharging the aquifers, but this recharge can be hindered when the recharge zones are covered with the construction and settlements. It is very necessary to identify the recharge zones of a city or any region so that the related departments or governments can avoid the coverage of recharge zones by the settlements either by construction parks or forests. Quetta City has led to unmanageable abstraction and use of groundwater causing deterioration in groundwater quantity and quality (Ahmed et al., 2019). Some researchers employed the inverse interpolation technique (IDW) in GIS environments of various parameters to develop spatial distribution maps of water quality in Iraq (Al-Hadithi et al., 2019).

For each parameter, these parameters were used to calculate water quality index values which were also reassigned to the GIS environment to generate the IWQI maps.

3.4 Groundwater level

Groundwater table data was obtained from the Irrigation Department and Water and Sanitation Authority (WASA) of the year 2019. The number of observational tube wells under study was 72. The average groundwater level is indicated on the diagram in Fig. 7. The map is divided based on grid lines, and the average water table is denoted on the diagram. However, climate alterations over time, such as an increase in average temperature and a decrease in average precipitation have caused the groundwater table to decline. But the most important problem arising is the rapid urbanization and increased population growth of Quetta. Being the largest business and educational center, migration to Quetta City has increased drastically (Ghani et al., 2019). The population density affects the groundwater resources due to overexploitation and wastewater infiltration in other urban units in Pakistan such as Lahore (Muhammad et al., 2016).

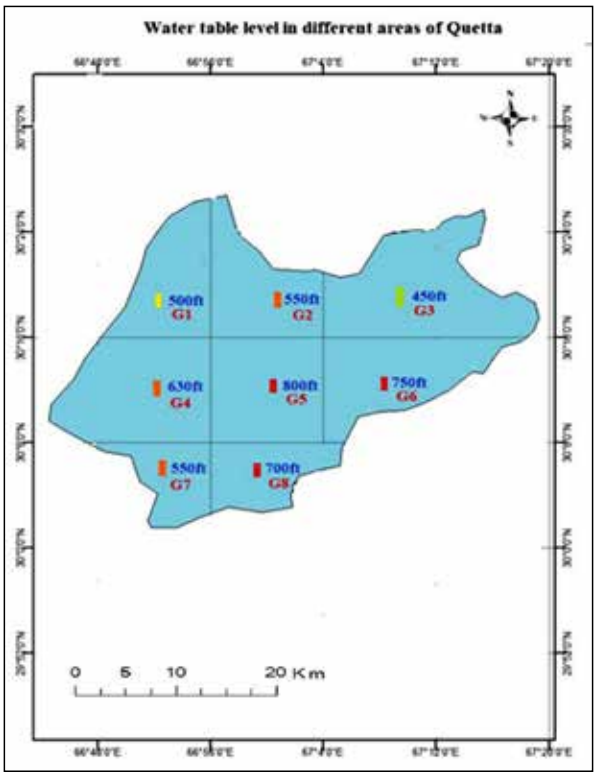

Figure 7. Map indicating groundwater levels in different regions of study area

According to the data presented, the deepest groundwater level is found in the main city labeled as G5, which is 800ft, and as the urban population expands downwards, the

water level is 700ft in G8, which is mainly due to the over-exploitation of groundwater reservoirs over the past few years (Kakar et al., 2020). G3 is the mountainous region of Hannah Urak where the water table is at the lowest 400ft. Dams, such as Hannah Jheel, Spin Karez, and Wali Tangi, are also constructed in this region which has water almost all year round, contributing to the maintenance of groundwater table. Although regions G1, G2, and G3 are mountainous, regions of the valley still contain a human population that depends on groundwater for drinking purposes. The water table has not yet exceeded 500ft on average, below the ground in this region. In terms of recharge, extraction, and urbanization, the aquifers of Quetta need insight research studies to evaluate the behavior of the aquifer to future stresses and to find a future strategy for operating the system.

Groundwater is an essential local and regional natural resource worldwide and is often in high demand. As groundwater is a common resource, it is frequently overused, resulting in the decline of water tables and water resource security reduction over time. Major factors, causing groundwater over-exploitation in Balochistan, are increased rate of irrigated fruits and vegetable cultivation, drought, mass installation of tube-wells, inefficient irrigation practices, lack of efficient government policies and subsidies that promote groundwater development, and lack of effective groundwater governance (Khair et al., 2019). More than 72% of the rural population in Balochistan depends on dug wells and streams for drinking water (Akhtar et al., 2021).

The Quetta District population has increased from 0.26 million in 1975 to 1.452 million in 2014 at a growth rate of 3 percent, and an increase in urbanization rate is 4.2%. Urbanization's impact on groundwater is one of the key factors that need to be studied in Quetta City. A study was conducted to explore urban growth through satellite images that are classified and processed to quantify the LU/LC changes, which highlight an increase in urbanization in the central region of the Quetta Valley (Dawood et al., 2021). Water streams and Channels indicated in Fig 6 through the watershed model show the flow of water towards the middle of the valley, and if it is not infiltered into the ground, it flows down the valley. Although drought and climate change do have an impact on groundwater availability due to the intense extraction of groundwater through tube-wells as a result of increased population and drinking water demand in the city, the groundwater table is the deepest in city region G5 (Ghani et al., 2019). Tam also concluded in their study that extensive groundwater abstraction as a result of rapid urban population growth was the major cause of groundwater table decline in the city, whereas the change in land use practice, resulting from increased urbanization and decreased agricultural activity and natural land only causes a slight decrease of groundwater recharge (Tam & Nga, 2018). The land cover changes have created water-related issues, such as the water balance, evapotranspiration, groundwater recharge, and water erosion due to forest reduction in the Quiscab River subbasin (Gonzalez-Celada et al., 2021).

In fig.7, the study area is divided according to the gridlines regions as G1, G2, G3, G4, G5, G6, G7, and G8. The recharge of groundwater is also not supported in G5 region due to the overconstructed areas and unplanned settlements as shown in Fig. 4. This site is suitable for the recharge of groundwater aquifers as all the water streams are moving down the mountainous region into G5 region, but due to the rise in urban land and construction, i.e., from 152.4 km^2 in 2014 to 283.3 km^2 in 2020, the infiltration of the water is not possible (Wakode et al., 2018), and the water moves out of the valley through G8 region.

Vegetation was abruptly reduced from 158.3 km^2 in 2014 to 75.15 km^2 in 2017 due to less rainfall and droughts, but it increased gradually to 242.5 km^2 in 2020. Droughts have occurred in Balochistan province, for many years with destructive impacts. The lack of proper monitoring and mitigation measures for droughts in this area increases the vulnerability of the province's agriculture and economy to more destructive impacts (Naz et al., 2020).

4. Recommendations

- Quetta is a small valley surrounded by numerous mountain ranges, being the provincial headquarters of Balochistan, the population pressure has always been higher due to numerous facilities so there is an imperative need for good urban planning.
- There is a need for extensive research to identify recharge zones, and the government should clear out those areas for parks to support the groundwater recharge, delay actions dams should be constructed to increase the recharge.
- The concerned departments should work on the promotion of artificial recharge of groundwater because, in the rainy season, a lot of water flows out of the valley.

5. Conclusions

This study concluded that unplanned construction is creating a lot of environmental problems, as a result of land classification, uncontrolled and increased urbanization is detected around the valley which is also reducing the recharge opportunity, especially in city areas i.e., G5 and G8. The flow of population in this area is higher due to the plain topography and so the demand for fresh drinking water is also higher. The excessive construction of tube wells to overcome the drinking water demand of the human population is deteriorating groundwater levels.

Due to several droughts over the past years, the vegetative land, reduced to a very small number in 2017, i.e., 75.15 km^2 but has increased gradually again to 242.5 km^2 in 2020, mainly because of regular precipitation in rainy seasons and snowfall. Since the water supply of the valley utterly depends on groundwater and the economy of Balochistan largely depends on agriculture, the conclusions from this study support the suggestion that water resources management strategies are based on rainwater smart irrigation techniques or tools.

The study area particularly has two vegetation types which are seasonal and orchard vegetation. In seasonal vegetation areas, the whole land is usually not cultivated

by the farmers due to the scarcity of irrigation water and associated tubewell maintenance or pumping costs. Consequently, most of the area remains unsown or barren. Likewise, where orchard vegetation is occurring, the plantation of trees is carried out in grids with several meters distance between plants, therefore the proportion of actual vegetation to the total area is fairly low, and the presence of significant bare soil surface could contribute to the detection of barren land during land classification.

According to the rainfall fluctuating patterns in the Balochistan Province, water reuse or recycling techniques need to be adopted at the local level. The strenuous decline of the groundwater table means that the urbanization or LULC and impermeabilization of the soil have largely affected the natural recharge process, and most of the precipitation is either converted into runoff or lost through evapotranspiration. Overall, this study indicates that the urbanization process has altered the natural hydrological cycle.

Acknowledgements

The authors would like to thank the Pakistan Science Foundation of Pakistan, which has provided financial support for this research work through the project "An Integrated Modelling Approach Used to Estimate the Impact of Climate Change and Human-induced Pressure on Stressed Groundwater Resources of Quetta Sub-Basin, Balochistan" Project No. PSF/Res/B-BUITEMS/Earth (100).

References

Adham, A., Sayl, K. N., Abed, R., Abdeladhim, M. A., Wesseling, J. G., Riksen, M., Ritsema, C. J. (2018). A GIS-based approach for identifying potential sites for harvesting rainwater in the Western Desert of Iraq. International Soil and Water Conservation Research, 6(4), 297-304.

Ahmad, N., Uddin, Z., Rehman, J. u., Bakhsh, M., Ullah, H. (2020). Evaluation of radon concentration and heavy metals in drinking water and their health implications to the population of Quetta, Balochistan, Pakistan. International Journal of Environmental Analytical Chemistry, 100(1), 32-41.

Ahmed, Z., Akhtar, M,M. , Aimal, K, K., Muhsan, E., Rehman, J. U. (2019). Evaluation of Groundwater Vulnerability to Contamination by Drastic Risk Mapping in Quetta Valley, Balochistan. Evaluation, 4(1).

Akhtar, M. M., Mohammad, A. D., Ehsan, M., Akhtar, R., ur Rehman, J., Manzoor, Z. (2021). Water resources of Balochistan, Pakistan—a review. Arabian Journal of Geosciences, 14(4), 1-16.

Al-Hadithi, M., Hasan, K., Algburi, A., & Al-Paruany, K. (2019). Groundwater quality assessment using irrigation water quality index and GIS in Baghdad, Iraq. Jordan Journal of Earth and Environmental Sciences, 10(1), 15-20.

Bashir, H., and Ahmad, S. S. (2017). Exploring geospatial techniques for spatiotemporal change detection in land cover dynamics along Soan River, Pakistan. Environmental monitoring and assessment, 189(5), 222.

Bhatti, S. S., Khattak, M. U. K., Roohi, R. (2008). Planning water resource management in Pishin-Lora river basin of Balochistan using GIS/RS techniques. Paper presented at the 2008 2nd International Conference on Advances in Space Technologies.

Bronstert, A., Niehoff, D., Bürger, G. (2002). Effects of climate and land-use change on storm runoff generation: present knowledge and modelling capabilities. Hydrological processes, 16(2), 509-529.

Butt, A., Shabbir, R., Ahmad, S. S., Aziz, N. (2015). Land use change mapping and analysis using Remote Sensing and GIS: A case study of Simly watershed, Islamabad, Pakistan. The Egyptian Journal of Remote Sensing and Space Science, 18(2), 251-259.

Dawood, F., Akhtar, M. M., Ehsan, M. (2021). Evaluating urbanization impact on stressed aquifer of Quetta Valley, Pakistan. Desalination and Water Treatment, 222, 103-113.

Durrani, I. H., Adnan, S., Ahmad, M., Khair, S., Kakar, E. (2018). Observed long-term climatic variability and its impacts on the ground water level of Quetta alluvial. Iranian Journal of Science and Technology, Transactions A: Science, 42(2), 589-600.

Earman, S., and Dettinger, M. (2011). Potential impacts of climate change on groundwater resources–a global review. Journal of Water and Climate Change, 2(4), 213-229.

Ghani, A., Chaudary, Z. A., Rehman, H., Azhar, A. H., Masood, M. (2019). Assessment of Sustainable Groundwater Extraction rate for Quetta city using MODFLOW. Pakistan Journal of Engineering and Applied Sciences, 24.

Gonzalez-Celada, G., Rios, N., Benegas-Negri, L., Argotty-Benavides, F. (2021). Impact of the climate change and the land use/land cover change in the hydrological and water erosion response in the Quiscab River subbasin. TECNOLOGIA Y CIENCIAS DEL AGUA, 12(6), 363-421.

Jabeen, N., Farwa, U., Jadoon, M. (2017). Urbanization in Pakistan: a governance perspective. Journal of the Research Society of Pakistan, 54(1), 127-136.

Kakar, N., Kakar, D. M., Barrech, S. (2020). Land subsidence caused by groundwater exploitation in Quetta and surrounding region, Pakistan. Proceedings of the International Association of Hydrological Sciences, 382, 595-607.

Khair, S. M., Mushtaq, S., Reardon-Smith, K. (2015). Groundwater Governance in a Water-Starved Country: Public Policy, Farmers' Perceptions, and Drivers of Tubewell Adoption in Balochistan, Pakistan. Groundwater, 53(4), 626-637.

Khair, S. M., Mushtaq, S., Reardon-Smith, K., Ostini, J. (2019). Diverse drivers of unsustainable groundwater extraction behaviour operate in an unregulated water scarce region. Journal of environmental management, 236, 340-350.

Khan, A. S., Khan, S. D., Kakar, D. M. (2013). Land subsidence and declining water resources in Quetta Valley, Pakistan. Environmental earth sciences, 70(6), 2719-2727.

Khan, I., Javed, T., Khan, A., Lei, H., Muhammad, I., Ali, I., Huo, X. (2019). Impact assessment of land use change on surface temperature and agricultural productivity in Peshawar-Pakistan. Environmental Science and Pollution Research, 26(32), 33076-33085.

Legesse, D., Vallet-Coulomb, C., Gasse, F. (2003). Hydrological response of a catchment to climate and land use changes in Tropical Africa: case study South Central Ethiopia. Journal of hydrology, 275(1-2), 67-85.

Mahar, W. A., Amer, M., Attia, S. (2018). Indoor thermal comfort assessment of residential building stock in Quetta, Pakistan. Paper presented at the European Network for Housing Research (ENHR) Annual Conference 2018.

Mahar, W. A., Knapen, E., Verbeeck, G. (2017). Methodology to determine housing characteristics in less developed areas in developing countries: A case study of Quetta, Pakistan. Paper presented at the European Network for Housing Research (ENHR) Annual Conference 2017.

Muhammad, A. M., Zhonghua, T., Sissou, Z., Mohamadi, B., Ehsan, M. (2016). Analysis of geological structure and

anthropological factors affecting arsenic distribution in the Lahore aquifer, Pakistan. Hydrogeology Journal, 24(7), 1891-1904.

Naz, F., Dars, G. H., Ansari, K., Jamro, S., Krakauer, N. Y. (2020). Drought Trends in Balochistan. Water, 12(2), 470.

Oluwatoyin, O., & Olatunji, O. B. A. (2022). Evaluation of aquifer characteristics within Birnin Kebbi metropolis, Northwestern Nigeria using geoelectric survey. Jordan Journal of Earth & Environmental Sciences, 13(1).

Rawat, J., and Kumar, M. (2015). Monitoring land use/cover change using remote sensing and GIS techniques: A case study of Hawalbagh block, district Almora, Uttarakhand, India. The Egyptian Journal of Remote Sensing and Space Science, 18(1), 77-84.

Rawat, J., Biswas, V., Kumar, M. (2013). Changes in land use/cover using geospatial techniques: A case study of Ramnagar town area, district Nainital, Uttarakhand, India. The Egyptian Journal of Remote Sensing and Space Science, 16(1), 111-117.

Roy, B., and Saha, P. (2016). Temporal analysis of land use pattern changes in chittagong district of Bangladesh using Google Earth and ArcGIS. Paper presented at the Proceedings of the Annual Int'l Conference on Chemical Processes, Ecology & Environmental Engineering (ICCPEE'16), Pattaya, Thailand.

Rukundo, E., and Doğan, A. (2019). Dominant Influencing Factors of Groundwater Recharge Spatial Patterns in Ergene River Catchment, Turkey. Water, 11(4), 653.

Samanta, S., Pal, D. K., Palsamanta, B. (2018). Flood susceptibility analysis through remote sensing, GIS and frequency ratio model. Applied Water Science, 8(2), 66.

Singh, P., Gupta, A., Singh, M. (2014). Hydrological inferences from watershed analysis for water resource management using remote sensing and GIS techniques. The Egyptian Journal of Remote Sensing and Space Science, 17(2), 111-121.

Sultana, N., & Hasan, M. K. (2024). Identifying Climate Scenarios and an Index-Based Assessment of Household Vulnerability to Climate Change in the South-West Coastal Region of Bangladesh.

Tam, V. T., and Nga, T. T. V. (2018). Assessment of urbanization impact on groundwater resources in Hanoi, Vietnam. Journal of environmental management, 227, 107-116.

Tomer, M. D., and Schilling, K. E. (2009). A simple approach to distinguish land-use and climate-change effects on watershed hydrology. Journal of hydrology, 376(1-2), 24-33.

Wakode, H. B., Baier, K., Jha, R., Azzam, R. (2018). Impact of urbanization on groundwater recharge and urban water balance for the city of Hyderabad, India. International Soil and Water Conservation Research, 6(1), 51-62.

Wani, S. P., and Garg, K. K. (2009). Watershed management concept and principles.

Yang, P., Ames, D. P., Fonseca, A., Anderson, D., Shrestha, R., Glenn, N. F., & Cao, Y. (2014). What is the effect of LiDAR-derived DEM resolution on large-scale watershed model results? Environmental modelling & software, 58, 48-57.

Zhang, W., and Chang, N.-B. (2013). Impact of Climate Change on Physical and Biogeochemical Processes in the Hydrologic Cycle: Challenges and Perspectives. British Journal of Environment & Climate Change, 3(1), 1-8.

JJEES

JJEES (2025) 16 (2): 144-153
ISSN 1995-6681

Jordan Journal of Earth and Environmental Sciences

Evaluation of Organic Pollution Using Palmer's Algal Pollution Index in Ami River, Gorakhpur, (Uttar Pradesh) India.

Sarwat Jahan* and Ajay Singh

Natural Product Laboratory, Department of Zoology and Environmental Science, Deen Dayal Upadhyaya Gorakhpur University, Gorakhpur-273009 (U.P) India.

Received on 20 May 2024, Accepted on 31 December 2024

Abstract

This study investigates the organic pollution status of the Ami River in the GIDA (Gorakhpur Industrial Development Authority) sector-13, Gorakhpur district through seasonal sampling conducted from 2021 to 2022. Utilizing the Palmer pollution index, the research assesses the algal genera as indicators of organic pollution across four selected sites during the rainy, winter, and summer seasons. 41 algal genera across 9 classes were identified, with Bacillariophyceae (14), and Chlorophyceae (14) being the most prevalent algal group and Microystis, Pinnularia. Synedra, Cosmarium, Spirogyra, Zygnemagiganteume, Zygnemaczurde, Anabaena, Nostoc, and Spirulina are most common species in all seasons. Results indicate a significant organic pollution load, with the Palmer pollution index revealing high levels: 12 in sites 1, 2, and 3, and 17 in site 4 during the rainy seasons. In summer, values escalated to 31 for sites 1, 2, and 4, and 32 for site 3, indicating very high organic pollution across all sites. Winter assessments showed a reduction to 26, yet they are still indicative of high pollution levels. The findings underscore the detrimental effects of industrial discharges on the river ecosystem and highlight the need for continuous monitoring to address the declining algal diversity and effectively manage pollution levels.

Keywords: *Algal diversity, organic pollution, Palmer's index, Ami River.*

1. Introduction

Rivers are the lifelines of our planet, providing essential freshwater resources that power everything from agriculture to industry. Yet, these vital waterways face an unprecedented threat, particularly in urban areas where human activities have pushed many rivers to their breaking point (Khatri and Tyagi 2015; Nehme, et al. 2021). This threat leads to poor water quality and river degradation. It can also negatively disturb the living organisms that rely on it (Bassem 2020). In recent years, the health of our rivers has become increasingly concerning, with many showing signs of severe degradation due to rapid industrialization, municipal waste discharges agricultural runoff, and untreated sewage disposal (Maheshwari et al. 2014; Maheshwari, 2011; Abboud et al. 2021).

But nature has given us a remarkable tool to monitor these changes in algae (Omar 2010). Several studies have assessed the level of organic pollution in water bodies using algae as a bioindicator in rivers (Bhatnagar and Bhardwaj 2013, Noel and Rajan 2015, Salem et al. 2017). Various studies have demonstrated the utility of algal communities in assessing environmental changes (Omar 2010). Palmer's pollution index is a tool to describe changes in the organic pollution stage in freshwater bodies using algal population (Palmer 1969). Several researchers accessed the Palmer index to evaluate the water quality of various freshwater bodies, mostly rivers. In India, phytoplankton as a bioindicator of rivers has also been assessed using Palmer's algal pollution index (Wagh and Jondhale 2018; Singh and Sharma 2018).

This study marks the first comprehensive assessment of organic pollution in the Ami River using algal diversity as a bioindicator, contributing valuable insights into the river's ecological status. The findings will not only enhance our understanding of algal populations in this region but may also inform state governments and communities about necessary conservation efforts to protect the Ami River from ongoing pollution threats.

2. Material and Method

2.1 Ami River Description

Ami River originates from Sikhara Tal, Siddharthnagar, and flows further towards Basti, Sant Kabir Nagar, and Gorakhpur. Ami's journey starts from origin to end. It goes through a distance of about 102 km out of which the contaminated stretch lies between Basti to Sohgaura, Rudhauli, and Gorakhpur districts of approximate length of 80 km. Latitude is 26º33′02″N, and longitude is 83º26′45″E. The lethal effluents come from isolated large industries and GIDA. Nowadays, the Ami River is a holder for all the 5th, untreated sewage, and worst, all of them are centered in the industrial town in the Gorakhpur District. 266 industrial units were established, including paper mills, textile manufacturing, and food processing units. These discharge millions of untreated effluents into the drain every day. Captivating Decadal development into consideration, the expected population in 2019 was approximately 48,725, and the estimated generation of sewage was approximately 5.3 MLD (Mega liters Per Day).

* Corresponding author e-mail: sarwatj1995@gmail.com

2.2 Study area

Adilapar Village faces a high pollution load due to industrial discharges from GIDA through a drain into the river Ami, requiring urgent attention. 22 km from Gorakhpur, Bharsar Village, and industrial area sector, GIDA-13, Adhila Bazaar (Figure.1). It is excruciating to mention that the river gets victimized by industrial pollution. Beyond Adilapar, the GIDA drain meets the river, and it is converted into a river, which is a below-E category of CPCB (Central Pollution Control Board). It is noticed that the residents of more than 100 habitations downstream of the drain (Sarya) often complain of colds, mystery fevers, nausea, and high blood pressure. 158 units, including paper mills and textile manufacturing, which discharges some 45 million liters of untreated effluent into the drain every day.

2.2.1 Sampling sites:

Four selected sampling sites respectively shown as (Figures 2 and 3)

- Site 1: Near Ramlila Samiti (Effluent after Treatment)
- Site 2: Semrahwa Baba Mandir (Just Entry Point into the River)
- Site 3: 200 meter upstream river.
- Site 4: 200 meter downstream river.

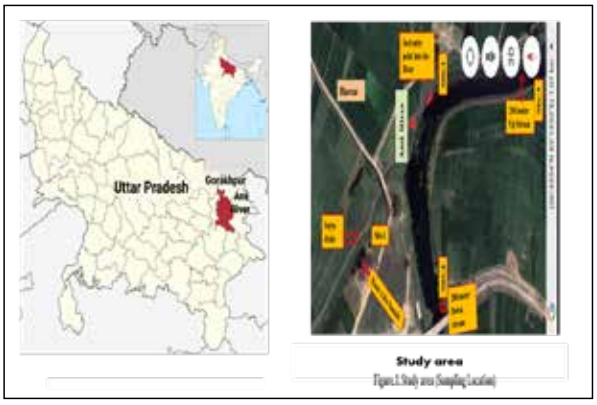

Figure 1. Location map and satellite image of Ami River

Figure 2. Selected sampling sites of Sarya drain and Ami River

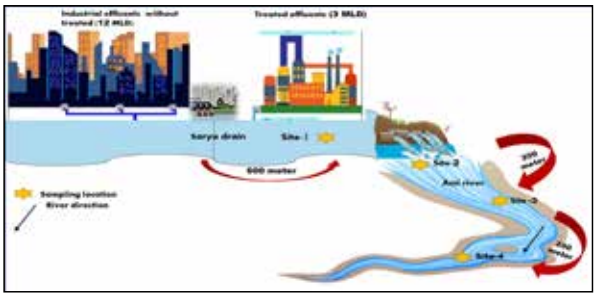

Figure 3. Diagrammatic representation of sampling location of Sarya drain and Ami River

2.3 Phytoplankton sampling and identification

The phytoplankton samples were collected by plankton net of standard bolting silk cloth no-25 (mesh size-0.03-0.04mm) by filtering 100 liters of water through it. This sieved residue, collected in the tube of 100 ml capacity attached at the end of the net, was transferred into a labeled glass bottle and transported to the lab under dark conditions and preserved 4% formaldehyde and 5% lugol solution. Phytoplankton were counted with the help of the Sedgwick Rafter Slide. The phytoplankton samples were observed under the electron microscope (Magnüs MXL plus). The Phytoplankton were identified by using books and literature (Bilgrami et al. 1991; Baird et al. 2017; Mahendra and Anand 2009).

2.4 Palmer's algal pollution

The present study rated the river water samples as high or low organically polluted, based on algae population by employing the Palmer pollution index (1969). Palmer developed a list of 20 algal genera and 20 algal species that are most tolerant to organic pollution with individual pollution index scores and formulated the pollution index scale as given below (Table 1). A score lower than 0-10 means a lack of organic pollution, 0-15 means that the river lacks moderate organic pollution, 15-19 indicates a high probability of organic pollution in the river, and 20 or more signifies high pollution in the river.

Table 1. Algal Genus Pollution Index (Palmer 1969)

Genus	*Index*	*Genus*	*Index*
Anacystis(Microystis)	**1**	***Micractinium***	1
Ankistrodesmus	**2**	***Navicula***	3
Chlamydomonas	**4**	***Nitzschia***	3
Chlorella	**3**	***Oscillatoria***	5
Closterium	**1**	***Pandorina***	1
Cyclotella	**1**	***Phacus***	2
Euglena	**5**	***Phormidium***	1
Gomphonema	**1**	***Scenedesmus***	4
Lepocinclis	**1**	***Stigeoclonium***	2
Melosira	**1**	***Syndra***	2

3. Result and Discussion

3.1 Phytoplankton Diversity

During the study period, 43 species of phytoplankton, belonging to 9 phyla, 9 classes, 21 orders, 30 families, and 2 sub-families were recorded. Forty-three species were identified of phytoplankton representing 5 groups namely Bacillariophyta, Chlorophyta, Cyanobacteria, Cyanophyta, Cyanobacteria, Dypnophyta, Myzozoa and. Euglenozoa. Bacillariophyceae includes 14 genera and species, Chlorophyceae 14 species, Cynophyceae 8 species, Dypnophyceae 4 species and Euglenophyceae 2 species, shown as (Plates, 1, 2, 3, and 4). The observation that algal diversity peaks in summer while declines during the rainy season is attributed to several factors, including changes in light availability, water temperature, and nutrient dynamics. During summer, increased sunlight and warmer temperatures likely create optimal conditions for phytoplankton growth. In contrast, heavy rain can lead to sedimentation and dilution of nutrients, creating unstable substrate conditions that adversely affect phytoplankton

proliferation. From an ecological perspective, understanding these seasonal shifts is crucial as they influence food webs within aquatic ecosystems. A decline in phytoplankton diversity could lead to reduced food availability for higher trophic levels, potentially impacting fish populations and overall biodiversity. The dominance of Bacillariophyceae (diatoms) across various studies aligns with previous research indicating their resilience to pollution (Abdel-Hamid et al. 2019). Their ability to thrive in polluted waters suggests a level of adaptability that may allow them to outcompete other groups under certain environmental stress. However, this raises questions about the health of the ecosystem as a whole, while diatoms may flourish under polluted conditions. Such dominance could indicate an imbalance within the community structure (Panigrahi and Patra, 2013; Annalakhmi and Amsath 2012; Jahan and Singh 2022). The correlation between industrial effluents and decreased phytoplankton diversity noted in the Ami River serves as a critical ecosystem. The findings that forty-five species were reported by (Jahan and Singh 2022) alongside concerns over pollution emphasize the need for ongoing monitoring and management strategies aimed at reducing industrial runoff. The distribution of phytoplankton in the Ami River is shown in Table (2).

Table 2. Distribution of phytoplankton at different sites during rainy winter and summer in Ami River at Gorakhpur.

Algal classes	Algal genera	Rainy				Winter				Summer			
		Site-1	Site-2	Site-3	Site-4	Site-1	Site-2	Site-3	Site-4	Site-1	Site-2	Site-3	Site-4
Bacillariophyceae	***Amphora***	+	+	+	+	+	+	+	+	+	+	+	+
	Cyclotella	-	+	+	+	-	-	-	-	-	-	-	-
	Diatoma	-	-	-	-	+	+	+	+	+	+	+	+
	Fragiliara	-	-	+	-	+	+	+	+	+	+	+	+
	Gainardia	-	-	-	-	-	-	-	-	+	+	+	+
	Gyrosigma	-	-	-	-	+	+	+	+	+	+	+	+
	Gamphonema	+	+	+	-	-	-	-	-	+	+	+	+
	Navicula	-	+	+	+	-	-	-	-	+	+	+	+
	Nitzschia	+	+	+	+	+	+	+	+	+	+	+	+
	Melosira	-	-	-	-	+	+	+	+	-	-	-	-
	Pleuroigma	-	-	-	+	-	-	-	-	+	+	+	+
	Pinnularia	+	+	+	+	+	+	+	+	+	+	+	+
	Synedra	+	+	+	+	+	+	+	+	+	+	+	+
	Suriella	-	-	-	+	-	-	-	-	-	-	-	-
Chlorophyceae	***Ankistrodesmus***	-	-	-	-	+	+	+	+	+	+	+	+
	Chlorella	-	-	-	-	+	+	+	+	+	+	+	+
	Chaetophora	-	-	-	-	-	-	-	-	+	+	+	+
	Cosmarium	+	+	+	+	+	+	+	+	+	+	+	+
	Chlorocccus	-	-	-	-	+	+	+	+	+	+	+	+
	Closterium	-	-	-	-	-	-	-	-	+	+	+	+
	Oedogonium	-	-	-	-	-	+	+	+	+	+	+	+
	Scenedesmus	-	-	-	-	+	+	+	+	-	-	-	-
	Spirogyra	+	+	+	+	+	+	+	+	+	+	+	+
	Stigeodonium	-	-	-	-	-	-	-	-	+	+	+	+
	Ulothrix	-	-	-	-	+	+	+	+	+	+	+	+
	Volvox colony	+	+	+	+	-	-	-	-	+	+	+	+
	Zygnemagiganteume	+	+	+	+	+	+	+	+	+	+	+	+
	Zygnemaczurde	+	+	+	+	+	+	+	+	+	+	+	+
Cynophyceae	***Anabaena***	+	+	+	+	+	+	+	+	+	+	+	+
	Aphanizmenon	-	-	-	+	+	+	+	+	+	+	+	+
	Nostoc	+	+	+	+	+	+	+	+	+	+	+	+
	Microystis	+	+	+	+	+	+	+	+	+	+	+	+
	Merismopedia	-	-	-	-	+	+	+	+	-	-	-	-
	Oscillatoria	-	-	-	+	+	+	+	+	+	+	+	+
	Phormidium	+	+	+	+	-	-	-	-	+	+	+	+
	Spirulina	+	+	+	+	+	+	+	+	+	+	+	+
Dypnophyceae	***Ceratiumhirndinella***	-	-	-	-	+	+	+	+	+	+	+	+
	Dinophysis acuminate	-	-	-	-	-	-	-	-	+	+	+	+
	Gymnodonium	+	+	+	+	-	-	-	-	+	+	+	+
	Gonyaeslaxspinifera	-	-	-	-	+	+	+	+	-	-	-	-
Euglenophyceae	***Euglena species***	-	-	-	-	+	+	+	+	+	+	+	+
	Phacus species	-	-	-	-	-	-	-	-	+	+	+	+

Note (+) = Present, (-) = Negative

Plate 1. Bacillariophyceae

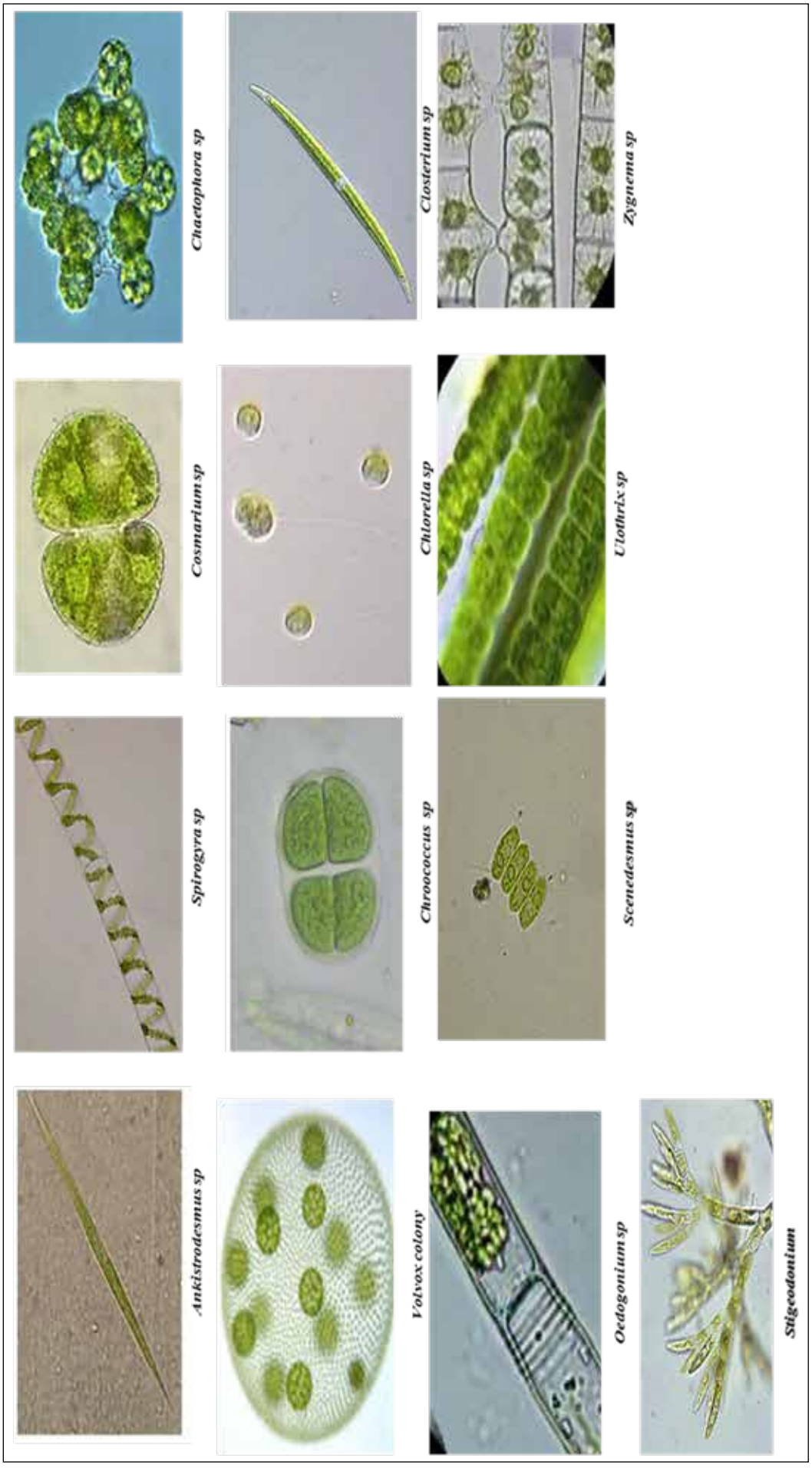

Plate 2. Chlorophyceae

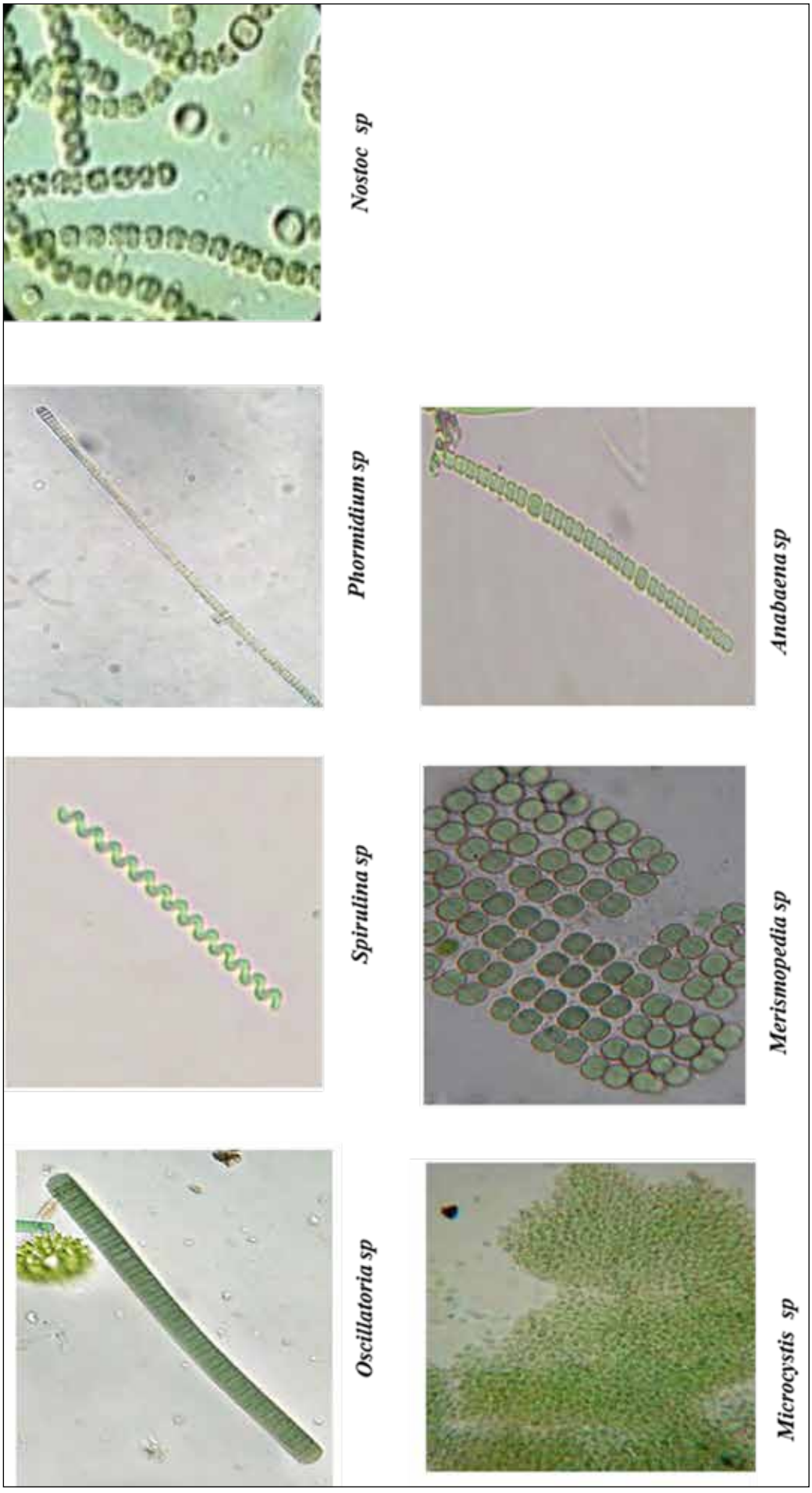

Plate 3. Cynophyceae

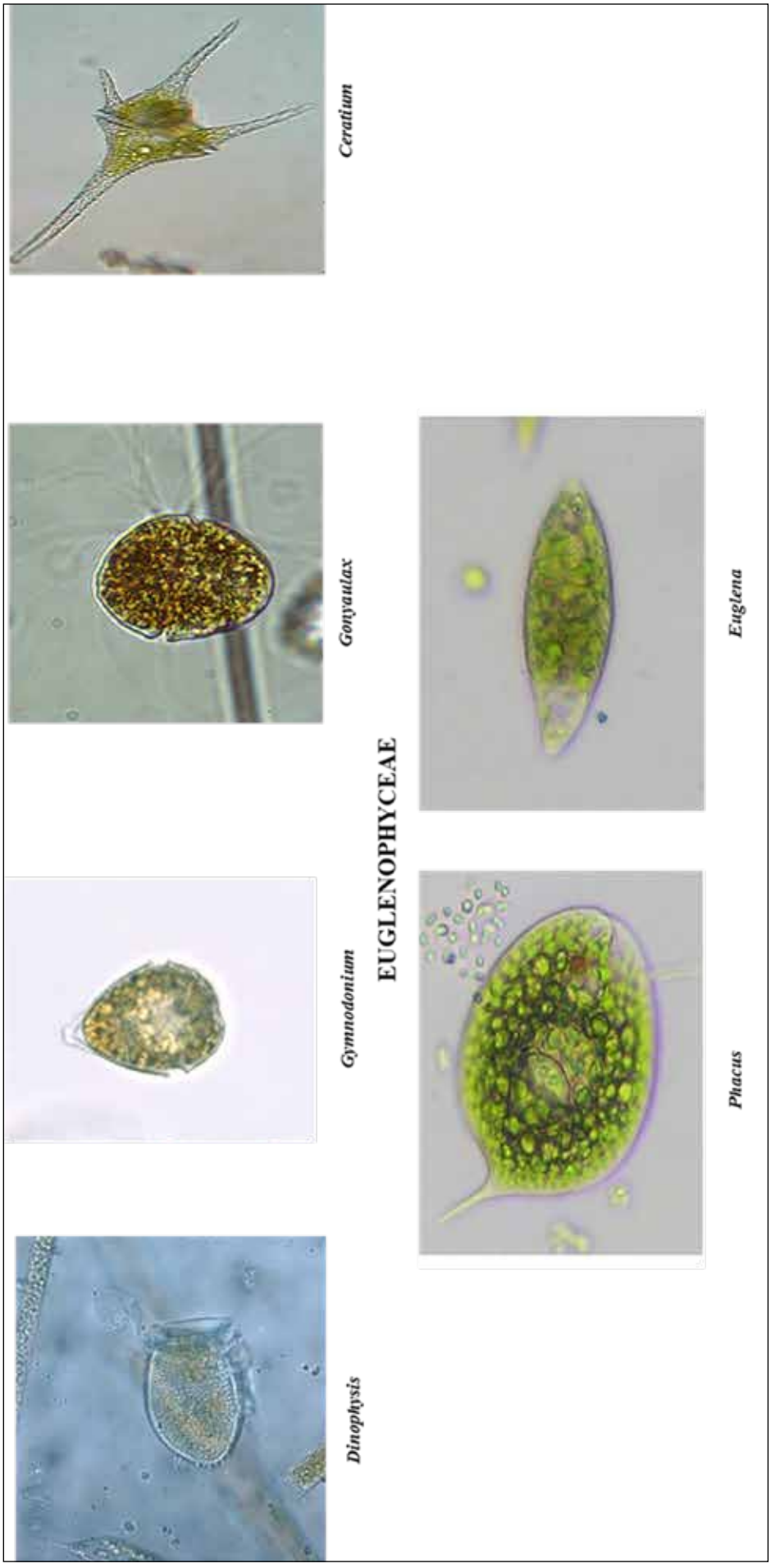

Plate 4. Dypnophyceae and Euglenophyceae

3.2 Level of Organic Pollution in the Ami River

The algae studied in genera and species, which can tolerate organic pollution, was reported by Palmer (1969). They prepared a list of 60 genera and 80 species, which can tolerate organic pollution. Algal species, reported in the present study, were recorded with the Palmer's index (Palmer 1969), along with the sign of occurrence. However, the highest score was recorded during summer, (32) at site 3 and winter, (25) at all the sites. The lowest score was recorded in rain (12) at site 2, and site 3, respectively as shown in (Table 3). The present investigation shows a high organic pollution load in summer and winter, and moderate organic pollution was recorded in the rainy season, during the study period in the Ami River.

A similar study, conducted by Jafari, and Gunale (2006), recorded site-1 (16), site-2 (36), and site-3 (41), in Mutha River, Pune. According to Palmer's index, all the ponds illustrate possible high levels of organic pollution. Pond-1(15), Pond-2 (19), Pond-3 (19), and Pond-4 (16), which showed moderate levels of pollution. The fourth pond showed the presence of Microystis indicating the deteriorated quality of water (Jose and Kumar 2011). The Palmer's score at stations A and B was 16 each. At stations C and D, the score was 24. These indicate moderate pollution load in A and B stations and confirm a high organic pollution at C and D stations in Pichhola Lake, Udaipur (Mishra et al. 2017). The pollution index at location D1-(15) shows moderate organic pollution, while locationsD2-(33) and D3-(25) respectively show evidence of high organic pollution The Deothan reservoir is highly polluted according to Palmer's index. So, it is urgent to avoid human interference in this natural reservoir (Wagh and Jondhale 2018). While total score pollution index at station (1) was 18, station (2) was 21, while station (3) was 17 recorded from Shatt Al-Arab River, Iraq. Station (1) indicated probable organic pollution and Stations 2 and 3 were greater than 20 indicating the confirmed high organic pollution (Al Kanani et al. 2018). Puttenahalli Lake is highly organically polluted and has reported the highest pollution index during pre-monsoon (28), monsoon (22), and during post-monsoon (23), recorded. The highest Palmer pollution index was recorded in the lake during all three seasons revealing the threatened condition of the lake (Veena, et al. 2022).

The study indicates that biological aspects with Physicochemical properties reveal a glossy polluted nature of the river having almost insignificant self-purification capacity to assimilate pollution in this stretch. The main sources of pollution in the river are industrial effluents, municipal water discharges, agricultural runoff, and human excreta. Thus, wastes discharged in Ami at Barshar (Gorakhpur) caused an adverse impact on the phytoplankton community structure and degraded the riverine habitat. Consequences of pollution are regarded as changes in qualitative and quantitative characteristics of the biological spectrum expressed as diversity (Pielou, 1969). Susceptible species are reduced and resistant species are favored as a result of pollution (Palmer 1963, Shevchenko et.al. 2020, Henson et.al. 2021, Yadava et. al. 1987). Physiological investigation at different sites of the Ami River suggests that algal pollution of the river is quite poor due to the continuous discharge of industrial wastes through the drain, containing different toxicants, and agricultural run-off with high oxygen-demanding wastes which probably acted synergistically leading to a very poor algal population despite of nutrient in the river water. The members of Bacillariophyceae appear to be best adapted in the polluted habitat as indicated by 14 species out of 41. The present investigation revealed that the effluents discharged from industries are very harmful to the phytoplankton as well as the aquatic ecosystem.

Table 3. Palmer's pollution index during 2021-2022

Genus &Species	Palmer's Pollution Index (1969)	Rainy				Winter				Summer			
		Site-1	Site-2	Site-3	Site-4	Site-1	Site-2	Site-3	Site-4	Site-1	Site-2	Site-3	Site-4
Anacystis(Microystis)	**1**	1	1	1	1	1	1	1	1	1	1	1	1
Ankistrodesmus	**2**	-	-	-	-	2	2	2	2	2	2	2	2
Chlamydomonas	**4**	-	-	-	-	-	-	-	-	-	-	-	-
Chlorella	**3**	-	-	-	-	3	3	3	3	3	3	3	3
Closterium	**1**	-	-	-	-	-	-	-	-	1	1	1	1
Cyclotella	**1**	1	1	1	1	-	-	-	-	-	-	1	-
Euglena	**5**	-	-	-	-	5	5	5	5	5	5	5	5
Gomphonema	**1**	1	1	1	-	-	-	-	-	1	1	1	1
Lepocinclis	**1**	-	-	-	-	-	-	-	-	-	-	-	-
Melosira	**1**	-	-	-	-	1	1	1	1	-	-	-	-
Micractinium	**1**	-	-	-	-	-	-	-	-	-	-	-	-
Navicula	**3**	3	3	3	3	-	-	-	-	3	3	3	3
Nitzschia	**3**	3	3	3	3	3	3	3	3	3	3	3	3
Oscillatoria	**5**	-	-	-	5	5	5	5	5	5	5	5	5
Pandorina	**1**	-	-	-	-	-	-	-	-	-	-	-	-
Phacus	**2**	-	-	-	-	-	-	-	-	2	2	2	2
Phormidium	**1**	1	1	1	1	-	-	-	-	1	1	1	1
Scenedesmus	**4**	-	-	-	-	4	4	4	4	-	-	-	-
Stigeoclonium	**2**	-	-	-	-	-	-	-	-	2	2	2	2
Syndra	**2**	2	2	2	2	2	2	2	2	2	2	2	2
	Total	**12**	**12**	**12**	**17**	**26**	**26**	**26**	**26**	**31**	**31**	**32**	31

4. Conclusion

The Ami River has been significantly impacted by the discharges of industrial effluents from multiple sources, including the Bharsar layout and domestic and agricultural activities in the Adilapar area. This pollution has had detrimental effects on the river ecosystem, leading to a noticeable decrease in the diversity of phytoplankton and an alarming increase in the organic load, present in the water. The detrimental impact of industrial effluents and other pollutants has given rise to a pressing environmental concern that demands immediate attention and remedial action. Protective measures must be taken to address the pollution of the Ami River. This includes the implementation of stricter regulations governing the disposal of industrial waste and the adoption of sustainable practices in domestic and agricultural activities near the river. Additionally, there is a critical need for collaborative efforts that involve government authorities, industries, and local communities to devise and implement effective strategies to restore the ecological balance of the Ami River and safeguard the overall health of its ecosystem. By prioritizing the protection and restoration of the Ami River, we can work towards ensuring a sustainable and thriving environment for current and future generations. Concerted efforts must be made to mitigate the sources of pollution and promote responsible environmental stewardship to preserve the Ami River as valuable natural resources for years to come.

Acknowledgment

Authors thank the Natural Product Laboratory and the supervisor for their guidance.

References

Abboud, I.A. and Shawabkeh, M. (2021). Water quality of Qunayya Spring-Jordan. Jordan Journal of Earth and Environmental Science. 12(3): 254-268

Abdel-Hamid, O.M.and Galal, T.M. (2019). Effect of pollution type on the phytoplankton community structure in lake Mariut, Egypt. Journal of Botany 59(1): 39-52.

Al Kanani, H. M and Al-Essa Saleh, A.K. (2018). Assessment of Shatt Al-Arab River Water Quality by Using Palmer's Algal Index, Basrah, Iraq. Basrah Journal of Agricultural Sciences 31(1):70-77.

Annalakhmi, G. and Amsath, A. (2012). Studies on the hydrobiology of River Cauvery and Its Tributaries Arasalar from Kumbakonam Region (Tamil Nadu, India) With Reference To Phytoplankton. International Journal of Plant, Animal and Environment Sciences 2(2): 37-46.

Baird, R.B., Eaton, A. D. and Rice, E.W., Eds. (2017). Standard Methods for the Examination of Water and Wastewater. 23rd Edition, American Public Health Association, American Water Works Association, Water Environment Federation, Washington D.C.

Bassem, S.M. (2020). Water pollution and aquatic biodiversity. Biodiversity International. J.4 (1):10-16.

Bhatnagar, M. and Bhardwaj, N. (2013). Biodiversity of algal flora in river Chambal at Kota, Rajasthan. Nature. Environment Pollution. Technology. 12(3): 547- 549.

Bilgrami, K. S. (1991). Biological profile of the Ganga: Bacteria and Bacteriophages. In C. R. Krishnamurti, T.S. Bilgrami, T. M. Das, & R. P Mathur (Eds.), The Ganga: A Scientific study. (pp. 72–77). New Delhi: Northern Book Center.

Henson, S.A., Cael, B.B., and Allen, S.R. (2021). Future phytoplankton diversity in a changing climate. Natural Community 12(5372)

Jafari, N G; Gunale, V R (2006). Hydrobiologcal Study of Algae of an Urban Freshwater River. Journal of Applied. Sciences. Environmental. Mitigation. 10 (2):153 – 158.

Jahan, S. and Singh, A. (2022). Various industrial effluents are threatening phytoplankton diversity in the Ami River. World Journal of Pharmaceuticals Research. 11(16):1881-1894

Khatri, N. and Tyagi, S. (2015). Influences of natural and anthropogenic factors on surface and groundwater quality in rural and urban areas. Front. Life Sciences. 8:1. 23-39.

Jose, L. and Kumar, C. (2011). Evaluation of Pollution by Palmer's Algal Pollution Index and Physico-Chemical Analysis of Water in Four Temple Ponds of Mattancherry, Ernakulam, Kerala. Nature Environment and Pollution Technology 10, No. 3.

Maheshwari, R. Singh, U. Singh, P., Singh, N., Lal, J. B, Rani, B. How Not To Stop the Flow. (2014). Journal of Advanced Scientific Research, 5(2):7-15.

Maheshwari, R. (2011) How Not To Stop the Flow. Journal of Advanced Scientific Research, 2(03):1-5.

Mahendra, P.G., Anand, N. (2009). Manual of freshwater algae of Tamil Nadu. Bishen Singh Mahendra Pal Singh.p. 1-112.

Mishra, V., Sharma, S.K, Sharma, B.K., Sharma, L.L. And Shukla, A. (2017) Seasonal Phytoplankton Diversity Using Palmer's Pollution Index of Pichhola Lake Dist.-Udaipur (Rajasthan) India. International Journal of Pure and Applied Bioscience. 5(4): 185-1861.

Nehme, N. Haydar, C.M., Al Jarf, Z., Abbass, F.A, Moussa, N., Youness, G., and Tarawneh, K. (2021). Assessment of the physicochemical and microbiological water quality of Al-Zahrani River Basin, Lebanon. Jordan Journal of Earth and Environmental Science. 12(3):206-213.

Noel, S.D. and Rajan, M.R. (2015). Evaluation of organic pollution by Palmer's algal genus index and physicochemical analysis of Vaigai River at Madurai India. Natural Research Conservation. 3(1): 7-10.

Omar. (2010). Perspective on the use of algae as biological indicators for monitoring and protecting aquatic environments, with special reference to Malaysian freshwater ecosystems. Tropical Life Science Research. 21(2): 51-67.

Palmer, CM. (1963). The effect of pollution on river algae. Bull.N.Y.Acad.sc. 198:1061-1062.

Palmer, C.M. (1969). A composite rating of algae tolerating organic pollution. Journal of Physiology, 65: 111-126.

Panigrahi, S and Patra, A.K. (2013). Studies of Seasonal Variation in phytoplankton diversity of river Mahanadi, Cuttack, Odisha. Indian Journal of Science Research, 4(2): 211-217.

Salem, Z., Ghobara, M. and El-Nahwary, A.A. (2017). Spatiotemporal evaluation of the surface water quality in the middle Nile Delta using Palmer's algal pollution index. Egypt. Journal of Basic Applied Sciences. 4(3): 219-226.

Schevchenko, T., Klochenko, P., and Nezbrytska, I. (2020). Response of phytoplankton to heavy pollution of water bodies. Oceanology & Hydrobiology Studies. 49(3):267-280.

Singh, S. and Sharma, R C. (2018). Monitoring of algal taxa as bioindicator for assessing the health of the high altitude wetland, Dodi Tal, Garhwal Himalaya, India. International Journal of Fisheries and Aquatic Studies. 6(3): 128-133.

Veena, S., Kumar, M. and Nandini, N. (2022). Algal Species Diversity and Palmer Pollution Index of Puttenahalli Lake in Bengaluru, India. Journal of Scientific Research.13 (10):41-46

Verma, S.R., Sharma, P., Tyagi, A., Santa Rani, Gupta and Dalele R.C. (1984). Limnologia (Berlin) 15:69.

Wagh, B.D. and Jondhale.A.S. (2018). Estimation of Organic Pollution by Palmer's Algal Index of Deothan Reservoir, Akole Taluka, Ahmednagar. Journal of Emerging Technologies and Innovative Research. 5:12.

Yadav, S.K., Sharma, S.P. Thapliyal, N.K. and Sahu B. (2008). Indian, Journal of Environment and Ecoplanning 15(3):557.

JJEES

JJEES (2025) 16 (2): 154-162
ISSN 1995-6681

Jordan Journal of Earth and Environmental Sciences

Residents' Perception of Household and Similar Waste Management Practices in Coastal Localities (Dairas) of Annaba District (Wilaya): Annaba, El Bouni and Chétaibi (North-East Algeria)

Amine Bey Djebar*[1], Rafik Kebbab[1],
Kaouther Lebdjiri[1], Rachid Amara[2], Hassen Touati[3] and Hocine Frihi[4]

[1] EMMAL Laboratory, Badji Mokhtar Annaba University, Badji Mokhtar University, Annaba - Algeria.
[2] University of Littoral Côte d'Opale, Dunkerque - France
[3] May 8, 1945 University, Guelma - Algeria
[4] Bioressources Marines Laboratory, Badji Mokhtar Annaba University.

Received on January 19, 2024, Accepted on January 11, 2025

Abstract

In 2023, 46 million Algerians produced around 13 million tons of household and similar waste (HSW), representing a market value of around US$100 million, managed by 5,000 companies. In order to understand the socio-demographic characteristics and context of the residents of 3 coastal localities in the Annaba District, namely Annaba, El Bouni, and Chétaibi. We used an anonymous survey to assess residents' perceptions of the management of their (HSW) and their sorting practices.

A random selection of 36 bins (1,44 kg) of waste was sorted out to show that organic materials are in the majority (62%). At the same time, plastics, paper/cardboard, glass, and metals are informally recycled . Due to a lack of adequate knowledge, the people, surveyed, perceived the time and effort required to sort waste as a constraint rather than a necessity for a comfortable lifestyle. Among married adults, women are more involved in sorting waste than men did, as was observed in both blocks of flats and detached houses.

The idea of living in a household highlights four aspects of household waste management and the dynamics within households: the complexity of waste management, the role of gender, the size of the household, and its motivations and the need for collective solutions. Living in a household is not just about sharing a living space but also about managing domestic, social and environmental challenges together.

The more people living in a household, the less motivation there is to sort waste. Biological recovery of organic matter through composting is proposed as the first solution, and almost 80% of those questioned are prepared to make a financial contribution to improving HSW management. Integrated management is needed to clarify the institutional, regulatory, and technical contexts of recovery, recycling, and reclamation systems.

Keywords: *Annaba, Algeria, management, household waste, social perception.*

1. Introduction

The size, distribution, and composition of a population on harming the environment, although this relationship is complicated and controversial. According to the World Bank report (2022), HSW is steadily increasing in absolute and per capita terms. Over 2.1 billion tons of waste are produced annually worldwide, and overpopulation will generate over 3.4 billion tons by 2050 (Kaza et al., 2018).

In Algeria, waste management requires a shift towards a circular economy, which is essential if the environmental transition is to be successful. This involves replacing the traditional linear model (produce, consume, discard) with sustainable practices, aimed at transforming waste into resources and rethinking production and consumption patterns. Although many promising waste management policies have been designed and adopted (Bouadam et al., 2022), their implementation has not produced the expected results. Waste remains a major challenge for all regions of the country (National Waste Agency (2020). The costs of waste management and disposal are borne mainly by local authorities, in contradiction with the polluter-pays principle (Law 30-10 TEOM, revised in the Algerian Finance Law of 2022), which stipulates that the polluter should bear the cost of the nuisance he/she causes.

Annaba District, located in northeastern Algeria and including the seaport coastline, represents a major strategic asset for its socio-economic and human development. However, this fragile ecosystem is constantly threatened by a growth in population and infrastructure saturation, leading to a substantial increase in HSW. Despite the allocation of substantial human, material, and financial resources, HSW management remains questionable, whether in terms of collection, transport, sorting, treatment, disposal, recovery, and satisfaction with the quality of services given.

* Corresponding author e-mail: aminedjebar48@gmail.com

To promote eco-citizenship in the three coastal localities; Annaba, El Bouni, and Chétaibi, residents can adopt simple gestures, such as reducing waste at sources through selective sorting. Better waste management starts at home, and selective sorting helps to recover recyclable materials and reduce the volume of waste destined for landfills. In addition, municipalities can play a crucial role by involving residents in a composting program for organic waste.

Composting can provide a natural fertilizer for gardens and green spaces, as well as reducing the amount of waste sent to landfill. In short, active participation by residents and municipalities can promote more responsible waste management and help preserve the environment. However, the reality and the practice are completely different. Food scraps that account for 62% of HSW are not sorted (Djebar et al., 2021), unlike metals, bread, paper, and plastics, which have been collected and recycled in recent years by the involvement of the informal sector and economic incentives (Cheniti et al., (2020); Kebaili et al., 2022).

To analyse how socio-professional factors, such as age, income, level of education, type of dwelling, distance, and financial participation influence household behaviour in terms of HSW management, a survey was carried out with the aim of assessing the perception of HSW management in order to increase the awareness and responsibility of the population and local authorities on this issue.

2. Materials and methods

2.1 Description of the study area

Annaba is a coastal city, located in the North Eastern of Algeria, extending over 1439 km^2, with a population estimated at 609500 in 2021. It is bordered by the Mediterranean Sea to the north and by three districts: Skikda to the west, El Tarf to the east, and Guelma to the south (Fig. 1). It is also a popular tourist destination with a 122.5 km seafront and over 6260 accommodation beds. Annaba District is composed of six localities:three are situated on the coast and the other three inland. Each locality is structured by one or more municipalities, making a total of twelve in the whole district. In this survey, devoted to the perception of HSW management, the three coastal localities were selected: Annaba, El Bouni, and Chétaibi (Fig. 1). In Annaba, waste collection was spatially organized around an administrative division and was carried out in container and door-to-door modes by public industrial and commercial establishments, which is responsible for waste management and improving the living environment of citizens. These are the public establishments for the management of technical landfill centres since 2009, urban improvement (since 2016), and clean Annaba (since 2016) under the authorities of the Directorate of the Environment in Annaba District, which provided us with collection data.

2.2. Waste separation and quantification

To analyse the HSW, a random selection of 36 garbage cans (3/month) was made during 2022, from which 1440 kg of mixed waste was manually sorted. The MODECOM method, proposed by the Waste Management Guide (2002), was used to classify waste, with a few adjustments adapted to local specificities. Waste was classified into six distinct categories according to its nature: organic waste, plastic, paper-cardboard, glass, metals, and complex compounds.

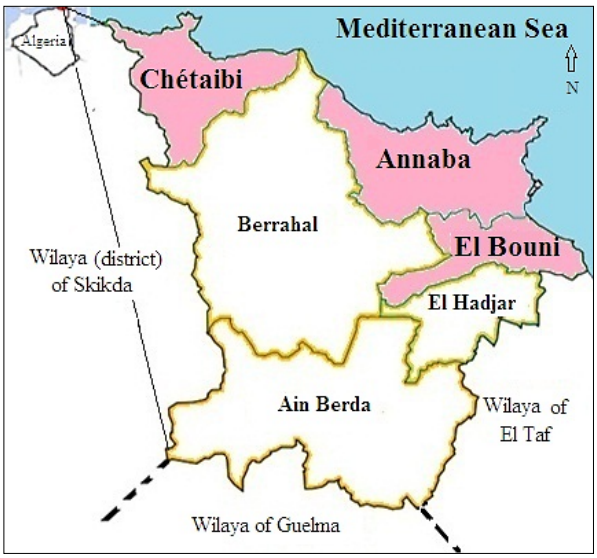

Figure 1. Location of the study area and territorial organisation of Annaba District (Wilaya) North Eastern of Algeria, with its aix localities (Dairas); three coastal: Annaba, El Bouni, and Chetaibi and three inlands: AïnBerda, El Hadjar, and Berrahal.

2.3. Survey technique and data collection

The anonymous survey was conducted between January and March 2023 in the study areas in order to understand residents' perceptions of HSW management. Random samples from 210 habitats were selected (70 samples/locality). Respondents were interviewed based on a questionnaire adopted and modified by Asante et al., (2016), to obtain information on their sociodemographic profiles, perception of HSW management, and sorting practices (Dlamini et al., 2017). The protocol comprises 19 variables grouped into three series: the first of which aims to determine the socio-demographic profile of respondents by asking seven questions related to gender (GE), age (AG), number of people in the household (NPH), level of education (LVE), profession (PRF), type of house (TOH) and monthly income (MIC) in Algerian dinar (DZD).

The second series focuses on households' perceptions of HWS management with four questions: quality of the HSW service (QWS), knowledge of an uncontrolled landfill in the commune (KUDC), the acceptable distance for building a waste depot from home (ADWD) and the distance residents are willing to travel to deposit their bottle waste in a specific sorting garbage bin (DTTSS).

The third series aims to understand the relationship between the sociodemographic characteristics of the respondents and their sorting practices through eight questions whether residents buy bottled water and/or drinks in plastic bottles (BPW), Why they buy bottled water in plastic bottles (WBPB), whether they are ready to sort their waste (RSW), whether they are members of an association or would like to join one shortly (MBA), whether they are prepared to pay an extra 1 DZD for a bottle of water (P1ED), whether they agree to contribute financially to waste collection (APFCW), the maximum amount they are

prepared to pay/year (MWP/Y), and finally whether they prefer this amount to be included in their electricity bill or a special payment (PAI).

The reliability of the survey was assessed using Cronbach's alpha test (1951), with a result deemed acceptable ($\alpha = 0.8902$).

2.4. Statistical method used

The Rcmdr and Facto Mine R packages of the R software (version 4.1.2 of 2020) were used to analyse the data, collected during the survey on HSW management. Descriptive analyses enabled us to report on the frequency and percentage of sociodemographic characteristics, as well as on the disposal method and households' perceptions of waste management.

The Chi^2 goodness-of-fit test was used to determine relationships between categorical variables. Only factor loading values of 0.7 were considered for significant selection and interpretation. Principal component analysis (PCA) was used to identify the grouping of variables and to determine the interdependent factors within a given concept. We first present the descriptive statistics of all variables before discussing the results of the correlation analysis between sociodemographic factors and respondents' backgrounds on the one hand, and practices and perceptions regarding HSW management, on the other hand, before presenting the results of PCA.

3. Results

The three studied localities comprised a total population of 511139 inhabitants who generated an average of 120807 tons of HSW in 2022 (0.66 kg/inhabitant/day). The highest volume of waste was reached during the Ramadan period which was 11395 tons. A family of three to four people produces between two and three kg of HSW per day, with the largest fraction being organic matter, reaching 62%. Complex compounds accounted for 17%, followed by plastics (10%), paper and cardboard (8%), various metals (1%), and glass (2%) (Fig. 2). On the beaches of the three districts, 90% of the HSW was made up of plastics, particularly protective masks (polypropylene and rubber), and other packaging used for beverages and domestic needs.

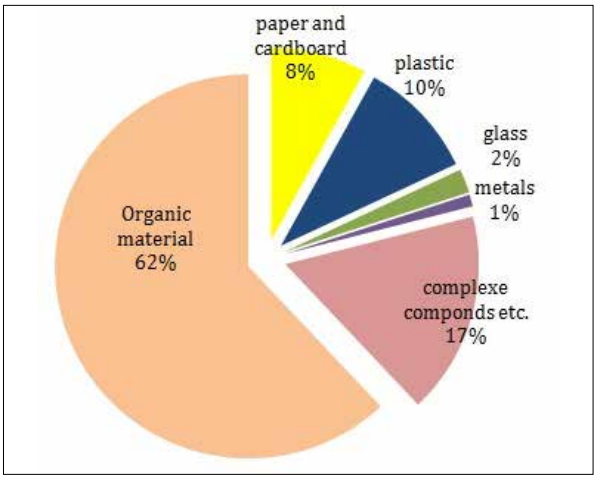

Figure 2. Distribution of household and similar waste discharged by the populations of the three coastal localities of Annaba: Annaba, El Bouni, and Chétaibi

3.1 Data analysis

3.1.1 Sociodemographic characteristics and respondents' backgrounds

The majority of respondents were male (N = 168; 80%), married (N = 129; 61%), and 28% were aged between 25 and 35 years. In the three coastal towns, the majority of households consisted of two (32%) to three (36%) persons. Respondents with primary education (N = 66) accounted for 31% of the respondents, followed by those with secondary education (30%, N = 62), and those with university education (22%, N = 46). Approximately 26% of respondents work in the public sector, 46% live in apartment blocks, and 39% (N = 82) earn between DZD 21,000 and DZD 40,000 per month, with the highest number of salaries above DZD 100,000 in Annaba District (Table 1). The chi-squared test showed a highly significant difference between the coastal districts only for the type of housing (TOH) ($\chi^2 = 30.68$; $p < 0.001$).

Gender was highly correlated, respectively, with MBA (r = 0.99), PRF (r = 0.98), DTTSS (r = 0.97), RSW (r = 0.96), BPW (r = 0.95) and APFCW (r = 0.91). It remains strongly correlated with PAI (r = 0.87) and the residents' age (r = 0.75). This variable is negatively correlated with NPH (r = -0.97), MIC (r = -0.88), and LVE (r = -0.86) (Annex).

Age (AG) was highly correlated with seven variables. PRF had the highest correlation (r = 0.8202), followed by BPW (r = 0.8092), RSW (r = 0.7773), MBA (r = 0.7729), GE (r = 0.7528), APFCW (r = 0.7509), and MWP/Y (r = 0.7458). However, age was negatively correlated with NPH (r = -0.8219).

The number of individuals in the household (NPH) was strongly correlated with LVE (r = 0.86), followed by MIC (r = 0.81) and ADWD (r = 0.80). This parameter was negatively correlated with nine variables, almost perfectly correlated with RSW (r = -0.99), BPW (r = -0.98), MBA (r = -0.97), APFCW (r = -0.97), GE (r = -0.9700), PRF (r = -0.96), DTTSS (r = -0.92), and finally, MWP/Y (r = -0.91). The NPH was also negatively correlated with age (r =-0.82) and PAI with a correlation coefficient of r = -0.76 (Annex).

The level of education (LVE) was positively correlated with NPH (r = 0.86), P1ED (r= 0.78), WBPB (r = 0.77), and ADWD (r = 0.74). This variable was negatively correlated with the following variables, respectively: DTTSS (r= -0.93), MBA (r = -0.87), PRF (r = -0.86), GE (r = -0.86), BPW (r = -0.8643), RSW (r = -0.86), MWP/Y (r = -0.83), APFCW (r = -0.82), and PAI (r = -0.70). Profession (PRF) was highly correlated with six variables: MBA (r = 0.98), GE (r =0.98), BPW (r = 0.97), DTTSS (r = 0.96), MWP/Y (r = 0.96), and RSW (r = 0.95). This variable remains positively correlated with APFCW (r = 0.89), age (r = 0.82), and PAI with a correlation coefficient of r = 0.80.

Our results show a highly significant and inversely proportional correlation between PRF and NPH (r = -0.96), LVE (r = -0.86), MIC (r = -0.85), the ADWD (r = -0.84), and P1ED with r = -0.73. The type of housing (TOH) was negatively correlated with the QWS quality of HSW service in the locality (r = -0.93) (Annex). Monthly income (MIC) was positively correlated with NPH (r = 0.81), ADWD (r =0.80), and P1ED (r = 0.70). This parameter was negatively correlated with nine variables: MBA (r = -0.88), GE (r = -0.88), BPW (r = -0.86), RSW (r = -0.86), PRF (r = -0.85), MWP/Y (r = -0.82), DTTSS (r = -0.82), APFCW (r = -0.80), and PAI (r = -0.75) (Annex).

Table 1. Sociodemographic characteristics and respondents' backgrounds in three coastal localities of the District of Annaba (N = 210).

		Coastal localities					
Variable	Description	Annaba	El Bouni	Chétaibi	F. (N)	%	χ^2 (p-value)
GE	Male	52 (37M)	55 (42M)	61 (50M)	168	80	3.75 (0.15)
	Female	18 (12M)	15 (11M)	09 (5M)	42	20	
AG	25-35	20	17	22	59	28	8.53 (0.38)
	35-45	11	13	16	40	19	
	45-55	19	12	14	45	21	
	55-65	17	18	13	48	23	
	65-75	03	10	05	18	09	
NPH	1	04	06	03	13	06	6.38 (0.89)
	2	24	22	21	67	32	
	3	20	27	29	76	36	
	4	12	08	06	26	12	
	5	06	04	06	16	08	
	6	02	02	03	07	03	
	7 and +	02	01	02	05	02	
LVE	University and +	18	13	15	46	22	3.24 (0.91)
	High school student	24	20	22	66	31	
	Secondary	19	22	21	62	30	
	Primary	07	10	08	25	12	
	Others	02	05	04	11	05	
PRF	Public function	16	19	19	54	26	4.93 (0.96)
	Liberal profession	06	03	05	14	07	
	Trader	09	11	11	31	15	
	Farmer	08	10	10	28	13	
	Worker	15	11	13	39	19	
	Retirement	14	12	08	34	16	
	Unemployed	02	04	04	10	05	
TOH	Individual house	18	16	42	76	36	30.68 (0.00)***
	Building	37	44	16	97	46	
	Traditional house	15	10	12	37	18	
MIC	- 20 000 DZD	03	05	12	20	10	23.56 (0.09)
	21 to 40 000	19	27	36	82	39	
	41 to 60 000	22	16	11	49	23	
	61 to 80 000	08	06	03	17	08	
	81 to 100 000	06	07	03	16	08	
	101 to 120 000	05	05	02	12	06	
	121 to 140 000	04	02	01	07	03	
	141 to 160 000	02	01	01	04	02	
	+ 161000	01	01	01	03	01	

*: Significant difference, **: highly significant, ***: very highly significant. (GE) Gender, (AG) Age, (NPH) Number of People in the Household, (LVE) Level of Education, (PRF) Profession, (TOH) Type of House, and Monthly Income (MIC) in Algerian Dinar (DZD).

3.1.2. Household Practices and Perceptions Regarding HSW Management

Approximately, 45% of households (N = 94), where the majority live in Annaba District (N = 37) and El Bouni (N = 32), consider the quality of solid waste management service to be good (Table 2). Furthermore, half of the residents are unaware of the existence of illegal dumpsites in their respective localities, 40% of them accept the construction of a landfill 5 km away from their homes, and 45% do not want to travel more than 100 m to deposit their bottles in a specific sorting bin. In the three localities, only 7% of the respondents are willing to travel more than 1000 m to do so. The Chi-square test shows no significant difference between the variables of household practices and perceptions regarding solid waste management in the four cases, $p > 0.05$ (Table 2).

Quality of the HSW service (QWS) was highly negatively correlated with the TOH (r= -0.93), while knowledge of illegal dumpsites (KUDC) was not correlated with any variables (Annex). The accepted distance for the construction of a solid waste management landfill (ADWD) was strongly

positively correlated with the P1ED (r = 0.93). However, it was strongly correlated with NPH (r = 0.80), MIC (r = 0.80), and LVE (r = 0.74). Quality of the HSW service (QWS) was also highly negatively correlated with BPW (r = -0.90), PRF (r = -0.84), RSW (r = -0.83), MBA (r = -0.81), APFCW (r = -0.80), DTTSS (r = -0.77), and GE (r = -0.77).

The distance to travel to deposit bottle waste in a specific sorting bin (DTTSS) was highly correlated with GE (r = 0.97), PRF (r = 0.96), MBA (r = 0.96), MWP/Y (r = 0.96), BPW (r =0.92), and willingness to sort waste (r = 0.91). This relationship remains strongly positively correlated with two variables: PAI (r = 0.86) and APFCW (r = 0.84). However, there was a strong negative correlation between LVE (r = -0.93) and the number of individuals in the household (r = -0.92). This variable also remains negatively correlated with MIC (r = -0.82), ADWD (r = -0.77), and P1ED (r = -0.74) (Annex).

Table 2. Correlation between Household Practices and Perceptions Regarding HSW Management (N = 210).

Coastal localities							
Variable	Description	Annaba	El Bouni	Chétaibi	F. (N)	%	χ^2 (p-value)
QWS	Good	37	32	25	94	45	9.07(0.06)
	Average	29	25	36	90	43	
	Bad	04	13	09	26	12	
KUDC	Yes	39	31	34	104	50	1.86(0.40)
	No	31	39	36	106	50	
ADWD	1 Km	16	12	23	51	24	8.48(0.20)
	5 Km	28	31	26	85	40	
	10 Km	16	22	17	55	26	
	+ 10 Km	10	05	04	19	09	
DTTSS	- 100m	26	35	34	95	45	11.26(0.18)
	100 to 300m	15	15	12	42	20	
	300 to 500m	12	9	10	31	15	
	500 to 1000m	13	06	09	28	13	
	+ 1000m	04	05	05	14	07	

(QWS) Quality of the HSW service, (KUDC) knowledge of an uncontrolled landfill in the commune, (ADWD) The acceptable distance for building a waste depot from home and thedistance residents are willing to travel to deposit their bottle waste in a specific sorting garbage bin (DTTSS).

3.1.3. Relationship between sociodemographic characteristics, respondents' Background, and Household Practices (HSW Sorting Practices)

The eight sets of data illustrate the relationship between sociodemographic characteristics, respondents' background, and household practices. Our results show that 93% (N = 196) of respondents purchase water and/or soft drinks in plastic bottles, and 75% do so because they believe tap water is polluted. The majority of residents (82%; N = 173) are willing to sort their waste, and 84% are members of an association or would like to join one soon. 52% of respondents in both the localities of Annaba and El Bouni or Chétaibi are willing to pay up to 2 DZD extra for the purchase of a bottle of water, 79% are willing to contribute financially to solid waste management collection, 73% are willing to spend up to 1000 DZD / year, and 66% would like this amount to be integrated into water or electricity bills for practical reasons (Table 3).

The Chi-square test showed that there were five significant differences among the eight selected variables. These differences pertain to the purchase of water and/or soft drinks in plastic bottles with a χ^2 of 10.25 ($p < 0.001$), acceptance of paying one DZD for the purchase of a bottle of water with a χ^2 of 30.50 ($p = 0.000$), financial participation in solid waste management collection with a χ^2 of 8.31 ($p > 0.01$), maximum amount accepted to pay per year with a χ^2 of 18.43 ($p < 0.001$), and the preference for integrating financial participation into electricity or water bills with a χ^2 of 15.87 ($p < 0.001$) (Table 3).

Purchasing water and/or soft drinks in plastic bottles (BPW) was very highly correlated with RSW (r = 0.98), MBA (r = 0.97), PRF (r = 0.97), APFCW (r = 0.95), GE (r = 0.95), DTTSS (r = 0.92), and MWP/Y (r = 0.89). This parameter was highly correlated with age (r = 0.80) and PAI (r = 0.70). This variable was very highly negatively correlated with NPH (r = -0.98) and ADWD (r = -0.90). It was strongly correlated with the LVE (r = -0.86), MIC (r = -0.86) and P1ED (r = -0.78) (Annex). The reason for purchasing water in plastic bottles (WBPB) was strongly positively correlated with LVE (r = 0.77).

The willingness to sort waste (RSW) was also highly positively correlated with the BPW (r = 0.98), APFCW (r = 0.98), MBA (r = 0.97), GE (r = 0.96), PRF (r = 0.95), DTTSS (r = 0.91), and MWP/Y (r = 0.90). It was also correlated with age (r = 0.77) and PAI (r = 0.75). This relationship was strongly negatively correlated with NPH (r = -0.99), LVE (r = -0.86), MIC (r= -0.86), ADWD (r = -0.83), and P1ED (r = -0.70).

Being a member of an association or planning to join one soon (MBA) was highly correlated with 7 variables: gender (r = 0.99), PRF (r = 0.98), RSW (r = 0.97), BPW (r =0.97), DTTSS (r = 0.96), MWP/Y (r = 0.96), and APFCW (r = 0.92). With the preference for PAI (r = 0.84), this variable remains strongly correlated. However, it was strongly negatively correlated with the NPH (r = -0.97), MIC (r = -0.88), LVE (r = -0.87), ADWD (r = -0.81) and P1ED (r = -0.70).

Acceptance of paying one DZD extra for the purchase of one bottle of water (P1ED) was strongly positively correlated with ADWD (r = 0.93), LVE (r = 0.78), and MIC (r = 0.70). However, it was negatively correlated with BPW (r = -0.78), DTTSS (r = -0.74), PRF (r = -0.73) and MBA (r = -0.70).

Acceptance of financial participation in the collection of solid waste (APFCW) was positively correlated with eight variables: RSW (r = 0.98), BPW (r = 0.95), MBA(r = 0.92), GE (p = 0.91), and PRF (r = 0.89), DTTSS (r = 0.8429), MWP/Y (r = 0.82), and age (r = 0.75). However, it was strongly negatively correlated with NPH (r = -0.97), LVE (r = -0.82), ADWD (r = -0.80) and MIC (r = -0.80). The maximum amount you would be willing to pay per year (MWP/Y) was positively correlated with gender (r = 0.97), MBA (r = 0.96), DTTSS (r = 0.96), PRF (r = 0.96), PAI (r= 0.93), RSW (r = 0.90), and BPW (r = 0.89). It was also positively correlated with APFCW (r = 0.82) and age (r = 0.74). On the contrary, it was negatively correlated with NPH (r = -0.91), level of education (r = -0.83), and MIC (r = -0.82).

The preference for the payment to be integrated into electricity bills or in a special payment (PAI) was strongly correlated with MWP/Y(r = 0.93), and it was strongly correlated with six variables: GE (r = 0.87), DTTSS (r = 0.86), MBA (r = 0.84), PRF (r = 0.80), RSW (r = 0.75), and BPW (r = 0.70). This preference was strongly negatively correlated with NPH (r = -0.76), MIC (r = -0.75), and LVE (r = -0.70) (Annex).

Table 3. Correlation between socio-demographic characteristics of respondents and HSW management practices (Waste Sorting Practices).

Coastal localities							
Variable	Description	Annaba	El Bouni	Chétaibi	F. (N)	%	χ^2 (p-value)
BPW	Yes	67	69	60	196	93	10.25 (0.000)***
	No	03	01	10	14	07	
WBPB	Have a baby	09	07	6	22	10	4.00 (0.400)
	Have a sick	13	06	11	30	14	
	Polluted tap water	48	57	53	158	75	
RSW	Yes	61	55	57	173	82	1.83 (0.390)
	No	9	15	13	37	18	
MBA	Yes	55	59	62	176	84	2.59 (0.270)
	No	15	11	08	34	16	
P1ED	1 DZD	25	10	32	67	32	30.50 (0.000) ***
	2	37	37	35	109	52	
	5	08	23	3	34	16	
APFCW	Yes	63	50	52	165	79	8.31 (0.010)*
	No	07	20	18	45	21	
MWP/Y	1000 DZD	41	49	63	153	73	18.43 (0.001)**
	2000	19	10	05	34	16	
	+ 2000	10	11	02	23	11	
PAI	Electricity water bills	38	42	59	139	66	15.87 (0.000) ***
	Special payment	32	28	11	71	34	

*: Significant difference, **: highly significant, ***: very highly significant

(WPW) Do they buy bottled water and/or drinks in plastic bottles? (WBPB) Why do they buy bottled water? (RSW) Are they prepared to sort their waste? (MBA) Are they members of an association or would like to join one shortly? (P1ED) Are they prepared to pay one Algerian Dinar (DZD) more for a bottle of water? (APFCW) Are they willing to contribute financially to waste collection? (MWP/Y) Are they willing to pay the maximum amount per year? (PAI) Do they prefer this amount to be included in their electricity bill or to be the subject of a special payment?

Annex. Matrix of correlations of sociodemographic variables, household practices and perceptions regarding HSW Management.

	AG	MBA	BPW	P1ED	KUDC	RSW	DTTSS	ADWD	APFCW	PAI	TOH	LVE	NPH	WBPB	PRF	QWS	MIC	GE	MWP.Y
AG	1.0000																		
MBA	0.7729	1.0000																	
BPW	0.8092	0.9744	1.0000																
P1ED	-0.4381	-0.7080	-0.7844	1.0000															
KUDC	-0.1587	-0.1813	-0.1085	0.3309	1.0000														
RSW	0.7773	0.9774	0.9857	-0.7012	0.0088	1.0000													
DTTSS	0.6804	0.9691	0.9237	-0.7476	-0.3122	0.9161	1.0000												
ADWD	-0.6733	-0.8138	-0.9023	0.9385	0.2334	-0.8300	-0.7766	1.0000											
APFCW	0.7509	0.9270	0.9596	-0.6632	0.1691	0.9853	0.8429	-0.8067	1.0000										
PAI	0.5130	0.8426	0.7004	-0.3559	-0.2765	0.7501	0.8609	-0.4139	0.6581	1.0000									
TOH	-0.4245	-0.1782	-0.3791	0.6029	0.0744	-0.2584	-0.1050	0.6775	-0.2991	0.3554	1.0000								
LVE	-0.5494	-0.8741	-0.8643	0.7883	0.1449	-0.8621	-0.9375	0.7483	-0.8233	-0.7062	0.1509	1.0000							
NPH	-0.8219	-0.9772	-0.9802	0.6639	0.0111	-0.9942	-0.9209	0.8015	-0.9753	-0.7621	0.2383	0.8638	1.0000						
WBPB	-0.0966	-0.5088	-0.4548	0.3296	-0.2872	-0.5402	-0.5941	0.2220	-0.5556	-0.5460	-0.3185	0.7712	0.5428	1.0000					
PRF	0.8202	0.9892	0.9733	-0.7396	-0.2809	0.9546	0.9699	-0.8422	0.8933	0.8061	-0.2540	-0.8696	-0.9623	-0.4421	1.0000				
QWS	0.3872	0.0453	0.2495	-0.3434	0.1576	0.1619	-0.1020	-0.5045	0.2378	-0.4577	-0.9309	0.0944	-0.1393	0.4690	0.0956	1.0000			
MIC	-0.5421	-0.8892	-0.8620	0.7094	0.2051	-0.8600	-0.8288	0.8003	-0.8080	-0.7584	0.1864	0.6797	0.8172	0.2969	-0.8546	-0.1037	1.0000		
GE	0.7528	0.9977	0.9577	-0.6712	-0.1790	0.9690	0.9701	-0.7749	0.9150	0.8761	-0.1111	-0.8683	-0.9700	-0.5299	0.9815	-0.0163	-0.8875	1.0000	
MWP.Y	0.7458	0.9680	0.8927	-0.5790	-0.2980	0.9040	0.9648	-0.6741	0.8247	0.9340	0.0152	-0.8320	-0.9197	-0.5041	0.9618	-0.1536	-0.8296	0.9789	1.0000

3.2. Principal Component Analysis (PCA) of the studied coastal localities

The factorial plots of the first two principal axes clearly showed a distinct inter-locality variation (Fig. 3). Together, they explain 64.14% of the total variation. The first principal axis explains 45.14% of the total variation and was positively correlated with 10 variables: gender (r = 0.98), MBA (r = 0.98), RSW (r = 0.97), BPW (r = 0.97), APFCW (r = 0.92), MWP/Y (r = 0.84), PAI (r = 0.80), PRF (r = 0.74), DTTSS (r = 0.59), MIC (r = -0.613), and age (r = 0.49) (Fig. 3). However, this axis was negatively correlated with NPH (r = -0.610), ADWD (r = -0.51), and weakly correlated with LVE (r = -0.36) and KUDC (r = -0.17). The second principal axis explains 19% of the total variation and was positively correlated with four variables: PE1D (r = 0.81), QWS (r = 0.78), TOH (r = 0.77), and strongly negatively correlated with WBPB (r = -0.92) (Fig. 3).

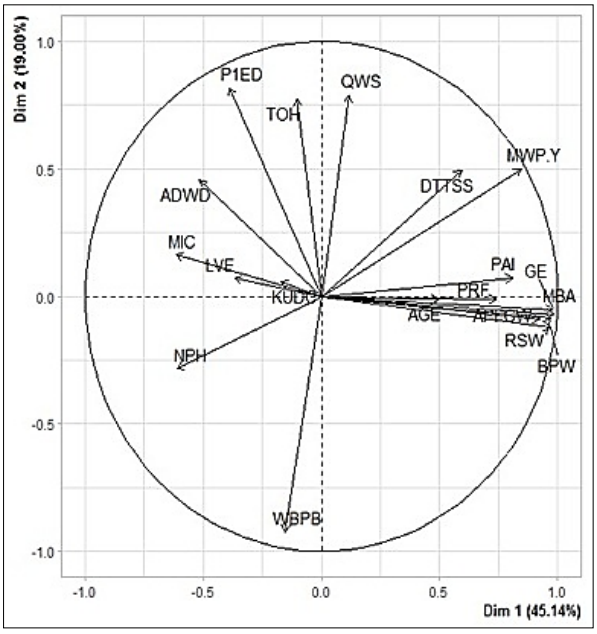

Figure 3. Principal Component Analysis representation of the 3 coastal localities of Annaba: Annaba, El Bouni, and Chétaibi.

The factorial plot of the first two principal axes clearly showed an inter-locality variation, where the two axes together explain 64.14% of the total variation (Fig. 4).

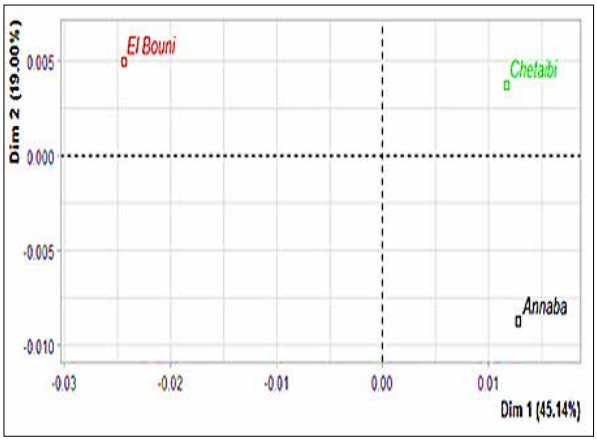

Figure 4. Representation of an inter-locality factorial plot.

4. Discussion

Due to the complexity of its treatment and the associated environmental risks, the management of waste electrical and electronic equipment is a major challenge (Haniyeh et al., 2021). Despite this, scientists and sociologists often do not show much interest in this issue. In this context, a survey consisting of (19) questions was conducted among residents of three coastal localities in the Annaba district in northern Algeria: Annaba, El Bouni, and Chétaibi. This study allowed for the analysis of HSW composition, evaluation of residents' perceptions, and a better understanding of the sociodemographic characteristics and backgrounds of the respondents. The obtained results will help tailor HSW management program planning to the specific needs of the population.

Organic waste, which accounts for 62% of the waste, disposed of by the populations of Annaba's three coastal localities, reflects a trend widely observed in most developing countries, as highlighted by numerous authors (Campuzano and Gonzalez-Martinez (2016), Fadhullah et al., (2022), and Ulloa-Murillo et al., (2022). It can also be seen in the Report on the Solid Waste Management in Algeria (2014). This type of waste generates unpleasant odors and attracts insects and rodents. However, it can be composted to produce a residue rich in humus and mineral compounds. To encourage this practice, it is suggested to provide each household with a distinct-colored bin, labelled with an explanatory manual

in Arabic and French, containing simple drawings showing the step-by-step process. Additionally, it would be useful to install large-capacity collection and composting bins for organic waste in each neighbourhood.

For over four years, (21) companies, specializing in the recovery and recycling of metals, paper cardboard, and various types of plastics have been operating in the Annaba District. Thanks to their activity, these wastes have been maintained at respective rates of 1%, 8%, and 10%, while complex compounds such as textiles, shoes, hazardous waste, inert diapers, and other disposable products reached 17%. However, it should be noted that the majority of waste collection activities for these HSW were informal.For example, a kilogram of plastic bottles (PET) is currently sold for between 70 and 100 DZD.

The second objective of this study was to determine the socio-professional variables that influence the behaviour of respondents, especially in terms of waste sorting and participation in improving HSW management in their localities. The perception and behaviour of a population regarding the management of HSW in a coastal environment were explored through a simple survey. According to Sawaya et al., (2023) and Rai et al., (2021), individual perception was shaped by the context and current situation, as well as values, moods, social circumstances, and individual expectations.

Currently, the majority of respondents do not sort their waste, except for metals (high demand by type), bread (religious belief compliance), and plastic (increased awareness). However, out of the (210) residents of the three coastal districts of Annaba, N = 173 (82%) are willing to sort their waste in the future. This particularity gives us hope that it is possible to increase waste sorting practices and expand them to other HSW. The respondents lack adequate knowledge of the crucial importance of source waste sorting. They are unaware that the volume of HSW dumped in landfills is constantly increasing, thereby, jeopardizing the remaining space in technical landfills at a rapid pace. According to studies, it is important to consider gender differences and traditional roles to encourage household participation in waste management. The correlations between the selected parameters can be explained by socio-economic, cultural and behavioural factors. For example, larger households may have a higher total income because several members contribute financially. At higher income levels, household size often decreases due to educational, occupational, and family choices, influenced by access to more resources. It has been found that young couples often start with lower incomes and smaller. According to our observations, the type of housing strongly influences HSW management practices and perceptions. People, living in apartment buildings (46%) and individual houses (36%), are more likely to sort their waste, as reported by Vassanadumrongdee and Kittipongvises (2018). These two types of housing accommodate respondents with high and medium incomes in the three coastal districts of Annaba, where waste collection services are well-provided. Contrary to the suggestions of Adeoti Adetola et al., (2010), economic considerations do not seem to play a major role in the perceptions and attitudes of respondents regarding HSW management practices. However, during our interviews, we found that the higher the monthly income of the interviewed person or the total household income is, the higher their value of financial participation in HSW management will be. Low income has a negative influence on respondents' perceptions and attitudes toward the quality of HSW management in their district, as suggested by Parfitt et al., (197) and Kaoje et al., (2017).

We also noticed that the number of people in the household influences waste sorting. Households with one to three people tend to have more significant eco-friendly behaviours than households with four or more people. This result is similar to that of the study by Addo et al., (2017), who reported that households with more than four people were less likely to engage in waste management practices compared to households with fewer than four people. In contrast, Osbjer et al., (2015) associated waste management practices with a higher number of people in households, which could be due to the need to handle waste generated by larger populations within the household. For sustainable HSW management, local policies should no longer be limited to waste collection and transportation to landfills. It is essential to focus on understanding, instilling, and involving the population in source waste sorting and collection.

5. Conclusions

Improving household waste sorting practices in Annaba, El Bouni, and Chétaibi requires a comprehensive, multi-dimensional approach. Local authorities must prioritise initiatives such as large-scale composting, improving accessibility to selective collection points and promoting community involvement in sustainable waste management. Integrating these efforts with the principles of the circular economy, supported by public-private partnerships and the development of innovative infrastructure, can significantly improve the efficiency of waste management systems. In addition, strict regulations, such as a ban on single-use plastics and targeted education campaigns, will play a key role in the adoption of environmentally friendly behaviour. Together, these measures can turn waste management into a cornerstone of environmental protection and improved living conditions for local people. Municipalities must take specific measures to improve waste management. This includes adopting community and local approaches, such as setting up waste management cooperatives and building modern treatment facilities. Finally, education and awareness-raising play a key role, with programmes aimed at schools and communities to encourage waste sorting and reduction at source.

Acknowledgments

Authors are grateful to the technical services of the public industrial and commercial establishment of Annaba proper and the staff of the Environmental Department of the Wilaya of Annaba for their assistance. Gratitude is also given to Prof. Hamid Boudjelida for reading the manuscript.

References

Addo, H.O., Dun-Dery, E.J., Afoakwa, E, Elizabeth., A, Ellen, A., and Rebecca, M. (2017). Correlates of domestic waste management and related health outcomes in Sunyani, Ghana: a protocol towards enhancing policy. BMC Public Health; 17 (1): 615.

Adeoti, A., and Obidi, B. (2010) Poverty and preference for improved solid waste management attributes in delta-state, Nigeria, Journal of Rural Economics and Development. University of Ibadan, Nigeria. Vol. 19 n° 1, 15-33.

Asante, K.P., Kinney, P., Zandoh, C., Vliet, E.V., Nettey, E., Abokyi, L., Owusu-Agyei, S., and Jack, D. (2016). Childhood Respiratory Morbidity and Cooking Practices Among Households in a Predominantly Rural Area of Ghana. African Journal of Infectious Diseases (AJID); 10 (2): 102-110.

Bouadam, R., Zaidi, H., Soukehal, I., Makhloufi, S., and Badreddine, H. (2022). Composting as a sustainable alternative to eliminate household and similar Waste in developing countries. Humanities & Social Sciences Reviews; 10, N° 6: 01-14.

Campuzano, R., and Gonzalez-Martinez, S. (2016). Characteristics of the organic fraction of municipal solid waste and methane production: A review. Waste Management.; 54:3-12.

Cheniti, H., Serradj T., Brahamia, K. 2020. Generation and physical characterization of household waste in Annaba city. Environ. Eng. Manag. J. 19: 713-720.

Cronbach, L. J. 1951. Coefficient alpha and the internal structure of tests, Psychometrika .

Djebar, A.B., Dahel, A.T., Kebbab, R., Lebdjiri, K., Frehi, H., and Djebar, B. (2021). Gestion intégrée des déchets ménagers et assimilés dans 3 dairas côtières de la wilaya d'Annaba: Annaba, El Bouni et Chétaibi. 1st International seminar on pollution, health, environment and bio-monitoring. SIPSEB 21 December 27-28, Skikda - Algeria.

Dlamini, B.R., Isaac, R., and Ayodeji, P.I. (2017). Community Resident's Opinions and Perceptions on the Effectiveness of Waste Management and Recycling Potential in the Umkhanyakude and Zululand District Municipalities in the KwaZulu-Natal Province of South Africa Sustainability; 9, 1835.

Fadhullah, W., Imran, N.I.N., Syed Ismail, S.N., Jaafar, M.H., Abdullah, H. (2022). Household solid waste management practices and perceptions among residents in the East Coast of Malaysia.BMC Public Health; 22, 1.

Haniyeh, J., Neematollah, J., Gert, M., Satyanarayana, N., Michael, N. (2021). Adoption of sustainable solid waste management and treatment approaches: A case study of Iran. Waste Manag. Res; 39 (7): 975-984.

Kaoje, A., Sabir, A.A., Yusuf, S., Jimoh, A.O., and Raji, M.O. (2017). Residents' perception of solid waste disposal practices in Sokoto, Northwest Nigeria. African Journal of Environmental Science and Technology; 11. no. 2: 94-102.

Kaza, S., Yao, L.C., Bhada-Tata, P., VanWoerden, F. (2018). What a Waste 2.0: A Global Snapshot of Solid Waste Management to 2050. Urban Development, World Bank, Washington DC

Kebaili, F.K., Baziz-Berkani, A., Aouissi, H.A., Mihai, F.C., Houda, M., Ababsa M., Azab M., Petrisor, A.I., and Fürst, C. (2022). Characterization and Planning of Household Waste Management: A Case Study from the MENA Region. Sustainability; 14 (9), 5461.

Law 30-10 of 19 Joumada El Oula 1424 corresponding to July 19, 2003 (Household Waste Removal Tax) relating to the protection of the environment within the framework of sustainable development; reassessed in the Finance Law. (2022.)

National Waste Agency (2020). Rapport sur l'état des déchets en Algérie

Osbjer, K., Boqvist, S., Sokerya, S., Kannarath, C., San, S., and Davun, H. (2015). Household practices related to disease transmission between animals and humans in rural Cambodia. BMC Public Health; 15 (476): 1-10. 54: 3-12.

Parfitt, J., and Flowerdew, R. (1997). Methodological problems in the generation of household waste statistics: Ananalysis of the United Kingdom's National Household Waste Analysis Programme. Applied Geography; 17, Issue 3: 231-244

Rai, A., and Umashankar, S. (2021) Domestic Waste Disposal Practices and Perception towards Solid Waste Management in Selected Areas of Bangalore, India. International Journal of Environment and Climate Change DOI:10.9734/ijecc/2021/v11i930471

Rcmdr and FactoMineR from R software (4.1.2). R Core Team. (2020). A language and environment for statistical computing. R Foundation for Statistical Computing, Vienna, Austria.

Report on the Solid Waste Management in Algeria (2014). Deutsche Gesellschaftfür Internationale Zusammenarbeit (GIZ) GmbH, in cooperation with Agence Nationale de Gestion des Déchets (ANGed).

Sawaya, R., H. Kourani , J. Halwani, N. Nehme. (2023) Landfills in the Context of Municipal Solid Waste Management in Lebanon: A review focusing on Greater Beirut Area Jordan Journal of Earth and Environmental Sciences 14 (4): 241-253.

Ulloa-Murillo, L.M., Villegas, L. M., Rodríguez-Ortiz, A. R., Duque-Acevedo M., and Cortés-Garcí F.J. (2022) Management of the Organic Fraction of Municipal Solid Waste in the Context of a Sustainable and Circular Model: Analysis of Trends in Latin America and the Caribbean. International Journal of Environmental Research and Public Health. 19 (6041):2-25. DOI:10.3390/ijerph19106041

Vassanadumrongdee, S., and Kittipongvises, S. (2018). Factors influencing source separation intention and willingness to pay for improving waste management in Bangkok, Thailand. Sustainable Environment Research; 28: 90-99.

Waste Management Guide. (2002) Guide for public higher education or research establishments. www.sdfp.Lnet.fr

World Bank. (2022). Trends in Solid Waste Management. (n.d.). Retrieved March 20, 2022.

JJEES

JJEES (2025) 16 (2): 163-172
ISSN 1995-6681

Jordan Journal of Earth and Environmental Sciences

Geological Structures Assessment in Wadi Hagul, Northwestern Gulf of Suez, Egypt, Using Gravity and Magnetic Techniques

Mahmoud S. Etman[1, 2*], Abdel-Monem S. Mohamed[1], Salah Saleh[1], Sayed A. Mohamed[3] and Karrar O. Fergawy[2]

[1]National Research Institute of Astronomy and Geophysics, Helwan, Cairo, Egypt
[2]Department of Geology, Faculty of Science, Aswan University, Aswan, Egypt
[3]National Authorities for Remote Sensing and Space Science (NARSS), Cairo, Egypt

Received on November 2, 2024, Accepted on January 11, 2025

Abstract

Wadi Hagul, an overlooked geological site in the northwestern region of Egypt's Gulf of Suez, is undergoing investigation through gravity and aeromagnetic measurements to ascertain the subsurface structure and foundational strata. Aeromagnetic and gravity-based prospecting techniques yield useful information about the region. The total aeromagnetic intensity (TMI) was derived by reducing the aeromagnetic data to the north magnetic pole (RTP). Maps, depicting Bouguer variations, were generated from corrected gravity data. Filtering approaches identified local anomalies and assessed the depths of both deep and shallow locations using radially powered spectrum integration. The depths of anomalies varied from 1 km to 3 km for both magnetic and gravity data. Bouguer gravity and magnetic data produced two-dimensional (2D) models and depth maps of the basement surfaces, indicating depths ranging from 300 m to 10000 m. The data analysis disclosed structural tendencies in various orientations (NE-SW, E-W, and NW-SE). Ten two-dimensional models demonstrated a deepening of foundation rocks in the center and southwestern regions. Employing forward 2D modeling alongside a structural map derived from the tilt derivative filter and Euler deconvolution solution, we generated a preliminary basement terrain map indicating diverse depths and tectonic activity in the central and southern regions of Wadi Hagul. Crustal thickness increases in the central and southwestern areas while decreases in the northeastern and southeastern directions.

Keywords: *Wadi Hagul; 2D Modeling; Crustal Structure; Bouguer Anomaly; RTP; Data Processing.*

1. Introduction

The Wadi Hagul region includes the El Galala El Bahariya plateau and the mountains of Ataqa, Kaheilyia, Abou Treifiya, and Akheider. It is situated near the Cairo-Sokhna and Suez-Sokhna thoroughfares. The Gulf of Suez and the coastline area serve as habitats for wadis. Research suggests various migration phases from the Neogene to the late Miocene. The Red Sea formed as the Arabian Plate moved northward along the Gulf of Suez (Bosworth, 2015). Seismic activity has migrated to the Jubal Island area at the Gulf of Suez entrance, conforming to regional structural patterns (Roberts et al., 1988). The WNW to NW tectonic trend indicates active faulting, with earthquakes predominantly occurring on faults aligned WNW-ESE to NW-SE within extensional stress regimes (Abd El-Aal et al., 2019). Human activities can worsen soil compaction, leading to increased movement and tremors in areas that were previously less affected (Etman et al., 2024). Gravity and Magnetic (GM) techniques are utilized to ascertain structural patterns and evaluate crustal thickness, employing regional-residual isolation and Tilt Derivative (TDR) filters to delineate tectonic processes influencing the basement surface and sedimentary strata (Gaber et al., 2022). A crustal structure model was developed utilizing the forward modeling technique (GM-System) over ten profiles.

The depth of the basement was assessed utilizing 3D Euler deconvolution and 2D profiles. Aeromagnetic and Bouguer gravity data were analyzed to obtain insights into the structural characteristics and basement depths of the region for optimal planning. This work utilizes Bouguer gravity and reduction to North Magnetic Pole (RTP) aeromagnetic data to further our comprehension of Wadi Hagul's geodynamic evolution by delineating subsurface structures and basement relief in tectonically active regions. Figure 1 presents a location map of Wadi Hagul, including a geodetic network, fault lines, and seismic occurrences in the time period from 1950 to 2023.

2. Geologic Setting

The area encompasses a variety of rock types from the Jurassic to Quaternary eras, as shown by prior studies. The predominant rock units are strata from the Middle and Upper Eocene, Miocene, and Quaternary eras (Hassan, 2008). The Jurassic phase is characterized by multicoloured sandy rocks interspersed with layers of siltstone and clay. The Cretaceous series in the area has three distinct units:

* Corresponding author e-mail: mahmoud.etman@nriag.sci.eg

chalky limestone, Galala, and Malha. Eocene formations are prevalent in Gabal El-Galala El-Bahariya, Gabal Ataqa, Um Zeita-Kahallya, and Akheider-Rammlyia. The Eocene strata, mostly composed of carbonates interspersed with various quantities of clastic, constitute the stratigraphic series (Salem, 1988). Nonconformity distinguishes late Eocene layers from Oligocene and Miocene deposits. The Oligocene rocks are divided between lower variegated strata (sandstone and flint gravel) and top basalt layers of the Gabal El Ahmer formation, together with dolerite intrusions (Salem, 1988), (El-Enain et al., 1995). The Miocene sequence forms the Sadat, Hommath, and Hagul Fformations. In the Upper Miocene, the Hagul formation, mostly consisting of carbonate and sandstone, was formed (Abdallah, 1993), (O'Connor et al., 1990).

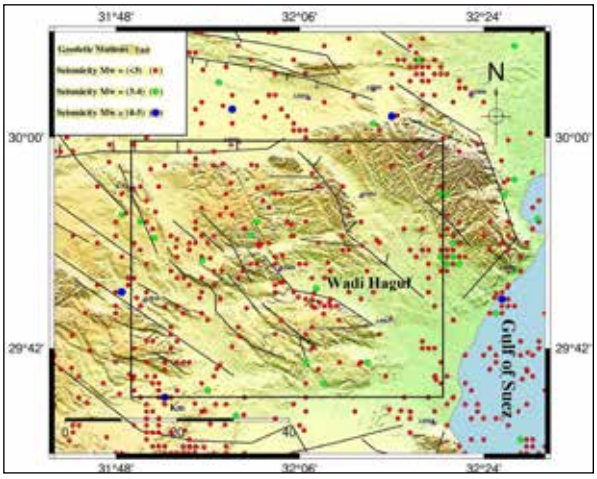

Figure 1. Location map showing Wadi Hagul, the geodetic network, and seismic events and highlighting fault lines in the investigated region.

The Upper Miocene strata consist of 45-meter-thick argillaceous and calcareous sandstone, situated above these layers. The base of the water well has a thin stratum of limestone, sandstone, and clay, indicative of the Middle Miocene epoch. The region's intricate structural configuration is shaped by the Syrian Arc System and the Gulf of Suez Rift, leading to faulting, bending, and anomalies. Four tectonic episodes have been recognized as responsible for structural deformations: The Upper Oligocene, Upper Miocene, Lower Miocene, and After-Miocene epochs. The Pliocene sediments consist of gravels formed from a combination of flint and limestone, usually embedded in a sandy matrix. The Quaternary sediments, about 4 meters in thickness, consist of wadi deposits, sand, and gravel. The subsurface stratigraphy of the study area was established using data from boreholes conducted by Egypt's Geological Survey in 1999. The topographical and structural characteristics of the Hagul were mostly influenced by the first two occurrences, resulting in more deformation compared to subsequent events by) Abd Allah et al., 1965). Recent and paleo-earthquakes have created geological deformation patterns in the Wadi Hagul region and its vicinity, retaining sedimentary strata. The examination of several data types indicates that the Hagul fault zone mostly governs the average depth of earthquakes in Wadi Hagul, ranging from 1 to 35 kilometres into the Earth's upper crust. The study region and its vicinity include a moderate topography characterized by many hills and small mountains. The elevation progressively ascends westward, merging with the Eocene limestone plateau in the central region of the northern Eastern Desert by) Abd Allah et al., 1965). The area between Gebel Ataqa and the Northern Galala Plateau links the Cairo-Suez region to the Gulf of Suez. Various fault types impact the Eocene and Miocene strata. NNW-SSE faults are often identified as gravity faults, distinguished by intermediate throw length ratios, significant throws, and shallow dip angles. The faults impacting the Eocene limestone plateau delineate prominent wadis, including Wadi Hagul and Wadi Hommath. East-West faults are characterized by moderate lengths, significant throws, intermediate throw-to-length ratios, and steep dip angles. They originated in the late Eocene and continued into the Oligocene (Salem, 1988). Faults classified as WNW-ESE exhibit moderate displacements, minimal throw length ratios, and steep dip angles. They are mostly located around Gebel El-Galala El-Bahariya and Gebel Ataqa, inside the low hilly landscape. Tectonic joints in this region are oriented northeast-southwest, north-south, and northwest. The region has seen considerable faulting, some folding, and non-depositional conformities. Previous studies by (Abdallah, 1993), (Safei El-Din, 1988).)Youssef et al., 2003) have examined the geological formations of the Wadi Hagul area. Figure 2 illustrates the composite stratigraphic column for the investigated region and its adjacent areas.

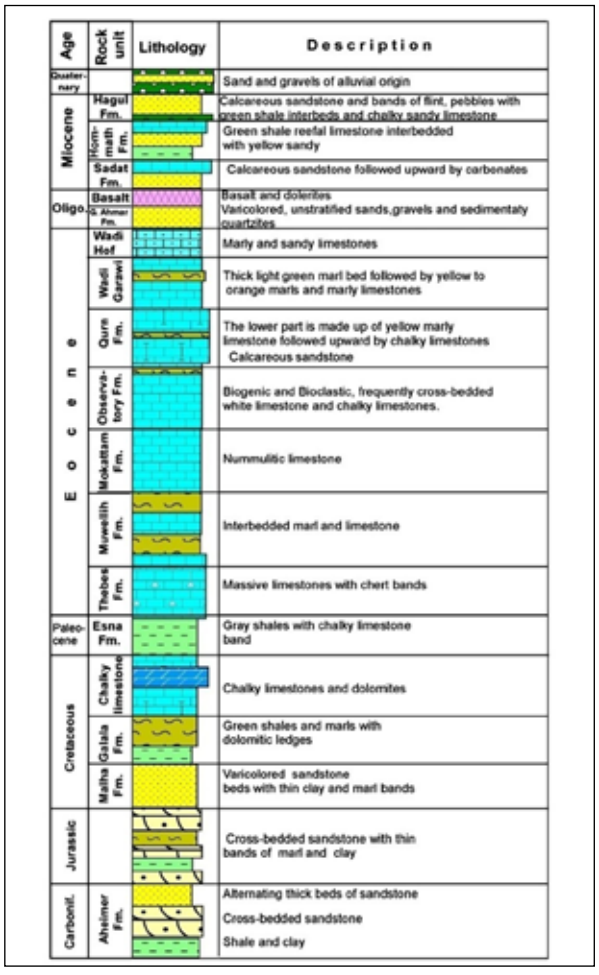

Figure 2. A modified and synthesized stratigraphic column of the study area (Araffa et al., 2017).

3. Material and Methods

The total field intensity (TF) magnetic and Bouguer gravity datasets are important research datasets. The magnetic method is recognized as one of the most often used geophysical methods for exploring the Earth's interior. It aids in the examination of many exploration obstacles, including horizontal geomagnetic oscillations from the Earth's crust to the uppermost of the globe. This technique employs differences in subsurface attraction to detect changes in the Earth's magnetic field (Hinze et al., 2013). In highly conductive materials, the dissipation of eddy currents (secondary magnetic fields) occurs at a much slower rate compared to low-conductivity materials (Al-Amoush et al., 2017).

The aeromagnetic data for the area was obtained from a total intensity magnetic map (TIM) digitized at a resolution of 1:50,000. In 1983, the Egyptian Geological Survey and Mining Authority (EGSMA) commissioned the West Geophysical Service of America's Aero Service Branch for an investigation. The flight lines were positioned 120 meters above the Earth's surface, with a separation of 1.5 km in the NE-SW (45°/225°) direction and 5 km in the NW-SE (135°/315°) orientation. The magnetic field strength in the area was recorded at 41,742 nano Tesla (nT), with an average inclination and declination angles of 39.5 N and 2.0 E, respectively (A. service, 1984).

Two drilled wells were used to verify the precision of the modeled profiles. Figure 3 illustrates the Total Magnetic Intensity (TMI) map of the study area. Subsequently, to account for the effects of oblique magnetization, the TMI data were reduced to the pole (RTP) with the methodology outlined in (Baranov et al., 1964). The power spectrum curve of the RTP magnetic data was examined to detect localized and enduring magnetic anomalies. The energy spectrum graph exhibited two linear segments corresponding to shallower and deeper magnetic fields (Dosoky et al., 2023). There are established processing steps for interpreting magnetic data (Sundararajan et al., 2022). Edge detection methods (EDT) were used in a qualitative analysis of the data to identify patterns and correlations. Multiple EDTs, such as tilt derivative (TDR), Euler deconvolution (ED), and vertical derivative (VDR), were used in the analysis. Prior studies have similarly used EDT to delineate fundamental structural characteristics (Oguama et al., 2021), (Basantaray et al., 2022). The quantitative analysis included magnetic depth estimate techniques including Power Spectrum Analysis (Spector et al., 1970). Euler Deconvolution (ED) by (Thompson et al., 1982), (Reid et al., 1990) and 2D Magnetic Modeling (Talwani et al., 1964).

The RTP aeromagnetic and gravity measurements underwent comprehensive processing and enhancement using the Oasis Montaj software version 7.0. Gravity prospecting was conducted in the area due to its cost-effectiveness and non-invasive nature. This method is passive and does not require external energy input to collect data (Numan et al., 2019). The gravity method is used to detect fluctuations in the Bouguer field caused by subsurface density changes. This approach is essential for geological study, including mapping near-surface voids, evaluating metallic ore deposits, defining salt formations, and monitoring variations in volcanic fluid and gas compositions. It is used in regional Earth characterization to ascertain crustal structures, pinpoint prospective places for resource exploration, and formulate investigative models (Hinze et al., 2013). In 1984, the General Petroleum Company created a Bouguer anomaly map at a scale of 1:200,000, with a contour interval of 1 mGal, an observation spacing of 1000 m, and a line spacing of 5000 m (EGPC, 1984).

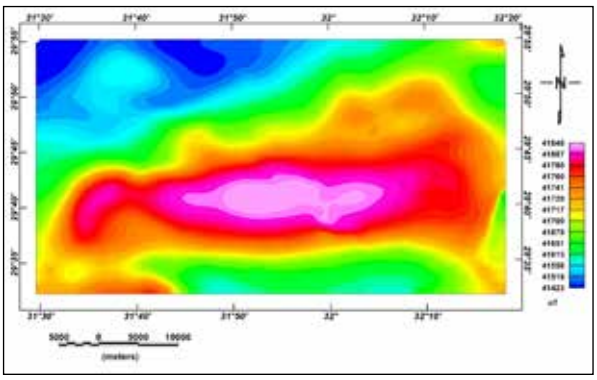

Figure 3. The total magnetic intensity (TMI) of the investigated region.

The standard values of 2670 kg/m^3 and 0.3086 mGal/m were used to implement the Bouguer and Free-Air corrections, correspondingly. Gravity measurements are affected by elevation, density, and crustal composition. Regional Bouguer anomalies provide insights into isostatic equilibrium patterns and mass boundary fluctuations throughout the crust and upper mantle (Tealeb et al., 1986). Recent studies demonstrate a significant link among Bouguer anomalies, surface topography, and crustal thickness (Woollard, 1959), (Pick et al., 1973) and (Riad et al., 1985). Nevertheless, it is crucial to acknowledge that gravity measurements alone cannot conclusively ascertain the density distribution in the planet's deepest regions (Tealeb et al., 1986). The Gravity and Magnetic (GM) dataset underwent regional-residual separation analysis to distinguish anomalies caused by shallow geological factors from those arising at greater altitudes (Gaber et al., 2020). In this process, the identified field is subtracted from the regional field to get the local anomaly. Residual variations, stemming from shallow origins, have steep gradients and elevated frequencies, whereas regional anomalies are often extensive and smooth, indicative of their connection to deeper and bigger formations (Bassett et al., 2015). Residual anomalies have significance in geophysical exploration. The remaining components are isolated using various procedures, and a reliable method to ascertain the depths of different Gravity and Magnetic (GM) prospects characterized by varying densities or magnetic susceptibilities is via the analysis of the radial energy spectrum of (GM) data. Depth estimate findings are essential for measuring sediment thickness in sedimentary basins. The structural index (SI) of (0.5) for magnetic data and (1) for gravity data is used in the Euler method for identifying gravity and magnetic anomalies. Faults or contacts at different depths within the research region are delineated by Euler deconvolution. The

suitable SI value is contingent upon the source geometry, with values of two for spheres, one for horizontal cylinders, zero for faults, and negative one for contacts.

A structural index of zero or one is advised for identifying gravitational anomalies. Optimal results are achieved for SI = 0.5 and 1. Trends in structural elements are shown in rose diagrams derived from the gravity map, together with the Convolution of Euler using structural values of 1 (Araffa et al., 2018). Subsurface characteristics, including fault positions, depths, geological affiliations, lineaments, dykes, and sills, are ascertained by the 3D Euler approach. To do this, data on the causal components is necessary, measured by the structural index (SI). The SI numbers denote the degree of field displacements contingent upon the configuration of the source (Salem et al., 2008), (Eweis et al., 2022).

4. Results and Discussions

The overall magnetic intensity (Figure 3) and the accompanying RTP (Figure 4) exhibit a northward displacement in anomalies, which correlates with the magnetic inclination of the study area. There is an increase in the number of variants, a decrease in their aerial coverage, and an increase in their vertical relief. The RTP aeromagnetic anomaly shown in Figure 4 reveals a maximum reading of about 41850 nT in the north and a minimum decrease of around 41400 nT in the south (it is 41401 in the Fig. 4). The RTP map exhibits only positive anomalies characterized by diverse dimensions, forms, basins, lineation, and modest gradient extensions. The anomalies often manifest in the northeast, east-northeast, southeast, and northwest directions. The largest amplitude of 41,850 nT is seen in the northern region, whilst the lowest amplitude of 41,400 nT, directed ENE, is recorded in the southern area. The map illustrates significant magnetic anomalies in the northeastern, northwestern, and eastern areas. The highest magnetic measurements fluctuate between 41,850 and 41,710 nT. A contrasted low magnetic anomaly is detected in the southern regions, with values ranging from 41401 to 41559 nT.

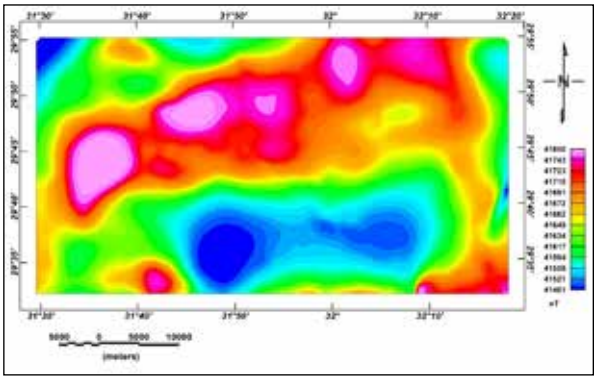

Figure 4. Reduction to Magnetic Pole (RTP) aeromagnetic map.

In the study region, the Bouguer anomalies (Figure 5) display four major anomalies. The western, northern, and southwest anomalies trend northwest with negative gravity values (-48 mGal), while the eastern anomaly trends northeast and the western anomaly with negative gravity values reaching -9 mGal. With amplitudes ranging from -48 to -9 mGal and a trend from west-northwest to east-northeast, four low anomalies basins or down-faulted blocks are indicated on the map. The significant negative anomaly in the eastern region, with an amplitude of -9 mGal, is associated with a high density.

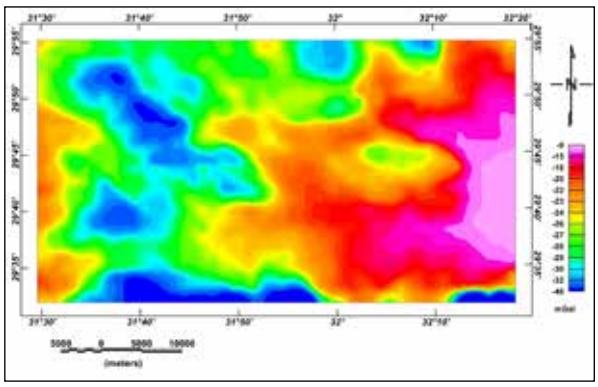

Figure 5. A Bouguer gravitational map of the investigation region.

Figure 6a illustrates the regional gravitational mapping, featuring a cut-off wave number of 0.023 Rad/m and four distinct Bouguer anomalies that range from -37 to -12 mGal. The low-pass magnetic and Bouguer maps presented in Figures 6a and 6b illustrate deep magnetic sources, indicating both positive and negative anomalies within the study area. Figure 6b presents a regional magnetic anomaly map that indicates the presence of buried correlated resources, characterized by magnetic intensity levels between 41,450 and 41,783 nT. In the illustrated region, low magnetic anomalies are predominantly found in the southern areas, while high magnetic RTP anomalies are concentrated in the northeastern and western sections. The subject exhibits an additional east-west trend in its central and southern regions, while most regional irregularities are oriented in the northeast-southwest and northwest-southeast directions, consistent with the Gulf of Suez pattern. A comparison of the regional map in Figure 6b with the RTP map in Figure 4 reveals notable similarities across most regions, including central, northeast, and certain areas in the west, indicating the regional origin of RTP anomalies in specific locations.

After the removal of regional effects, the high-pass gravity and magnetic (GM) maps presented in Figures 7a and 7b reveal irregularities that suggest the presence of multiple causal GM entities at shallower depths. The high-pass Bouguer anomaly map reveals elongated anomalies with amplitudes ranging from -11 to 8 mGal in the ENE, WNW, and E-W orientations. Figure 7b illustrates a residual aeromagnetic anomaly pattern characterized by high frequencies, small wavelengths, and minimal magnetic variations, which delineate near-surface structures in the study area. Upon removal of the regional magnetic field, the local RTP map reveals dispersed low and high-frequency anomalies with amplitudes ranging from -117 to 110 nT., indicating significant northwest, north-south, east-west, and northeast trends. The Fast Fourier Transform (FFT) distinguishes between regional (low-frequency) and local (high-frequency) elements. The power spectrum is depicted in Figure 8, with gravity in Figure 8a and aeromagnetic analysis in Figure 8b. The analysis of the radially summed energy spectrum reveals a low wave number slope (green line), indicating deep sources, while high wavenumbers

(blue line) imply shallow contributions. Long-wavelength aberrations from deep sources are represented on regional maps, with depths of 3000 m in the Bouguer measurements and the RTP dataset. Small wavelength anomalies from shallow sources are seen in the residual maps, suggesting depths of 1000 m in the Bouguer data and the aeromagnetic measurements.

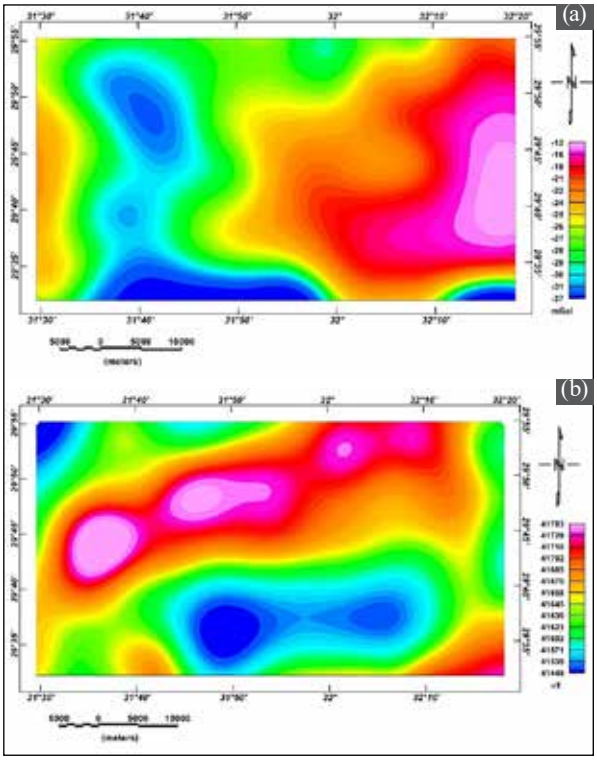

Figure 6. Low-pass filters for regional analysis on both a) the Bouguer and b) RTP anomaly maps, with a 0.023 cycles/km cut-off wave number.

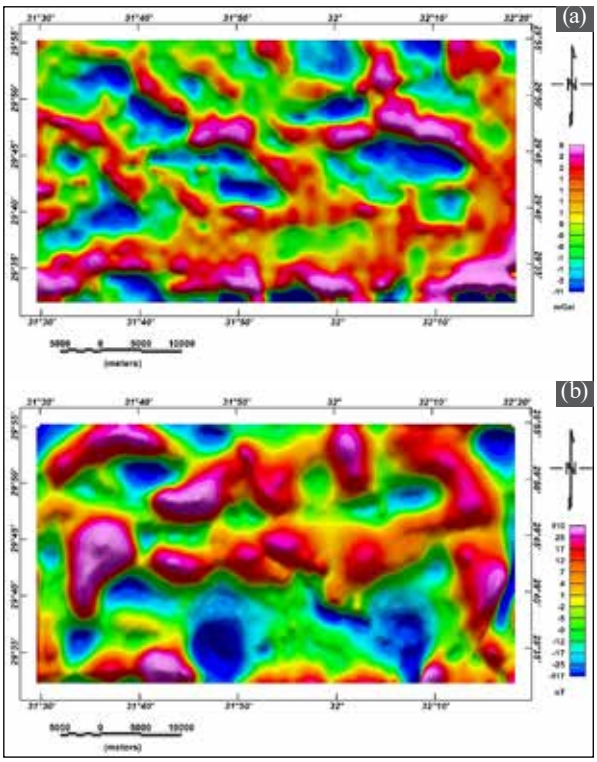

Figure 7. High-pass residual filters are applied to both a) the Bouguer and b) RTP anomaly maps, with a 0.023 cycles/km cut-off wave number.

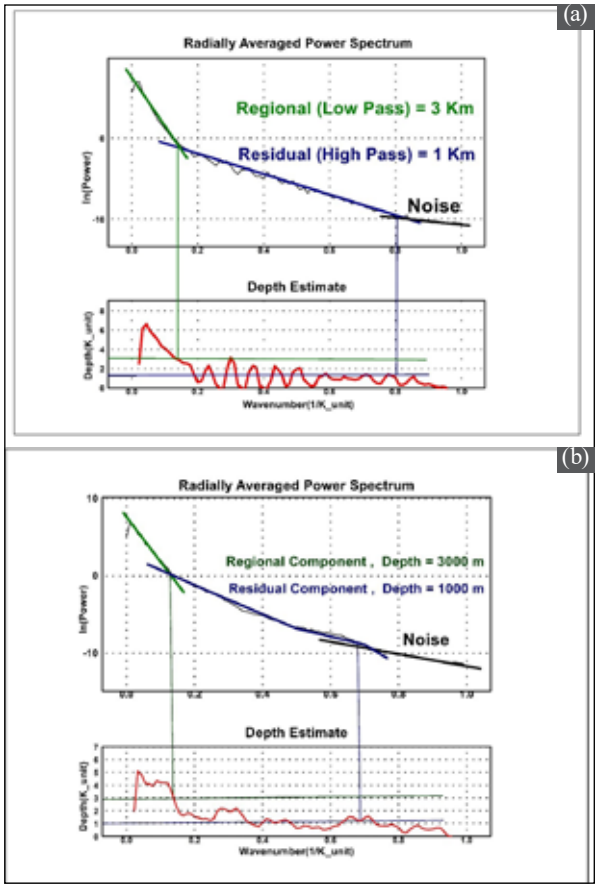

Figure 8. Two types of data are analysed using radial power spectrum evaluation and depth estimation: a) Reduced-to-pole (RTP) aeromagnetic data and b) Bouguer gravity measurements.

By considering the lateral slope, the Tilt Derivative (TDR) approach corrects the vertical variation in prospective measurements (Miller et al., 1994). The TDR gravity map (Fig. 9a) highlights uplifted and down-faulted block boundaries. The TDR magnetic map (Fig. 9b) shows distinct boundaries with varied dimensions, shapes, and orientations of magnetic sources, which differ from the gravity map. The depths of the magnetic boundaries appear shallower than those of the gravity boundaries. TDR amplitudes are positive above the point of origin, null at its border, and negative outside the body's limits. The amplitudes vary from $-\pi/2$ to $+\pi/2$. The path along which the contour measurements collapse indicates the downthrown opposite faults. This method was used to identify the fault elements, as shown in Figure 9.

In Figure 10, a rose diagram illustrates trend orientations derived from the tilt derivative (TDR) in aeromagnetic data (RTP). The linear anomalies or faults in the Rose diagram display NW-SE in major trend and E-W, N-S, NE-SW in minor trends. In the reduced-to-pole aeromagnetic analysis, the limits of the likely basin-like structure in the south and the possibly raised basement block in the north are defined by the zero-point outlines of the tilt derivative (TDR). Many regular faults, which run along the edges of the basement and the sedimentary nature basin, influence and contribute to the formation of these geologic features. The 3D Euler approach on aeromagnetic fields was utilized to identify the lineaments and faults in the focal region, and Bouguer analysis was used to establish their positions and depths.

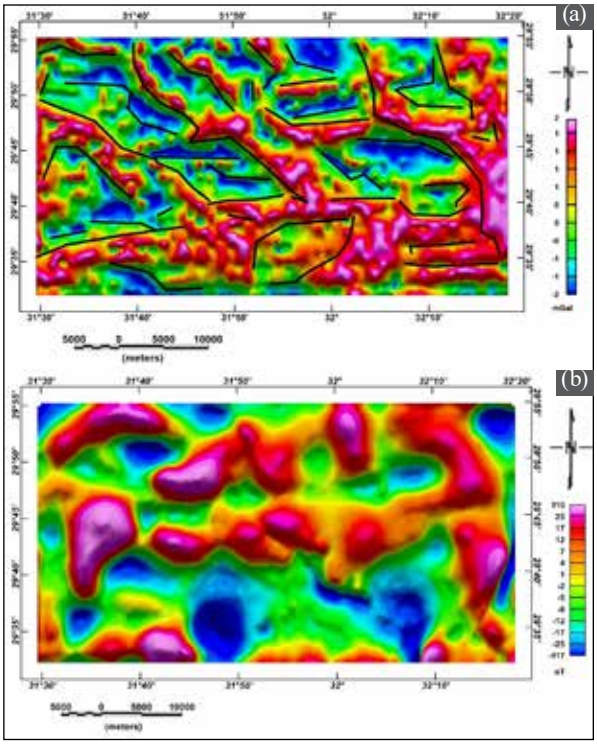

Figure 9. a) Gravity anomalies in the TDR map, b) Unusual magnetic fields in the TDR.

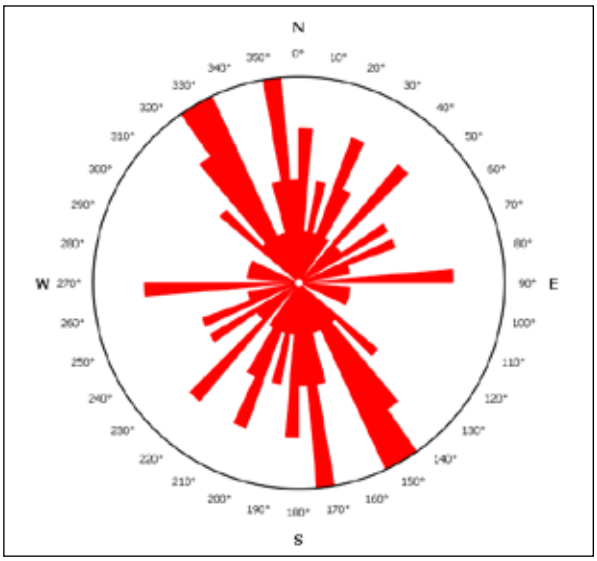

Figure 10. The trends in the Rose chart is extracted from the Tilt Derivative (TDR) aeromagnetic data (RTP).

Figure 11 shows the findings for the analysis of the region's Bouguer observations using the Euler methods. With the Bouguer map, lineaments, geological contacts, dykes, faults, and sills could all be precisely located (Figure 11) with SI = 1. According to the results of Bouguer data, the depth ranges from less than 500 meters and reaches a maximum of 3500. Trends in the east-west, east-northeast, and west-northwest directions are shown by the negative anomalies, while linear anomalies or faults show an east-west and NW-SE in major trends and E-W, NE-SW, N-S and WNW in minor trends as depicted in Figure 10 and 12. The Rose diagram (Figure 12) displays the principal orientation structure's NW-SE orientation and NE-SW, NW-SE in minor trends.

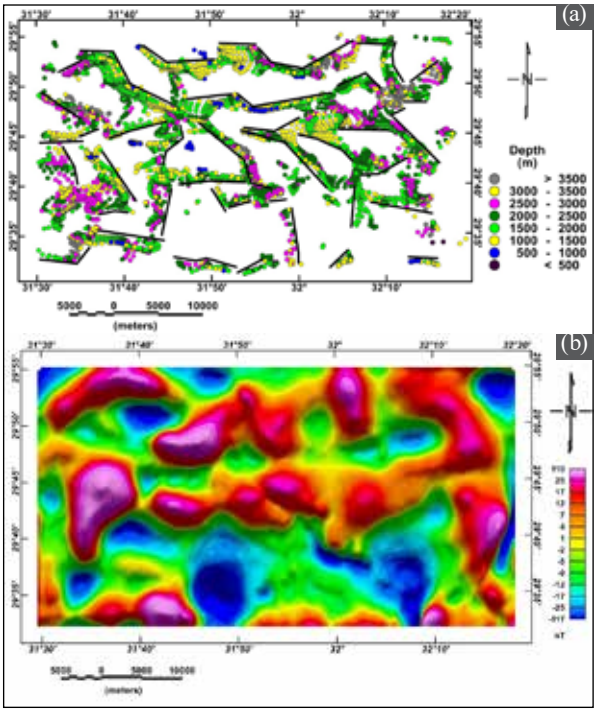

Figure 11. The Euler Deconvolution solutions map for SI (1) superimposed on the Bouguer anomalies pattern defines the position and depth of the faults.

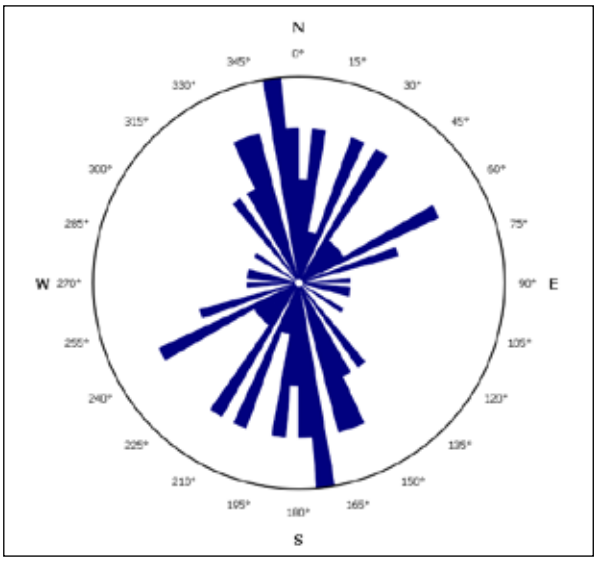

Figure 12. The trend of the patterns is extracted from the Euler Bouguer map is represented as a Rose diagram.

Profiles P1 through P10 are distributed across all regions (Figure 13). Figure 13 illustrates two wells that intersect the basement surface. Ten gravity and magnetic models were developed along profiles P1 to P10 utilizing the GM-SYS tool in Geosoft Oasis Montaj to analyze the composition and structures of the basement. Two layers of sedimentary material were produced, exhibiting densities of 2.67 g/cc and 2.2 g/cc, and the magnetic field equals zero magnetic susceptibility in this layer. The magnetic susceptibility of basement rocks was measured at 0.00776 (Figure 14). Acidic rocks exhibit low magnetic susceptibilities, suggesting the existence of regional granitic basement layers, whereas basaltic rocks are linked to higher susceptibilities (Telford et al., 1990). The profiles depicted on gravity and RTP aeromagnetic charts cross regions exhibiting varying GM

signatures and are oriented from south to north and westward, utilizing two reference wells (Figure 14). The modeling process entailed modifying depths, shapes, dimensions, and density contrasts to attain a close correspondence between observed and calculated gravity data. Two-dimensional models were created utilizing the Geosoft mapping system.

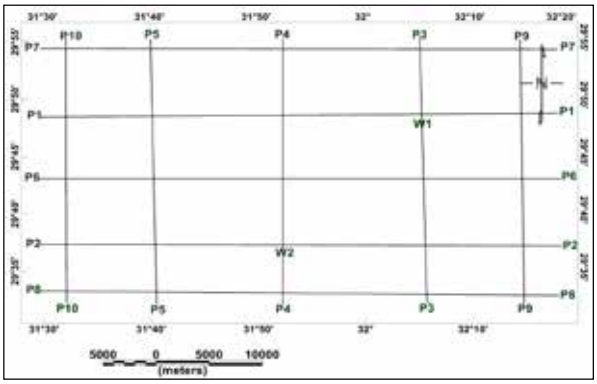

Figure 13. The base map displays the positions of the selected profiles for two-dimensional (2D) modelling of RTP and Bouguer gravity, along with the locations of the two well points.

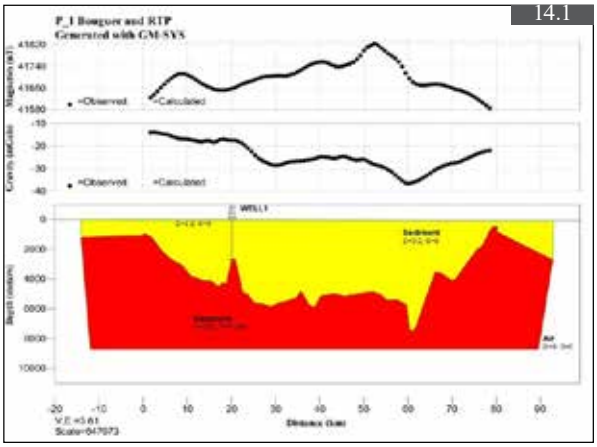

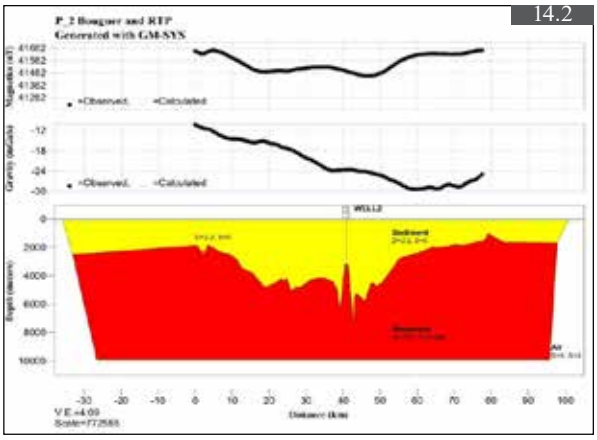

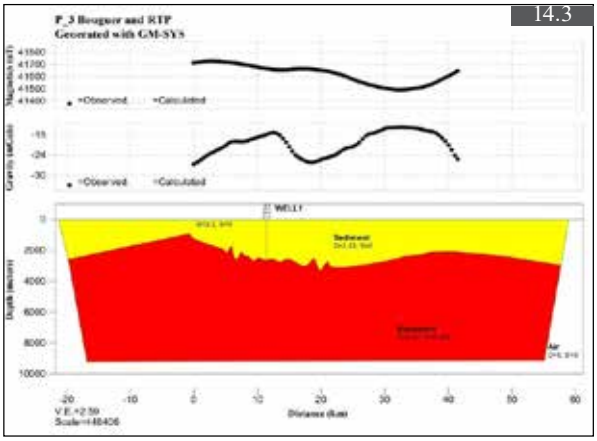

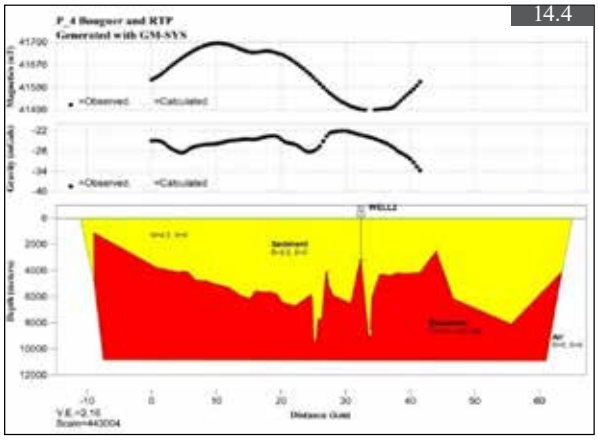

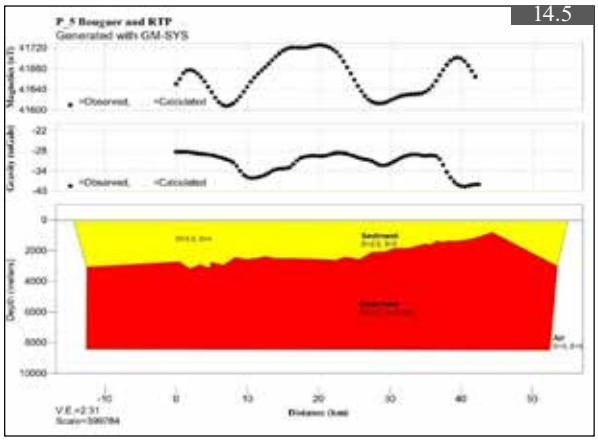

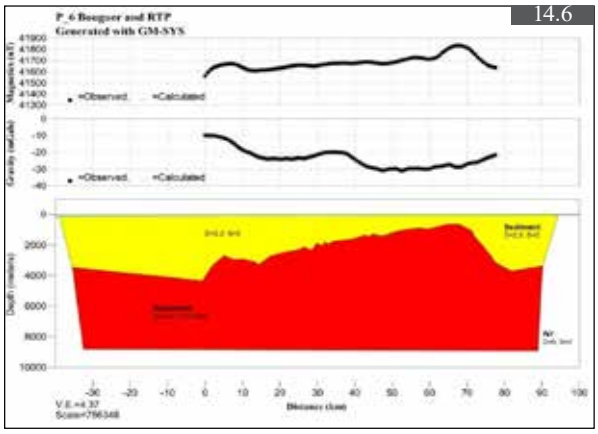

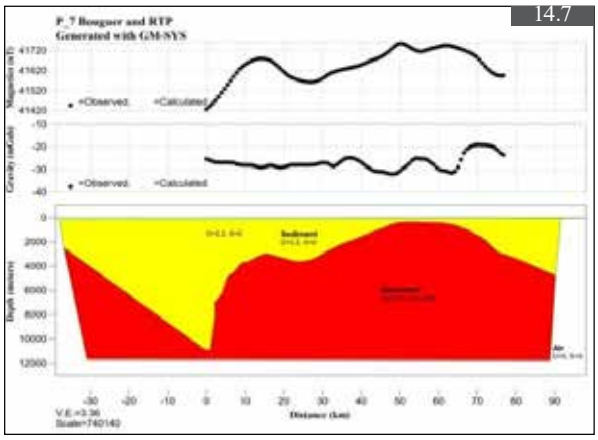

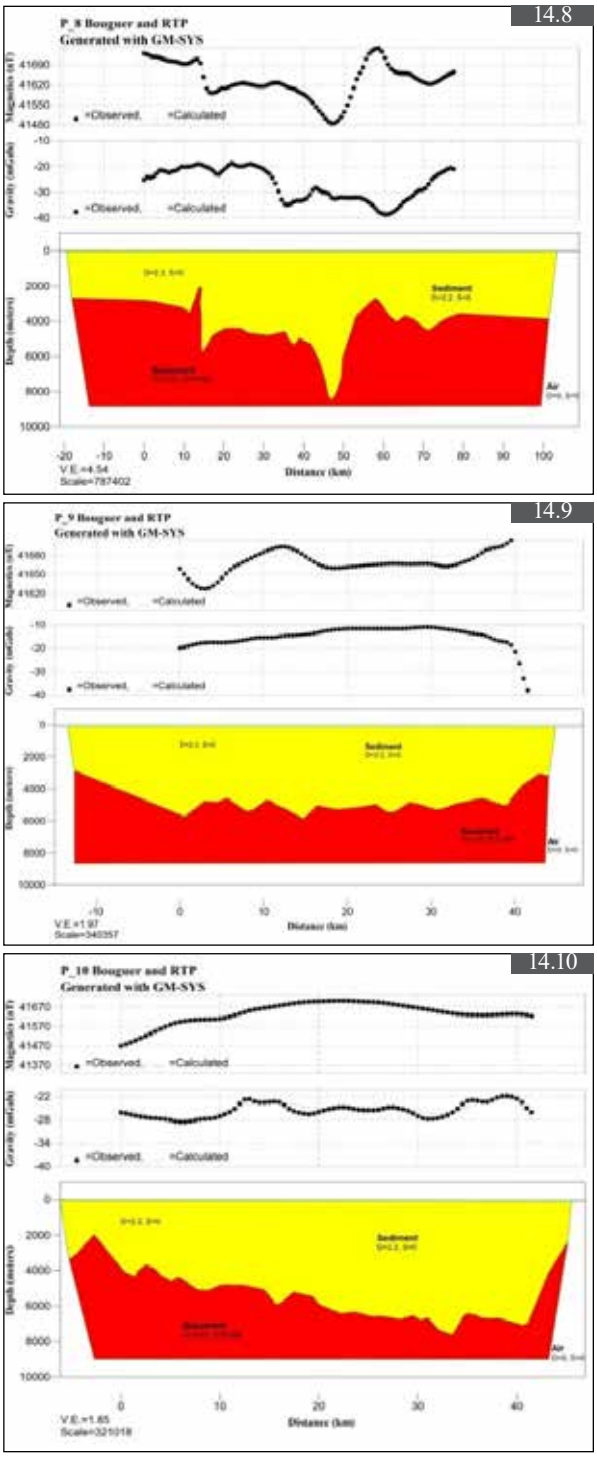

Figure 14. 2D gravity and magnetic model of profiles (P1:P10) of Wadi Hagul Area using reference depth's point.

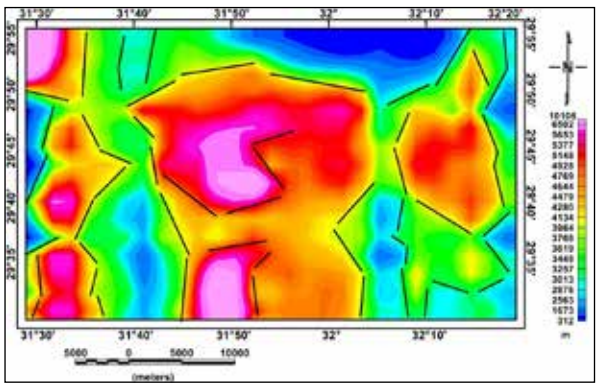

Figure 15. Relief map of the basement with lineaments in the study area.

The profiles indicated the existence of basement rock south of Wadi Hagul, with sedimentary thickness increasing in a northerly direction. The profiles were adjusted to reconcile observed and calculated data, with fitting errors between 0.1 and 3 percent. The densities of various rocks were assessed using magnetic and Bouguer measurements. The sedimentary cover and basement rocks were found to have average densities of 2.2 and 2.67 g/cm2, respectively, as determined through comparisons with prior research. Sequential modeling of the original magnetic and Bouguer data (Figure 14) produced more constrained interpretation results compared to independent modeling of each dataset. The forward modeling parameters and the resulting anomalies were established (Bhattacharyya et al., 1965).

The anomaly observed analyzing along these profiles indicates a gravity field ranging from -9 to -48 mGal, characterized solely by negative anomalies. The magnetic field displays a central positive anomaly with a magnitude of 41,850 nT, corresponding to the peak depth of the well. A northward shift in the magnetic field is generally observed. Two wells constrain the basement depths and sedimentary thickness along these profiles (Figure 14). The modeled section indicates a sedimentary cover depth between 300 and 1000 meters. The modeled sections reached a depth of 10 km, spanning an approximate distance of 90 km, corresponding to the basement layer depth.

Geophysical methods are progressively employed in research concerning crustal, shallow, and deep structures, in addition to archeology, mineralization, geothermal, and hydrogeological investigations such as previous studies of the following., (Sehsah et al., 2022), (Pham et al., 2021), (Saada et al., 2021) and (Saada, 2020). Depth variations on the basement surface map are shown using well data and information from 10 two-dimensional Bouguer and RTP magnetic profiles. The basement surface maps were derived from 10 Bouguer and aeromagnetic RTP profiles (P1 to P10), with their positions shown in Figure 14. The basement relief map (Figure 15) indicates a depth of 300 m, with shallower areas located in the southeastern, southwestern, and northeastern regions, and the shallowest depths identified in the extreme north and southeast. Deeper basement strata, about 10000 m under sea level, are located in the northwestern, south, eastern and central regions of the study area. The bottom layers in the center and northwest regions of the study area are noted to be thicker. The geophysical observations compiled here may also aid in the comprehension of comparable systems in different areas (El-Kelani, 2020). The magnetic anomalies (41,400 to 41,850 nT) identified in this study are similar to those reported in the Gulf of Aqaba by (Gaber et al., 2022) (41,200 to 41,900 nT). These anomalies are believed to be caused by variations in basement rock composition and depth. Both studies highlight the impact of regional tectonic activities on the distribution of magnetic anomalies. The NW-SE and NE-SW structural trends observed in this study align with orientations described by (Gaber et al., 2022), underscoring the influence of tectonic fault systems on subsurface features.

The magnetic and gravity anomalies in this study align with the findings of (Saada et al., 2021), displaying

comparable values in sedimentary basins characterized by NW-SE and NE-SW structural trends. The residual high-pass Bouguer and magnetic maps also mirror the patterns observed by (Saada et al., 2021), suggesting shallow sources and faulted blocks influenced by regional tectonic regimes. The Bouguer anomalies (-48 to -9 mGal) identified in this study are consistent with the results reported by (Gaber et al., 2020) in tectonically active areas characterized by thick sedimentary layers and faulted basement structures. The variations in basement depth (ranging from 300 to 10000 meters) are similar to those observed by (Gaber et al., 2020), indicating the influence of extensional tectonics and sedimentary processes.

5. Conclusions

Based on the Bouguer gravity and the RTP aeromagnetic data, considering the outcomes of the 2D for both aeromagnetic and Bouguer models, the following conclusions can be inferred:

- The basement section of the investigation area exhibits non-linearity, with depth variations from 250 to 9600 m, increasing towards the central and north-western regions.
- The structural elements in the region exhibit orientations in multiple directions, including NNW–SSE, E–W, and NE-SW. A significant fault has been identified in the south-eastern part of this region.
- The region exhibits a typical continental crustal structure, characterized by a decrease in crustal depth toward the northeast and southeast. Moving Northward increases density for both the crust and the upper sedimentary section.
- The tectonic analysis indicates significant uplift in the north-western and central regions of the study area, as illustrated by the basement relief depiction.
- Crustal thickness decreases in the SE and NE regions of Hagul, while it increases towards the central area.
- This study identifies structural components and depths within layers through the application of 2D forward modeling, Euler deconvolution, and filtering techniques. A 3D model of gravity and magnetic data is necessary.

Acknowledgment

Mahmoud S. Etman designed the study, gathered and evaluated the results, and authored the report. Abdel-Monem S. Mohamed participated in data gathering, manuscript preparation, and material creation. Sayed A. Mohamed contributed to data processing activities. Karrar O. Fergawy and Salah Saleh participated in data assessment and the formulation of findings. All contributors have reviewed and approved the last version of the paper.

Author Contributions

The authors wish to express their sincere appreciation to the Geodynamic Department, the NRIAG staff, and the NARSS team for their invaluable assistance in data collection.

Conflicts of Interest

The authors declare no conflict of interest.

Funding

The authors received no financial support for the research, authorship, and/or publication of this article.

References

Abdallah, M. (1993). Structural geology of the area between El Galala El-Bahariya and Gabal Okheider, Egypt (Doctoral dissertation, Ph. D. Thesis, Ain Shams University, Cairo).

Abd El-Aal, A. E. A. K., Hagag, W., Sakr, K., Saleh, M., Abd El-Aal, A. E. A. K., Hagag, W., ... & Saleh, M. (2019). Seismicity, seismotectonic and neotectonics in Egypt. In The Geology of Egypt. Cham: Springer International Publishing. (pp. 375-413).

Al-Amoush, H., Al-Shabeeb, A. R., Al-Adamat, R., Al-Fugara, A. k., Al Ayyash, S., Shdeifat, A., & Rajab, J. (2017). The Use of GIS Techniques and Geophysical Investigation for Flood Management at Wadi Al-Mafraq Catchment Area. Jordan Journal of Earth and Environmental Sciences, 8(2), 97-103.

Araffa, S. A. S., Mohamed, A. M., & Santos, F. M. (2017). Geophysical investigation in the Northwestern part of the Gulf of Suez, Egypt. Egyptian journal of petroleum, 26(2), 457-475.

Araffa, S. A. S., El-bohoty, M., Abou Heleika, M., Mekkawi, M., Ismail, E., Khalil, A., & Abd EL-Razek, E. M. (2018). Implementation of magnetic and gravity methods to delineate the subsurface structural features of the basement complex in central Sinai area, Egypt. NRIAG Journal of Astronomy and Geophysics, 7(1), 162-174.

A. service. (1984). "Final report on airborne magnetic/radiation survey in Eastern Desert, Egypt. Work Completed for the Egyptian General Petroleum Corporation (EGPC)," vol. Six volumes, Aero Service, Houston, Texas, USA.

Baranov, V., & Naudy, H. (1964). Numerical calculation of the formula of reduction to the magnetic pole. Geophysics, 29(1), 67-79.

Basantaray, A. K., & Mandal, A. (2022). Interpretation of gravity–magnetic anomalies to delineate subsurface configuration beneath east geothermal province along the Mahanadi rift basin: a case study of non-volcanic hot springs. Geothermal Energy, 10(1), 6.

Bassett, D., & Watts, A. B. (2015). Gravity anomalies, crustal structure, and seismicity at subduction zones: 1. Seafloor roughness and subducting relief. Geochemistry, Geophysics, Geosystems, 16(5), 1508-1540.

Bhattacharyya, B. K. (1965). Two-dimensional harmonic analysis as a tool for magnetic interpretation. Geophysics, 30(5), 829-857.

Bosworth, W (2015). "Geological evolution of the Red Sea: historical background, review, and synthesis," The Red Sea: The formation, morphology, oceanography and environment of a young ocean basin, pp. 45-78.

Dosoky, W., Elkhateeb, S. O., & Aboalhassan, M. (2023). Basement configuration and structural mapping using aeromagnetic data analysis of El Galala El Qibliya plateau area, Northeastern Desert, Egypt. Modeling Earth Systems and Environment, 9(2), 2039-2051.

EGPC. (1984). "Bouguer gravity map of Egypt, Scale 1:500,000. Corporation Egyptian General Petroleum.,".

El-Enain, A., & FM, A. MM, & Ismail, AS (1995). Petrography, Geochemistry and Depositional History of the Eocene Rocks in the Area between Northern Galala and Gabal Ataqa, Western Gulf of Suez, Egypt. Annals of the Geological Survey of Egypt, 20, 551-576.

El-Kelani, R. (2020). A Review of Gravity and Magnetic Studies in the Jordan Dead Sea Transform Zone. Jordan Journal of Earth & Environmental Sciences, 11(1).

Etman, M. S., Mohamed, S. A., Saleh, S., Mohamed, A. M. S., & Fergawy, K. O. (2024). Analyzing recent deformation in Wadi Hagul, Eastern Desert, Egypt, via advanced remote sensing and geodetic data processing. Journal of Applied Geodesy.

Eweis, A. M., Toni, M., & Basheer, A. A. (2022). Depicting the main structural affected trends by operating aeromagnetic survey in the western part of Koraimat-Alzafarana road and surround area, Eastern Desert, Egypt. Modeling Earth Systems and Environment, 8(2), 2803-2816.

Gaber, G. M., Saleh, S., & Toni, M. (2022). Crustal thickness and structural pattern evaluation of Sinai Peninsula using three-dimensional density modeling with aeromagnetic and earthquake data. Acta Geophysica, 70(2), 639-657.

Gaber, G. M., Saleh, S., & Toni, M. (2020). CRUSTAL STRUCTURE OF THE SINAI PENINSULA, USING GRAVITY DATA.

Hassan, S. M. (2008). Studying geological structures of Ayn-Sokhna area, north Eastern Desert, Egypt, by optimum utilization of data fusion techniques of some satellite image. Faculty of science, Helwan University, 207.

Hinze, W. J., Von Frese, R. R., Von Frese, R., & Saad, A. H. (2013). Gravity and magnetic exploration: Principles, practices, and applications. Cambridge University Press.

Miller, H. G., & Singh, V. (1994). Potential field tilt—a new concept for location of potential field sources. Journal of applied Geophysics, 32(2-3), 213-217.

Numan, N., & Ghaeb, F. (2019). Geological and Hydrogeological Implications of Gravity Data in the Aqra Plain Iraqi Kurdistan Region. JJEES, 145.

Oguama, B. E., Okeke, F. N., & Obiora, D. N. (2021). Mapping of subsurface structural features in some parts of Anambra Basin, Nigeria, using aeromagnetic data. Modeling Earth Systems and Environment, 7, 1623-1637.

O'Connor, E. "R. Said (ed.) 1990. The Geology of Egypt. x+ 734 pp. Rotterdam, Brookfield: AA Balkema. Price£ 51.00 (hard covers). ISBN 90 6191 856 1." Geological Magazine 128.6 (1991): 676-677.

Pham, L. T., Oksum, E., Do, T. D., Nguyen, D. V., & Eldosouky, A. M. (2021). On the performance of phase-based filters for enhancing lateral boundaries of magnetic and gravity sources: a case study of the Seattle Uplift. Arabian Journal of Geosciences, 14, 1-11.

Pick, M., Picha, J., & Vyskocil, V. (1973). Theory of the earth's gravity field. Amsterdam; New York: Elsevier Scientific Pub. Co.

Reid, A. B., Allsop, J. M., Granser, H., Millett, A. T., & Somerton, I. W. (1990). Magnetic interpretation in three dimensions using Euler deconvolution. Geophysics, 55(1), 80-91.

Riad, S., & El Etr, H. A. (1985). Bouguer anomalies and lithosphere-crustal thickness in Uganda. Journal of geodynamics, 3(1-2), 169-186.

Roberts H. H and S. P. Murray. (1988). "Gulfs of the Northern Red Sea: Depositional settings of abrupt siliciclastic-carbonate transitions," in Developments in Sedimentology, vol. 42: Elsevier, pp. 99-142.

Saada, S. A. (2020). Delineating the subsurface geological features of the Southern Abu Gharadig Basin, North Western Desert, Egypt, based on gravity and magnetic data. Geologica Carpathica, 71(1).

Saada, S. A., Mickus, K., Eldosouky, A. M., & Ibrahim, A. (2021). Insights on the tectonic styles of the Red Sea rift using gravity and magnetic data. Marine and Petroleum Geology, 133, 105253.

Safei El-Din, A. (1988). Geological and hydrogeological studies on the area between Gabal Ataqa and Northern Galala, Egypt (Doctoral dissertation, Ph. D. Thesis, Fac. Sci., Zagazig Univ. 271p).

Salem, A., Williams, S., Fairhead, D., Smith, R., & Ravat, D. (2008). Interpretation of magnetic data using tilt-angle derivatives. Geophysics, 73(1), L1-L10.

Salem, A. S. (1988). Geological and Hydrogeological Studies on the Area between Gebel Ataqa and Northern Galala Plateau.

Sehsah, H., & Eldosouky, A. M. (2022). Neoproterozoic hybrid forearc–MOR ophiolite belts in the northern Arabian-Nubian Shield: no evidence for back-arc tectonic setting. International Geology Review, 64(2), 151-163.

Spector, A., & Grant, F. S. (1970). Statistical models for interpreting aeromagnetic data. Geophysics, 35(2), 293-302.

Sundararajan, N., Pracejus, B., Ebrahimi, A., Al Hosni, T., & Al Neseiri, J. (2022). Integrated Geophysical Study for Delineation of Structures Favorable to Uranium Mineralization in Al-Amerat, Sultanate of Oman. Jordan Journal of Earth and Environmental Sciences, 13(3), 215-222.

Talwani, M. (1964). Computation of magnetic anomalies caused by two dimensional structures of arbitary shape. Computers in the mineral industries, 1, 464-480.

Tealeb, A., & Riad, S. (1986). Regional gravity anomalies of western Saudi Arabia and their geological significance. Egyptian Geophysical Society, 5, 50-78.

Telford, W. M., Geldart, L. P., & Sheriff, R. E. (1990). Applied geophysics. Cambridge university press.

Thompson, D. T. (1982). EULDPH: A new technique for making computer-assisted depth estimates from magnetic data. Geophysics, 47(1), 31-37.

Woollard, G. P. (1959). Crustal structure from gravity and seismic measurements. Journal of Geophysical Research, 64(10), 1521-1544.

Youssef, M. I., & Abd-Allah, A. (2003). Structural geology of the southeastern segment of the Cairo-Suez district, Egypt.

JJEES

JJEES (2025) 16 (2): 173-185
ISSN 1995-6681

Jordan Journal of Earth and Environmental Sciences

Integrating Optical and SAR Sentinel Data for Improved Land Cover Mapping in Northeastern Region of Pakistan

Iftikhar Ahmad Khan[1] and Junaid Aziz Khan[2*]

[1] Forest Department, Muzaffarabad-AJK, Pakistan
[2] National University of Science & Technology (NUST)Islamabad, Pakistan

Received on January 19, 2023, Accepted on January 12, 2025

Abstract

Accurate Land Use Land Cover (LULC) mapping is important for the planning and management of natural and manmade resources. Though widely used remote sensing data has largely facilitated land cover mapping from global to local scale, generally used optical data has some inherent limitations which can be compensated to some extent through the use of synergistically combined optical and SAR data. Ever-evolving data fusion techniques have encouraged the combined use of SAR and optical data for LULC classification. In this study, three different classification scenarios were analyzed. In the first and second cases, Sentinel-1 (S1) and Sentinel-2 (S2) data alone were tested, then, as a third step, integrated Optical-SAR dataset (S1+S2) with varying combinations of S1 & S2 input variables was evaluated for LULC mapping. In the case of Sentinel-1 SAR data, our results produced an overall accuracy (OA), ranging from 44.6% -63.01% with Kappa Coefficient (KC) of 0.33-0.55 where SAR-based Grey Level Co-occurrence Matrix (GLCM) textures contributed significantly toward increasing classification accuracy. In the spectral domain, the accuracy range spanned from 86% (KC=0.83) to 89.59% (KC=0.87), whereas a combined dataset that included features from both SAR and Optical sides yielded the highest overall accuracy of 93.12% with KC= 0.91.

Keywords: *Sentinel-1, Sentinel-2, GLCM Textures, Data Fusion, Random Forest, Land Cover Mapping*

1. Introduction

The concepts of land use and land cover (LULC) have been elaborately explained in the literature. Water, soil, and vegetation that constitute the biophysical cover of Earth's surface are identified as land cover, whereas land cover is exploited by humans for the purpose of land use (Lambin et al., 2000). Land cover maps serve as a source of practical information for multiple usages (Abdikan et al., 2016), and LULC detection and mapping is considered essential for many socio-economic and environmental applications that include conservation and management of natural resources, agricultural and forest monitoring, urban planning, estimation of crop yield, detection of oil spills, and mapping of catastrophic events like wildfires, tsunamis, and floods (Kavitha et al., 2021).

Utilizing Remote Sensing with its different forms has many advantages, such as (1) extensive pre-existing databases like Landsat, Sentinel-1, sentinel-2, and Hyperion (2) capacity to acquire regional perspectives of the vast regions (3) convenience in combining data from several sensors (4) no risk or difficulty in reaching distant places (5) coverage of a large range of energy ranges (e.g. UV, optical, infrared and so on) (6) availability of high-quality computer analysis software, and (7) efficient and cost-effective (Awawdeh et al., 2023). Remote sensing images are used as a common tool for land cover classification (Mercier et al., 2019). Observation, identification, mapping, and monitoring of land cover are immensely facilitated by remote sensing and digital image processing over a range of spatial, temporal, and thematic scales (Gómez et al., 2016). Remote sensors that operate on different physical principals to record land surface information can be categorized into optical, thermal, and RADAR sensors which make use of reflected, emitted, and scattered energy respectively for data acquisition (Joshi et al., 2016). However, optical and radar-based remote sensing methods are most commonly used for land surface data collection. Though most of the existing studies use optical remote sensing data for land cover classification, it is difficult to perform this job with optical remote sensing data alone due to spectral confusion (Hu et al., 2021). The usefulness of SAR data, as a complementary source of information, is well reported because it is argued that the Synthetic Aperture Radar (SAR) data, which is sensitive to soil moisture and geometric configuration of the land surface, provides complementary information for optical remote sensing data, thus, offering an opportunity to be used in combination with optical data (Zhang, H. et al., 2015). The use of multisource data to improve land cover classification has become widespread (Sukawattanavijit et al., 2017), and aspects, like complementarity, interoperability, and synergetic strengths of different sensors, have been exploited by many researchers to achieve improved results in areas of land cover classification, identification of threats and environmental and crop monitoring (Sandberg, 2016). Several studies (De Alban et al., 2018; Laurin et al., 2012; Symeonakis et al., 2018; H. Zhang et al., 2015) have successfully employed the combined use of optical and SAR data to improve land cover classification accuracy.

* Corresponding author e-mail: Junaid@igis.nust.edu.pk

Recently the European Space Agency has launched two new generation platforms that provide Sentinel-1 (C Band SAR) and Sentinel-2 (MSI) images. Unlike most SAR (Radarsat-2, ALOS-2, TerraSAR-X) and Optical data (GeoEye, Quickbird, IKONOS, SPOT, and Worldview), Sentinel-1 and Sentinel-2 images are available free of charge under an open license policy (Mercier et al., 2019). S2 has the potential for mapping six to twelve land cover classes, while using a single date image has been demonstrated by some recent studies (Clark, 2017; Haas and Ban, 2018; Hdoush et al., 2022; Immitzer et al., 2016; Mongus and Žalik, 2018). The application of S1 has been mostly confined to its combined use with S2 or Landsat data for achieving increased classification accuracy (Inglada et al., 2016; Kussul et al., 2017; Laurin et al., 2022; Zhou et al., 2018). In several instances, the potential of integrated use of Sentinel-1 (SAR) and Sentinel-2 (Optical) data has been reported that included areas like LULC classification (Carrasco et al., 2019; Clerici et al., 2017; Dobrinić et al., 2020; Hu et al., 2021; Tavares et al., 2019), forest cover prediction (Heckel et al., 2020; Poortinga et al., 2019), vegetation species identification (Bjerreskov et al., 2021; Mendes et al., 2019; Zhang, H. et al., 2018), crops type mapping (Blickensdörfer et al., 2022; Cai et al., 2019; Orynbaikyzy et al., 2020; Van Tricht et al., 2018), and wildfire assessment (Colson et al., 2018).

Fusion of multiple data sources can be performed at three different levels: viz pixel level, feature level, and decision level fusion. Due to the presence of speckle noise, pixel-level fusion is not recommended for SAR images, and the use of feature-level fusion can help avoid this problem (Zhang, H. et al., 2015). Numerous applications (Mercier et al., 2019; Tavares et al., 2019; Van Tricht et al., 2018) reported that the fusion of data from Sentinel-1 and Sentinel-2 images increased the quality and accuracy of classification. It is advocated that Random Forest (RF) can outperform the traditional parametric approaches because of its ability to deal with noise and unbalanced datasets (Abdullah et al., 2019), and it can perform well when large datasets with many different features are involved (Belgiu & Drăguţ, 2016). This study involves feature-level image fusion and a random forest classification algorithm to carry out LULC classification of the study area.

Review of relevant literature reveals that most of the studies (Hussain et al., 2020; Majeed et al., 2021) in this country have used optical data for land cover classification. However, hardly few studies (Ali et al., 2018; Zahid Khalil and Saad-ul-Haque, 2018) can be found that focused on the use of SAR data for land cover classification, and only a very few cases involved the combined use of SAR and optical data in application areas like mapping of impervious surfaces (Shrestha et al., 2021) and crop types (Tufail et al., 2022). Land cover mapping through integrated use of SAR and optical data has been neglected so far from the study area perspective, and this gap has also been identified by Ali et al., 2018. This study is an attempt to explore the potential of Sentinel-1 SAR and Sentinel-2 optical data for land cover classification in the area of interest separately and combining data from both sources. The study may benefit resource managers and planners, especially when land use change reports are to be prepared for reporting purposes under the REDD+ mechanism that focuses on climate change mitigation endeavors across the globe including the study-focused region.

2. Materials

2.1 Study Area

The selected study area is located in Pakistan's administered part of the State of Jammu and Kashmir known as Azad Jammu & Kashmir (AJK). The State lies between 73-75^0 E and 33-36^0 N and occupies an area of 13297 km^2. It comprises 3 administrative divisions and 10 districts with a population of 4.179 million. The State falls in the Himalayan belt with mountainous topography in northern districts (Neelum, Muzaffarabad, Hattian, Bagh, Haveli, Poonch, and Sudhnuti) and relatively low hilly and undulating terrain of southern districts (Kotli, Mirpur, and Bhimber). The chosen study area extent covers 2059 km^2. It mainly includes Poonch and Sudhnuti districts with a small portion of Bagh and Kotli districts (Figure 1). These districts lie almost at the center of the north-south projected map of the State and include representative land use land cover (LULC) types, such as water bodies, vegetation cover, settlements, bare soil, and grass. The area is characterized by a sub-tropical to temperate type of climate. Broadly, the area experiences four seasons: spring (March-April), summer (May-August), autumn (September-November), and winter (December-February). The area experiences a distinct rainfall pattern where most of the rain occurs in monsoon (July to September) with occasional winter showers (December to March). At high altitudes, most of the winter precipitation is received as snowfall whereas low-lying areas are showered with rain only. The average annual rainfall that occurred during the last 10 years ranges from 899 millimeters to 1132 millimeters. Rawalakot and Bagh Districts experience relatively cooler surface temperatures compared to the Sudhnutii and Kotli Districts. The average surface temperature recorded for the winter and summer seasons is 9.05^{0}C and 23.64^{0}C respectively. The maximum temperature spikes as high as 38.02^{0}C while the minimum temperature drops as low as -4.11^{0}C (Source: https://chrsdata.eng.uci.edu/)

Topography is mainly hilly where the slope varies from 0 to 57 degrees with rugged terrain on hill slopes and relatively plain valley stretches. The elevation range of the area stretches from 372 m to 3384 m above mean sea level (msl) where microclimate varies with altitude and sets conditions for vegetation of different types. Figure 2 characterizes the topography of the study area. Landscape portrays a mixture of different land use land cover (LULC) types where settlements, water channels, and bare soil, with fragmented patches of forest, are the most prominent features. The population of the two main districts (Poonch and Sudhnuti) is 0.818 million (PNDD, 2015). Since the area has been enjoying fast infrastructural development for the last two decades. Therefore, LULC is also changing rapidly with developmental processes where increasing population causes a notable change in built-up areas and natural as well as planted vegetation cover. The main forest types of the area include Subtropical Chir Pine, Moist Temperate Conifers,

and Scrub Forests. However, forest cover is predominantly occupied by Subtropical Chir Pine forest with Chir pine (Pinus roxburghii) as a typical species. Major species of the Moist Temperate Coniferous forest are blue pine (Pinus wallichana) and a few mixed broadleaved species. Scrub forest type is mainly dominated by wild olive (Olea cuspidata) and hop-bushes (Dedonia viscosa). As local communities are allowed to collect fuel wood and fodder from these forests and in addition to these rights, they are also entitled to grant of timber needed for house construction. Therefore, the heavy dependence on surrounding communities tends to increase pressure on forest resources, thereby aggravating the common environmental problems like deforestation, destruction of wildlife habitat, and landslides. Small average land holdings and scarcity of cultivable land restrict agriculture to narrow terraced land developed around houses on steep mountain slopes. Maize and wheat are the major agricultural products, whereas livestock rearing is also practiced at a limited scale to cater to household dairy needs.

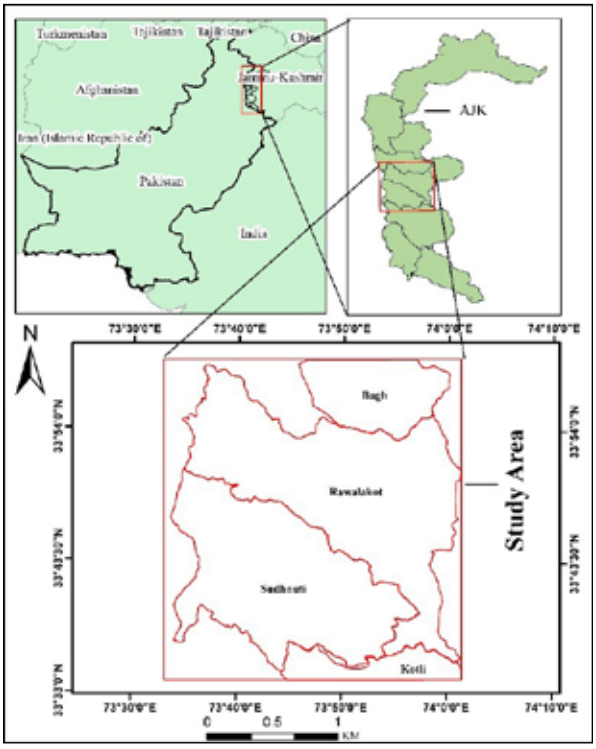

Figure 1. Study area map

2.2 Satellite Data

Using satellite imagery, detection, and mapping of land cover involves a number of steps that include selection of required sensor data, definition of land cover classes, data processing and feature extraction, preparation of input datasets for classification, decision of an appropriate classification method, and analysis of outputs.

Satellite data from Sentinel-1 (SAR) and Sentinel-2 (Optical) sensors were employed for land cover classification in the area of interest (AOI). The Sentinel data were downloaded from the official website (http://scihub.copernicus.eu./dhus/≠/home) available via the Copernicus Open Access Hub of the European Space Agency (ESA). Both Sentinel-1 and Sentinel-2 images were collected in Level 1 format which needed several preprocessing steps before use for further analysis.

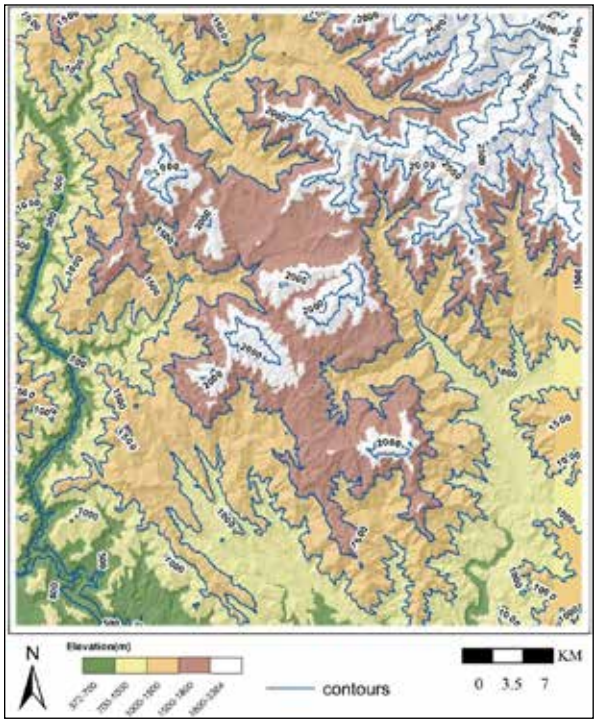

Figure 2. DEM depicting topography of the study area

2.2.1 Sentinel-1 (S1) SAR image

Sentinel 1 Synthetic Aperture Radar (SAR) mission is comprised of 1A and 1B polar-orbiting satellites. The European Space Agency (ESA) launched Sentinel 1A in April 2014 which was followed by Sentinel 1B in April 2016. The data captured in the 'C' band is delivered with dual polarization, i.e. Vertical-Horizontal (VH) and Vertical–Vertical (VV). The products that are suitable for Level-0, Level-1, and Level-2 processing are provided in three different operational modes known as Interferometry Wide Swath (IW), Strip map (SM), and Extra Wide Swath (EW). The Synthetic Aperture Radar imaging is carried out with a repeat cycle of 6 days (Liu et al., 2018). Sentinel 1 (S1) data is available free of charge for different applications under the open data license policy of ESA. A Ground Range Detected (GRD) S1 Level-1 product recorded in Interferometry Wide Swath (IW) mode, acquired on September 23, 2020, was downloaded for the study.

2.2.2 Sentinel-2 (S2) Optical Image

The Sentinel-2 (S2) is a high-resolution, wide-swath multi-spectral imaging mission. It comprises 2A and 2B satellites that were launched by the European Space Agency (ESA) in 2015 and 2017 respectively. A state-of-the-art multispectral imaging instrument (MSI), carried by Sentinel-2A, captures the data in 13 spectral bands with 10 m (four bands), 20 m (six bands), and 60 m (three bands) spatial resolution. A Sentinel 2A Level 1C multispectral image, acquired on September 17, 2020, corresponding to the study area, was downloaded for this study.

2.2.3 Multi-Sensor Dataset

Apart from S1 and S2-derived datasets, a third type of multi-sensor (S1+S2) dataset was also prepared to be exploited for land cover classification. The SAR VH, VV channels, and SAR-derived texture images were resampled to 20 m using the nearest neighbor resampling method, so

that they are compatible with stacking with S2A spectral bands and indices of 20 m spatial resolution. A separate dataset, consisting of four 10 m spatial resolution S2A spectral bands in combination with SAR VH, VV images, and SAR-based textures with their original resolution of 10 m, was also generated to be used for LULC classification. Image stacks, consisting of S2 and S1-derived features, were prepared in QGIS.

2.3 Reference Data

The dominant representative land use land cover classes of the area were considered for classification. Among these LULC types, water, vegetation, settlements, bare soil, and grasses are the key categories that were taken into account for detection and mapping purposes. Training samples of six land cover classes namely water, mixed forest, shrublands, bare soil, built-up area and grassland were selected based on knowledge of the area on high-resolution Google Image of the study site. Table 1 provides the description of land use/ land cover classes and selected training samples.

3. Methods

3.1 Pre-processing of S1 (SAR) Image

The preprocessing steps included calibration, speckle filtering, terrain correction, sub- setting, and image export. Sentinel 1 Level-1 products are not radiometrically corrected, therefore, calibration is required for the transformation of pixel values from simple digital numbers to SAR backscatter. Radiometric calibration was performed as the first step by calculating the sigma nought for the given image. Image calibration was followed by speckle filtering that was intended to remove speckle noise in the image. A Lee speckle filter with 3x3 windows was applied for speckle suppression that resulting in the production of a relatively smoother image. Since geometric distortions are inherently found in Level-1GRD images, geometric correction was also a necessary step. Range Doppler Terrain correction was applied to convert the image into a map system that was projected into WGS84 UTM Zone 43 N. Generally, it is easier to work with the image in decibel (db) format; therefore, the image was transformed from linear to db units. Finally, the image was subset to the desired extent of the study area with a 10 m pixel size. All these SAR image preprocessing steps were performed in SNAP 8.0 open-source software. A third band (VV-VH) was also produced from VH and VV polarization channels since this band combination is considered optimal for land cover classification (Abdikan et al., 2016).

Textural information of a satellite image is of foremost importance in land cover mapping (Sylla et al., 2021). SAR texture measures are recognized as a valuable source of information and it is believed that SAR textures may serve as a useful input for land cover classification because single pixel values in SAR imagery are not reliable due to inherent speckle noise (Zhu et al., 2012). Many methods and techniques have been developed for the calculation of image textures. However, among previously proposed methods, the Grey Level Co-occurrence Matrix (GLCM) approach is considered one of the most reliable statistical methods used for derivation of textures from a satellite image (Zakeri et al., 2017). In this study, the most commonly used texture measures were extracted for LULC mapping using the GLCM approach introduced by Haralick et al., 1973. These included Angular Second Moment (ASM), Contrast (CON), Dissimilarity (DIS), Homogeneity (HOM), Entropy (ENT), Mean (AVG), and Variance (VAR). Generally, image textures are worked out by considering a moving window of a specific size that performs some mathematical calculation around a pixel of interest (Kavitha et al., 2021). SAR textures were calculated for both VH and VV polarizations in SNAP software using window sizes of 7x7, 9x9, and 11x11, and different combinations of derived textures were used as input variables for classification.

3.2 Pre-Processing of Optical (S2) Image

The Sentinel-2A L1C provides top-of-atmosphere (TOA) reflectance, and the wavelengths of image bands range from 443 nm to 2190 nm. The downloaded S2 L1C tile was atmospherically corrected to obtain surface reflectance using the Sen2Cor application integrated with SNAP. The image was transformed from L1C to L2A and only the bands with 10 m spatial resolution (B2, B3, B4 & B8) and 20 m (B2, B3, B4, B5, B6, B7, B8A, B11 & B12) were used for further analysis with their original resolutions, whereas bands with 60 m spatial resolution were excluded for further consideration. These atmospherically corrected spectral bands were clipped to the study area extent and made ready for stacking and calculation of spectral indices. In addition to individual spectral bands, five indices (NDVI48, NDVI48a, NDVI56, NDVI57, and NDVI68a) were also calculated, using different combinations of spectral bands and included in the datasets prepared for land cover classification. Composites of S2A 20 m & 10 m spatial resolution spectral bands and calculated indices were produced, using different combinations, and an input dataset was prepared for categorization of images into predefined land cover classes. A description of land use /land cover classes of the study area and samples selected for classification purposes is provided in Table 1.

Table 1. A description of land use /land cover classes and samples selected for classification purpose

Sr No	Land Cover Class	Description of Class	No of Polygons	No of Pixels
1	Water	River, secondary, and tertiary water streams	8	894
2	Mixed Forest	Managed and unmanaged forest cover comprising predominantly of conifers with a mix of broadleaved trees	42	19746
3	Shrubland	Scrub forest inhabiting shrubby vegetation, short-statured woody and herbaceous flora	45	4254
4	Bare Soil	Bare land, sparsely vegetated areas with dominant soil background, exposed substrata due to landslides, ploughed terraces yet not cultivated, mud houses, and earthen roads	78	633
5	Built-Up	Settlements, manmade artificial structures, cemented and asphalt roads, rocks and boulders	69	1748
6	Grassland	Forest floor covered with grasses and herbs in open canopy forest, Grass covered farmlands, meadows, and grassy hill slopes	31	1764

3.3 Land Cover Classification

Land cover types, corresponding to pixel values of a satellite image, are extracted by means of a widely used method called image classification (Orlíková and Horák, 2019).

Satellite image classification has been carried out using numerous image classification techniques that can be grouped into different categories (Chowdhury, 2024). In recent years, the use of machine-learning algorithms has attracted a considerable amount of attention for LULC mapping while employing remotely sensed imageries (Adam et al., 2014; Maxwell et al., 2019). It is believed that machine-learning algorithms are more accurate and noise-resistant than common algorithms (Rodriguez-Galiano, V. F. et al., 2012). As far as LULC studies are concerned a machine learning algorithm that was introduced by Leo (Breiman, 2001) in 2001 known as random forest (RF) is deemed to be the most suitable model for land cover classification (Gislason et al., 2006; Guo et al., 2011).

Table 2. shows different scenarios of RF-based LULC classification carrid out using different combinations of S1 & S2 derived variables

Classification Scenario	Datasets	No of variables
	Sentinel-1 Based Datasets	
1	VH, VV, (VV-VH)	3
2	VHVV_11, (VH, VV)	16
3	VHVV_79, (VH, VV)	30
4	VH_7, VV_11, (VH, VV)	16
5	VH_11, VV_9, (VH, VV)	16
6	VH_7911, (VH, VV)	22
7	VV_7911, (VH, VV)	22
8	VH_7, (VH)	8
9	VH_11, (VH)	8
10	VV_7	7
11	VH_9	7
12	VV_9	7
13	VH_11	7
14	VH_9, VV_7	14
15	VV_9, (VH, VV)	9
	Sentinel-2 Based Datasets	
1	B2, B3, B4, B5, B6, B7, B8A, B11, B12	9
2	B2, B3, B4, B5, B6, B7, B8A, B11, B12 and indices (NDVI48, NDVI48a, NDVI56, NDVI57, NDVI68a)	14
3	B2, B3, B4, B8	4
4	B2, B3, B4, B8 and NDVI	5
	S1+S2 combination Based Datasets	
1	B2, B3, B4, B5, B6, B7, B8A, B11, B12 and VHVV_11 (VH, VV)	25
2	B2, B3, B4, B5, B6, B7, B8A, B11, B12 and indices (NDVI48, NDVI48a, NDVI56, NDVI57, NDVI68a) and VHVV_11, (VH, VV)	30
3	S2 indices and VHVV_11, (VH, VV)	21
4	B2, B3, B4, B8 and VHVV_11, (VH, VV)	20
5	B2, B3, B4, B5, B6, B7, B8A, B11, B12 and VH_7, VV_11, (VH, VV)	25
6	B2, B3, B4, B5, B6, B7, B8A, B11, B12, S2 derived indices (NDVI48, NDVI48a, NDVI56, NDVI57, NDVI68a) and VH_7, VV_11 (HV, VV)	30
7	B2, B3, B4, B8, and VH_7, VV_9, (HV, VV)	20

Note: SAR: VH, VV refer to SAR polarization images, VH_a, VV_b denote the VH, VV derived SAR textures with respective window size,
Optical: B1, B2 …. Refer to spectral band number of S2 image, NDVI = Normalized Difference Vegetation Index and ab denote the spectral bands used for derivation of a specific index

In this study, the Random Forest algorithm was chosen for land cover classification because previous research shows that RF performed excellently in classifying diverse remote sensing datasets (Gislason et al., 2006; Rodriguez-Galiano, V. F. et al., 2012) especially, when optical and radar data were used as combined datasets. It has been inferred that LULC classification accuracy can be improved effectively employing the fusion of optical and SAR images. Currently, three levels of image fusion are generally practiced in remote sensing. These methods include (i) pixel level (ii) feature level and (iii) decision-level image fusion. Since feature-level fusion takes into account factors, like feature information and correlation contained in the image itself, and obtains more macro-level feature-level information, therefore, it has been revealed that feature-level image fusion is considered a more appropriate technique than pixel pixel-level approach (Zhang, R. et al., 2020). Feature-level image fusion method was used in this study that involves the application of feature

stacking. Image stacks of S1 & S2 derived features were used as predictors for land cover classification. Input datasets for land cover classification contained diverse composites that were prepared from different S1 (SAR) and S2 (Optical) derived features. These datasets were generated separately from extracted variables of S1 and S2 images as well as band stacks were also produced by combining feature layers from both sources (S1+S2). The number of trees was set to 100 because it helps reduce time without causing any notable loss in accuracy (Mercier et al., 2019). The prepared set of training samples was used with a 50/50 ratio (Training and Validation). Figure 3 illustrates the spectral reflectance curves of LULC classes sampled for classification purpose. Different types of datasets based on S1 & S2 derived features/ variables (S1-alone, S2-alone, S1+S2 combined) were used for LULC classification (Table 2), and each classification scenario was examined to analyze the classification accuracy (Table 3). An error matrix with an equal number of rows and columns expresses the relationship between classification and validation data and is generally used as a standard to measure classification accuracy (Orlíková and Horák, 2019). Therefore, an error matrix was used to calculate the overall accuracy (OA), User accuracy (UA), and Producer accuracy (PA). The flow of the classification process is illustrated in Figure 4. Random Forest land cover classification was executed in Orfeo Toolbox integrated with QGIS open source software, whereas Arc-GIS and Arc-GIS Pro were used for map layout and extraction of spectral reflectance curves.

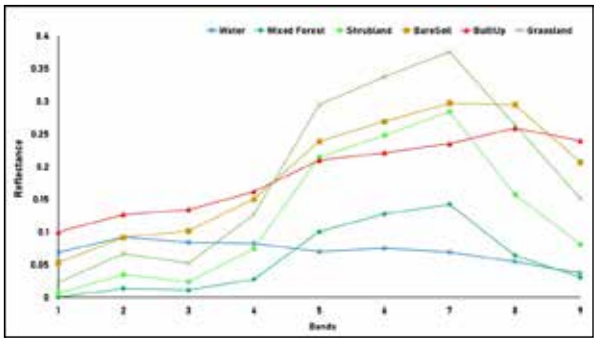

Figure 3. Reflectance spectra of LULC classes utilized for classification purposes.

Table 3. shows different scenarios of random forest classification with S1 & S2 derived set of variables and their associated overall accuracy and Kappa Coefficient value.

Classification Scenario	Sentinel-1 Based Datasets	Kappa Index Value	Overall Accuracy (OA%)
1	VH, VV, (VV-VH)	0.33	44.65
2	VHVV_11, (HV, VV)	0.55	63
3	VHVV_79 (HV, VV)	0.53	61
4	VH_7VV_11, (HV, VV)	0.53	61
5	VH_11, VV_9, (HV, VV)	0.51	59.84
6	VH_7911, (HV, VV)	0.52	60
7	VV_7911, (HV, VV)	0.43	52.91
8	VH_7, VH	0.35	47.93
9	VH_11, VH	0.52	60
10	VV_7	0.33	44.65
11	VH_9	0.41	50.95
12	VV_9	0.32	43.86
13	VH_11	0.52	60
14	VH_9, VV_7	0.50	59
15	VV_9, (VH, VV)	0.42	52
	Sentinel-2 Based Datasets		
1	B2, B3, B4, B5, B6, B7, B8A, B11, B12	0.85	88.12
2	B2, B3, B4, B5, B6, B7, B8A, B11, B12 and indices	0.87	89.59
3	B2, B3, B4, B8	0.83	86
4	B2, B3, B4, B8 and NDVI	0.84	87
	Sentinel-1 & Sentinel-2 (S1+S2) Based Datasets		
1	B2, B3, B4, B5, B6, B7, B8A, B11, B12 and HVVV11 (HV, VV)	0.90	91.87
2	B2, B3, B4, B5, B6, B7, B8A, B11, B12 and indices and VHVV_11 (VH, VV)	0.91	93.12
3	S2 indices and VHVV_11 (VH, VV)	0.74	79
4	B2, B3, B4, B8 and VHVV_11 (VH, VV)	0.84	87
5	B2, B3, B4, B8, NDVI and VHVV_11 (VH, VV)	0.86	88.57
6	B2, B3, B4, B5, B6, B7, B8A, B11, B12 and VH_7, VV_11, (HV, VV)	0.87	89
7	B2, B3, B4, B5, B6, B7, B8A, B11, B12, S2 derived indices (NDVI48, NDVI48a, NDVI56, NDVI57, NDVI68a) and VH_7, VV_11, (HV, VV)	0.87	89
8	B2, B3, B4, B8, and VH7VV9 (HV, VV)	0.83	86

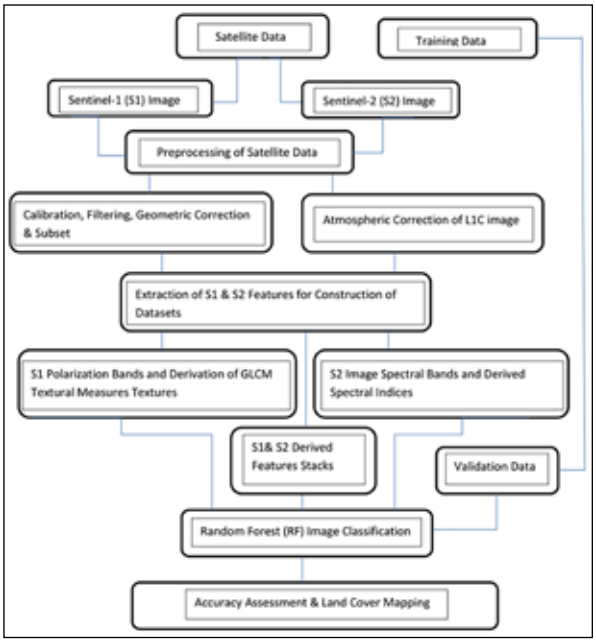

Figure 4. Diagram depicting flow of work

4. Results

Firstly, the image composites, produced from SAR VH, and VV polarizations, were used alone for land cover classification employing a random forest classifier. The image, consisting of VH-VV, and VV-VH polarimetric channels, produced an overall (OA) accuracy of 44.65% and a Kappa coefficient (KC) of 0.33. Afterward, different combinations of SAR-based datasets consisting of SAR textures (derived with varying window sizes of 7x7, 9x9, and 11x11) either alone or combined with SAR VH, and VV polarizations were exploited for classification purposes. These combinations presented different degrees of accuracy for land cover classification. Among the given S1- -alone datasets, a 16-layered image consisting of VH and VV polarization bands and derived SAR textures having window size 11x11 (denoted as VHVV_11) yielded the highest overall accuracy and Kappa coefficient (63.01%; KC= 0.55). Classification accuracy yielded by different combinations of Optical-SAR datasets with associated Kappa Index is furnished in Table 3.

Similarly, in optical domain band composites of S2A, spectral bands (20 m and 10 m spatial resolution) and derived spectral indices were analyzed for land cover classification. Individually, the band composite, consisting of B2, B3, B4, B5, B6, B7, B8A, B11, and B12 yielded overall accuracy and Kappa value of 88.12 % and 0.85 respectively whereas the highest overall accuracy of 89.58% with kappa statistics of 0.87 was recorded when nine layers of spectral bands were tried in combination with derived spectral indices. A dataset containing four spectral bands (10 m resolution) gave 86.34% OA (KC= 0.83) and the addition of the NDVI layer to this set of variables led to an increase in OA of 87.40 (KC= 0.84).

The third type of dataset, used for RF-based LULC classification, consisted of features from both S1A and S2A images. Several image stacks were structured by combining data from Sentinel-1 and Sentinel-2 sources and employed to extract six predefined land cover classes using an RF classifier. The results provided different levels of accuracy. Out of the tested range of multiple combinations a thirty (30) layered feature stack developed by integrating SAR VH, VV polarizations, textures (ASM, Contrast, Dissimilarity, Homogeneity, Entropy, Mean and Variance derived from HV, VV polarizations using window size of 11x11), S2 spectral bands (B2, B3, B4, B5, B6, B7, B8A, B11 & B12) and spectral indices (NDVI48, NDVI48a, NDVI56, NDVI57, NDVI68a) produced highest overall accuracy of 93.12% and kappa coefficient value of 0.91. The indicated dataset (S1+S2 integrated features stack) proved to be the best combination among all of the datasets employed for the LULC classification of the study area. Table 3 shows different scenarios of the datasets that were used for LULC classification and their results in terms of overall accuracy and kappa coefficient. Error matrix (Table 4) demonstrates the overall accuracy (OA), Producer's accuracy, User's accuracy, and Kappa Coefficient (KC) value for the best-performing model. Figure 5 shows the classified image next to the Sentinel-2 natural color image whereas Figure 6 highlights the classified and reference land cover classes from the study area.

Table 4. Confusion matrix portraying accuracy statistics for best-performing combination of variables derived from SAR and Optical satellite data

	Reference							
	LC Classes	**Water**	**Mixed Forest**	**Shrublands**	**Bare Soil**	**Built-Up**	**Grasses**	**User's Accuracy**
Mapped	Water	77	0	0	1	2	0	0.96
	Mixed Forest	0	74	6	0	0	0	0.92
	Scrubland	0	4	73	1	0	2	0.91
	Bare Soil	1	0	5	68	3	3	0.85
	Built-Up	0	0	0	0	80	0	1
	Grasses	0	0	5	0	0	75	0.93
	Producer's Accuracy	0.98	0.94	0.82	0.97	0.94	0.93	
	Overall Accuracy= 93% Kappa Index= 0.91							

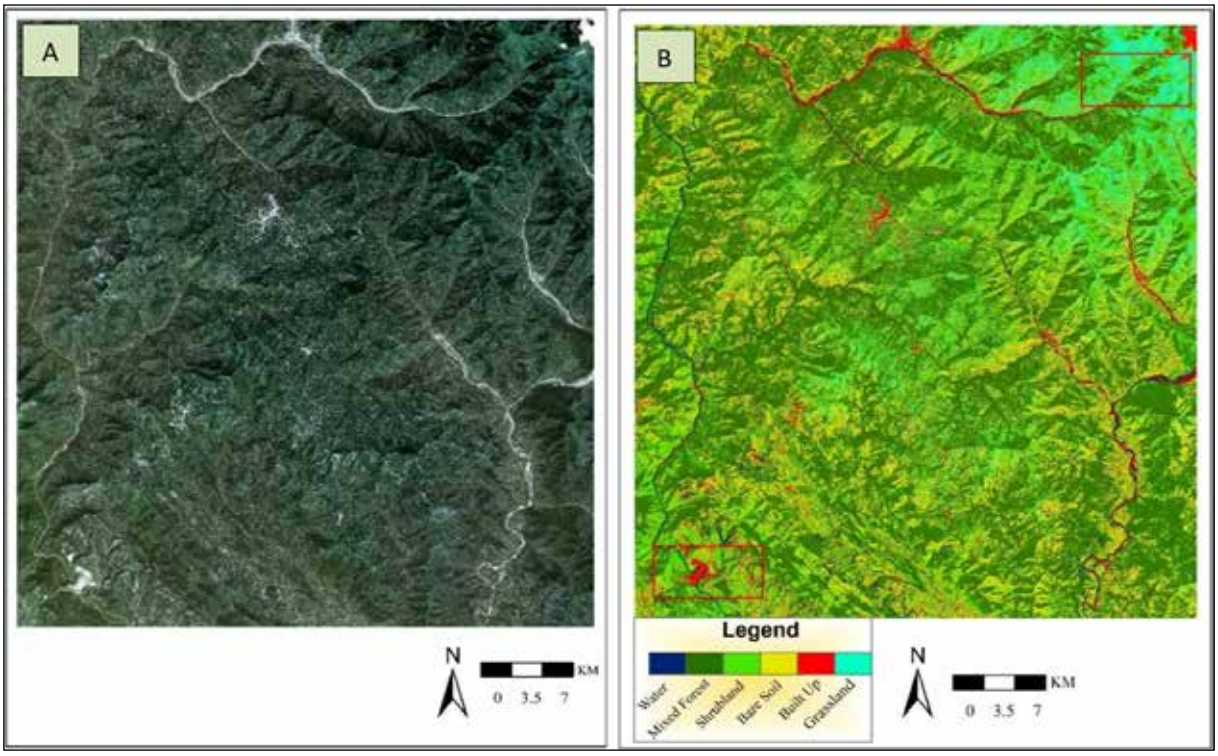

Figure 5. (**A**) Sentinel-2 natural colour image (**B**) A final LULC map obtained from combined use of Sentinel-1 and Sentinel-2 (S1+S2) derived features. Sections marked with red boxes highlight the classification accuracy shown in figure 6

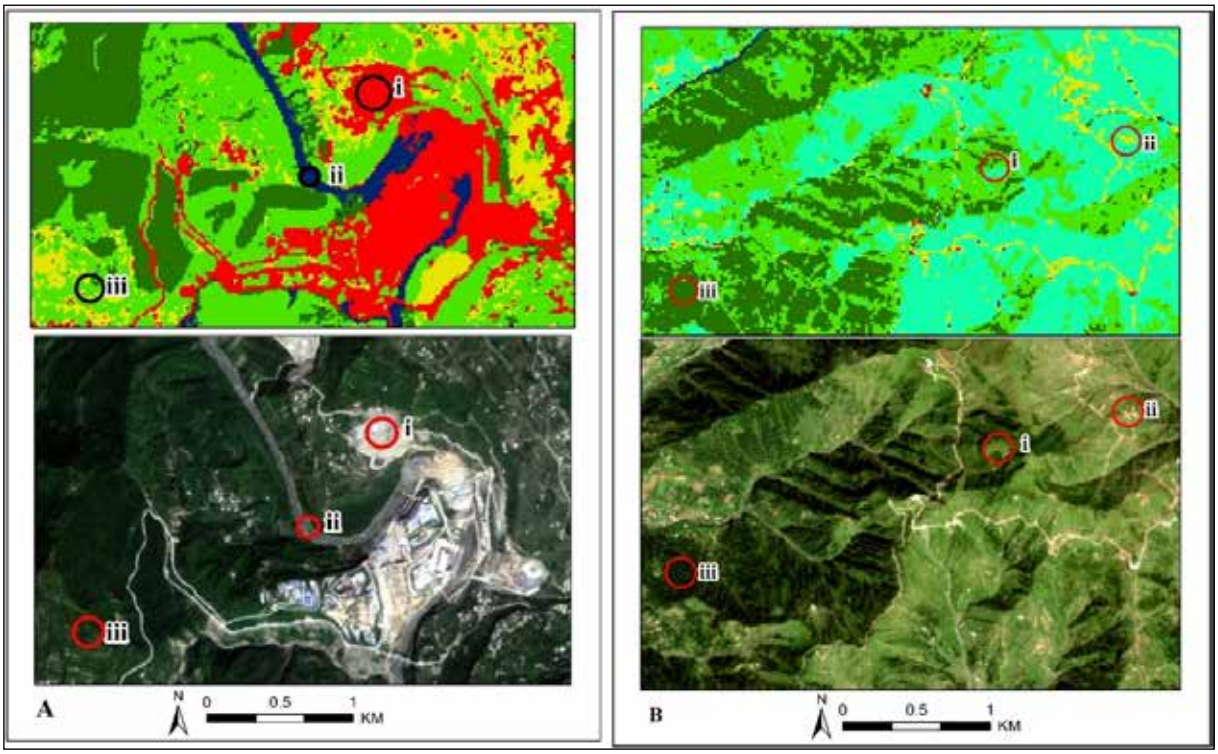

Figure 6. Comparison of mapped and reference land cover classes using high resolution Sentinel-2 natural color image and clips from final LULC map. (**A**). i. Built up, ii. Water, iii. Shrublands (**B**). i. Grassland, ii. Bare Soil, iii. Mixed Forest

5. Discussion

Several studies have involved the integrated use of RADAR and optical data for land use land cover classification in different parts of the world and they have reported different levels of contribution from these two different data types in classification success both in their individual as well as in combined capacity. In this study, Sentinel-1 derived data set consisting of VH-VV and VV-VH variables produced an overall accuracy of 44.65% where the Kappa coefficient was 0.33. Our results are in line with some of the recently conducted studies that used Sentinel-1 data for land cover classification. For instance, Clerici et al. (2017) achieved only 20.12% overall accuracy with the Random Forest method where a Sentinel-1 image of the

study area (in Colombia) was categorized into six LULC types. In another case, Mendes et al. (2019) applied RF to map vegetation types with Sentinel-1 scene in Mato Grasso, Brazil and reported an overall accuracy and kappa coefficient range of 45.51%-56.21% and 0.31-0.42 respectively. In the Moravian-Silesian region of the Czech Republic Orlíková and Horák (2019) categorized the S1 imagery into three land cover classes (Arable land, Grasses, and vine orchids) and indicated an overall accuracy of 46.28% and 61.5% for pixel-based classification that was performed at two different selected sites. Similarly, Nuthammachot and Stratoulias (2019) investigated the potential of the S1 image to classify five land cover classes across an area chosen in Thailand. They achieved an overall accuracy of 58.50% with a 0.48 Kappa coefficient value and the authors have reasoned that the SAR image was not able to clearly extract the pre-defined land cover classes except water and misclassification was more evident in forest and urban land cover classes. The study underlined that classification confusion was more pronounced in hilly parts of the selected site.

It has been learned that SAR textures help improve classification accuracy (Zhu et al., 2012). The inclusion of SAR textures significantly improved the classification accuracy in our case. We tried different combinations of SAR VH, VV polarizations, and 7 texture measures (ASM, Contrast, Dissimilarity, Homogeneity, Entropy, Mean, and Variance) that were derived, using windows of different sizes (7x7, 9x9, 11x11). These combinations produced results with varying ranges of overall accuracy and Kappa coefficient. Among the employed combinations, the lowest OA of 47.93% (Kappa statistic 0.35) was noted for a set of eight variables that contained VH polarization and seven texture measures (window size 7x7), whereas the highest OA (63.01%; Kappa value 0.55) was given by a dataset (consisting of 16 variables) that was developed by combining VH, VV polarization with their respective textures features (7 each) that were extracted using window size of 11x11. Datasets, consisting exclusively of SAR textures excluding polarization layers, were also examined for land cover classification, and different results were achieved for these applications. Amongst the textures derived from a single polarization band VV based textures (7x7 window size) yielded the lowest accuracy (OA= 44.65, Kappa Coefficient= 0.33), whereas VH-associated textures (window size of 11x11) generated the best results (OA= 60.37, Kappa Coefficient= 0.52). SAR dataset created merely from backscattering components produced low producer's and user's accuracies (34% and 22%) for the shrubland but these accuracies started improving with the introduction of SAR textures and increased up to 61% and 34% with VHVV_11. Different combinations of SAR polarizations and texture variables with corresponding OA accuracy and Kappa values have been shown in Table 3. Results of our study about the role of Sentinel-1 derived textures in LULC classification are supported by several studies where GLCM SAR textures proved useful towards improving LULC classification accuracy. This refers to Tavares et al. 2019 where the study attempted to extract 12 land cover classes in Brazil employing Random Forest (RF) classifier and obtained 56.01% (KC=0.41) overall accuracy while using Sentinel-1 data alone but the classification accuracy increased to 61.61% (KC=0.48) when SAR textures were also combined with Sentinel-1 data. In another example, Zakeri et al. (2017) performed a land cover classification task in Tehran (Iran) while using SAR backscatter data and SAR textures and it was revealed that Sentinel-1 textures performed better than Sentinel-1 backscatter-only scenarios. When GLCM-based Sentinel-1 textures (window size 11x11) were included for LULC classification the OA accuracy increased from 45.7% to 54.2% with respective increase in kappa coefficient from 0.29 to 0.41. It was reported by Inglada et al. (2016) that Sentinel-1 GLCM textures contained most of the information needed for accurate classification. In general, the usefulness of SAR textures has also been demonstrated by an array of studies that involved the application of SAR textures derived from sensors other than Sentinel-1 for LULC classification. SAR textures played an influential role in many Land cover classification studies (e.g. De Alban et al. 2018; Laurin et al. 2012; Zhu et al. 2012). In our study, SAR textures derived from the VH polarization band with window size 11x11 made a notable difference in all cases. When combined, these texture measures alone produced OA accuracy of 60.37 with a 0.52 kappa coefficient value and they played an influential role in all the datasets that involved their contribution (Table 3).

In this study a dataset from the optical domain (Sentinel-2), consisting of 9 spectral bands (B1, B2, B3, B4, B5, B6, B7, B8A, B11, and B12 (20 m spatial resolution) provided OA of 88.12% and kappa coefficient value was 0.85. The inclusion of Sentinel-2 derived five spectral indices (NDVI48, NDVI48a, NDVI56, NDVI57, and NDVI68a) helped increase the OA accuracy to 89.58% with a Kappa coefficient of 0.87. A four-layered optical (S2) dataset (B2, B3, B4, and B8 with 10 m spatial resolution) resulted in OA and Kappa index of 86.34 and 0.83 respectively whereas inclusion of NDVI in this dataset (5 variables) improved both OA accuracy (87.40%) as well as Kappa index (0.84).

Integration of SAR and optical data (S1+S2) which refers to feature level Optical -Radar data fusion further improved the classification accuracy than yielded by SAR or optical dataset alone. A data stack (25 layers) generated through the integration of 16 layers of SAR data (VH, VV texture features derived with window size 11x11) and 2 polarization bands) combined with 9 layers of optical data (spectral bands) produced an OA of 91.87% and a kappa coefficient of 0.90. The inclusion of five spectral indices (stack of 30 variables) further enhanced the classification accuracy, and this S1 + S2 data combination produced the highest overall accuracy of 93.12% (KC=0.91). In the case of 10 m spatial resolution spectral bands, a features stack, generated by integrating 14 VH, VV derived textures (11x11), 2 polarizations, and 4 spectral bands with NDVI layer (21 variables), resulted in 88.57% OA accuracy with KC=0.86. In the case of 10 m spatial resolution optical data, it proved to be the best SAR/ Optical combination. Similarly, many other combinations of SAR and Optical data were tested for LULC classification. For example, S2 spectral bands (20 m) and SAR-derived texture measures (VH_7x7 and VV_11x11) combined with

two polarization bands (25 feature layers) provided 89% of OA accuracy with a kappa coefficient of 0.87. The addition of five spectral indices to this combination (30 variables) made no difference and gave the same results (OA=89%, KC=0.87). Using another stack of 20 layers (VH_7, VV_9 textures with two polarizations and four 10 m spectral bands) an OA accuracy of 86.40% (KC= 0.83) was obtained and similarly in another type of such combination that was developed by stacking four 10 m spectral bands and VH, VV SAR polarization bands (6 layers) OA accuracy of 86.71 (KC= 0.84) was achieved (Table 3).

Integrated use of SAR and Optical data, particularly Sentinel-1 and Sentinel-2 images have been used successfully in several studies aimed at LULC classification, forest and vegetation mapping, crop types identification, and in various other fields. Borges et al. 2020 conducted land cover mapping in Tanzanian Savanah where nine land cover classes were mapped by using S1 and S2 data through the Random Forest classification approach. The study concluded that optical models performed better than their radar counterparts and that overall accuracy for all given scenarios was improved by the combination of multi-sensor (S1+S2) data. The study also revealed that Sentinel-1 data was not able to distinguish well between most of the land cover classes and a higher degree of confusion was observed between forest, woodland, and bushland. It identified "Grassland' reasonably but overestimated the shrubland. Dobrinić et al. (2020) used S1 and S2 satellite data for classification of five land cover types in France. The classification results show that using RF classier S1 data provided an accuracy of 70.41% (KC=0.61) whereas S2-based results were better (Accuracy=84.17% with 0.80 Kappa Coefficient) than S1. The highest classification accuracy of 85.47% (KC=0.81) was achieved with the integrated use of S1 and S2 multisource data. The significance of SAR textures was also evident in the case of SAR-Optical data integration (S1+S2) where the indicated GLCM textures enhanced the overall accuracy from 89.58% (observed in the case of the optical dataset) to 93.12% with a corresponding increase in Kappa coefficient from 0.87 to 0.91 respectively. Here, again the recorded producer's and user's accuracies for the shrubland cover class have enhanced from 77%, 86% to 82%, and 91% respectively with the inclusion of texture features (calculated via window size 11x11).

Most of the cases that investigated the potential of SAR and optical data for LULC classification separately as well as in combination concluded that SAR data alone resulted in the lowest accuracy compared to which optical data performed better whereas the combination of both SAR and Optical data further improved the classification results and produced the highest overall accuracy. The findings of this study are well aligned with several studies (Lopes et al., 2020; Mercier et al., 2019; Poortinga et al., 2019; Tavares et al., 2019) that used Sentinel-1 and Sentinel-2 data for Random Forest based classification of LULC. These studies investigated the ability of Sentinel-1 and Sentinel-2 datasets for classification independently as well as in integration and ascertained that Sentinel-1 yielded the lowest accuracy. Sentinel-2 fetched better results relative to Sentinel-1 while the best overall accuracy was realized when S1 and S2 data were used in combined mode.

6. Conclusion

This study attempted to investigate the role of integrated use of freely and conveniently available SAR (Sentinel-1) and Optical (Sentinel-2) in an area with complex mountainous topography and different land cover classes. Three different scenarios were analyzed for the classification of land cover in the selected area of interest. An efficient machine learning classifier known as Random Forest was employed for classification and the achieved results were used to assess the accuracy of classification. The study reflects that feature-level Optical-SAR data fusion proved successful in improving OA classification accuracy. The highest overall accuracy of 93.12% was observed when features derived from both SAR and Optical images were used in the integration. As signified in many studies, GLCM textures extracted from SAR polarization bands played an important role in this case in improving OA classification accuracy. Though observed increase in OA accuracy is only 3.5% yet it may prove very beneficial when LULC mapping is carried out at the level of State's extent. This finding may help and encourage resource managers and planners to conduct wall-wall LULC mapping across the State while utilizing free-of-charge and continuously available S1 and S2 data and sophisticated open-source software to prepare reports needed as a part of MRV reporting requirement under REDD+ that is an incentive-based mechanism aimed at mitigation of climate change impacts at the global level.

References

Abdel-Rahman, E. M., Mutanga, O., Adam, E., and Ismail, R. (2014). Detecting Sirex noctilio grey-attacked and lightning-struck pine trees using airborne hyperspectral data, random forest and support vector machines classifiers. ISPRS Journal of Photogrammetry and Remote Sensing 88: 48–59.

Abdikan, S., Sanli, F. B., Ustuner, M., and Calò, F. (2016). Land cover mapping using sentinel-1 SAR data. In International Archives of the Photogrammetry, Remote Sensing and Spatial Information Sciences - ISPRS Archives (Vol. 41). International Society for Photogrammetry and Remote Sensing.

Abdullah, A. Y. M., Masrur, A., Gani Adnan, M. S., Al Baky, M. A., Hassan, Q. K., and Dewan, A. (2019). Spatio-temporal patterns of land use/land cover change in the heterogeneous coastal region of Bangladesh between 1990 and 2017. Remote Sensing 11(7).

Adam, E., Mutanga, O., Odindi, J., and Abdel-Rahman, E. M. (2014). Land-use/cover classification in a heterogeneous coastal landscape using RapidEye imagery: evaluating the performance of random forest and support vector machines classifiers. International Journal of Remote Sensing 35(10): 3440–3458.

Ali, M. Z., Qazi, W., and Aslam, N. (2018). A comparative study of ALOS-2 PALSAR and landsat-8 imagery for land cover classification using maximum likelihood classifier. Egyptian Journal of Remote Sensing and Space Science 21: S29–S35.

Amani, M., Mahdavi, S., Afshar, M., Brisco, B., Huang, W., Mohammad Javad Mirzadeh, S., White, L., Banks, S., Montgomery, J., and Hopkinson, C. (2019). Canadian Wetland Inventory using Google Earth Engine: The First Map and Preliminary Results. Remote Sensing 11(7): 842.

Awawdeh, M., Alkhateeb, E., and Al-Radaideh, N. (2023). The Use of Remote Sensing and GIS for Mapping Silica Sand

Deposits in Jordan. Jordan Journal of Earth and Environmental Sciences 14(3): 232–240.

Bjerreskov, K. S., Nord-Larsen, T., and Fensholt, R. (2021). Forest type and tree species classification of nemoral forests with Sentinel-1 and 2 Time Series data.

Blickensdörfer, L., Schwieder, M., Pflugmacher, D., Nendel, C., Erasmi, S., and Hostert, P. (2022). Mapping of crop types and crop sequences with combined time series of Sentinel-1, Sentinel-2 and Landsat 8 data for Germany. Remote Sensing of Environment 269.

Borges, J., Higginbottom, T. P., Symeonakis, E., and Jones, M. (2020). Sentinel-1 and sentinel-2 data for savannah land cover mapping: Optimising the combination of sensors and seasons. Remote Sensing 12(23): 1–21.

Breiman, L. (2001). Random forests. (Robert E. Schapire, Ed.)Machine Learning. The Netherlands: Kluwer Academic Publishers.

Cai, Y., Lin, H., and Zhang, M. (2019). Mapping paddy rice by the object-based random forest method using time series Sentinel-1/Sentinel-2 data. Advances in Space Research 64(11): 2233–2244.

Cánovas-García, F., Alonso-Sarría, F., Gomariz-Castillo, F., and Oñate-Valdivieso, F. (2017). Modification of the random forest algorithm to avoid statistical dependence problems when classifying remote sensing imagery. Computers & Geosciences 103: 1–11.

Carrasco, L., O'Neil, A. W., Daniel Morton, R., and Rowland, C. S. (2019). Evaluating combinations of temporally aggregated Sentinel-1, Sentinel-2 and Landsat 8 for land cover mapping with Google Earth Engine. Remote Sensing 11(3).

Chowdhury, M. S. (2024). Comparison of accuracy and reliability of random forest, support vector machine, artificial neural network and maximum likelihood method in land use/ cover classification of urban setting. Environmental Challenges 14(October 2023): 100800.

Clark, M. L. (2017). Comparison of simulated hyperspectral HyspIRI and multispectral Landsat 8 and Sentinel-2 imagery for multi-seasonal, regional land-cover mapping. Remote Sensing of Environment 200: 311–325.

Clerici, N., Valbuena Calderón, C. A., and Posada, J. M. (2017). Fusion of sentinel-1a and sentinel-2A data for land cover mapping: A case study in the lower Magdalena region, Colombia. Journal of Maps 13(2): 718–726.

Colson, D., Petropoulos, G. P., and Ferentinos, K. P. (2018). Exploring the Potential of Sentinels-1 & 2 of the Copernicus Mission in Support of Rapid and Cost-effective Wildfire Assessment. International Journal of Applied Earth Observation and Geoinformation 73: 262–276.

De Alban, J. D. T., Connette, G. M., Oswald, P., and Webb, E. L. (2018). Combined Landsat and L-band SAR data improves land cover classification and change detection in dynamic tropical landscapes. Remote Sensing 10(2).

Dobrinić, D., Medak, D., and Gašparović, M. (2020). Integration of multitemporal sentinel-1 and sentinel-2 imagery for land-cover classification using machine learning methods. In International Archives of the Photogrammetry, Remote Sensing and Spatial Information Sciences - ISPRS Archives (Vol. 43). International Society for Photogrammetry and Remote Sensing.

Gislason, P. O., Benediktsson, J. A., and Sveinsson, J. R. (2006). Random forests for land cover classification. Pattern Recognition Letters 27(4): 294–300.

Gómez, C., White, J. C., and Wulder, M. A. (2016, June 1). Optical remotely sensed time series data for land cover classification: A review. ISPRS Journal of Photogrammetry and Remote Sensing. Elsevier B.V.

Guo, L., Chehata, N., Mallet, C., and Boukir, S. (2011). Relevance of airborne lidar and multispectral image data for urban scene classification using Random Forests. ISPRS Journal of Photogrammetry and Remote Sensing 66(1): 56–66.

Haas, J., and Ban, Y. (2018). Urban Land Cover and Ecosystem Service Changes based on Sentinel-2A MSI and Landsat TM Data. IEEE Journal of Selected Topics in Applied Earth Observations and Remote Sensing 11(2): 485–497.

Haralick, R. M., Shanmugam, K., and Dinstein, I. (1973). Textural Features for Image Classification. IEEE Transactions on Systems, Man, and Cybernetics SMC-3(6): 610–621.

Hdoush, A. A. azeez, Makhamreh, Z., Al-Weshah, R., and Qutishat, D. (2022). Land Suitability Evaluation Esing FAO Approach and Spatial Analysis for Mujib Basin – Jordan. Jordan Journal of Earth and Environmental Sciences 13(3): 158–167.

Heckel, K., Urban, M., Schratz, P., Mahecha, M. D., and Schmullius, C. (2020). Predicting forest cover in distinct ecosystems: The potential of multi-source Sentinel-1 and -2 data fusion. Remote Sensing 12(2).

Hu, B., Xu, Y., Huang, X., Cheng, Q., Ding, Q., Bai, L., and Li, Y. (2021). Improving urban land cover classification with combined use of sentinel-2 and sentinel-1 imagery. ISPRS International Journal of Geo-Information 10(8).

Hussain, S., Mubeen, M., Ahmad, A., Akram, W., Hammad, H. M., Ali, M., Masood, N., Amin, A., Farid, H. U., Sultana, S. R., Fahad, S., Wang, D., and Nasim, W. (2020). Using GIS tools to detect the land use/land cover changes during forty years in Lodhran District of Pakistan. Environmental Science and Pollution Research 27(32): 39676–39692.

Immitzer, M., Vuolo, F., and Atzberger, C. (2016). First experience with Sentinel-2 data for crop and tree species classifications in central Europe. Remote Sensing 8(3).

Inglada, J., Vincent, A., Arias, M., and Marais-Sicre, C. (2016). Improved early crop type identification by joint use of high temporal resolution sar and optical image time series. Remote Sensing 8(5).

Joshi, N., Baumann, M., Ehammer, A., Fensholt, R., Grogan, K., Hostert, P., Jepsen, M. R., Kuemmerle, T., Meyfroidt, P., Mitchard, E. T. A., Reiche, J., Ryan, C. M., and Waske, B. (2016). A review of the application of optical and radar remote sensing data fusion to land use mapping and monitoring. Remote Sensing. MDPI AG.

Kavitha, A. V., Srikrishna, A., and Satyanarayana, C. (2021). A Review on Detection of Land Use and Land Cover from an Optical Remote Sensing Image. IOP Conference Series: Materials Science and Engineering 1074(1): 012002.

Kelley, L. C., Pitcher, L., and Bacon, C. (2018). Using Google Earth Engine to Map Complex Shade-Grown Coffee Landscapes in Northern Nicaragua. Remote Sensing 10(6): 952.

Kussul, N., Lavreniuk, M., Skakun, S., and Shelestov, A. (2017). Deep Learning Classification of Land Cover and Crop Types Using Remote Sensing Data. IEEE Geoscience and Remote Sensing Letters 14(5): 778–782.

Lambin, E. F., Rounsevell, M. D. A., and Geist, H. J. (2000). Are agricultural land-use models able to predict changes in land-use intensity? Agriculture, Ecosystems and Environment 82(1–3): 321–331.

Laurin, G. V., Laurin, G. V., Balling, J., Corona, P., Mattioli, W., Papale, D., and Puletti, N. (2022). Above-ground biomass prediction by Sentinel-1 multitemporal data in central Italy with integration of ALOS2 and Sentinel-2 data. 12(1).

Laurin, G. V., Liesenberg, V., Chen, Q., Guerriero, L., Del Frate, F., Bartolini, A., Coomes, D., Wilebore, B., Lindsell, J., and Valentini, R. (2012). Optical and SAR sensor synergies for forest and land cover mapping in a tropical site in West Africa. International Journal of Applied Earth Observation and Geoinformation 21(1): 7–16.

Liu, Y., Gong, W., Hu, X., and Gong, J. (2018). Forest type identification with random forest using Sentinel-1A, Sentinel-2A, multi-temporal Landsat-8 and DEM data. Remote Sensing 10(6).

Lopes, M., Frison, P. L., Crowson, M., Warren-Thomas, E.,

Hariyadi, B., Kartika, W. D., Agus, F., Hamer, K. C., Stringer, L., Hill, J. K., and Pettorelli, N. (2020, April 1). Improving the accuracy of land cover classification in cloud persistent areas using optical and radar satellite image time series. Methods in Ecology and Evolution. British Ecological Society.

Mahdianpari, M., Salehi, B., Mohammadimanesh, F., and Motagh, M. (2017). Random forest wetland classification using ALOS-2 L-band, RADARSAT-2 C-band, and TerraSAR-X imagery. ISPRS Journal of Photogrammetry and Remote Sensing 130: 13–31.

Majeed, M., Tariq, A., Anwar, M. M., Khan, A. M., Arshad, F., Mumtaz, F., Farhan, M., Zhang, L., Zafar, A., Aziz, M., Abbasi, S., Rahman, G., Hussain, S., Waheed, M., Fatima, K., and Shaukat, S. (2021). Monitoring of land use–Land cover change and potential causal factors of climate change in Jhelum district, Punjab, Pakistan, through GIS and multi-temporal satellite data. Land 10(10).

Maxwell, A. E., Strager, M. P., Warner, T. A., Ramezan, C. A., Morgan, A. N., and Pauley, C. E. (2019). Large-Area, High Spatial Resolution Land Cover Mapping Using Random Forests, GEOBIA, and NAIP Orthophotography: Findings and Recommendations. Remote Sensing 11(12): 1409.

Maxwell, A. E., Warner, T. A., and Fang, F. (2018). Implementation of machine-learning classification in remote sensing: an applied review. International Journal of Remote Sensing 39(9): 2784–2817.

Mendes, F. de S., Baron, D., Gerold, G., Liesenberg, V., and Erasmi, S. (2019). Optical and SAR remote sensing synergism for mapping vegetation types in the endangered Cerrado/Amazon ecotone of Nova Mutum-Mato Grosso. Remote Sensing 11(10).

Mercier, A., Betbeder, J., Rumiano, F., Baudry, J., Gond, V., Blanc, L., Bourgoin, C., Cornu, G., Ciudad, C., Marchamalo, M., Poccard-Chapuis, R., and Hubert-Moy, L. (2019). Evaluation of Sentinel-1 and 2 Time Series for Land Cover Classification of Forest–Agriculture Mosaics in Temperate and Tropical Landscapes. Remote Sensing 11(8): 979.

Millard, K., and Richardson, M. (2015). On the Importance of Training Data Sample Selection in Random Forest Image Classification: A Case Study in Peatland Ecosystem Mapping. Remote Sensing 7(7): 8489–8515.

Mongus, D., and Žalik, B. (2018). Segmentation schema for enhancing land cover identification: A case study using Sentinel 2 data. International Journal of Applied Earth Observation and Geoinformation 66: 56–68.

Nuthammachot, N., and Stratoulias, D. (2019). Fusion of Sentinel-1a and Landsat-8 images for improving land use/land cover classification in Songkla Province, Thailand. Applied Ecology and Environmental Research 17(2): 3123–3135.

Orlíková, L., and Horák, J. (2019). Land cover classification using sentinel-1 SAR data. In ICMT 2019 - 7th International Conference on Military Technologies, Proceedings. Institute of Electrical and Electronics Engineers Inc.

Orynbaikyzy, A., Gessner, U., Mack, B., and Conrad, C. (2020). Crop type classification using fusion of sentinel-1 and sentinel-2 data: Assessing the impact of feature selection, optical data availability, and parcel sizes on the accuracies. Remote Sensing 12(17).

PNDD (2015). AZAD JAMMU & KASHMIR AT A GLANCE. Azad Jammu & Kashmir , Planning & Development Department, Bureau of Statistics .

Poortinga, A., Tenneson, K., Shapiro, A., Nquyen, Q., Aung, K. S., Chishtie, F., and Saah, D. (2019). Mapping plantations in Myanmar by fusing Landsat-8, Sentinel-2 and Sentinel-1 data along with systematic error quantification. Remote Sensing 11(7): 1–19.

Praticò, S., Solano, F., Di Fazio, S., and Modica, G. (2021). Machine Learning Classification of Mediterranean Forest Habitats in Google Earth Engine Based on Seasonal Sentinel-2 Time-Series and Input Image Composition Optimisation. Remote Sensing 13(4): 586.

Rodriguez-Galiano, V. F., Ghimire, B., Rogan, J., Chica-Olmo, M., and Rigol-Sanchez, J. P. (2012). An assessment of the effectiveness of a random forest classifier for land-cover classification. ISPRS Journal of Photogrammetry and Remote Sensing 67(1): 93–104.

Rodriguez-Galiano, Victor F., and Chica-Rivas, M. (2014). Evaluation of different machine learning methods for land cover mapping of a Mediterranean area using multi-seasonal Landsat images and Digital Terrain Models. International Journal of Digital Earth 7(6): 492–509.

Sandberg, M. (2016). Land cover mapping with multi-temporal SAR and optical satellite data. Aalto University.

Shrestha, B., Stephen, H., and Ahmad, S. (2021). Impervious surfaces mapping at city scale by fusion of radar and optical data through a random forest classifier. Remote Sensing 13(15).

Sukawattanavijit, C., Chen, J., and Zhang, H. (2017). GA-SVM Algorithm for Improving Land-Cover Classification Using SAR and Optical Remote Sensing Data. IEEE Geoscience and Remote Sensing Letters 14(3): 284–288.

Sylla, D., Mouissa, H., M-Cakadje-Konan, L., and Hauhouot, C. (2021). An object oriented classification approach for mapping land cover from Landsat and Sentinel image data in the north of Ivory Coast. Jordan Journal of Earth and Environmental Sciences 12(4): 337–343.

Tavares, P. A., Beltrão, N. E. S., Guimarães, U. S., and Teodoro, A. C. (2019). Integration of sentinel-1 and sentinel-2 for classification and LULC mapping in the urban area of Belém, eastern Brazilian Amazon. Sensors (Switzerland) 19(5).

Teluguntla, P., Thenkabail, P. S., Oliphant, A., Xiong, J., Gumma, M. K., Congalton, R. G., Yadav, K., and Huete, A. (2018). A 30-m landsat-derived cropland extent product of Australia and China using random forest machine learning algorithm on Google Earth Engine cloud computing platform. ISPRS Journal of Photogrammetry and Remote Sensing 144: 325–340.

Tufail, R., Ahmad, A., Javed, M. A., and Ahmad, S. R. (2022). A machine learning approach for accurate crop type mapping using combined SAR and optical time series data. Advances in Space Research 69(1): 331–346.

Van Beijma, S., Comber, A., and Lamb, A. (2014). Random forest classification of salt marsh vegetation habitats using quad-polarimetric airborne SAR, elevation and optical RS data. Remote Sensing of Environment 149: 118–129.

Van Tricht, K., Gobin, A., Gilliams, S., and Piccard, I. (2018). Synergistic use of radar sentinel-1 and optical sentinel-2 imagery for crop mapping: A case study for Belgium. Remote Sensing 10(10).

Xia, J., Falco, N., Benediktsson, J. A., Du, P., and Chanussot, J. (2017). Hyperspectral Image Classification With Rotation Random Forest Via KPCA. IEEE Journal of Selected Topics in Applied Earth Observations and Remote Sensing 10(4): 1601–1609.

Zahid Khalil, R., and Saad-ul-Haque (2018). InSAR Coherence-based land cover classification of Okara, Pakistan. Egyptian Journal of Remote Sensing and Space Science 21: S23–S28.

Zakeri, H., Yamazaki, F., and Liu, W. (2017). Texture analysis and land cover classification of tehran using polarimetric synthetic aperture radar imagery. Applied Sciences (Switzerland) 7(5).

Zhang, H., Lin, H., and Li, Y. (2015). Impacts of feature normalization on optical and SAR data fusion for land use/land cover classification. IEEE Geoscience and Remote Sensing Letters 12(5): 1061–1065.

Zhang, H., Wang, T., Liu, M., Jia, M., Lin, H., Chu, L. M., and Devlin, A. T. (2018). Potential of combining optical and dual polarimetric SAR data for improving mangrove species discrimination Using Rotation Forest. Remote Sensing 10(3).

Zhang, R., Tang, X., You, S., Duan, K., Xiang, H., and Luo, H.

(2020). A novel feature-level fusion framework using optical and SAR remote sensing images for land use/land cover (LULC) classification in cloudy mountainous area. Applied Sciences (Switzerland) 10(8).

Zhou, T., Zhao, M., Sun, C., and Pan, J. (2018). Exploring the impact of seasonality on urban land-cover mapping using multi-Season Sentinel-1A and GF-1 WFV images in a subtropical monsoon-climate region. ISPRS International Journal of Geo-Information 7(1).

Zhu, Z., Woodcock, C. E., Rogan, J., and Kellndorfer, J. (2012). Assessment of spectral, polarimetric, temporal, and spatial dimensions for urban and peri-urban land cover classification using Landsat and SAR data. Remote Sensing of Environment 117: 72–82.

JJEES

JJEES (2025) 16 (2): 186-194
ISSN 1995-6681

Jordan Journal of Earth and Environmental Sciences

Effect of Bushfire on Soil Physicochemical Properties in Rubber (*Hevea brasiliensis*) Plantations of Tropical Nigeria

Paul Orobosa Orobator *

Department of Geography and Regional Planning, Faculty of Social Sciences, University of Benin, Benin City, Edo State, Nigeria

Received on December 5, 2023, Accepted on January 12, 2025

Abstract

The study examined the effect of bushfire on soil physicochemical properties in rubber (Hevea brasiliensis) plantations of tropical Nigeria. The objectives of the study were to: (i) determine the concentration levels of the physicochemical properties of soil in the burnt and unburnt *H. brasiliensis* plantations, and (ii) evaluate the differences in the soil quality properties of soil in the burnt and unburnt *H. brasiliensis* plantations. Forty composite soil samples were collected from both *H. brasiliensis* plantations at 0-15cm and 15-30cm soil depths. Soil physicochemical properties were analyzed using standard laboratory procedures. At the same time, data obtained were statistically examined using both descriptive (range, mean, standard deviation, and coefficient of variation) and inferential (student t-test) statistics. The results revealed that compared to the unburnt *H. brasiliensis* plantation; soil pH, effective exchange cation capacity, soil organic matter, total organic carbon, total nitrogen, phosphorus, potassium, copper, and manganese had higher values in the burnt *H. brasiliensis* plantation, whereas, the values of calcium, sodium, magnesium, iron and zinc were lower. Significant differences ($p < 0.05$) in clay, phosphorus, iron, zinc, and calcium were detected. The study concluded that bushfire has a positive impact on soil pH, effective exchange cation capacity, soil organic matter, total organic carbon, total nitrogen, phosphorus, potassium, copper, and manganese, while the effect on calcium, sodium, magnesium, iron, and zinc was negative.

Keywords: *Fire, Impacts, Physicochemical properties, Rubber tree, Soil quality*

1. Introduction

Fires are a significant cause of disruption in a number of different environments (Bowman et al., 2009 cited in Hamad et al., 2013). Presently, bushfires are extensive ecological incidences, affecting over 100 million hectares of forest biomes, which suffer their detrimental effects (Blinkova et al., 2025). Bushfire is a major ecological phenomenon in most tropical agricultures. Rubber (Hevea brasiliensis) plantation evolutions are both environmentally and economically consequential at global, national, and local scales. Globally, whereas previous research (Al−Khayri & Khan, 2024; Kukavskaya et al., 2024; Samburova et al., 2023; Amoako & Gambiza, 2022; Xifré-Salvadó et al., 2021; Chungu et al., 2020; Alcañiz et al., 2018; Keesstra et al., 2017; Muñoz-Rojas et al., 2016; Muqaddas et al., 2015; Xue et al., 2014; Nabatte & Nyombi, 2013; Aref et al., 2011; Kara and Bolat, 2009; Ekinci, 2006; Certini, 2005; etc.) had examined and documented findings of the effect of fire on soil properties in varied flora ecosystems. Empirical data on bushfire impacts on the physicochemical properties of soil in *H. brasiliensis* plantations are unavailable.

In tropical Nigeria, prior in-depth studies (Itohanmwen & Umweni, 2024; Orobator & Odjugo, 2024; Orobator and Odjugo, 2023; Orobator, 2022; Orobator et al., 2020; Umar et al., 2012; Umar et al., 2010; Orimoloye et al., 2012; Ugwa et al., 2005; Esekhade & Ugwa, 2008; Aweto, 1987; Onuwaje &Uzu, 1982; etc.) have been undertaken in *H. brasiliensis* plantations. However, these investigations did not also examine the impacts of bushfires on soil physicochemical properties in *H. brasiliensis* plantations. Soil is a significant resource for life that offers a diversity of goods and services to meet the needs of humans on earth (Anache et al., 2017 cited in Attah et al., 2022). Soil physicochemical properties (sand, silt, clay, bulk density, water repellency, pH, effective cation exchange capacity, soil organic matter, organic carbon, nitrogen, phosphorus, calcium, sodium, magnesium, potassium, iron, copper, manganese, zinc, etc.) are significant quantifiable soil quality indicators that impact the capability of soils to sustain crop production (Orobator, 2019). Nevertheless, these soil quality parameters can be influenced by fire (Xifré-Salvadó et al., 2021; García-Redondo et al., 2024; Blinkova et al., 2025). Every year, bushfire incidences are widespread in most parts of Nigeria particularly during the dry season (Orobator and Odjugo, 2023). Esekhade et al., (2005) stated that the impact of bushfires on *H. brasiliensis* plantations should not be underestimated because of its ecological significance. Consequently, Certini (2005) reported that inquiries on bushfire's effect on soil quality properties demand exigent and unbroken responsiveness from environmental researchers. Recently, Garrido-Ruiz et al., (2022) recommended that more empirical studies be carried out to reveal the impact of bushfire on soil properties in agricultural land uses.

The incidence of no existing experiential evidence on the effect of bushfire on soil physicochemical properties in *H. brasiliensis* plantations makes it challenging to understand and predict bushfire effects on soil physicochemical

* Corresponding author e-mail: orobosa.orobator@uniben.edu

properties in *H. brasiliensis* plantations. This drawback further limits the development of sustainable approaches that are aimed at managing and conserving soils affected by bushfires in *H. brasiliensis* plantations. Therefore, the need to investigate the bushfire impact on the physicochemical properties of soils in *H. brasiliensis* plantations is currently compelling and essential. To fill this research gap, this study aimed to investigate through an empirical assessment, the effect of bushfire on soil physicochemical properties in *H. brasiliensis* plantations of tropical Nigeria. The objectives of the research were to: (i) determine the level of concentrations of the physicochemical properties of soil in the burnt and unburnt *H. brasiliensis* plantations, and (ii) examine the differences in the soil quality properties between the burnt and unburnt *H. brasiliensis* plantations. The positive and negative impacts of bushfire on soil physicochemical properties, revealed by this research, will offer contemporary data that will support the task of biogeographers, soil geographers, soil scientists, fire ecologists, and tree plantation managers toward evolving strategies for the sustainable management of soil quality in burnt *H. brasiliensis* plantations.

2. Material and methods

2.1. Study area

The study was carried out in Rubber Research Institute of Nigeria (RRIN), Iyanomo, Ikpoba Okha Local Government Area, Edo State, Nigeria. RRIN lies within latitudes 60 08' 54.99'' – 60 10' 0.48''N and longitudes 50 34' 9.12'' – 50 36' 44.64''E respectively (Figure 1). The total land area is 2,078 hectares, out of which 496 hectares is occupied with matured *H. brasiliensis* trees. 109 hectares is cultivated with young *H. brasiliensis* plantations, while the nursery beds occupy 4.2 hectares (Umar et al., 2012). Whereas the soils are typically the ferrallitic soil type (Areola, 1991), the climate is tropical rainforest. The rainfall pattern is bimodal, characterized by an extended rainy season that begins in early March with short rainy period stretching from September to late October (Ugwa et al., 2005). RRIN is bordered by Obagie, Uhie, Iyanomo, Obaretin, Obayantor I, and Ogbekpen communities respectively (Fig.1). The locals of these communities are mostly farmers whose farms are adjacent to the *H. brasiliensis* plantations in RRIN.

2.2. Fieldwork

After a detailed reconnaissance survey, two *H. brasiliensis* plantations (unburnt and burnt) adjacent to each other with similar ecological characteristics (soil type, climate, topography, and age) and situated in the premises of RRIN were identified and adopted for the investigation. Information from the staff of RRIN indicated that the fire that affected the burnt *H. brasiliensis* plantation was anthropogenically triggered. Soil samples were collected from the unburnt (control plot) and burnt *H. brasiliensis* plantations (treatment site) from two sampling points randomly selected from 10 plots of 20 × 20m at prearranged soil depths of 0 – 15cm and 15 – 30cm. Initial 40 soil samples were augured from each of the burnt and unburnt *H. brasiliensis* plantations, making a total of 80 soil samples. In making a composite soil sample, 2 composite soil samples emerged from the 20 plots of 20 × 20m, making 40 soil samples. A total of 40 composite soil samples were collected, air-dried, crushed, and thoroughly mixed and sieved through a 2 mm mesh and analyzed for soil physicochemical properties.

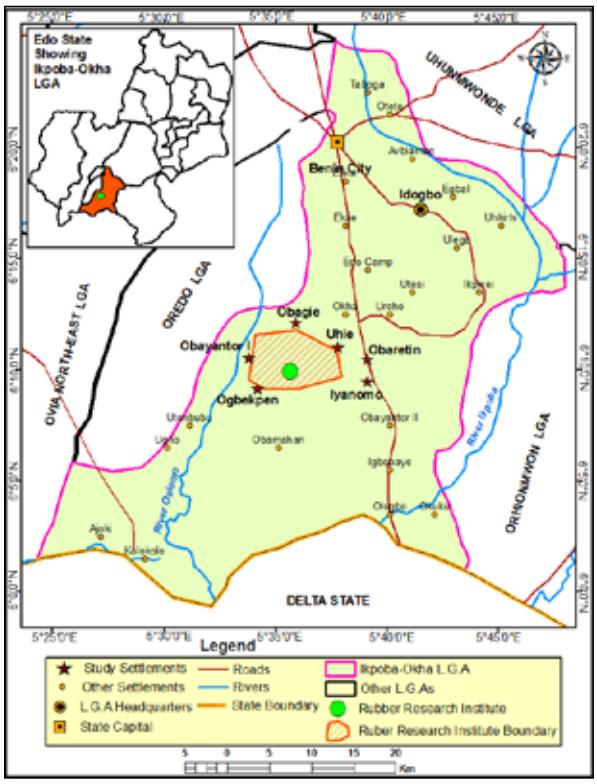

Figure 1. Location of Rubber Research Institute of Nigeria (RRIN), Iyanomo, Edo State, Nigeria

2.3. Laboratory analyses

Soil texture was analyzed by hydrometer method (Gee and Or, 2002; Khudhur et al., 2018). Bulk density was determined by the core method (Nnaemeka et al., 2013). Soil water repellency (SWR) was analyzed with the classical Water Drop Penetration Time (WDPT) (Wietinga et al., 2017). Soil pH was determined electrometrically in 1:2.5 soil/water ratios (Hendershot et al., 1993) and organic carbon was determined using the method defined by Nelson and Sommers (1996). Total nitrogen was analyzed using modified micro Kjeldahl method (Bremner and Milvaney, 1982). Soil organic matter content (SOM) was measured by the potassium dichromate oxidation method (Nelson and Sommers, 1996). The Bray II method was used to determine total available phosphorus (Olsen and Sommers, 1982). Extract for available P was prepared with ammonium fluoride and P obtained by means of molybdenum blue method (Murphy and Riley, 1962). For estimation of exchangeable Ca, Mg, K and Na, soil samples was first percolated with 1N ammonium acetate solution (pH = 7.0). The atomic absorption spectrophotometer was adopted to analyze for exchangeable Ca and Mg whereas the digital flame photometry was used to estimate exchangeable Na and K (Onyekwelu et al., 2008). Effective cation exchange capacity was determined by saturating 10g of soil with normal natural ammonium acetate solution, washing out the excess ammonium with methanol and afterward distillation of the absorbed ammonium into boric solution. The distillate will titrate alongside standard hydrochloric acid (Nnaemeka

et al., 2013). The amount of potassium in the samples was analyzed using the flame photometer (Adekunle, 2011). Manganese, copper, iron and zinc were determined by the atomic absorption spectrophotometry method (Tan et al., 2012).

2.4. Data analysis

Descriptive statistics (range, mean, standard deviation and coefficient of variation) was used to analyze the data. Descriptive statistics aided the soil physicochemical properties' concentration values to be presented in a meaningful and comprehensible way, which in turn, permitted for a simplified explanation of the data set. Comparative analysis was also performed using the student's t-test to determine statistically significant differences. The student's t-test compared the means of each soil quality property (Al-Achi, 2019). This was done between the unburnt and burnt *H. brasiliensis* plantations. Levels of significance are described as non-significant ($p > 0.05$) and significant ($p < 0.05$) respectively. The statistical techniques were adapted to achieve the objectives of the study specifically. IBM Statistical Package for Social sciences (SPSS) 20.0 and Microsoft Excel version 2010 were used for the statistical analyses.

3. Results

3.1. Sand, Silt, Clay, BD, and SWR

Soil physical and chemical properties of unburnt and burnt *H. brasiliensis* plantations are indicated in Table 1 and Table 2. Sand showed higher concentration levels in the topsoil of the unburnt *H. brasiliensis* plantation (742 gkg^{-1}) compared to the burnt *H. brasiliensis* plantation (730 gkg^{-1}), and no statistically significant differences were detected between both *H. brasiliensis* plantations ($p > 0.05$). Compared to the burnt *H. brasiliensis* plantation (189 gkg^{-1}), a higher concentration level of silt was observed in the topsoil of the unburnt *H. brasiliensis* plantation (205 gkg^{-1}). A non-significant difference was observed ($p > 0.05$). The concentration level of clay in the unburnt *H. brasiliensis* plantation at the topsoil (58 Mg m^{-3}) was lower than the burnt *H. brasiliensis* plantation (81 Mg m^{-3}). Significant difference was observed in clay contents ($p < 0.05$) in the subsoil.

Table 1. Soil physical properties of unburnt and burnt *H. brasiliensis* plantations

Soil parameter	Depth (cm)	Unburnt *H. brasiliensis* plantation				Burnt *H. brasiliensis* plantation				*p*-value
		Range	Mean	Std.	CV (%)	Range	Mean	Std.	CV (%)	
Sand (gkg^{-1})	0 - 15 15 - 45	680 - 800 520 – 660	742 589	43.60 49.00	5.88 8.32	580 - 880 510 - 710	730 620	77.10 68.10	10.56 10.98	0.32 0.08
Silt (gkg^{-1})	0 - 15 15 - 45	140 - 290 180 – 280	205 239	53.10 33.10	25.90 13.84	100 - 250 190 - 320	189 244	44.30 51.80	23.44 21.23	0.23 0.38
Clay (gkg^{-1})	0 - 15 15 - 45	20 - 100 120 – 220	58 172	27.80 29.70	47.93 17.27	20 - 170 50 - 200	81 136	52.10 49.20	64.32 35.39	0.13 0.01*
BD ($Mg\ m^{-3}$)	0 - 15 15 - 45	0.23 - 1.94 0.63 - 1.94	1.04 1.26	0.58 0.51	55.76 40.47	0.57 - 1.73 0.69 - 1.92	1.12 1.20	0.36 0.42	32.14 35.00	0.38 0.35
SWR	0 - 15 15 - 45	15.11 - 20.67 15.97 - 23.6	18.00 19.07	2.18 2.36	12.11 12.38	12.87 - 19.91 15.78 - 23.30	17.07 20.04	2.51 2.25	14.70 11.23	0.20 0.16

Note: BD = Bulk density, SWR =Soil water repellency
* Statistically significant differences at $p < 0.05$.

Higher mean value of SWR was detected in the unburnt *H. brasiliensis* plantation (18.00) than the burnt *H. brasiliensis* plantation (17.07) at the topsoil, nevertheless, no statistically significant differences were found.

3.2.Soil pH, ECEC SOM, TOC, TN and P

Soil pH indicated lower values in the topsoil (4.75) and subsoil (4.51) of the unburnt *H. brasiliensis* plantation than the topsoil (4.82) and subsoil of the burnt *H. brasiliensis* plantation (4.57), however, no statistically significant differences were detected between both *H. brasiliensis* plantations ($p > 0.05$). ECEC concentration levels were lower in the topsoil (1.07 cmol kg^{-1}) and subsoil (151 cmol kg^{-1}) of the unburnt *H. brasiliensis* plantation than the topsoil (1.42 cmol kg^{-1}) and subsoil of the burnt *H. brasiliensis* plantation (166 cmol kg^{-1}). Nonetheless, no statistically significant differences were detected between both *H. brasiliensis* plantations ($p > 0.05$).

A higher concentration level of SOM was detected in the burnt *H. brasiliensis* plantation (1.74 g kg^{-1}) than in the unburnt *H. brasiliensis* plantation (1.47 g kg^{-1}) at the topsoil. However, no significant difference ($p > 0.05$) was observed. TOC did not indicate significant differences ($p > 0.05$). TOC showed higher concentration levels in the burnt *H. brasiliensis* plantation (1.00 gkg^{-1}) than in the unburnt *H. brasiliensis* plantation (0.94 gkg^{-1}) at the topsoil. TN indicated a higher concentration level in the burnt plantation (0.13 gkg^{-1}) than the unburnt *H. brasiliensis* plantation (0.12 gkg^{-1}) at the topsoil, but no statistically significant differences were detected between the unburnt and burnt *H. brasiliensis* plantations ($p > 0.05$). A higher concentration level of P was detected in the burnt *H. brasiliensis* plantation (6.52 gkg^{-1}) of the topsoil than in the unburnt *H. brasiliensis* plantation (4.41 gkg^{-1}), and did reveal significant differences ($p < 0.05$) in the topsoil.

3.3. Ca, Na, Mg and K

Ca indicated lower concentration levels in the topsoil (13.40 cmol kg^{-1}) and subsoil (8.44 cmol kg^{-1}) of the burnt *H. brasiliensis* plantation than in topsoil (18.71 cmol kg^{-1}) and subsoil (13.40 cmol kg^{-1}) of the unburnt *H. brasiliensis* plantation. Ca showed no statistically significant differences in the topsoil of the unburnt and burnt *H. brasiliensis* plantations but did so in the subsoil ($p < 0.05$). Lower concentration levels of Na were detected in the topsoil (74.55 cmol kg^{-1}) and subsoil (48.48 cmol kg^{-1}) of the burnt *H. brasiliensis* plantation than in topsoil (94.40 cmol kg^{-1})

and subsoil (63.99 cmol kg^{-1}) of the unburnt *H. brasiliensis* plantation. Na indicated no statistically significant differences ($p > 0.05$). Mg concentration levels were lower in the topsoil (41.88 cmol kg^{-1}) and subsoil (27.23 cmol kg^{-1}) of the burnt *H. brasiliensis* plantation than in topsoil (53.03 cmol kg^{-1}) and subsoil (35.95 cmol kg^{-1}) of the unburnt *H. brasiliensis* plantation. Mg showed no statistically significant differences ($p > 0.05$). K indicated higher level in the burnt *H. brasiliensis* plantation (37.91 cmol kg^{-1}) than the unburnt *H. brasiliensis* plantation (33.82 cmol kg^{-1}) at the topsoil, but no statistically significant ($p > 0.05$) differences were detected between the unburnt and burnt *H. brasiliensis* plantations.

Table 2. Soil chemical properties of unburnt and burnt *H. brasiliensis* plantations

Soil parameter	Depth (cm)	Unburnt *H. brasiliensis* plantation				Burnt H. *brasiliensis* plantation				*p*-value
		Range	Mean	Std.	CV (%)	Range	Mean	Std.	CV (%)	
pH	0 - 15 15 - 45	4.16 - 5.43 4.06 - 5.17	4.75 4.51	0.50 0.38	10.52 8.42	4.32 - 5.36 3.89 - 5.11	4.82 4.57	0.34 0.37	7.05 8.09	0.36 0.35
ECEC (cmol kg^{-1})	0 - 15 15 - 45	0.31 - 2.59 0.57 - 3.28	1.01 1.57	0.75 0.94	74.25 59.87	0.31 - 2.59 0.92 - 3.25	1.42 1.66	0.54 0.71	38.02 42.77	0.12 0.41
SOM (g kg^{-1})	0 - 15 15 - 45	0.15 - 2.50 0.24 - 1.19	1.47 0.74	0.73 0.33	49.65 44.59	0.40 - 3.00 0.19 - 1.28	1.74 0.72	0.78 0.39	44.82 54.16	0.22 0.43
TOC (g kg^{-1})	0 - 15 15 - 45	0.64 - 1.45 0.14 - 0.69	0.94 0.43	0.31 0.19	32.97 44.18	0.23 - 1.74 0.11 - 0.74	1.00 0.41	0.45 0.22	45.00 53.65	0.35 0.43
TN (g kg^{-1})	0 - 15 15 - 45	0.07 - 0.18 0.02 - 0.09	0.12 0.05	0.04 0.02	33.33 40.00	0.04 - 0.21 0.01 - 0.12	0.13 0.05	0.06 0.03	46.15 60.00	0.27 0.41
P (mg kg^{-1})	0 - 15 15 - 45	1.43 - 8.36 0.7 - 7.16	4.41 3.24	2.43 1.94	55.10 59.87	2.42 - 10.64 1.75 - 7.28	6.52 3.66	2.70 2.10	41.41 57.37	0.04* 0.31
Ca (cmol kg^{-1})	0 - 15 15 - 45	5.76 - 43.78 7.67 - 33.66	18.71 13.40	10.52 7.51	56.22 56.04	6.78 - 32.14 4.48 - 15.86	15.90 8.44	7.51 3.32	47.23 39.33	0.27 0.04*
Na (cmol kg^{-1})	0 - 15 15 - 45	23.29 - 195.83 32.82 - 132.59	94.40 63.99	52.40 32.48	55.50 50.75	30.33 - 129.97 25.38 - 118.94	74.55 48.48	32.68 27.25	43.83 56.20	0.21 0.15
Mg (cmol kg^{-1})	0 - 15 15 - 45	13.08 - 110.02 18.44 - 74.49	53.03 35.95	29.44 18.25	55.51 50.76	17.04 - 73.02 14.26 - 66.82	41.88 27.23	18.36 15.31	43.83 56.22	0.81 0.15
K (cmol kg^{-1})	0 - 15 15 - 45	14.64 - 75.20 7.88 - 55.91	33.82 22.46	18.37 14.88	54.31 66.25	7.70 - 96.18 4.64 - 29.47	37.91 16.03	29.96 7.70	79.02 48.03	0.38 0.13
Fe (mg kg^{-1})	0 - 15 15 - 45	84.18 - 658.3 51.92 - 413.02	312.24 194.47	175.88 109.74	56.32 56.43	97.50 - 219.50 76.52 - 358.59	173.08 149.10	41.10 83.49	23.74 55.99	0.02* 0.17
Cu (mg kg^{-1})	0 - 15 15 - 45	6.29 - 32.34 3.39 - 24.04	14.54 9.65	7.90 6.40	54.33 66.32	3.31 - 41.36 2.0 - 12.67	16.30 6.89	12.88 3.31	79.01 48.04	0.38 0.13
Mn (mg kg^{-1})	0 - 15 15 - 45	1.95-10.02 1.05-7.45	4.50 2.99	2.44 1.98	54.22 66.22	1.03 - 12.82 0.62 - 3.93	5.05 2.13	3.99 1.02	79.00 47.88	0.36 0.13
Zn (mg kg^{-1})	0 - 15 15 - 45	1.68 - 13.17 1.04 - 8.26	6.24 3.88	3.51 2.19	56.25 56.44	0.20 - 4.39 1.53 - 7.17	2.89 3.48	1.41 1.69	48.78 48.56	0.01* 0.33

3.4. Fe, Cu, Mn and Zn

The concentration levels of Fe in the unburnt *H. brasiliensis* plantation at the topsoil (312.24 mgkg^{-1}) and subsoil (194.47 mgkg^{-1}) were higher than in the burnt *H. brasiliensis* plantation at the topsoil (173.08 mgkg^{-1}) and subsoil (149.10 mg kg^{-1}). In addition, a statistically significant difference was observed at the topsoil ($p < 0.05$). Cu did not indicate significant differences ($p > 0.05$) in the unburnt and burnt *H. brasiliensis* plantations, but a higher concentration value was observed in the topsoil (16.30 mg kg^{-1}) of the burnt *H. brasiliensis* plantation than in the subsoil (14.54 mg kg^{-1}) of the unburnt *H. brasiliensis* plantation. Lower concentration level of Mn was found in the topsoil (4.50 mgkg^{-1}) of the unburnt *H. brasiliensis* plantation than in the topsoil (5.05 mgkg^{-1}) of the burnt *H. brasiliensis* plantation, and no statistically significant difference ($p > 0.05$) was observed. However, a higher concentration level of Zn was observed in the topsoil (6.24 mg kg^{-1}) of the unburnt *H. brasiliensis* plantation than in the topsoil (2.89mg kg^{-1}) of the burnt *H. brasiliensis* plantation, and a statistically significant difference was observed ($p < 0.05$).

4. Discussion

4.1. Sand, Silt, Clay, BD and SWR

The lower sand values observed in the burnt *H. brasiliensis* plantation suggested the negative impact of bushfire on sand in this biome. This lower value maybe the resultant effect of the decomposition of kaolinized sand grains (Ulery and Graham, 1993). The non-significant difference may account for the similar low variability (< 15 %) of the sand content. This result contrasts with the findings of Edem et al., (2013), who reported a significantly higher mean value of 838.50 gkg^{-1} in the burnt plantation than the unburnt site (772.60 gkg^{-1}). Heydari et al., (2017) reported that this may be the outcome of oxides and hydroxides of Al and Si, created by kaolin obliteration that can prompt fortification of particles, development of aggregates in sand magnitude, and increase in coarse particles proportion due to fire. Alcañiz et al., (2018) also observed an increase in sand content and noted that it may be due to the formation of unstable soil aggregates. Lower silt content in the topsoil of the burnt *H. brasiliensis* plantation than the unburnt *H. brasiliensis* plantation revealed a negative impact of bushfire

on silt. Although the findings disagreed with Aref et al., (2011), who reported that fire did not affect silt contents, it is congruent with the non-significant difference that was observed in the study. The higher clay content in the topsoil of the burnt *H. brasiliensis* plantation inferred more bushfire-positive effects on clay. This may be due to the aggregation of clay particles, caused by heating from bushfire (da Silva and Batalha, 2008). The result of the research is similar to the outcomes of Pierson et al., (2008) who reported that clay fractions increased after fire.

The higher BD value in the topsoil of the burnt *H. brasiliensis* plantation implied that bushfire influenced BD positively. This may be accredited to the breakdown of soil masses and clogging of pores by ash and clay minerals (Certini, 2005). The presence of voids in the soil horizon may also account for high BD in the burnt soils (Heydari et al., 2017). Similarly, in a Pinus massoniana forest, Xue et al., (2014) reported that compared to unburnt soils, an increase in BD was observed in the burnt plantation. Unlike the unburnt *H. brasiliensis* plantation, the lower BD content in the subsoil of the burnt plantation may be attributed to soil vapor expansion (Alcañiz et al., 2018). The higher soil water repellency (SWR) value in the subsoil of burnt *H. brasiliensis* plantation is indicative of a downward heat gradient (Glenn and Finley, 2009). Dissimilar from the topsoil of the *H. brasiliensis* burnt plantation, the higher SWR value in the unburnt *H. brasiliensis* plantation suggested the effect of climatic conditions, foliage and organic strata is ordinarily made up of hydrophobic substances (Alcañiz et al., 2018). Correspondingly, in in a Pinus halepensis forest, Keesstra et al., (2017) reported higher SWR on the topsoil of unburnt plantations.

4.2. Soil pH, ECEC SOM, TOC, TN and P

The higher pH mean value in the burnt *H. brasiliensis* plantation at the topsoil and subsoil inferred that the burnt *H. brasiliensis* plantation is less acidic than the unburnt *H. brasiliensis* plantation. This showed the positive effects of bushfires on soil pH. The lixiviation of alkaline metals from the ash into the soil system and the depletion of hydrogen ions may account for it (Xue et al., 2014). After the incidence of a fire, it is typical for soil pH to experience an increase, primarily owing to the contribution of ashes that offer oxides, carbonates, and basic cations occasioned by the burning of organic matter (Gonzales et al., 2024). The acidic state of the unburnt *H. brasiliensis* plantation may be due to the materialization of new humus and the leaching of bases (Garrido-Ruiz et al., 2022). Similarly, in Zagros oak (Quercus brantii Lindl.) forests, Heydari et al., (2017) noted that pH values were higher in burnt plantations. The detected non-significant difference of pH between the unburnt and burnt *H. brasiliensis* plantations at both soil depths ($p > 0.05$) may be due to the similarity of the pH values. The general high acidic status of the soils can be ascribed to incidences of high rainfall, resulting to the leaching of soil nutrients (Iwara et al., 2011). The oxidation of charred materials may be responsible for the higher ECEC contents in the burnt *H. brasiliensis* plantation at both the topsoil and subsoil.This result indicates the positive impact of bushfire on ECEC. The released soluble inorganic ions during burning of SOM may also be accredited for the higher ECEC concentration values in the burnt site (Granged et al., 2011). The results are similar to those reached by Edem et al., (2013) and Tabi et al., (2013), who reported that the ECEC contents increased in the soils of burnt plantation.

Soil organic matter (SOM) serves as a potent aggregating agent, holding sand, silt, and clay fractions into aggregates (Farid et al., 2024). The higher SOM content in the burnt *H. brasiliensis* plantation implies that bushfire influenced SOM positively. This may be ascribed to the effects of the prevalence of charred materials on the burnt soil (Xifré-Salvadó et al., 2021). This result agreed with Fonseca et al., (2017), who reported that SOM contents were more in burnt plantation than the unburnt plot. Similarly, in a tropical dry forest, Kennard and Gholz (2001) reported a higher concentration of SOM in burnt soils. The integration of unburnt or partly burnt slash fragments into the soil could be accountable for it (Alcañiz et al., 2018). The detected non-significant difference suggested that bushfire did not significantly enhance the SOM concentrations of soils in the burnt *H. brasiliensis* plantation than the unburnt *H. brasiliensis* plantation.

The higher TOC concentration levels in the burnt *H. brasiliensis* plantation at the topsoil revealed bushfire-positive impacts on TOC. This may be attributed to outward feedback of burnt material and ash. The burnt debris returns to the soil as constituents lesser than 2 mm in the form of ash, which is bulked in the top layer, and this instigates an increase in TOC concentrations (Novara et al., 2013). The total aggregate of TOC is a portion of stored SOM (Orobator, 2014). Besides, TOC in soils largely aids in providing energy for soil and microorganisms which help to decompose organic material (Bridges, 1978). Generally, Caon et al., (2014) stated that TOC increases were connected to the formation of charcoal, fusion of ash into the soil, decomposition of partly burnt woody fragments and flora recovery. The findings of the current study aligned with Ferran et al., (2005), who observed higher TOC contents in the burnt soil than in the unburnt soil. In contrast, Kutiel and Naveh (1987) reported that TOC content of the A horizon (0–5 cm) was significantly lower in the burnt sites than the unburnt sites in a mixed oak and pine forest. Fire can cause a significant decline in TOC concentration due to mineralization of C from the soil organic matter (Caon et al., (2014). The insignificant differences in TOC inferred that bushfire did not significantly affect the TOC of soils in the burnt *H. brasiliensis* plantation compared to the unburnt *H. brasiliensis* plantation.

The higher TN content in the topsoil of burnt *H. brasiliensis* plantation inferred bushfire-positive impacts on TN. In burnt plantations, increases in TN concentration are observed largely due to the accumulation of ash (Mataix-Solera and Guerrero, 2007). In addition, owing to fire incidence, Ferran et al., (2005) reported that TN in the soil horizons increased due to the increase in potentially mineralizable N concentrations. This result of the investigation contrasted the findings of Muqaddas et al., (2015) and Emeterio et al., (2016). Nevertheless, the results

of the current study aligned with the outcomes of Kutiel and Naveh (1987). Mataix-Solera and Guerrero (2007) reported that TN concentrations diminished due to its absorption through the germination of herbaceous plants. The observed insignificant differences in TN inferred that bushfire did not considerably influence the TN of soils in the burnt *H. brasiliensis* plantation when matched with the unburnt *H. brasiliensis* plantation.

Higher levels of P, detected in both the topsoil and subsoil of the burnt *H. brasiliensis* plantation deduced bushfire positive impacts on P. Bushfire, leads to the enrichment of available P in the soils (Aref et al., 2011), and the deposition of ash after burning helps to fertilize the soil by direct discharge of P (Edem et al., 2013). Besides, the rapid transformation of instantly available P to mineral P and insoluble P forms such as apatite was accountable for the increase of available P in the burnt soil (Pardini et al., 2004). The result of the study agreed with Heydari et al., (2017), who stated that P values were higher in burnt soils. However, the findings contradicted Edem et al., (2013), who reported that that P contents were lower in burnt plantations. These contradictory outcomes of prior studies implied the different ways varied biomes due to their peculiar ecosystem properties respond to fire effects. The significant differences of P deduced that bushfire did significantly impact P contents in the burnt *H. brasiliensis* plantation, compared to the unburnt *H. brasiliensis* plantation. Similarly, in soils of the semi-arid Ebro Valley of northeastern Spain, Badía and Martí (2003) observed a significant increase in P due to fire; implying also a significant positive effect.

4.3. Ca, Na, Mg and K

The lower concentration levels of Ca in the topsoil of the burnt *H. brasiliensis* plantation indicated the negative impact of bushfire on Ca. This may be due to higher thresholds of vaporization and subsequent volatilization (Zhang and Biswas, 2017). Statistically significant differences, detected between the unburnt and the burnt *H. brasiliensis* plantations at the subsoil, deduced that bushfire did substantially improve the Ca. The lower value of Na, detected in the burnt *H. brasiliensis* plantation, inferred that bushfire has a negative influence on Na in *H. brasiliensis* plantations. The lower concentrations of Na in the burnt *H. brasiliensis* plantation may be due to flora uptake during post-fire succession (Caon et al., 2014). However, the insignificant differences in Na suggested that the influence of bushfire on Na in the burnt *H. brasiliensis* plantation was not substantial compared to the unburnt *H. brasiliensis* plantation. The lower Mg contents in the topsoil and subsoil of the burnt *H. brasiliensis* plantation implied the negative effect of bushfire on Mg. This agreed with the findings of Chungu et al., (2020), who found that Mg contents decreased due to fire in a Eucalyptus grandis forest. Nonetheless, the insignificant differences in Mg observed for this study implied that the influence of bushfire on Mg was not considerable. Higher contents of K observed in the topsoil of the burnt *H. brasiliensis* plantation deduced that bushfire positively impacted K. This incidence may be due to the effect of burnt wood and ash on the soils (Pereira et al., 2019). Wood ash contains more K (Nottidge and Nottidge, 2012). The findings of the current study agreed with Thomaz et al., (2014) and Ying et al. (2018). Similarly, Scharenbroch et al. (2012) reported higher K values in burnt Oak (Quercus) forest. Statistically detected significant differences deduced that bushfire did substantially improved K in the burnt *H. brasiliensis* plantations.

4.4. Fe, Cu, Mn and Zn.

The higher concentration level of Fe in the unburnt *H. brasiliensis* plantation at both the topsoil and subsoil suggested that bushfire has a detrimental effect on Fe. Similarly, the results of Norouzi and Ramezanpour (2013) revealed that concentrations of Fe were lower in the burnt soil. The significant difference suggested that the observed negative effect of bushfires on Fe was substantial. The higher Cu content in the topsoil of the burnt *H. brasiliensis* plantation inferred the positive effect of bushfire on Cu. This may be due to observed higher levels of SOM in the burnt *H. brasiliensis* plantation. Cu is primarily found to attach to SOM fraction in the soil which is the most vital soil parameter defining Cu bioavailability (Oku et al., 2012). However, the insignificant difference inferred that the observed bushfire impact on Cu was not remarkable. The higher Mn, the higher value observed in the topsoil of the burnt *H. brasiliensis* plantation implied the positive impact of bushfire on Mn. This may be due to a build-up of ash in the form of amorphous and crystal-like oxides (Certini, 2005). However, the insignificant difference inferred that the observed bushfire impact on Mn was not significant. The detected lower Zn concentration in the burnt *H. brasiliensis* plantation revealed the damaging influence of bushfire on Zn in this biota. This may be due to the effect of erosion and leaching in sandy soils of the burnt *H. brasiliensis* plantation especially during the rainy seasons. Sandy soils are highly erodible during heavy rains once the vegetative cover has been reduced by burning (Ladrach, 2009). The significant difference suggested that the observed detrimental influence of bushfires on Zn was substantial.

5. Conclusion

The comprehensive study has generated valuable insights into the impacts of bushfires on the physicochemical properties of soils in tropical *H. brasiliensis* plantations. The results indicated that compared to the unburnt *H. brasiliensis* plantation; the level of concentrations of pH, ECEC, SOM, TOC, TN, P, K, Cu, and Mn were higher in the burnt *H. brasiliensis* plantation, whereas Ca, Na, Mg, Fe and Zn were lower. Significant differences ($p < 0.05$) in clay, P, Fe, Zn, and Ca were observed between the unburnt *H. brasiliensis* and burnt *H. brasiliensis* plantations. The study results revealed that bushfire has positive effects on pH, ECEC, SOM, TOC, TN, P, K, Cu, and Mn in *H. brasiliensis* plantations. However, the impact of bushfires on Na, Mg, and Zn was negative. The study demonstrated that while bushfire had a significant positive impact on P, it had a significant negative effect on Fe, Zn, Clay, and Ca. The research concluded that bushfires have varying effects (positive and negative) on specific physicochemical properties of soil in *H. brasiliensis* plantations. Future research could compare the impact of bushfires on *H. brasiliensis* plantations with other tropical agricultural systems to determine whether these effects are

specific to rubber plantations or prevalent across different tropical tree ecosystems.

References

Adekunle, I. M. (2011). Bioremediation of Soils Contaminated with Nigerian Petroleum Products Using Composted Municipal Wastes. Bioremediation Journal, 15, 30-241.

Al-Achi, A. (2019). The Student's t-Test: A Brief Description. Research & Reviews: Journal of Hospital and Clinical Pharmacy, 5, 1, 1-3.

Alcañiz, M., Outeiro, L., Francos, M., Úbeda, X. (2018). Effects of prescribed fires on soil properties: A review. Science of the Total Environment, 613–614, 944–957.

Al−Khayri, J.M., and Khan, T. (2024). Impacts of forest fires on soil: Exploring the effects on biotic and abiotic components. SYLWAN, 168(8), 601−614. 0.26202/sylwan.2024031.

Amoako, E. E., and Gambiza, J. (2022). Effects of anthropogenic fires on some soil properties and the implications of fire frequency for the Guinea savanna ecological zone. Ghana. Scientific African, 6.1-11.

Aref, I.M., Atta, H.A., Ghamde, A.R.M. (2011). Effect of forest fires on tree diversity and some soil properties. International Journal of Agriculture and Biology, 13, 659-664.

Areola, O. (1991). Ecology of Natural Resources. Avebury, England. Academic Publishing Group. p116- 118.

Attah, U. E., Chinwendu, O. C., Ekene, B. (2022). Anthropogenic Influence on Soil Quality Dynamics and Potential Ecological Risk in Agricultural Soils of the Nworie River Watershed, Nigeria. Jordan Journal of Earth and Environmental Sciences. JJEES, 13(2), 130-145.

Aweto, A.O. (1987). Physical and nutrient status of soils under rubber (*H. brasiliensis*) of different ages in south-western Nigeria. Agricultural Systems, 23, 63-72.

Badía, D., and Martí, C., (2003). Plant ash and heat intensity effects on chemical and physical properties of two contrasting soils. Arid Land Research and Management, 17, 23–41.

Blinkova, O., Raichuk, L., McDonald.I. (2025). Firstyear postfire alterations of Scots pine forest: composition, relationships, and ecological consequences. Landscape Ecology, 40, 9.https://doi.org/10.1007/s10980-024-02022-8.1-19.

Bremner, J.M., and Mulvaney, C.S. (1982). Nitrogen-total. In Methods of Soil Analysis. Miller, R. H.,Keeney, D.R. (Eds.) Chemical and Microbiological Properties,2:595-624. Madison, WI:American Society of Agronomy. Retrieved from https://www.scirp.org/(S(351jmbntvnsjt1aadkposzje))/.../ReferencesPapers.aspx.

Bridges, E.M. (1978). Interaction of soil and mankind in Britain. European Journal of Soil Science, 29,125-139.

Caon, L., Vallejo, V.R., Ritsema, C.J., Geissen, V. (2014). Efects of wildfire on soil nutrients in Mediterranean ecosystems. Earth-Science Reviews, 139, 47–58.

Certini, G. (2005). Effects of fire on properties of forest soils: a review. Oecologia, 143, 1 - 10.

Chungu, D., Ng'andwe, P., Mubanga, H., Chileshe, F.(2020).Fire alters the availability of soil nutrients and accelerates growth of Eucalyptus grandis in Zambia. Journal of Forest Research, 31, 1637 - 1645.10.1007/s11676-019-00977-y.

da Silva, D.M., Batalha, M.A. (2008). Soil–vegetation relationships in cerrados under different fire frequencies. Plant Soil, 311, 87–96.

Edem, I. D., Usoroh, A.D., Ijah, C.J. (2013). Soil properties dynamics induced by passage of fire during agricultural burning. International Journal of Plant and Soil Science. 2,111- 126.

Ekinci, H. (2006). Effects of forest fire on some properties of soil. International Journal of Agriculture and Biology, 8,102-106.

Esekhade, T.U., and Ugwa, I.K. (2008). Nutrient uptake in rubber and banana cultivar intercrop on an ultisol in Nigeria. In proceedings of the 42nd Annual Conference of the Agricultural Society of Nigeria. Ebonyi State University. Abakaliki, Nigeria. pp 44 - 447.

Esekhade, T.U., Monkwunye, M.U.B.,Adeoye, G.O. (2005). Effect of rubber based cropping systems on vegetative traits; below-ground interaction and yield of inter crops. Proceedings of 39th Annual Conference of Agriculture Society of Nigeria. University of Benin. Benin City. p262 - 265.

Emeterio, L.S., Múgica, L., Ugarte, M. D., Goica, T., Canals, R.M. (2016). Sustainability of traditional pastoral fires in highlands under global change: Effects on soil function and nutrient cycling. Agriculture Ecosystems & Environment, 235,155-163.

Farid, A., Alam, M.K., Goli, V.S.N.S., Akin, I.D., Akinleye, T., Chen, X., Cheng, Q., Cleall, P., Cuomo, S., Foresta, V. (2024). A review of the occurrence and causes for wildfires and their impacts on the geoenvironment. Fire, 7, 295. https://doi.org/10.3390/fire7080295.

Ferran, A., Delitti, W., Vallejo, V.R., (2005). Effects of fire recurrence in Quercus coccifera L. shrublands of the Valencia Region (Spain): II. plant and soil nutrients. Plant Ecology, 177, 71–83.

Fonseca, F., Figueiredo, T., Nogueira, C., and Queirós, A. (2017). Effect of prescribed fire on soil properties and soil erosion in a Mediterranean mountain area. Geoderma, 307,172 - 180.

García-Redondo, C., Díaz-Raviña, M., Regos, A. (2024). Long-Term Cumulative Effects of Wildfires on SoilVegetation Dynamics in the "Baixa Limia–Serra do Xurés" Natural Park. Spanish Journal of Soil Science, 14, 13103. doi: 10.3389/sjss.2024.13103.

Garrido-Ruiz, C., Sandoval, M., Stolpe, N., and Sanchez-Hernandez, J.C. (2022). Fire impacts on soil and post fire emergency stabilization treatments in Mediterranean-climate Regions. Chilean Journal of Agricultural Research, 82, 335-347.

Gee, G.W., and Or, D. (2002). Particle Size Analysis. In: Dane, J.H. and Topp, G.C., Eds., Methods of Soil Analysis, Part 4, Physical Methods, Soils Science Society of America, Book Series 5: 255-293.

Glenn, N.F., and Finley, C.D. (2009). Fire and vegetation type effects on soil hydrophobicity and infiltration in the sagebrush-steppe. Journal of Arid Environments, 74, 653-659.

Gonzales, H., Ocana,C.L., Cubas, J.A., Vega-Nieva, D.S., Ruíz, M., Santos, A. and Barboza, E. (2024). Impact of forest fire severity on soil physical and chemical properties in pine and scrub forests in high Andean zones of Peru. Trees, Forests and People, 18,1- 12.100659.

Granged, A. J. P., Jordán, A., Zavala, L.M., Muñoz-Rojas, M., Mataix-Solera, J. (2011). Short- term effects of experimental fire for a soil under eucalyptus forest (SE Australia). Geoderma, 167–168.

Hamad, A. Abu., Jasper, A., Uhl, D. (2013). Charcoal Remains from the Mukheiris Formation of Jordan – the First Evidence of Palaeowildfire from the Anisian (Middle Triassic) of Gondwana. Jordan Journal of Earth and Environmental Sciences, 5,1,17- 22.

Heydari, M., Rostamy, A., Najafi, F., Dey, D.C. (2017). Effect of fire severity on physical and biochemical soil properties in Zagros oak (Quercus brantii Lindl.) forests in Iran. Journal of Forestry Research, 28, 95-104.

Hendershot, H.W., Lalande, H.L., and Duquette, M. (1993). Soil Reaction and Exchangeable Acidity in: Soil Sampling and Methods of Analysis. Cartar, M.R. (Ed.), Canadian. Society of Soil Science. London, pp.141-145.

Itohanmwen, F.E. and Umweni, A.S. (2024).Land Suitability Evaluation Study for Oil Palm (Eleais guineensis) and Rubber (Hevea brasiliensis) Cultivation in Esan North East Local

Government Area of Edo State, Nigeria. African Scientist, 25(2), 182-197.

Iwara, A.I., Ewa, E. E., Ogundele, F.O., Adeyemi, J. A., Otu, C. A. (2011). Ameliorating Effects of Palm Oil Mill Effluent on the Physical and Chemical Properties of Soil in Ugep, Cross River State, South-Southern Nigeria. International Journal of Applied Science and Technology, 1, 106 – 112.

Kara, O., and Bolat, I. (2009). Short-term effects of wildfire on microbial biomass and abundance in black pine plantation soils in Turkey. Ecological Indicators, 9,1151–1155. https://doi.org/10.1016/j.ecolind.2009.01.002.

Keesstra, S., Wittenberg, L., Maroulis, J., Sambalino, F., Malkinson, D., Cerdà, A., Pereira, P. (2017).The influence of fire history, plant species and post-fire management on soil water repellency in a Mediterranean catchment: The mount Carmel range, Israel. Catena, 149,857-866.

Kennard, D.K. and Gholz, H.L. (2001). Effects of high-intensity fires on soil properties and plant growth in a Bolivian dry forest. Plant Soil, 234,119–129.

Khudhur, N.S., Khudhur, S.M., Ahmad, I.N. (2018). An Assessment of Heavy Metal Soil Contamination in a Steel Factory and the Surrounding Area in Erbil City. Jordan Journal of Earth and Environmental Sciences,9,1,1 – 11.

Kukavskaya, E.A., Bogorodskaya, A.V., Buryak, L.V., Kalenskaya, O.P. and Conard, S.G. (2024).Effects of Wildfire and Logging on Soil CO2 Efflux in Scots Pine Forests of Siberia. Atmosphere, 15, 1117.10.3390/atmos15091117.

Kutiel, P., and Naveh, Z. (1987). Effect of fire on nutrients in a pine forest soil. Plant and Soil, 104,269-274.

Ladrach, W. (2009). The effects of fire in agriculture and forest ecosystems. International Society of Tropical Foresters (ISTF NEWS). Special Report. 12.

Mataix-Solera, J., and Guerrero, C. (2007). Efectos de los incêndios forestales en las propriedades edáficas. In: Mataix-Solera,Jorge et al. Incendios Forestales, Suelos y Erosion Hídrica. Alicante, España: CEMACAM Font RojaAlcoi, 5- 40.

Muñoz-Rojas, M., Lewandrowski, W., Erickson, T.E., Dixon, K.W., Merritt, D.J. (2016). Understanding environmental drivers in the regulation of soil respiration dynamics after fire in semi-arid ecosystems.Geophysical Research Abstracts, 18, 1-3.

Muqaddas, B., Zhou, X., Lewis, T., Wild, C., Chen, C. (2015). Long-term frequent prescribed fire decreases surface soil carbon and nitrogen pools in wet sclerophyll forest of Southeast Queensland, Australia. Science of the Total Environment, 536, 39-47.

Murphy, J., and Riley, J.P. (1962). A modified single solution for determination of phosphate in natural water. Analytica Chemica Acta, 27, 31-36.

Nabatte, P., and Nyombi, K. (2013). Effects of pine plantation surface fires on soil chemical properties in Uganda. Research Journal of Agriculture and Forestry Sciences, 1, 10-14.

Nelson, D.W., and Sommers, L.E. (1982). Total Carbon, Organic Carbon and Organic Matter in: Sparks, D. L. (Eds.), Methods of Soil Analysis. Part 3. SSSA Books Series No 5, SSSA Madison.

Nnaemeka, C.C., Esio, U.O., Igba, A.J. (2013). Physical and chemical characteristics of forest soil in southern Guinea Savanna of Nigeria. Agriculture, Forestry and Fisheries, 2.229- 234.

Nottidge, D. O. and Nottidge, C. C. (2012). Effect of different rates of wood ash on exchangeable aluminum, growth, nodulation, nitrogen accumulation and grain yield of soybean (Glycine max (l.) merrill) in an acid ultisol. Global Journal of Agricultural Sciences, 11, 2, 81-87.

Norouzi, M., and Ramezanpour, H. (2013). Effect of Fire on Chemical Forms of Iron and Manganese in Forest Soils of Iran. Environmental Forensics, 14,169-177.

Novara, A., Gristina, L., Rühl, J., Pasta, S., D'Angelo, G., La Mantia, T., Pereira, P. (2013). Grassland fire effect on soil organic carbon reservoirs in a semiarid environment. Solid Earth, 4,381-385.

Oku, E., Iwara, A., Ekukinam, E. (2012). Effects of age of rubber (*H. brasiliensis* Muell Arg.) plantation on pH, organic carbon, organic matter, nitrogen and micronutrient status of Ultisols in the humid forest zone of Nigeria. Kasetsart Journal of Social Sciences,46,684- 693.

Olsen, S.R., and Sommers, L.E. (1982). Phosphorus in: Methods of Soil Analysis. Page, A. L., Miller, R. H., Keeney, D.R. (eds). Maidson, W. I American Society of Agronomy. 1572.

Onuwaje, O.U., and Uzu, F. (1982). Growth response of rubber seedlings to N, P and K fertilizer in Nigeria, Nutrient Cycling in Agroecosystems, 3,169-175.

Onyekwelu, J.C., Mosand, R., Stimm, B. (2008). Tree species diversity and soil status of primary and degraded tropical rainforest ecosystems in South-Western Nigeria. Journal of Tropical Forest Science, 20,193-204.

Orimoloye, J.R., Akinbola, G.E., Idoko, S.O., Waizah, Y., Esemuede, U. (2012). Effects of rubber cultivation and associated land use types on the properties of surface soils. Nature and Science, 10, 48-52.

Orobator, P. O. and Odjugo P. A. O. (2024). Natives' perception on causes and mitigation of bushfire in rubber plantations: A social-ecological system approach. Acta Geographica Universitatis Comenianae (AGUC), 68 (1), 113-138.

Orobator, P.O., and Odjugo, P.A.O. (2023). Do locals' perception of bushfire impact on rubber trees match or mismatch with empirical data? Evidence from Edo State, Nigeria. Kastamonu University Journal of Forestry Faculty, 23, 52-63.

Orobator, P.O. (2022). Effect of bushfire on soil bacteria and fungi in perennial tree plantation Ecosystems. Journal of Geographic Thought and Environmental Studies (JOGET), 17, 1- 11.

Orobator, P.O., Ekpenkhio, E., Noah, J. (2020). Effects of rubber (Hevea brasilensis) plantation of different age stands on topsoil properties in Edo State. Nigeria, Journal of Geographic Thought and Environmental Studies (JOGET), 15, 15-23.

Orobator, P.O. (2019). Impact of bushfire on soil and vegetation properties of Hevea brasiliensis (rubber) plantations in Iyanomo, Edo State, Nigeria. Ph.D. Thesis, University of Benin.

Orobator, P.O. (2014). Soil quality under different land uses in Okodobo village, Benin City, Edo State. M.Sc. Thesis, University of Benin.

Pardini, G., Gispert, M., Dunjó, G., (2004). Relative influence of wildfire on soil properties and erosion processes in different Mediterranean environments in NE Spain. Science Total Environment, 328, 237–246.

Pereira, P., Mataix- Solera, J., Úbeda, X., Rein, G., and Cerdà, A. (2019). Fire effects on soil properties. CSIRO Publishing, Clayton South, Victoria, Australia, p390.

Pierson, F.B., Robichaud, P.R., Moffet, C.A., Spaeth, K.E., Williams, C.J., Hardegree, S.P., Clark, P.E. (2008).Soil water repellency and infiltration in coarse-textured soils of burned and unburned sagebrush ecosystems. Catena, 74, 98-108.

Samburova, V., Schneider, E., Rüger, C.P., Inouye, S., Sion, B., Axelrod, K., Bahdanovich, P., Friederici, L., Raeofy, Y., Berli, M., Lutz, A., Zimmermann, R., Moosmüller, H. (2023). Modification of soil hydroscopic and chemical properties caused by four recent California, USA Megafires. Fire, 6,1-26. https://doi.org/10.3390/fire6050186.

Scharenbroch, B.C., Nix, B., Jacobs, K.A., Bowles, M.L. (2012). Two decades of low- severity prescribed fire increases soil nutrient availability in a Midwestern, USA oak (Quercus) forest. Geoderma, 183–184.

Tabi, F. O., Mvondo Ze, A. D., Boukong , A., Mvondo, R.J., Nkoum, G. (2013). Changes in soil properties following slash and burn agriculture in the humid forest zone of Cameroon.

African Journal of Agricultural Research, 8, 1990-1995.

Tan, D., Jin, J., Jiang, L., Huang, S., Liu, Z. (2012). Potassium assessment of grain producing soils in North China. Agriculture, Ecosystems and Environment, 148, 65–71.

Thomaz, E.L., Antoneli, V., Doerr, S.H. (2014) Effects of fire on the physicochemical properties of soil in a slash-and-burn agriculture. Catena, 122,209–215.

Ugwa, I.K., Orimoloye, J.R., Esekhade, T.U. (2005). Nutrients status of some soils supporting rubber (Hevea brasiliensis Arg. Muell) in Midwestern Nigeria, Nigeria Agricultural Journal, 36, 169-176.

Ulery, A.L. and Graham, R.C. (1993). Forest fire effects on soil color and texture. Soil Science Society of America Journal, 57(1), 135-140.

Umar, H.Y., Ugwa, I. K., Uche, U. (2012). Economy of coagula production in Rubber Research Institute of Nigeria (RRIN): trend analysis. International Research Journal of Library, Information and Archival Studies, 2, 38-42.

Umar, H.Y., Esekhade, T.U., Idoko, S.O., Ugwa, I.K. (2010). Production analysis of budded rubber stumps in Rubber Research Institute of Nigeria (RRIN). Journal of Agricultural Sciences, 1, 34-43.

Wietinga, C., Ebel, B.A., Singh, K. (2017). Quantifying the effects of wildfire on changes in soil properties by surface burning of soils from the Boulder Creek Critical Zone Observatory. Journal of Hydrology, 13, 43-57.

Xifré-Salvadó, M.À., Prat-Guitart, N., Francos, M., Úbeda, X., Castellnou, M. (2021). Effects of Fire on the Organic and Chemical Properties of Soil in a Pinus halepensis Mill, Forest in Rocallaura, NE Spain. Sustainability, 13, 5178.

Xue, L., Li, Q., and Chen, H. (2014). Effects of a bushfire on selected physical, chemical and biochemical soil properties in a Pinus massoniana Forest in South China. Forests, 52947- 2966.

Ying, H.S., Bin Wasli, M.E., Perumal, M. (2018). Soil characteristics under intensified shifting cultivation for upland rice cultivation in upland Sabal, Sarawak, Malaysia. Biotropia, 25, 72–83.

Zhang Y. and Biswas A (2017). The effects of forest fire on soil organic matter and nutrients in boreal forests of North America: a review. Adaptive Soil Management, 465–476.

JJEES

JJEES (2025) 16 (2): 195-204
ISSN 1995-6681

Jordan Journal of Earth and Environmental Sciences

Groundwater Recharge Estimation and Salinity Risk in Magra Plain (Algeria)

Abdelmadjid Boufekane[1*], Djamel Maizi[1], Gianluigi Busico[2], Mohamed Meddi[3]

[1] Geo-Environment Laboratory, Department of Geology, Faculty of Earth Sciences and Country Planning, University of Sciences and Technology Houari Boumediene (USTHB), 16111, Algiers, Algeria.

[2] DiSTABiF - Department of Environmental, Biological and Pharmaceutical Sciences and Technologies, Campania 7 University "Luigi Vanvitelli", Via Vivaldi 43, 81100 Caserta, Italy.

[3] GEE Research Laboratory, Ecole Nationale Supérieure d'Hydraulique de Blida, 09000, Blida, Algeria.

Received on January 18, 2024, Accepted on January 17, 2025

Abstract

In this study, an approach for assessing groundwater recharge and identifying areas at risk of salinity pollution was developed in Magra Plain (Algeria). This approach is based on the hydraulic characteristics of the vadose zone, precipitation, evapotranspiration, and soil moisture, using the Hydrus-1D model. The groundwater recharge was estimated in relationship to the annual cumulative values of the soil's actual evaporation and actual transpiration, while the salinization was evaluated in relationship to the water content variation and salt dynamic in the soil profiles from September 2021 to August 2022. The results showed that the groundwater recharge of the Magra Plain varies from 3.81% to 6.19% of the total precipitation, the salinity risk of the aquifer is related to natural conditions due to climate change (temperatures, precipitation) and the thickness of a permeable layer (lithology). This modeling approach will provide an effective means of assessing the risks associated with irrigation with saline water in semi-arid regions.

Keywords: *Groundwater recharge, Soil, Salinity, Hydrus-1D, Semi-arid region, Algeria.*

1. Introduction

Groundwater resources are considered the most important source of freshwater worldwide, particularly in arid and semi-arid regions, e.g. Algeria, due to the lack of water resources. Moreover, in such countries, the risk of soil and aquifer salinization is extremely increased due to the effect of climate changes on precipitation and temperature regimes, limiting the availability of drinking water (Chen et al., 2019; Panda et al., 2020). This risk becomes even higher especially in irrigation where the utilization of salty water for irrigation could exacerbate soil and groundwater salinization (Pulido-Bosch et al., 2018; Tomaz et al., 2020). So, the analysis of water salinity finalized its reduction and mitigation, and management become mandatory in many irrigated areas around the world (Ayars et al., 1999; Djoudi et al., 2023). The scenario is made even more problematic by the fact that the phenomenon of groundwater salinization could be exacerbated by anthropogenic endorheic pollution and over-exploitation of aquifers, leading to a deterioration in groundwater quality (Khezzani and Bouchemal, 2018; Mastrocicco et al., 2021).

In the aquifer system, the vadose zone can act as a filter, removing or decreasing the pollutant concentration, introduced into the subsoil such as fertilizers and pesticides (Elkayam et al., 2015; Gumiero et al., 2019; Rama et al., 2022). Moreover, the vadose media also include soil horizons where many biochemical and physical processes are responsible for pollutant degradation could occur (Amundson et al., 2007; Al-hamed et al., 2022). These depuration characteristics are mainly attributable to the high organic matter concentrations and clay contents, which can trigger pollutant biological degradation, transformation, and sorption (De Mastro et al., 2022; Ewis et al., 2022). Therefore, the vadose zone can effectively be considered a buffer zone, protecting the groundwater resources and the knowledge of its hydrogeological mandatory, so to correctly understand all the processes involved in groundwater pollution mitigation (Selker et al., 1996; Stephens, 1996).

Groundwater recharge also plays a key role in groundwater availability and quality. It is one of the main components of the hydrological cycle, and it is responsible for groundwater replenishment. Anyway, its amount greatly varies both in time and space according to several hydrogeological and climatic factors (Smerdon et al., 2010; Busico et al., 2021). In addition, the migration and transformation of pollutants in the unsaturated zone are mainly caused by the percolation of meteoric water and accompanying physical and chemical processes like adsorption-desorption and dissolution-precipitation reactions between pollutant and soil particles (Rama et al., 2022; Xue et al., 2023).

Consequently, a proper and reliable assessment of groundwater recharge becomes mandatory to correctly estimate water resource availability and to assess aquifer vulnerability to pollutants (Scanlon et al., 2002). Many methodologies could be utilized for this purpose; the most common include water balance (Afsari et al., 2022), hydrological modeling (Razack et al., 2019), water table

* Corresponding author e-mail: boufekane_ab@yahoo.fr

evolution (Boufekane et al., 2022), and natural rainfall infiltration (Ntona et al., 2022). However, changes in the piezometry and groundwater quality can be caused by many factors. Certain changes are caused by human activities (overexploitation, anthropogenic pollution) (Salifu et al. 2017; Dişli 2018), and others occur because of natural phenomena (low rainfall, high evapotranspiration) (Gain et al., 2012; Wang et al., 2022).

Among these, groundwater and solute modeling allows the understanding of all those transport processes within the unsaturated zone (Tarawneh et al., 2021). They are the methods for the analysis of different pollution scenarios, allowing the adoption of the best management actions.

Today, several models (numerical and analytical models) have been developed to assess groundwater recharge and solute transfer in the unsaturated zone, such as DAISY (Hansen et al., 1990), TOUGH2 (Pruess, 1991), SHAW (Flerchinger et al., 1996), SWAP (Van Dam et al., 1997), HYDRUS-1D (Šimůnek et al., 1998a; Šimůnek et al., 1998b), UNSATH (Fayer, 2000), and COUP (Jansson and Karlberg, 2001).

Among these, the model of Hydrus-1D (Šimůnek et al., 2005) is one of the most widely used models despite the common drawbacks of all numerical models, such as lack of input data for proper calibration and validation procedure (Ma et al., 2023; Ramos et al., 2023). The model uses two main equations for the calculation of water movement (Richards's equation, 1931) and solute transport (advection-dispersion equation, 1961) which require an iterative implicit technique (Damodhara et al., 2006). The model also allows the simulation of water, heat, and solute transport in one, two, or three-dimensional variably saturated porous media (Saâdi et al., 2018).

In this scenario, the main goals of this study are to estimate the potential groundwater recharge and the salinization risk degree for groundwater under different natural conditions and to highlight the role of vadose zone buffer property for the aquifer system, using the Hydrus-1D model. Water, leaching in two soil profiles with different hydrological characteristics, will be simulated to understand how the recharge and salt concentration repond to geological and sediment characteristics. This study will offer new insight into irrigation water regulation in the Magra Plain (Algeria), providing sustainable agriculture and water development.

2. Materials and methods

2.1. Study area

The Magra plain is located in the east of M'Sila Province (Central High Plateaus of Algeria) (Figure 1). Three morphological units characterize the whole region: i) the Hodna Mountains, ii) the Magra Plain and iii) Soubella Valley. The area shows a flat topography with an average altitude of 567 m a.m.s.l. (Amroune, 2018) and geographically is located a few km from the Chott El Hodna (Salt Lake) and between eastern longitude 4° 49' 45" – 5° 10' 30" E and northern latitude 35° 30' 00" – 35° 40' 30" N.

The climate is classified as semi-arid with low and irregular precipitations (around 210 mm/year) and an average temperature of 19 °C for the period 1969-2015 (Amroune et al., 2020). The climatic pattern in the area is characterized by a cool dry season (spring), followed by a hot dry summer, and recently by cold and very low rainy seasons (autumn and winter). According to the Thornthwaite (1948) method and for the period 1969-2015, the evapotranspiration, runoff, and infiltration in the region are 735 mm (350%), 10 mm (5%), and 12 mm (6%), respectively. Moreover, the agricultural water deficit due to groundwater abstraction is estimated to be around 690 mm distributed throughout the year (Amroune, 2018).

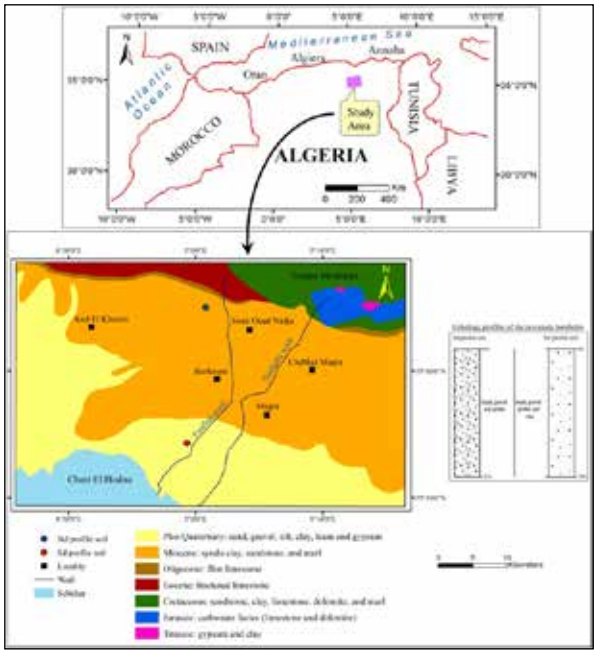

Figure 1. Location of the Magra Plain and geological map (Guiraud, 1970).

This plain is drained by two wadis (Ennfida Wadi and Soubella Wadi), flowing southward and feeding one of the largest Chott in Algeria (Chott El Hodna-Sebkhat) that are ephemeral salt lakes, present in the Saharan region of Africa.

Cereal crops, whose development and extension are highly dependent on the availability of water resources in sufficient quantity and quality, mainly represent agriculture. Groundwater is the main resource in this region.

2.1. Study area

The Magra Plain is characterized by the presence of black soils derived from alluvial parent material with a clay loam or silty clay loam texture (Madani, 2023). The soils are characterized as follows:

- Mountainous area (located in the north): here the Calcaric regosols are the most diffuse soils, even though they are very little developed due to the higher slope. They have a shallow, medium to fine-grained, unconsolidated parent material, possibly alluvial in origin, and no significant soil horizon and often show accumulations of calcium carbonate or gypsum.

- Central and South area: the Isohumic soils are present and are more evolved than in the mountainous area. Moreover, approaching the Chott El Hodna (South), the soils are affected by salts.

Two profiles, belonging to the plain, were selected. The dataset of the two profiles was collected and assembled during a geotechnical study which was carried out in the area of the two profiles (Nd and Sd profiles) to a depth of 25 meters, in October-December 2021. The first is located in the northern agricultural perimeters, and the second is located in the southern part. Both profiles are characterized by direct infiltration toward the surface water table (Figure 1). More precisely, the Nd profile, located in the north, has a sandy-clay texture throughout its depth (25 meters). Its dry residue varies between 1 and 2 gL^{-1} (average value of 1.5 gL^{-1}). On the other hand, the Sd profile, located to the south, is marked by a sandy texture over its entire depth (25 meters). Its dry residue varies between 2 and 4 gL^{-1} (average value of 3 gL^{-1}).

2.3. Geology and Hydrogeology

According to Flandrin (1951), Bertraneu (1955), Guiraud (1969), and Sonatrach (2005) (Amroune et al., 2017), different geological formations characterize the study area and are described below chronologically (Figure 1).

- - The Triassic formations, appearing diapirs from (gypsum and clay), outcrop in the northeast of the region.
- - The Jurassic formations made of carbonate facies (limestone and dolomite) form part of the reliefs of Hodna Mountains in the northeast of the region.
- - The Cretaceous formations are made of impermeable bedrock such as sandstone, clay, limestone, dolomite, and marl and form part of the reliefs of the Hodna Mountains in the northeast.
- - The Eocene formations consist of fractured limestone representing the karstic aquifer in the North of the region.
- - The Oligocene deposits consist of flint limestone and impermeable bedrock which characterize the North of the region.
- - The Miocene deposits are essentially made of sandy clay, sandstone, and marl forming the major aquifer of the area, which occupies most of the plain.
- - The Plio-Quaternary deposits are mainly formed by sand, gravel, conglomerate, silt, clay, loam, and gypsum. They represent a very productive aquifer, operated by small wells and boreholes (maximum depth: 150 meters), located in the east and south of the region.

In the southwest region, a natural outlet of the plain is observed; it is the Chott El Hodna (Sebkhat) that receives all surrounding surface waters. This Chott acts as a drainage system for water from the floods in the Magra Plain. This area also shows important salt deposits within geological formations.

- Hydrogeologically, a complex multiple aquifer characterizes the study area. It is made up of two hydrogeological units:
- The first aquifer, hosted in the Eocene formations and made of fractured limestone (karstic aquifer), characterizes the north of the region.
- The second aquifer, the object of this study hosted in the Mio-Plio-Quaternary formations, is an unconfined aquifer, made of heterogeneous alluvium sediments. This aquifer represents the most important aquifer in the Magra Plain, and several wells and boreholes exploit it with depths not exceeding 80 meters.

According to the data of the National Resources Water Agency (ANRH) during the dry season of 2012, the piezometric level varies from 200 m in the South and up to 600 m in the North. The general groundwater flow is oriented from the northern side (Hodna Mountains) towards Chott El Hodna (Sebkhat) to the southwest side and it is mainly recharged for meteoric water. The large Chott (Sebkhat) is the natural outlet for groundwater.

Hydraulic conductivity varies from 2×10^{-2} to 7×10^{-2} m/s while transmissivity ranges between 5×10^{-3} and 8×10^{-3} m^2/s and aquifer thickness varies between 150 and 300 m (Grine, 2009). However, the hydraulic gradient ranges between 2.3×10^{-3} and 8.1×10^{-3} (Grine, 2009), where the discharge water from the Hodna Mountains flows into the Magra plain, during the winter period or the flood events.

2.4. Hydrus-1D model simulation

2.4.1. Hydrus-1D model presentation

Hydrus-1D is a process-based model widely used in water and soil systems to simulate water flow, solute transport, and moisture distribution. The model was developed at California University (Šimůnek et al., 2006) to simulate the effects of irrigation on water and soil chemistry (Azhdari, 2008).

Several studies were performed worldwide, such as the United States (Šimůnek et al., 1998b; Šimůnek et al., 2005), Sweden (Gladnyeva and Saifadeen, 2012), Iran (Tafteh and Sepaskhah, 2012), China (He et al., 2017), India (Sangita et al., 2018), and Tunisia (Kanzari et al., 2018).

The Hydrus-1D model can simulate the one-dimensional water flow, heat, and solute transport in variably saturated soils (Šimůnek et al., 2006) in steady or transient regimes, using several metric systems and multiple time steps. This model is based on the Richards equation as well as the advection-dispersion equations in the case of water flow and solute transport, respectively.

Hydrus-1D solves the modified Richards' equation by eliminating the term that reflects water uptake by the roots, so that the mathematical expression for the Richards' equation will be (Šimůnek et al., 2006):

$$\frac{\partial \theta}{\partial t} = \frac{\partial}{\partial z}\left[K\left(\frac{\partial h}{\partial z} + 1\right)\right] \quad (1)$$

where:

h Water pressure head [L],

θ Volumetric water content [L^3 L^{-3}],

K unsaturated hydraulic conductivity [LT^{-1}],

t the time,

z the spatial coordinate.

The equations of Mualem and Van Genuchten (MVG) (1980) (Van Genuchten, 1980; Mualem, 1976) are used to develop the water retention curve (θ(h)). The latter relates the volumetric water content in the pressure potential to the hydraulic conductivity curve (K(h)), as a function of its saturation state measured by h. The retention curve represented by the equation of van Genuchten (1980) is:

$$\theta(h) = \begin{matrix} \theta_r + \frac{\theta_s - \theta_r}{1 + |\alpha h^n|^m} \\ \theta_s \end{matrix} \quad \begin{matrix} h < 0 \\ h \geq 0 \end{matrix} \quad \text{Where: } m = 1 - \frac{1}{n}, n > 1 \qquad (2)$$

Where:

θ_r is the residual water content [$L^3\ L^{-3}$],

θ_s is the saturated water content [$L^3\ L^{-3}$],

h is the water pressure head [L],

α [L^{-1}] and n are shape parameters.

According to Flandrin (1951), Bertraneu (1955), Guiraud (1969), and Sonatrach (2005) (Amroune et al., 2017), different geological formations characterize the study area and are described below chronologically (Figure 1).

$$K(h) = \begin{matrix} K_s r S_e^{1/2} \left[1 - \left(1 - S_e^{1/m}\right)^n\right]^2 \\ K_s \end{matrix} \quad \begin{matrix} h < 0 \\ h \geq 0 \end{matrix} \qquad (3)$$

With:

K_s the saturated hydraulic conductivity [LT^{-1}],

S_e the effective saturation [-],

r the pore connectivity parameter [-] equal to 0.5.

The equation that governs the solute transport in a variably saturated soil is the advection-dispersion equation, defined in Hydrus-1D as:

$$\frac{\partial \rho S}{\partial t} + \frac{\partial \theta C}{\partial t} = \frac{\partial}{\partial z}\left\{\theta . D \frac{\partial C}{\partial z}\right\} - q\frac{\partial C}{\partial z} \qquad (4)$$

Where:

z the spatial coordinate,

C and S solute concentrations in the liquid [ML^{-3}] and solid [MM^{-1}] phases,

S = KdC where Kd [L^3M^{-1}] the partition coefficient,

q the volumetric flux density [LT^{-1}],

D the dispersion coefficient [L^2T^{-1}],

ρ the bulk soil density [ML^{-3}].

2.4.2. Boundary and initial conditions

The initial condition along with boundary conditions were considered a 25 m deep vertical soil profile:

- In the case of the solute transport, the boundary conditions were coincident with the observed values of groundwater salinity.
- In the case of recharge, the upper boundary coincides with the atmospheric limit condition with surface runoff, whereas the lower boundary condition has been taken as free drainage.

At the soil surface, the reference evapotranspiration was calculated via the Penman-Monteith model, with the daily values of maximum and minimum temperature, precipitation, average humidity, and wind speed.

The Van Genuchten hydraulic parameters (θ_r, θ_s, α, n, and K_s), were calculated using the evaporation method and the hydraulic parameter values were calculated in the calibration phase.

The lower boundary condition corresponds to deep drainage where the release rate q (n), at the base of the soil profile at node n is considered as a component of the water table position (Hopmans and Stricker, 1989):

$$q(n) = q(h) = -A_{qh}\exp(B_{qh}|\, h - GWL0L\,|) \qquad (5)$$

With:

q(h) is the discharge rate [cm day^{-1}],

h is the pressure head at the bottom of the soil profile [cm], A_{qh} and B_{qh} are empirical parameters in [cm day^{-1}] and [cm^{-1}] respectively,

GWL0L is the reference groundwater depth [cm].

Vertical drainage across the lower boundary of the soil profile, in this case, is approximated by a flux that depends on the water table level.

The rate for each year daily and a total period of two years (2016-2022) was simulated. The simulation for the total period corresponds to the period between the occurrence of the first and the last rainfall event of the considered year.

2.4.3. Climate data

Data period six years from the M'Sila meteorological station were collected (from 1 September 2016 to 31 August 2022). Figures 2, 3, and 4 show the data, used in the Penman-Monteith model: monthly variations of rainfall data, average values of maximum and minimum temperatures, average wind speed, and humidity, respectively.

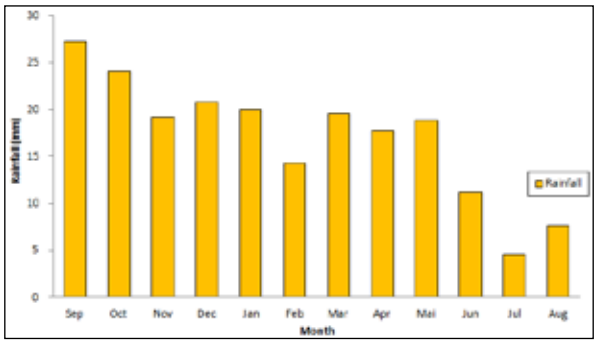

Figure 2. Average rainfall variations during the period September 2016 to August 2022.

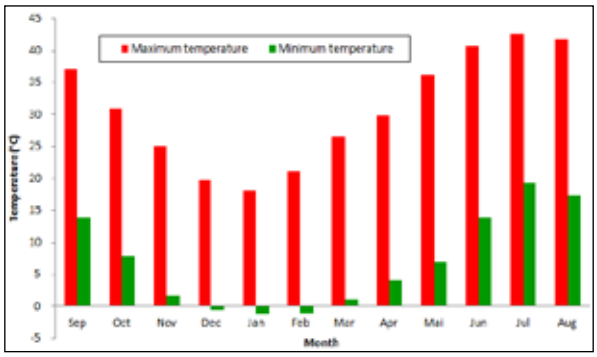

Figure 3. Daily average values of maximum and minimum temperatures during the period September 2016 to August 2022.

2.4.4. Groundwater recharge

The main results, estimated by Hydrus-1D, are actual soil evaporation, actual transpiration, and groundwater recharge. The simulated piezometric level is assumed to be at a depth where the pressure head (h) is equal to 0. The assumption of

a 1:1 gradient between h (pressure head) and z (soil depth) was checked to be valid for the present simulations (Leterme et al., 2012).

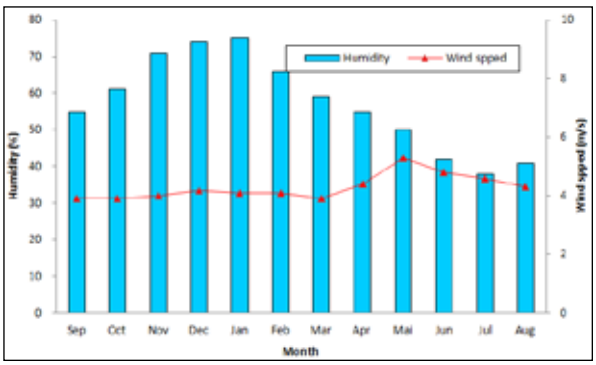

Figure 4. Average wind speed and humidity during the period September 2016 to August 2022.

2.4.5. Hydrus-1D input parameters

The Rosetta model was used to define the soil hydraulic parameters (Schaap et al., 2001). The factors of the water flow, i) saturated water content (), ii) residual water content (), iii) inverse of the air entry value (), iv) pore size distribution index (n), v) saturated hydraulic conductivity (), vi) the pore connectivity parameter for two different soil layers, were calculated using the soil texture and the measured bulk density. The core sampling method was used to determine the bulk density. The international pipette method was considered for the particle size distribution.

The calibration process allowed the estimation of soil hydraulic parameter values. In this study, the simulations were conducted for 730 days with a daily scale. It was carried out on silty and sandy soils that can be considered representative of the study area. For solute transport parameters, concentration flux was used as both the upper and the lower boundary conditions; it is calculated in the laboratory. Table 1 presents the soil hydraulic parameters, the Geometry information, and the solute transfer properties.

Table 1. Input parameters of Nd and Sd profiles.

Parameters	Values	
	Nd profile	Sd profile
Geometry information		
Depth (m) Number of layers	25 1	25 1
Time information		
Simulation time (days)	730	730
Hydraulic properties		
Layers (m) θ_r (cm^3cm^{-3}) θ_s (cm^3cm^{-3}) $\alpha(cm^{-1})$ n(–) K_s ($cm.d^{-1}$) L	0 – 25 0.065 0.42 0.07 0.51 1.60 0.5	0 – 25 0.075 0.54 0.75 0.89 2.46 0.5
Solute transfer properties		
Layer (m) Dispersion coefficient [L] K_d [M^{-1} L^3]	0 – 25 19 0	0 – 25 25 0

Moreover, the observed values of groundwater salinity show the following:

- For the Nd profile: the minimum and maximum values of water content were set to (θ = 0.1 cm^3cm^{-3}) and (θ = 0.3 cm^3cm^{-3}), respectively. The average value of dry residue is C = 1.5 g/L.
- For the Sd profile: the minimum and maximum values of water content taken were set to (θ = 0.1 cm^3cm^{-3}) and (θ = 0.3 cm^3cm^{-3}), respectively. The average value of dry residue is C= 3 g/L.

To resume, four different combinations in the model, representing different soil water contents and salt concentrations, were used to define the initial conditions (Table 2).

Table 2. Initial conditions of water content and solute concentration for Nd and Sd profiles.

Profiles	Nd profile		Sd profile	
Salt concentrations: C (gL^{-1})	1.5		3.0	
Water contents: θ (cm^3cm^{-3})	0.1	0.3	0.1	0.3

2.5. Model calibration and validation

The robustness of the model was checked, using two approaches: graphical and statistical methods. For the first approach, measured and simulated volumetric water contents, groundwater recharge, and soil salinities were shown as a function of soil depth for the different time steps. The second approach is based on the calculation of the root mean square error (RMSE):

$$RMSE = \sqrt{\frac{\sum_{i=1}^{n}(p_i - m_i)^2}{n}} \; X \; \frac{1}{\bar{m}} \; X \; 100 \qquad (6)$$

Where: n is the number of observations, m_i are the measured values, p_i are the predicted values, $\bar{m}$ and is the average value of observed data.

The model was initialized for 730 days. The results of soil water and salt content were obtained at the 183th, 365th, 548th, and 730th days of simulation.

3. Results and discussion

3.1. Variations in water and salt content

3.1.1. Water content variation

According to the obtained results during the simulation period (730 days), the results of the simulation for the Nd profile are shown in Figure 5. In this case, the water content values vary between 0.110 cm^3cm^{-3} and 0.150 cm^3cm^{-3} at the ground surface: it slightly increases from 0 to 15 m while from 15 m to the bottom of the profile. It remains almost constant from 0.147 to 0.178 cm^3cm^{-3}. However, the simulated water content values are always lower than the initial conditions, highlighting the continuous dewatering of the unsaturated zone due to the existence of a layer of low permeability (clay layer) for the entire soil profile.

Figure 6 shows the result for the Sd profile where the water content values vary between 0.130 cm^3cm^{-3} and 0.170 cm^3cm^{-3} at the ground surface, showing progressively increases accordingly with the soil depth (bottom of the profile) varying between 0.207 and 0.265 cm^3cm^{-3}.

Contrary to the Nd simulation, the Sd profile showed higher values of water content exceeding the initial conditions in some cases. This is probability due to the permeable nature of this soil (i.e.: sandy layer) which allows a greater infiltration of water after rain events.

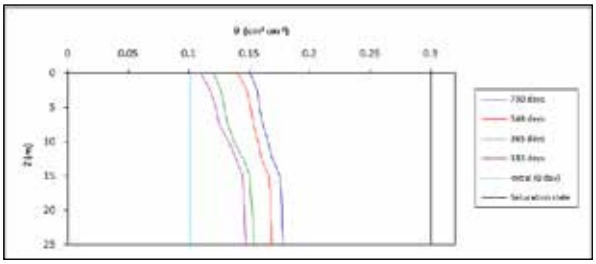

Figure 5. Variation of the water content for the Nd profile, for 730 days.

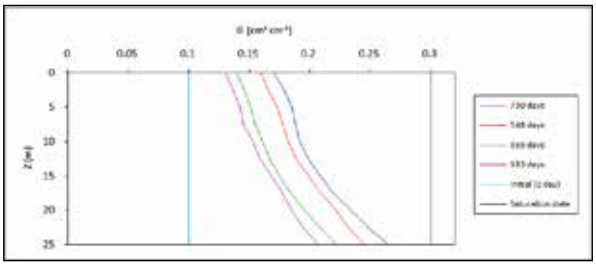

Figure 6. Variation of the water content for the Sd profile, for 730 days.

3.2.2. Salts content variation

As for the water content, the salt concentration trends obtained during the simulation period (730 days) showed similar results for all the combinations. According to the results shown in Figure 7, for the Nd profile, the concentration rate varies between 0.05 gL^{-1} and 0.25gL^{-1} at the ground surface. Moreover, it constantly increases until 0.69 gL^{-1} moving downward remaining constant in the last 5 meters (from 15 m to 25 m, the bottom of the profile) where the final value is 0.72 gL^{-1} after 730 days.

A general reduction in soil salinity, compared to the initial conditions (0.72 gL^{-1}), was shown when simulating the salt content profiles. A continuous leaching of salt is noticed through the unsaturated zone due to the presence of clayey intercalations that are able to slow down the spread of salt. These results highlighted the general low contamination risk for groundwater located below this kind of soil.

According to the results, shown in Figure 8, for the Sd profile, the concentration rate ranged between 0.32 gL^{-1} and 0.65 gL^{-1} at the ground surface. It constantly increases from 0.51 gL^{-1} to 0.94 gL^{-1} from 0 to 15 m and from 15 m to 25 m (bottom of the profile). The trends of the profile change and gradually increase towards the final salt concentration of 1.87 gL^{-1} after 730 days.

During the simulation period and under the initial conditions, the results of the variation of the solute concentration profiles showed the risk of high groundwater salinity in the area where the Sd profile is located. This can be explained by the presence of the sandy layer, which accelerates salt leaching into the aquifer and increases the salinity risk.

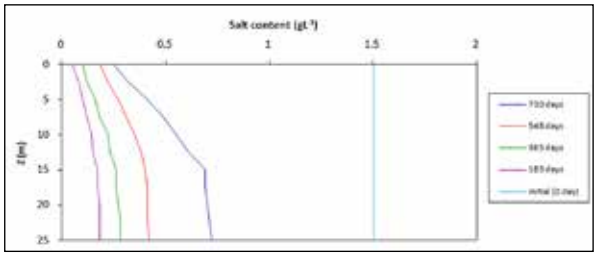

Figure 7. Variation of the salt content for the Nd profile, C = 1.5 gL^{-1}, for 730 days.

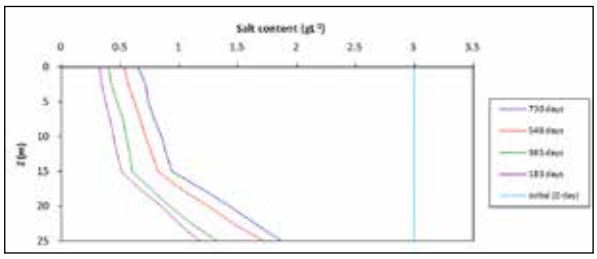

Figure 8. Variation of the salt content for the Sd profile, C = 3.0 gL^{-1}, for 730 days.

3.2.3. The calibration results of the Hydrus-1D model

The results of soil water and salt content were obtained at the 183th, 365th, 548th and 730th days of the simulation were presented in Table 3 where the proposed model (Hydrus-1D) shows better performance in the prediction of soil water and salt content (the RMSE values are equal to 0).

Table 3. Statistical evaluation (RMSE values) of the simulation results

	Nd profile			Sd profile		
	RMSE			RMSE		
	WCV	SCV (1.5 gL^{-1})	SCV (3.0 gL^{-1})	WCV	SCV (1.5 gL^{-1})	SCV (3.0 gL^{-1})
183th days of simulation	0.0723	0.1234	0.1154	0.0815	0.1272	0.1306
365th days of simulation	0.0739	0.1265	0.1183	0.0826	0.1298	0.1327
548th days of simulation	0.0754	0.1291	0.1211	0.0835	0.1316	0.1350
730th days of simulation	0.0776	0.1304	0.1238	0.0842	0.1332	0.1379

WCV: Water Content Variation
SCV: Salt Content Variation

3.3. Modeling of the groundwater recharge

The Hydrus- 1D model was used to estimate the potential groundwater recharge in the study area for the period September 2021 to August 2022. Based on the research results of Leterme et al. (2012), the model was used to simulate groundwater recharge in relation to annual values of actual soil evaporation and transpiration. The Penman-Monteith model was used to calculate intercepted water evaporation, potential soil evaporation, and potential transpiration. These variables will be used in the Hydrus-1D model.

In the current simulation, the results (Tables 4 and 5) show, that in the North zone of the plain (Nd profile), the simulated groundwater recharge is equal to an average of 8 mm/yr coincident with the 3.81% of total rainfall, while the actual ET (ETa) is 93.24% of the potential ET (ET0). For the south zone of the plain instead), (Sd profile) the simulated actual groundwater recharge is around 13 mm/yr (6.19% of total rainfall), and the actual ET (ETa) is 94.42% of the potential ET (ET0).

Table 4. Average values of rainfall, potential groundwater recharge, potential actual evapotranspiration and potential reference evapotranspiration during the period September 2021 to August 2022.

Zones of the plain	Rainfall (R)	Potential Groundwater recharge (GR)	Potential actual evapotranspiration (ETa)	Potential reference evapotranspiration (ET0)
	mm/yr			
North zone (Nd profile)	210	8	1021	1095
South zone (Sd profile)	210	13	1068	1131

Figure 9 shows the potential groundwater recharge for the two soil profiles Nd and Sd during the period September 2021 to August 2022. The Magra plain is characterized by low annual precipitation (210 mm), and groundwater recharge shows almost no seasonality. The average groundwater depth, used for the numerical simulations, is 10 mm (8 to 13 mm). The higher monthly recharge was obtained in December, January, February, and March. According to these recharge values, it concluded that the monthly groundwater recharge values are related to the monthly climatic parameters (precipitation, temperature, and evaporation) (Boufekane et al., 2019) and to the lithology of the unsaturated zone (permeable or impermeable layer) (Boufekane et al., 2022).

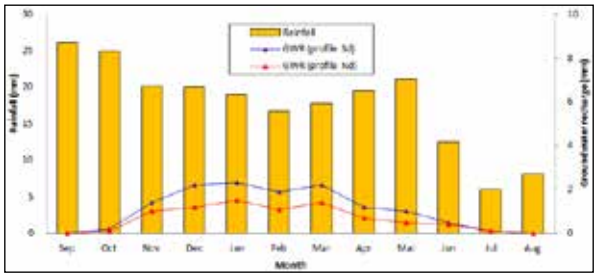

Figure 9. Potential groundwater recharge from two profiles soils during the period September 2021 to August 2022.

Table 5. Average monthly values of simulated potential groundwater recharge during the period September 2021 to August 2022.

	Potential Groundwater recharge (mm)												
Month	Sep	Oct	Nov	Dec	Jan	Feb	Mar	Apr	Mai	Jun	Jul	Aug	Total Year
Nd profile	0	0.1	1.0	1.2	1.5	1.1	1.4	0.7	0.5	0.4	0.1	0	**8.0**
Sd profile	0	0.2	1.4	2.2	2.3	1.9	2.2	1.2	1.0	0.5	0.1	0	**13.0**

In this semi-arid region, low-intensity rainfall does not play a very important role in groundwater recharge via infiltration and a considerable proportion of the precipitated water is lost via evaporation. Therefore, only torrential rains are capable of contributing to the groundwater supply.

The results of the simulation indicated that soil characteristics have a significant effect on soil water storage, and that the increasing use of irrigation amount could accelerate salt leaching as already stated also in different environments such as China (Zeng et al., 2014). Moreover, irrigation in agriculture significantly alters the water cycle, often with major environmental consequences, by increasing the salinity of recharge water from irrigated permeable soils and by recharging unconfined aquifers in drier regions such as Spain and South America (Foster et al., 2018).

4. Conclusion

In semi-arid regions like the Magra Plain (Algeria), salinization of groundwater due to intrinsic climatic characteristics, is a worrying issue to be managed and resolved. This study examined the interactions between the aquifer and the vadose zone to assess groundwater recharge and salinity risk. The main factors, influencing groundwater recharge salinity risk, are: rainfall, evaporation, soil nature, and vegetation.

The Hydrus-1D model was applied in the Magra plain. In the absence of soil layer information, except for texture, the approach, using combinations of initial conditions, is effective for predicting groundwater quality in the case of direct recharge. The results highlighted that the sandy layer accelerates infiltration towards the depths as well as the influence of water dynamics in the vadose zone. Conversely, the existence of clay intercalations in the unsaturated zone slows down the transit of water towards the aquifer (providing a good protection for groundwater). The sandy layer increases the salinity risk to the aquifer while the existence of clay intercalations in the unsaturated zone protects the aquifer against the filtrations of pollutants towards the groundwater. The recharge estimated during the period September 2021 to August 2022 varied from 8 to 13 mm (3.81% to 6.19% of total rainfall). The highest potential recharge was found for sandy clay and the lowest one for sandy soils. In addition, the decline in rainfall, the increase in temperature and evaporation will continue to threaten the groundwater resources (quantity and quality).

Finally, according to Hydrus-1D model results, as recommendations to improve this study, additional scenarios, including multi-factorial analysis study of rainfall, evaporation and groundwater recharge, and longer-term simulations, need to be considered to increase results reliability. Moreover, this elaboration can give useful insight to minimize the risks of groundwater overexploitation and salinity, especially, in arid and semi-arid regions.

References

Afsari, N., Murshed, S. B., Uddin, S. M. N., and Hasan, M. (2022). Opportunities and Barriers Against Successive Implementation of Rainwater Harvesting Options to Ensure Water Security in Southwestern Coastal Region of Bangladesh. Front. Water 4: 811918. https://doi: 10.3389/frwa.2022.811918

Al-hamed, T., Shiyab, S.M., Al-Bakri, J. (2022). Morpho-physiological Effects of Drought on Medicinal Plants and the Potential Use of Remote Sensing - A Review. Jordan Journal of

Earth and Environmental Sciences 13(2): 105-113. https://jjees.hu.edu.jo/files/Vol13No2/JJEES_Vol_13_No_2_P5.pdf

Amroune, A. (2018). Study of the hydrochemical contribution in the functioning knowledge of the alluvial aquifer in the northern region of Hodna (South-East Algeria). PhD thesis, University of Batna 2, Batna, Algeria. http://theses.univ-batna.dz

Amroune, A., Boudoukha, A., Boumazbeur, A., Benaabidate, L., Guastaldi, E. (2017). Groundwater geochemistry and environmental isotopes of the Hodna area, Southeastern Algeria. Desalination and Water Treatment 73: 225-236. https://doi.org/10.5004/dwt.2017.20642

Amroune, A., Mihoub, R., Enrico, G., Urena-Nieto Carlos U.N. (2020). Groundwater flow dynamics and distribution of hydrochemical facies using GIS in Hodna plain, M'Sila, southeastern Algeria. International Journal of Sustainable Development and Planning 15(6): 789-800. https://doi.org/10.18280/ijsdp.150601

Amundson, R., Richter, D.D., Humphreys, G.S., Jobbágy, E.G., Gaillardet, J. (2007). Coupling between biota and earth materials in the critical zone. Elements 3: 327-332. https://doi.org/10.2113/gselements.3.5.327

Ayars, J.E.,Tanji, K.K. (1999). Effects of drainage on water quality in arid and semiarid lands. In: Skaggs RW, Van Schilfgaarde J (eds) Agricultural drainage. ASA-CSSA-SSSA, Madison, pp 831-867. https://doi.org/10.2134/agronmonogr38.c25

Azhdari, K. (2008). Simulation of moisture distribution in soil in drip irrigation system using HYDRUS2D model. Journal of agricultural sciences and natural resources 15: 168-180.

Boufekane, A., Saibi, H., Benlaoukli, B., Saighi, O. (2019). Scenario modeling of the groundwater in a coastal aquifer (Jijel plain area, Algeria). Arabian Journal of Geosciences 12: 799. https://doi.org/10.1007/s12517-019-4965-0

Boufekane, A., Maizi, D., Madene, E., Busico, G., Zghibi, A. (2022). Hybridization of GALDIT method to assess actual and future coastal vulnerability to seawater intrusion. Journal of Environmental management 218: 115580. https://doi.org/10.1016/j.jenvman.2022.115580

Busico, G., Ntona, M.M., Carvalho, S. C. P., Patrikaki, O., Voudouris, K., Kazakis, N. (2021). Simulating future groundwater recharge in coastal and inland catchments. Water Resources Management 35(11): 3617-3632. https://doi.org/10.1007/s11269-021-02907-2

Chen, Y., Vigouroux, G., Bring, A., Cvetković, V., Destouni, G. (2019). Dominant hydro-climatic drivers of water temperature, salinity, and flow variability for the large-scale system of the Baltic Coastal Wetlands. Water 11(3): 552. https://doi.org/10.3390/w11030552

Damodhara, R.M., Raghuwanshi, N.S., Singh, R. (2006). Development of a physically based 1d-infiltration model for irrigated soils. Agricultural Water Management 85: 165-174. https://doi.org/10.1016/j.agwat.2006.04.009

De Mastro, F., Cacace, C., Traversa, A., Pallara, M., Cocozza, C., Mottola, F., Brunetti G. (2022). Influence of chemical and mineralogical soil properties on the adsorption of sulfamethoxazole and diclofenac in Mediterranean soils. Chemical and Biological Technologies in agriculture 9: 34. https://doi.org/10.1186/s40538-022-00300-8

Dişli E. (2018) Evaluation of hydrogeochemical processes for waters' chemical composition and stable isotope investigation of groundwater/surface water in karst-dominated terrain. Aquatic Geochemistry, The Upper Tigris River Basin, Turkey. https:// doi. org/ 10.1007/ s10498- 019- 09349-8

Djoudi, S., Pistre, S., Houha, B. (2023). Evaluation of Groundwater Quality and its Suitability for Drinking and Agricultural Use in F'kirina Plain, Northern Algeria. Jordan Journal of Earth and Environmental Sciences 14(3): 203-209. https://jjees.hu.edu.jo/files/Vol14/No.3/JJEES_Vol_14_No_3_P4.pdf

Elkayam, R.,Sopliniak, A., Gasser, G.,Pankratov, I., Lev, O. (2015). Oxidizer demand in the unsaturated zone of a surface-spreading Soil Aquifer Treatment system. Vadose Zone Journal 14: 11. https://doi.org/10.2136/vzj2015.03.0047

Ewis, D., Ba-Abbad, M.M., Benamor, A., Muftah H. El-Naas, M.H. (2022). Adsorption of organic water pollutants by clays and clay minerals composites: A comprehensive review. Applied Clay Science 229: 106686. https://doi.org/10.1016/j.clay.2022.106686

Fayer, M.J. (2000). UNSAT-H version 3.0: Unsaturated soil water and heat flow model. Theory, user manual, and examples. Pacific Northwest National Laboratory 13249.

Flerchinger, G.N., Hanson, C.L., Wight, J.R. (1996). Modeling evapotranspiration and surface energy budgets across a watershed. Water Resources Research 32: 2539-2548. https://doi.org/10.1029/96WR01240

Foster, S., Pulido-Bosch, A., Vallejos, Á., Molina, L., Llop, A., McDonal, A.M. (2018). Impact of irrigated agriculture on groundwater-recharge salinity: a major sustainability concern in semi-arid regions. Hydrogeology Journal 26: 2781-2791. https://doi.org/10.1007/s10040-018-1830-2

Gain, A.K., Giupponi, C., and Renaud, F.G. (2012). Climate change adaptation and vulnerability assessment of water resources systems in developing countries: a generalized framework and a feasibility study in Bangladesh. Water 4: 345–366. https://doi: 10.3390/w4020345

Gladnyeva, R., Saifadeen, A. (2012). Effects of hysteresis and temporal variability in meteorological input data in modeling of solute transport in unsaturated soil using HYDRUS-1D. Journal of Water Management and Research 68: 285-293. https://www.tidskriftenvatten.se/wp-content/uploads/2017/04/48_article_4604.pdf

Grine, R. (2009). Hydrogeological perspectives of the Hodnean basin. Master's thesis. USTHB, Algiers, Algeria. 140p.

Guiraud R, 1970. Geological map at 1:200,000 and notice of the Hodna basin. Edition FAO and MLARA, Algeria.

Gumiero, B.,Candonin, F., Boz, B., Da Borso, F., Colombani, N. (2019). Nitrogen Budget of Short Rotation Forests Amended with Digestate in Highly Permeable Soils. Applied Sciences 9: 4326. https://doi.org/10.3390/app9204326

Hansen, S., Jensen, H.E., Nielsen, N.E., Svendsen, H. (1990). NPo-research, A10: DAISY: soil plant atmosphere system model.

He, K., Yang, Y., Chen, S., Hu, Q., Liu, X., Gao, F. (2017). HYDRUS Simulation of Sustainable Brackish Water Irrigation in a Winter Wheat-Summer Maize Rotation System in the North China Plain. Water 9: 536. https://doi.org/10.3390/w9070536

Hopmans, J.W., Stricker, J.N.M. (1989). Stochastic analysis of soil water regime in a watershed. Journal of Hydrology 105: 57-84. https://doi.org/10.1016/0022-1694(89)90096-6

Jansson, P.E., Karlberg, L. (2001). Coupled heat and mass transfer model for soil-plant-atmosphere systems. Royal Institute of Technology. Department of Civil and Environmental Engineering, Stockholm.

Kanzari, S., Ben Nouna, B., Ben Mariem, S., Rezig, M. (2018). Hydrus-1D model calibration and validation in various field conditions for simulating water flow and salts transport in a semi-arid region of Tunisia. Sustainable Environment Research 28: 350-356. https://doi.org/10.1016/j.serj.2018.10.001

Khezzani, B., Bouchemal, S. (2018). Variations in groundwater levels and quality due to agricultural over-exploitation in an arid environment: the phreatic aquifer of the Souf oasis (Algerian Sahara). Environmental Earth Sciences 77(4): 142. https://doi.org/10.1007/s12665- 018- 7329-2

Leterme, B., Mallants, D., Jacques, D. (2012). Sensitivity of

groundwater recharge using climatic analogs and HYDRUS-1D. Hydrology and Earth System Science 16: 2485-2497. https://doi.org/10.5194/hess-16-2485-2012

Li, B., Wang, Y., Hill, R.L., Li, Z. (2019). Effects of apple orchards converted from farmlands on soil water balance in the deep loess deposits based on HYDRUS-1D model. Agricultural, Ecosystems & Environment 285: 106645. https://doi.org/10.1016/j.agee.2019.106645

Ma, X., Bai, Y., Liu, X., & Wang, Y. (2023). Analysis of water infiltration characteristics and hydraulic parameters of sierozem soil under humic acid addition. Water (Switzerland) 15(10): 1915. https://doi.org/10.3390/w15101915

Madani, D. (2023). Study of the impacts of land degradation linked to desertification on the landscape and the socio-economic aspect in the M'Sila region, Eastern Algeria. PhD thesis, University of Biskra, Algeria. http://thesis.univ-biskra.dz

Mastrocicco, M., Gervasio, M.P., Busico, G., Colombani, N. (2021). Natural and anthropogenic factors driving groundwater resources salinization for agriculture use in the Campania plains (Southern Italy). Science of the Total Environment 758: 144033. https://doi.org/10.1016/j.scitotenv

Mualem, Y. (1976). A new model for predicting the hydraulic conductivity of unsaturated porous media. Water Resources Research 12: 513-522. https://doi.org/10.1029/WR012i003p00513

Ntona, M.M., Busico, G., Mastrocicco, M., Kazakis, N. (2022). Modeling groundwater and surface water interaction: An overview of current status and future challenges. Science of The Total Environment 846: 157355. https://doi.org/10.1016/j.scitotenv.2022.157355

Panda, B., Chidambaram, S., Nagappan, G., Thilagavathi, R., Kamaraj, P. (2020). Multiple thematic spatial integration technique to identify the groundwater recharge potential zones - A case study along the Courtallam region, Tamil Nadu, India. Arabian Journal of Geosciences 13(24): 1284. https://doi.org/10.1007/s12517-020-06223-8

Pruess, K. (1991). TOUGH2: A general-purpose numerical simulator for multiphase fluid and heat flow. Berkeley, California: Lawrence Berkeley Lab.

Pulido-Bosch, A., Rigol-Sanchez, J., Vallejos, A., Andreu, J.M., Ceron, J.C., Molina-Sanchez, L., Sola, F. (2018). Impacts of agricultural irrigation on groundwater salinity. Environmental Earth Sciences 77(5): 197. https://doi.org/10.1007/s12665-018-7386-6

Ramos, T.B., Darouich, H., Oliveira, A.R., Farzamian, M., Monteiro, T., Castanheira, N., Paz, A., Alexandre, C., Gonçalves, M.C., Pereira, L.S. (2023). Water use, soil water balance and soil salinization risks of Mediterranean tree orchards in southern Portugal under current climate variability: Issues for salinity control and irrigation management. Agricultural Water Management 283: 108319. https://doi.org/10.1016/j.agwat.2023.108319

Razack, M., Jalludin, M., Gaba, A. H. (2019). Simulation of climate change impact on a coastal aquifer under arid climate. The Tadjourah Aquifer (Republic of Djibouti, Horn of Africa). Water 11: 2347. https://doi:10.3390/w11112347

Rawat, M., Sen, R., Onyekwelu, I., Wiederstein, T., Sharda, V. (2022). Modeling of groundwater nitrate contamination due to agricultural Activities - A systematic review. Water (Switzerland), 14(24): 4008. https://doi.org/10.3390/w14244008

Saâdi, M., Zghibi, A., Kanzari, S., 2018. Modeling interactions between saturated and unsaturated zones by Hydrus-1D in semi-arid regions (plain of Kairouan, Central Tunisia). Environment Monitoring Assessment 190: 170. https://doi.org/10.1007/s10661-018-6544-3

Salifu, M., Yidana, S.M., Anim-Gyampo, M., Appenteng, M., Saka, D., Aidoo, F., Gampson, E., Sarfo, M. (2017). Hydrochemical and isotopic studies of groundwater in the middle voltaian aquifers of the Gushegu district of the Northern region. Applied Water Science 7:1117–1129. https://doi.org/10.1007/s13201-015-0348-1

Scanlon, B.R., Healy, R.W., Cook, P.G. (2002). Choosing appropriate techniques for quantifying groundwater recharge. Hydrogeology Journal 10: 18-39. https://doi.org/10.1007/s10040-001-0176-2

Schaap, M.G., Leij, F.J., Van Genuchten, M.T., 2001. Rosetta: a computer program for estimating soil hydraulic parameters with hierarchical pedotransfer functions. Journal of Hydrology 251: 163-176. https://doi.org/10.1016/S0022-1694(01)00466-8

Selker, J.S., Duan, J., Parlange, J.Y.(1996). Green and Ampt infiltration into soils of variable pore size with depth. Water Resources Research 35: 1685-1688. https://doi.org/10.1029/1999WR900008

Šimůnek, J., Šejna, M., Saito, H., Sakai, M., Van Genuchten,M.T. (1998a). HYDRUS 1D software package for simulating the one-dimensional movement of water, heat, and multiple solutes in variably saturated media: IGWMC—TPS70 version 2.0. Colorado School of Mines.

Šimůnek, J., Šejna, M., Van Genuchten, M.T. (1998b). The HYDRUS-1D software package for simulating the one-dimensional movement of water, heat, and multiple solutes in variably saturated media, Version 2.0.

Šimůnek, J., Šejna, M., Van Genuchten, M.T. (2005). The Hydrus-1D Software Package for Simulating the One-dimensional Movement of Water, Heat, and Multiple Solutes in Variably-saturated Media; University of California-Riverside Research Reports: Riverside, CA, USA.

Šimůnek, J., Van Genuchten, M.T., Sejna, M. (2006). The HYDRUS Software Package for Simulating the Two and Three Dimensional Movement of Water, Heat, And Multiple Solutes in Variably Saturated Media. Technical Manual, Version 1.0, University of California.

Stephens, D.B. (1996). Vadose Zone Hydrology. Boca Raton, Florida: CRC Press.

Smerdon, B.D., Allen, D.M.,Neilsen, D. (2010). Evaluating the use of a gridded climate surface for modeling groundwater recharge in a semi-arid region (Okanagan Basin, Canada). Hydrological processes 24: 3087-3100. https://doi.org/10.1002/hyp.7724

Tafteh, R., Sepaskhah, A.R. (2012). Application of HYDRUS-1D model for simulating water and nitrate leaching from continuous and alternate furrow irrigated rapeseed and maize fields. Agricultural Water Management 113: 19-29. https://doi.org/10.1016/j.agwat.2012.06.011

Tarawneh, K., leyan, I., Alalwan, R., Sallam, S., Hammad, S. (2021). Assessment of heavy metals contamination levels in surfaces soil in Baqa'a area, Jordan. Jordan Journal of Earth and Environmental Sciences 12(4): 285-294. https://jjees.hu.edu.jo/files/Vol12No4/JJEES_Vol_12_No_4_P2.pdf

Tomaz, A., Palma, P., Fialho, S., Lima, A., Alvarenga, P., Potes, M., Costa, M.J., Salgado, R. (2020). Risk assessment of irrigation-related soil salinization and sodification in Mediterranean areas. Water 12(12): 3569. https://doi.org/10.3390/w12123569

Van Dam, J.C., Huygen, J., Wesseling, J.G., Feddes, R.A., Kabat, P., Van Walsum, P.E.V., Van Diepen, C.A. (1997). Theory of SWAP version 2.0; Simulation of water flow, solute transport and plant growth in the soil-water-atmosphere-plant environment (No 71, p. 167). DLO Winand Staring Center.

Van Genuchten, M.T. (1980). A closed-form equation for predicting the hydraulic, conductivity of unsaturated soils. Soil Science Society of America Journal 44: 892-898. https://doi.org/10.2136/sssaj1980.03615995004400050002x

Wang, X., Geng, X., Sadat-Noori, M., Zhang, Y. (2022).

Groundwater-seawater exchange and environmental impacts. Frontiers in Water 4: 928615. https://doi: 10.3389/frwa.2022.928615

Zeng, W., Xu, C., Wu, J. Wang, J. (2014). Soil salt leaching under different irrigation regimes: HYDRUS-1D modeling and analysis. Journal of Arid Land 6: 44-58. https://doi.org/10.1007/s40333-013-0176-9

Xue, S., Ke, W., Zeng, J., Tabelin C.B., Xie, Y., Tang, L., Xiang, C., Jiang, J. (2023). Pollution prediction for heavy metals in soil-groundwater systems at smelting sites. Chemical Engineering Journal 473: 145499. https://doi.org/10.1016/j.cej.2023.145499

JJEES

JJEES (2025) 16 (2): 205-212
ISSN 1995-6681

Jordan Journal of Earth and Environmental Sciences

Geomagnetic Storms: Their Occurrence and Relationship with Solar Activities during the Solar Cycles 23-24

Emad M. H. Takla[1*], Ahmed A. Khashaba and A. Abdelkader

National Research Institute of Astronomy and Geophysics (NRIAG), 11421 Helwan, Cairo, Egypt.

Received on May 15, 2024, Accepted on January 22, 2025

Abstract

Disturbances in the geomagnetic field are mainly connected with the solar activity, Solar Cycle (SC), configuration, and strength of several interplanetary/solar features. The current study aims to examine the occurrences of Geomagnetic Storms (GSs) with minimum Dst ≤ - 50nT and find out their connection with solar activities over two SCs (SCs 23 and 24). Five hundred twenty-four GSs (moderate, intense, and severe GSs) that occurred in the period from 1996 to 2019 were selected for this purpose. The occurrences of these GSs were compared with phases of the two SCs and halo Coronal Mass Ejections (CMEs) that occurred in the same period. Results of the current study indicate that the occurrence of GSs is highly correlated with the solar/sunspot cycle. It was observed that GSs are most likely occurring in phase with these SCs. The results also show positive correlations of the selected GSs versus the Sunspot Number (SN) and the halo CMEs with reasonably high values of correlation coefficients (R) especially for intense and super GSs. In addition, the study suggests that intense and super GSs are strongly depending on the magnitude and duration of the fluctuations in the Interplanetary Magnetic Field (IMF) parameters with relatively high correlation coefficients.

Keywords: *Geomagnetic storms, Solar cycle, Coronal Mass Ejections (CMEs), Interplanetary Magnetic Field (IMF), Disturbance Storm Time (DST).*

1. Introduction

The Solar Cycle (SC), also known as the sunspot cycle, is a roughly 11-year periodic variation observed in the activity of the Sun and can be measured in terms of changes in the Sunspot Number (SN). Amounts of solar radiations, ejected solar materials, and numbers of sunspots show synchronized variations through the period of a SC, starting from a period of minimum activity to a period of maximum activity and then back again to a period of minimum activity (Hathaway, 2010; Liu et al, 2011).

Changes occurring in association with the Sun's activities can influence the near-Earth environment. The interaction of ejected solar materials during large and violent solar eruptions, which are known as Coronal Mass Ejections (CMEs), with the Earth's environment is considered the main source of several space weather phenomena (NAS, 2008). The most significant phenomenon among them is the Geomagnetic Storm (GS), which is a significant disturbance in the Earth's magnetosphere. When this interaction is strong, serious and severe GSs are observed. When CMEs occur, it usually requires about 2-3 days from the launching of these CMEs for the generated GSs to reach the Earth and to affect its magnetic field. In addition, the capability of CMEs to cause significant GSs depends on several factors such as the type of CMEs, their speed, magnetic field orientation, source regions, origin, and also their influence on solar parameters near the Earth (Singh et al., 2021; Temmer, 2021).

In addition, numerous variations in the Interplanetary Magnetic Field (IMF) parameters can play an important role in controlling the occurrence of GSs (Fairfield and Cahill, 1966). For example, the magnitude of the average IMF (B) and the change in the direction of the north-south component of the IMF (Bz) are significant factors in controlling the quantity of solar energy that can be transferred to the Earth's magnetic field causing the GSs (Arnoldy, 1971). Therefore, GSs occur due to disturbed conditions in both the IMF and solar parameters caused by several space weather events (Akasofu and Chapman, 1963).

At the ground surface, a GS is observed as a quick drop in the intensity of the measured geomagnetic field. This decrease can last for several hours, after that, the intensity of the geomagnetic field undergoes a gradual recovery over a period that can be extended to several days. The study of these global disturbances (GSs) of the geomagnetic field is significant not only in understanding the interaction processes in the solar-terrestrial environment but also because such GSs can interrupt various important infrastructures such as the electric power systems which are very vulnerable to the negative effects of GSs (Kappenman, 1996). Moreover, GSs can cause many severe problems such as satellite damage, communication failure, and navigational problems (NAS, 2008 and 2009).

For the last few decades, the cause of GSs has been examined through several correlative studies (Wu and Lepping, 2006; Verma et al., 2009; Rathore, et al., 2014; Singh et al., 2017; Balachandran et al., 2021). However, many researchers have studied the influence of solar activity on the occurrence of the GSs; the results of these studies, taken

* Corresponding author e-mail: emad.takla@nriag.sci.eg

together, suggest further investigation of the impact of solar activity on the occurrence and intensity of the GSs. In the current research work, a statistical study has been performed to analyze GSs recorded during the SCs 23-24 by various geomagnetic observatories and identified with the help of the disturbance-storm time (Dst) index. Moreover, various IMF components and solar parameters were examined to identify their relationship to the occurrence of GSs.

2. Phases and classification of geomagnetic storms

As previously mentioned, a GS is a major turbulence in Earth's magnetic field that takes place when an efficient amount of energy is transferred from the solar wind to the space environment around the Earth. It is generally identified by variations in the DST index (Gonzalez et al., 1994). That index estimates the variations that occurred in the horizontal geomagnetic component (H-component) recorded at the magnetic equator by a number of magnetometers installed at equatorial geomagnetic observatories. The DST index is calculated based on hourly geomagnetic data and is reported in near real-time. The DST index ranges between +20 and −20 nano-Tesla (nT) during quiet times (Sugiura and Kamei, 1991).

Generally, a GS has three phases: the initial, main, and recovery phases, as shown in Figure 1. The initial phase is characterized by an increase of the DST index (or one-minute data of the H-component) by 20 - 50 nT in a short time (tens of minutes). The initial phase is also mentioned as a Storm Sudden Commencement (SSC). It is worth mentioning that not all GSs have an initial phase and not all abrupt increases in DST index are followed by GSs. The main phase of a GS is defined by DST index decreasing to less than −50 nT. Selecting the (−50 nT) as a value to define a GS is to some extent arbitrary. The main phase typically lasts for 2–8 hours. The recovery phase starts when the DST index increases from the minimum value up to the quiet time value (Gonzalez et al., 1994). The duration of recovery phase can vary from several hours to a few days. The size of a GS is classified according to the minimum DST index as moderate (−50 nT ≥ minimum of DST > −100 nT), intense (−100 nT ≥ minimum DST > −250 nT) or super-storm (minimum of DST ≤ −250 nT), see Cander and Mihajlovic (1998) for more details.y

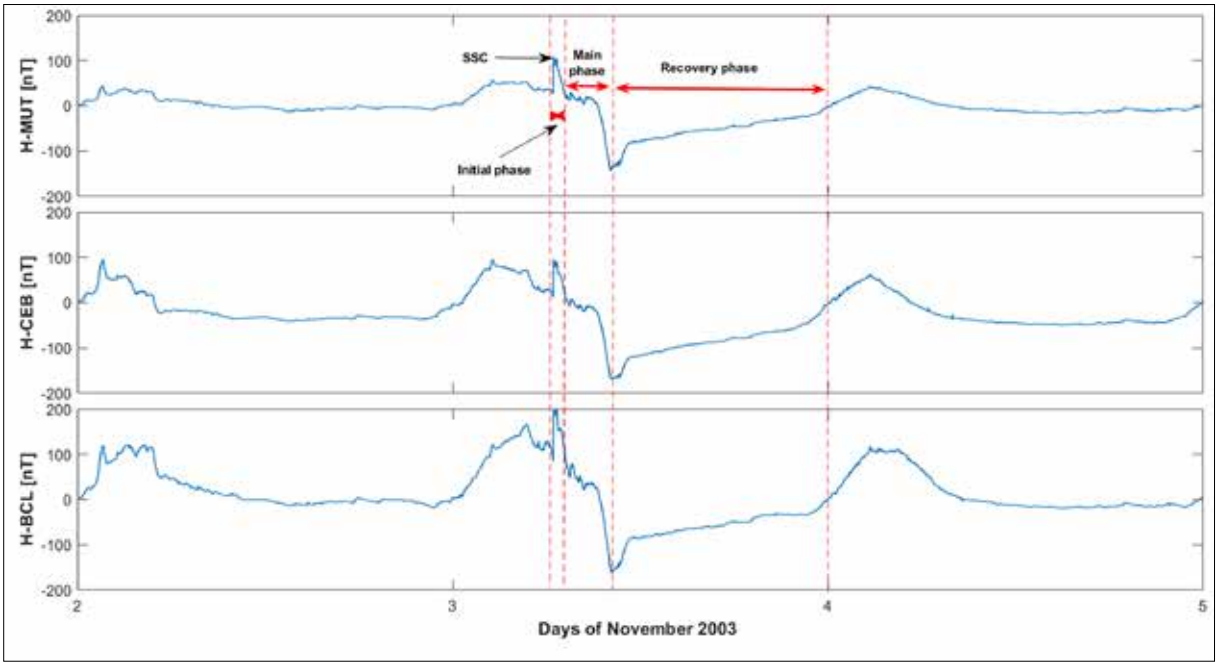

Figure 1. Geomagnetic data recorded at three geomagnetic stations located at equatorial and very low latitude regions showing geomagnetic storm occurred on 4 November 2003.

3. Data sources and selection criteria

The DST index data, provided by the World Data Center (WDC) for Geomagnetism, Kyoto, is used as the key to define and select the GSs. Three types of DST data are available, which are the real- time, provisional, and final DST indices. The occurrence of GSs, identified by the DST index data, is compared with the SN data, IMF components (B and Bz in nT), and solar parameters (Flow Pressure in nPa, and Electric Field Ey in mV/m), provided by the OMNI website (www.omniweb.gsfc.nasa.gov). The data of CMEs have been taken from the CME catalogue, which is produced at the CDAW Data Center by NASA and the Catholic University of America in cooperation with the Naval Research Laboratory.

Identification and selection of GSs, depending on the Dst index, follow the procedures of Loewe and Prölss (1997). According to the above-mentioned classification of GSs and depending on the Dst index data, five hundred twenty-four storms (DST ≤ -50 nT) that occurred during the SCs 23-24 from 1996 to 2019 were selected. In some events, DST data is found to show two minima before restoring to the quiet values. If a distinguished separation and a recovery period are observed between the two relative minima, they are considered as two GSs. On the contrary, if the two DST minima do not have a clear separation or recovery period, the GS is treated as a single event (Kamide et al., 1998).

4. Data analysis and results

The connection between solar activity and SC is known since long time ago. The solar activity can be measured by the occurrence of sunspots. As solar activity increases, the occurrence of sunspots does (Owens et al., 2021). According to that, the SC can be distinguished during its 11-year periodic variation into four phases, which are the minimum, ascending, maximum, and descending. The GSs have been observed after the appearance of sunspots, which indicates a connection between them (McIntosh et al., 2020). In addition, the occurrence of GSs depends on the phase of the SC. Since GSs and their effects on both space and ground-based infrastructures are of great interest to various research fields, several studies had investigated the long-term correlation between solar and geomagnetic activities.

The selected GSs during the 23 and 24 SCs are classified into two categories; four hundreds and four of them are classified as moderate GSs (-50 nT ≥ minimum Dst > -100 nT), while one hundred and twenty of them are classified as intensive and severe GSs (minimum Dst ≤ -100 nT). The current study refers to intense and super GSs as large GSs. The occurrences of the selected GSs were examined with the SN during the above-mentioned SCs to clarify the relationship between them. Figure 2 shows the selected GSs, compared with the sunspot cycle for SCs 23-24. In this figure, the yearly mean of the sunspots number is compared with the yearly number of all selected GSs with minimum Dst ≤ −50 nT (panel A), moderate GSs (panel B), and with large GSs (panel C). This figure clearly shows that GSs occur during all SC phases. For GSs with DST ≤ -50 nT, they exactly follow the phase of SCs, as shown in panel (A) of Fig. 2. During solar minima, few numbers of GSs occurred. Also, it is found that maximum numbers of GSs have occurred during solar maxima. Therefore, according to Fig. 2, the degree of the geomagnetic activities is comparative to that of the solar activities, which means that the occurrence rate of GSs tends to follow the SC pattern. In addition, moderate storms (panel (B) of Fig. 2) show similar temporal distribution where their occurrence is almost a coincidence with the phases of SC. On the contrary, large GSs do not exactly follow the phase of SCs and show different behavior mainly during the ascending and descending phases of the SCs, as shown in panel (C) of Fig. 2. Large GSs are mainly increased around the ascending, maximum, and descending phases of the SC-23. For SC 24, large GSs slightly increased during the ascending phase and with notable decrease during 2013.

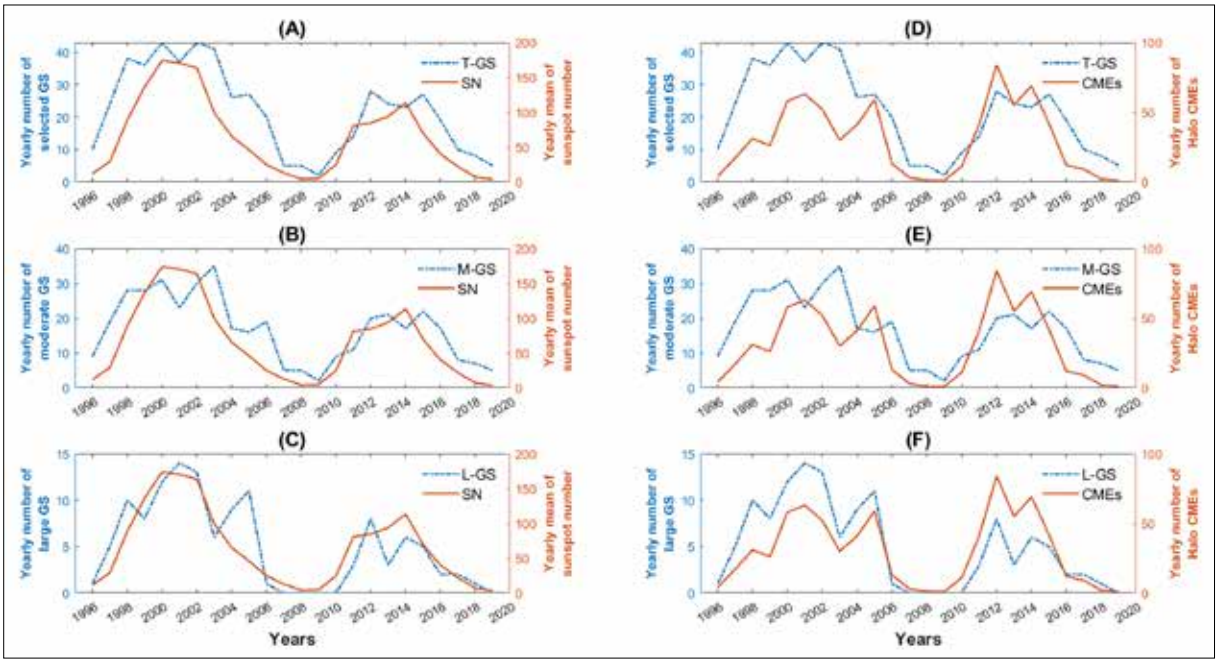

Figure 2. Yearly mean of SN during SCs 23 and 24 is superimposed on yearly numbers of all selected (T), moderate (M), and large (L) GSs (panels A, B, and C, respectively) while yearly number of halo CMEs during SCs 23 and 24 is superimposed on yearly numbers of all selected, moderate, and large GSs as presented in panels D, E, and F, respectively.

Since the occurrence of GSs varies in-phase with the sunspot cycle, correlations between SN and the GSs have been studied. Generally, scattered plots clarify the relation between pairs of datasets that have relationships varying with time. Thus, a similar approach is followed to test the nature of relationships and correlation between different categories of GSs and the SN. Moreover, the correlation coefficients (R) between them are calculated during the SCs 23-24. Figure 3 shows the correlation graphs between the SN and all selected GSs (panel A) with R= 0.87, moderate GSs as shown in panel B with R=0.82, and with large GSs (panel C) with R=0.84. These results confirm that the occurrence of GSs is highly correlated with the SN and phases of SCs.

An important observation is that the large GSs tend to occur more often during the ascending and descending phases of the SCs. (see panel (C) in Figure 2). Such an increase in the occurrence of large GSs during the ascending and descending phases of SCs can be linked with some space weather events, such as the CMEs. Therefore, the study is extended to examine the possible connection and influence of CMEs on the occurrence of GSs.

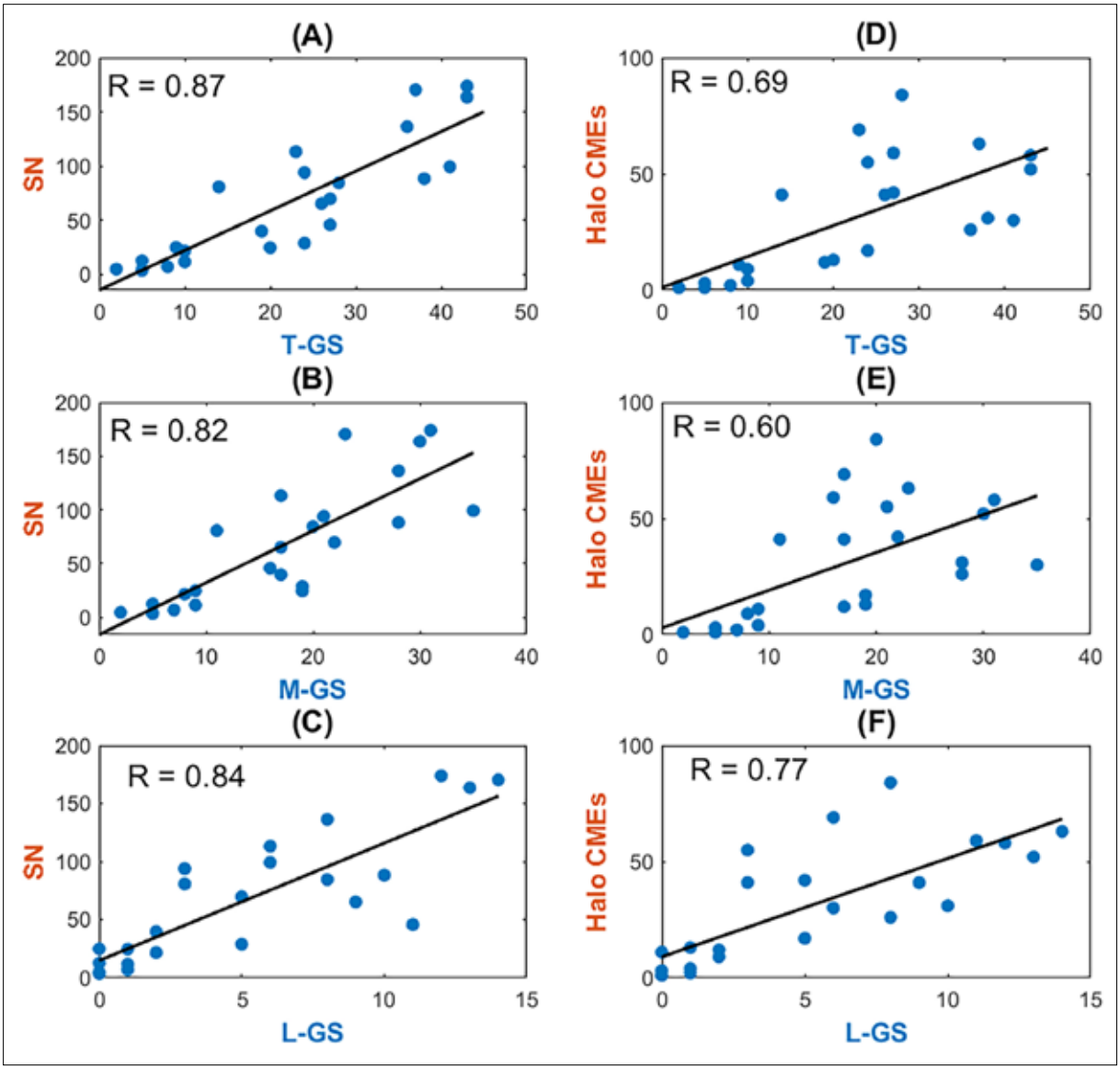

Figure 3. scattered pots of yearly mean of SN versus yearly numbers of all selected (T), moderate (M), and large (L) GSs during SCs 23 and 24 (panels A, B, and C, respectively) while scattered plots of yearly number of halo CMEs versus yearly numbers of all selected, moderate, and large GSs during SCs 23-24 are presented in panels D, E, and F, respectively. The regression lines are shown in solid black.

CMEs are the most common form of solar activity. The CMEs that are directed to the Earth are called halo CMEs (angular width = 360°). They got that name because of the way they look in coronagraph images (Howard et al., 1982). The halo CMEs are considered the main drivers of geomagnetic activity (Zhang et al., 2003). Thus, we have studied the correlation between halo CMEs and the selected GSs that were observed during the period of 1996-2019. In addition, we aimed to examine the expected association between the large GSs and the halo CMEs. Panels [D], [E], and [F] of figure 2 respectively show the relationship between the halo CMEs and selected, moderate, and large GSs. The large GSs are found to be in a good correlation with the halo CMEs (panel F) with peaks corresponding to the ascending and descending phases of SCs. The correlation plots of the halo CMEs against the selected, moderate, and large GSs are presented in panels [D], [E], and [F] of Figure 3 with correlation coefficients of 0.69, 0.6 and 0.77 respectively. This indicates that the occurrence of large GSs agrees with the occurrence of halo CMEs.

Since the space weather events such as CMEs are widely recognized as being responsible for generating disturbances in the solar parameters as well as Earth's magnetic field, we examined the temporal variations of some interplanetary and solar parameters along with the occurrence of GSs. The occurrence of GSs depends on various solar and interplanetary parameters (Akasofu, 1983, Gosling, 1993, Adebesin and Chukwuma, 2008). Therefore, the influence of magnitude of IMF (B), IMF (Bz), Flow Pressure (FP), and the Electric field (Ey) on the occurrence of GSs (as revealed from the DST index) for one month (continuous hourly data sets of April 2001) was investigated to determine the geoeffective parameters that are controlling the concurrence of GSs, as shown in figure 4. From visual inspection, there is a good correlation between the examined parameters during the occurrence of GSs (expressed by DST index), as shown in the period marked by red rectangles in Figure 4. On the other hand, periods of disturbance in the interplanetary and solar parameters were observed but with no corresponding remarkable change in the DST index (means no GSs) as it

presented by the blue rectangles in Figure 4. For better understanding of this observation, the correlation between the DST index and other parameters was examined and plotted in Figure 5, which indicates low correlation coefficients between the DST index and other parameters. The correlation coefficients of DST index versus IMF (B), IMF (Bz), FP, and Ey were (-0.41), (0.25), (-0.23), and (-0.24) respectively. The reason behind the obtained low correlation coefficients is that the occurrence of GSs can be controlled by other parameters or conditions such as the direction & magnitude of IMF, the solar wind speed, and the type of CMEs & solar flares.

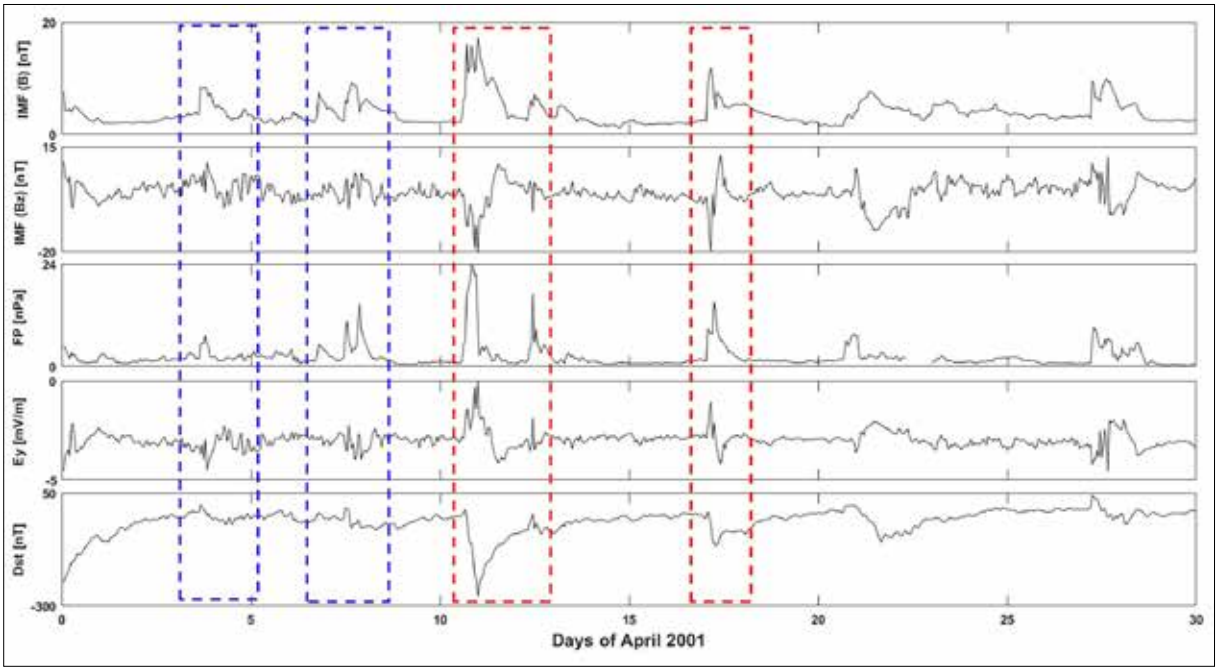

Figure 4. One-month hourly data of the IMF (B), IMF (Bz), FP, Ey and DST index during April 2001. Red rectangles indicate good correlations between the occurrence of GSs (expressed by DST index) and the fluctuations in IMF (B), IMF (Bz), FP, and Ey parameters, while blue rectangles indicate periods of disturbance in these parameters but with no corresponding GSs (no remarkable change in the DST index).

A series of powerful solar flares and CMEs erupted from the Sun during April 2001 and November 2003 (Lakhina et al., 2006). The impact of these events on the ground magnetic field measurements at polar and equatorial stations was studied to understand the obtained low values of correlation coefficients as revealed from Figure 5. The polar geomagnetic stations are Kotel'nyy (KTN) and Tixie (TIK), while the equatorial geomagnetic stations are Bac Lieu (BCL) and Cebu (CEB). (See Table 1).

Table 1. Geographic and geomagnetic coordinates of the geomagnetic stations used in the current study from MAGDAS/CPMN Network.

Station Name	Abbrev.	Country	Geographic Latitude	Geographic Longitude	Geomagnetic Latitude	Geomagnetic Longitude
Kotel'nyy	KTN	Russia	75.94	137.71	69.94	201.02
Tixie	TIK	Russia	71.59	128.78	65.67	196.88
Muntinlupa	MUT	Philippine	14.37	121.02	4.95	193.26
Cebu	CEB	Philippine	10.36	123.91	1.06	196.26
Bac Lieu	BCL	Vietnam	9.32	105.71	-0.36	178.3

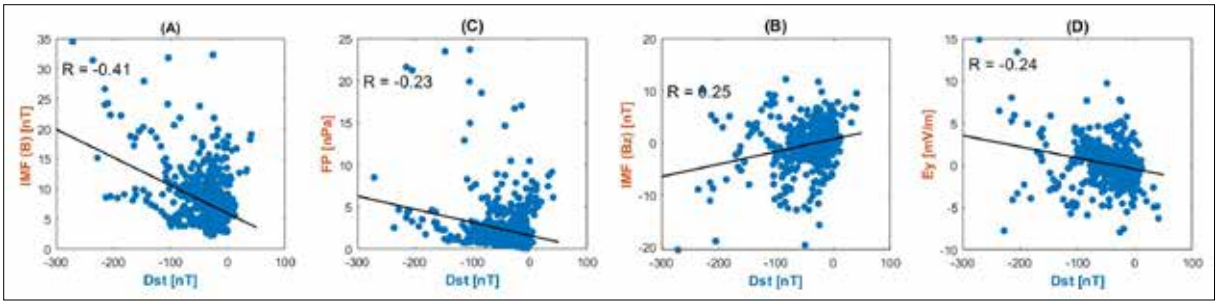

Figure 5. Scattered plots of the DST index against the IMF (B), IMF (Bz), FP, and Ey for one month (April 2001) are presented in panels (A), (B), (C), and (D) respectively. The regression lines are shown in solid black.

Figure 6 represents two different ground geomagnetic measurements in response to fluctuations in the interplanetary and solar parameters during two intervals of time. The ground geomagnetic measurements at polar and equatorial stations along with the variation in the interplanetary and solar parameters during the period between 10-14 April 2001 are presented in the left side panels of Figure 6 while in the right side panels for the period from 5-9 November 2003. One-minute data of the IMF (B), IMF (Bz), and Ey in the upper three panels are compared with the geomagnetic data recorded at two geomagnetic stations in the lower two panels. In the left side of this figure, the interplanetary and solar parameters show very intense fluctuations [IMF (B) 40nT nT and IMF (Bz) -35nT] from 10-14 April 2001. The impact of these intense fluctuations produced strong GS at both the polar (TIK) and equatorial (CEB) geomagnetic H-component data, with minimum values of -1960nT and -325nT respectively. On the other hand, the fluctuations during the period 5-9 November 2003 were limited, compared with those of 10-14 April 2001 where IMF (B) and IMF (Bz) were 15nT and -8nT respectively. In this case, a clear GS (-633nT) at only the polar station (KTN) was observed. At the equatorial station (BCL), such GS couldn't be observed due to the small amplitude fluctuations of IMF (B) and IMF (Bz) as well as their short duration. From this figure, it is clear that the intensity of the GS is controlled mainly by the magnitude of the IMF (B) and the negative IMF (Bz) as well as their duration. For that reason, a large magnitude of the southward IMF (Bz) with a long duration could give rise to stronger GS on 11 April 2001 than on 6 November 2003.

This result means that the geomagnetic disturbances observed by ground-based magnetometers can be limited to the polar region unless the fluctuations in the IMF (B) and IMF (Bz) magnitudes are significant and also have a long duration (several hours). This observation is very important and can be used to explain the obtained low correlation coefficients between the DST index and the interplanetary and solar parameters shown in Figure 5. When the fluctuations in interplanetary and solar parameters don't meet the requirements (concerning the intensity and duration) for generating equatorial GSs, they still are able to generate polar GSs, and since the DST index is computed from equatorial ground geomagnetic stations only, low correlations between the DST index and other interplanetary and solar parameters can be observed as shown in Figure 5.

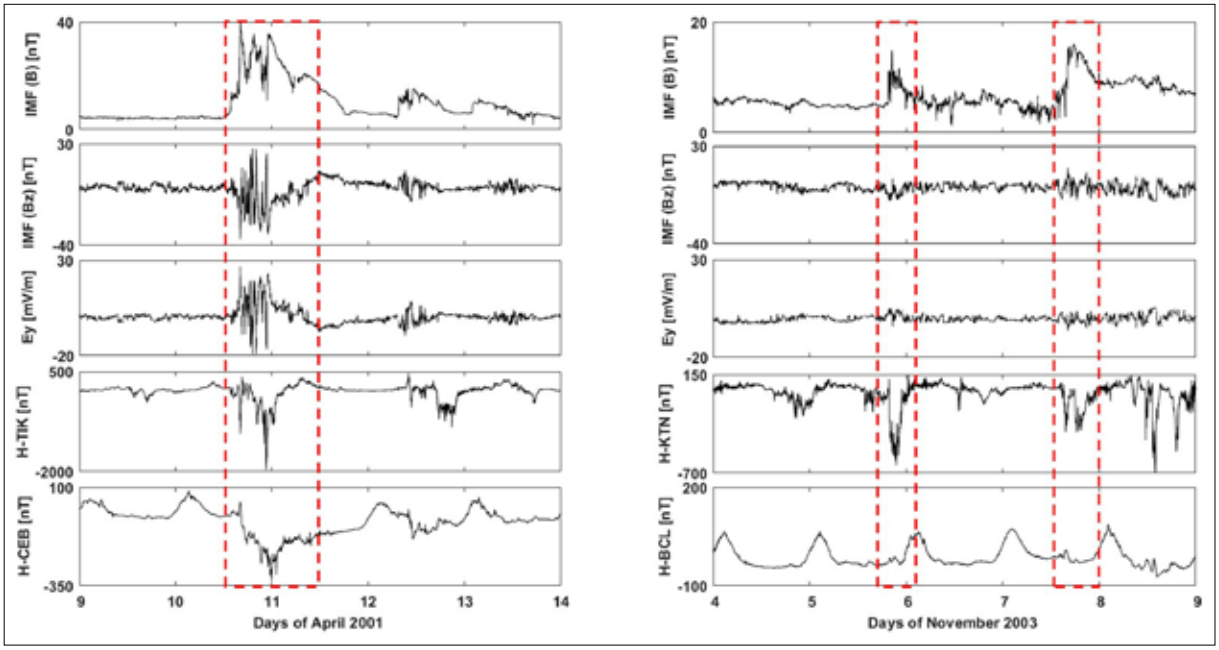

Figure 6. Left side (10-14 April 2001), the IMF (B), IMF (Bz), and Ey are presented in the top 3 panels respectively, while the variations of the horizontal geomagnetic component recorded at the TIK and CEB geomagnetic stations are presented in the bottom 2 panels, respectively. Right side (5-9 November 2003), the IMF (B), IMF (Bz), and Ey are shown in the top 3 panels, respectively, while the variations of the horizontal geomagnetic component recorded at the KTN and BCL geomagnetic stations are presented in the bottom 2 panels, respectively.

Moreover, the variations of the above-mentioned interplanetary and solar parameters were examined during the 120 large GSs that occurred in the period from 1996 to 2019 to confirm that observation and also to clarify their impact on the occurrence of GSs. All GSs were studied at their main phases (starting from the maximum values of DST index that occurred prior to the major decrease until reaching their minimum values). The interplanetary/solar parameters were examined during the same main-phase time frame. Thus, the correlations between these parameters and large GSs were examined. Figure 7 shows scattered plots and correlation coefficients of minimum DST index versus other parameters. The correlation coefficients of Dst index versus IMF (B), IMF (Bz), FP, and Ey were (-0.74), (0.76), (-0.52), and (-0.62), respectively. A high correlation of the DST index versus the IMF (B) and IMF (Bz) was observed. This analysis allows obtaining a remarkable degree of correlation between them. The correlation coefficients obtained from this research work strongly suggest that the magnitude and duration of IMF (B), and IMF (Bz) fluctuations play a key role in generating GSs.

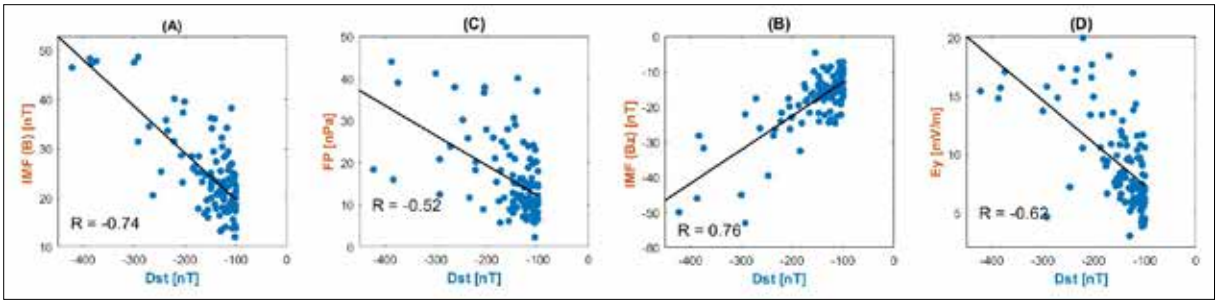

Figure 7. Scattered plots of the minimum DST index corresponding to large GSs occurred during the SCs 23-24 against the IMF (B), IMF (Bz), FP, and Ey are shown in panels (A), (B), (C), and (D) respectively. The regression lines are shown in solid black.

5. Conclusion

Several solar events cause abnormal fluctuations in the IMF and solar plasma emissions, which in turn cause GSs. Studying these GSs is important for space weather research. GSs with DST ≤ -50 nT (a total of 524 GSs) that occurred during the SCs 23-24 were selected to examine their occurrence and relationship to the solar activities. Occurrences of the selected GSs were compared with phases of the SCs and halo CMEs. The comparison showed that the geomagnetic activities tend to show a similar activity to the solar activities (SC). The occurrence of the selected GSs was in coincidence with phases of the SC. A significant relationship between GSs and both SN and halo CMEs was observed. In addition, large (intense and super) GSs are found to occur in association with the halo CMEs, as revealed by the correlation coefficients. The correlation of DST index versus several interplanetary and solar parameters was examined. The correlation coefficients obtained from this research work strongly suggest that the magnitude and the fluctuation duration of IMF (B) and IMF (Bz) have a strong impact and influence on the generation of GSs.

Thus, the study of solar events and their relationship with geomagnetic storms is essential for predicting space weather and its potential impacts. These insights allow for proactive measures to safeguard infrastructure, protect satellite systems, and enhance the safety and reliability of various communication and navigation systems. This contributes to the resilience of technological and societal systems in an increasingly space-dependent world.

Acknowledgment

Many thanks go to the World Data Center (WDC) for Geomagnetism Kyoto, Japan, OMNIweb, the CDAW Data Center, and the MAGDAS/CPMN networks for providing the data for this research work.

Statements and Declarations

- Ethics approval and consent to participate.
- Not applicable.
- Consent for publication
- All authors approved the final manuscript.
- Availability of data and materials
- Please contact the authors for data requests
- Competing interests
- The authors declare that they have no competing interest.
- Funding
- Not applicable.

References

Adebesin, B. O and Chukwuma, V. U. (2008). On the variation between Dst and IMF Bz during Intense and very intense geomagnetic storms. Acta Geod. Geoph. Hung., Vol. 43(1), Pp. 1- 15. doi:10.1556/AGeod.43.2008.1.1

Akasofu, S. I., and Chapman, S. (1963). Magnetic storms: The simultaneous development of the main phase (DR) and of polar magnetic substorms (DP). Journal Of Geophysical Research, 68, 3155-3158.

Akasofu, S.I. (1983). Solar-wind disturbances and the solar wind-magnetosphere energy coupling function, Space Sci. Rev., 34, 173-183.

Arnoldy, R. L. (1971). Signature in the interplanetary medium for substorms, J.Geophys. Res.,7 6 (22), 5189– 5201., doi:10.1029/JA076i022p05189.

Balachandran, R., Chen, L. J., Wang, S. and Fok, M. C. (2021). Correlating the interplanetary factors to distinguish extreme and major geomagnetic storms. Earth Planet. Phys., 5(2), 180–186. http://doi.org/10.26464/epp2021015.

Cander, L. R., and Mihajlovic, S. J. (1998). Forecasting ionospheric structure during the great geomagnetic storms. Journal of Geophysical Research: Space Physics. 103 (A1): 391–398.

Fairfield, D. H., and L. J, Cahill, Jr. (1966). Transition Region Magnetic Field and Polar Magnetic Disturbances, J. Geophys. Res., 71, 155-169.

Gonzalez, W. D., Joselyn, J. A., Kamide, Y., Kroehl, H. W., Rostoker, G., Tsurutani, B. T., and Vasyliunas, V. M. (1994). What is a geomagnetic storm? J. Geophys.Res., 99, 5771–5792.

Gosling, J.T. (1993). The solar flare myth. J. Geophys. Res., 98, 18937–18949, DOI: 10.1029/93JA01896.

Hathaway, D.H. (2010). The Solar Cycle. Living Rev. Sol. Phys. 7, 1. https://doi.org/10.12942/lrsp-2010-1

Howard, R.A., Michels, D.J., Sheeley Jr., N.R. and Koomen, M.J. (1982). The observation of a coronal transient directed at Earth. Astrophys. J. Lett., 263, L101–L104, DOI: 10.1086/183932.

Kamide, Y., Yokoyama, N., Gonzalez, W., Tsurutani, B. T., Daglis, I. A., Brekke, A., Masuda, S. (1998). Two step development of geomagnetic storms, J. Geophys. Res.,103, pp 6917-6922.

Kappenman, J. G. (1996). Geomagnetic Storms and Their Impact on Power Systems,‖ IEEE Power Engineering Review.

Lakhina, G. S., Alex S., Mukherjee S., and Vichare G., (2006). On magnetic storms and substorms , ILWS WORKSHOP 2006, GOA, FEBRUARY 19-24.

Liu, L. B., Wan, W. X., Chen, Y. D., et al. (2011). Solar activity effects of the ionosphere: A brief review. Chinese Sci Bull, 56: 1202−1211, doi: 10. 1007/s11434-010-4226-9.

Loewe, C. A., and Prölss, G. W. (1997). Classification and Mean Behavior of Magnetic Storms, J. Geophys. Res. 102, 14209.

McIntosh, S. W., Chapman, S., Leamon, R. J., Egeland, R., & Watkins, N. W. (2020). Overlapping magnetic activity cycles and the sunspot number: Forecasting sunspot cycle 25 amplitude. Solar Physics, 295(12), 163. https://doi.org/10.1007/s11207-020-01723-y

NAS (National Academy of Sciences) (2008). Severe Space Weather Events—Understanding Societal and Economic Impacts Workshop Report, National Academies Press, Washington, D.C.

NAS, (2009). Severe Space Weather Events—Understanding Societal and Economic Impacts: A Workshop Report - Extended Summary, National Academies Press, Washington, D.C.

Owens, M. J., Lockwood, M., Barnard, L. A., Scott, C. J., Haines, C., Macneil, A., (2021). Extreme Space-Weather Events and the Solar Cycle. Solar Physics. 296 (5):82. doi:10.1007/s11207-021-01831-3. ISSN 1573-093X. S2CID 236402345.

Rathore, B.S., Gupta, D.C. and Parashar, K.K. (2014). Relation between Solar Wind Parameter and Geomagnetic Storm Condition during Cycle-23. International Journal of Geosciences, 5, 1602-1608. http://dx.doi.org/10.4236/ijg.2014.513131.

Singh, A.K., Bhargawa, A., Siingh, D., Singh, R.P. (2021). Physics of Space Weather Phenomena: A Review. Geosciences, 11, 286.

Singh, S., A. C. Panday, Kalpana Singh & A. P. Mishra, (2017). Effect of geomagnetic storms and their association with solar wind velocity and IMF during solar cycle 23 and 24, International Journal of Pure and Applied Physics. ISSN 0973-1776, 13, Number 1, pp. 35-43.

Sugiura, M., Kamei, T. (1991). Equatorial Dst index 1957–1957–1986. In: Berthelier A, Menvielle, M. (eds) IAGA bull 40. International Service of Geomagnetic indices, Saint-Maur-des-Fosses.

Temmer, M. (2021). Space weather: the solar perspective. Living Rev Sol Phys 18, 4.

Verma, P.L., Tripathi, A.K. and Sharma, S. (2009). Geomagnetic Storms In Relation With Halo and Partial Halo Coronal Mass Ejections and Disturbances in Solar Wind Plasma Parameters, J. Plasma Fusion Res. SERIES, Vol. 8.

Wu, C. C., and Lepping, R. P. (2006). Solar cycle effect on geomagnetic storms caused by interplanetary magnetic clouds. Annales Geophysicae, 24 (12), pp.3383-3389.

Zhang, J., Dere, K. P., Howard, R. A., and Bothmer, V. (2003). Identification of Solar Sources of Major Geomagnetic Storms between 1996 and 2000, Astrophys. J. 582, 520.

JJEES

JJEES (2025) 16 (2): 213-219
ISSN 1995-6681

Jordan Journal of Earth and Environmental Sciences

Sustainable Contractors' All Risks (CAR) Policy Underwriting Model of Indonesia Non-Life Insurance

Maria Agnes[1*], Raldi Hendro Koestoer[1,2], Ahyahudin Sodri[1], Yuki M. A. Wardhana[1]

[1]School of Environmental Science, Universitas Indonesia
[2]Indonesia Coordinating Ministry for Economic Affairs

Received on 23 November 2023, Accepted on 24 January 2025

Abstract

Considering the indirect negative environmental and social impacts that may result from Contractors' All Risks (CAR) policy underwriting activities, there is a dire need to implement the sustainability concept and integrate the environmental and social risks into these underwriting activities. As a result of this integration, the sustainable Contractors' All Risks (CAR) policy underwriting activities are expected to reduce risk and contribute to economic, environmental, and social sustainability. The focus of this study is two-fold: the first is to define the risk criteria to be assessed against the environmental and social risks, while the second is to propose a conceptual model of sustainable Contractors' All Risks (CAR) policy underwriting for Indonesia's non-life insurance which expected to aspire non-life insurers in Indonesia to eventually establish their internal sustainable underwriting guidelines.

Keywords: *Environmental and social risks management; Sustainable underwriting; Insurance; Non-life insurance; Underwriting. JEL Classification: G220.*

1. Introduction

Environmental and social risks have been repeatedly identified as the most severe over the last few years (World Economic Forum, 2022) and instigated global awareness of the importance of sustainability. As a result, this set of circumstances has also caused the notion of transformations in the insurance sector (Chiaramonte et al., 2020; Johannsdottir, 2014). In this sense, insurers demonstrate increasing efforts to be able to emerge as sustainable, even if the implicit potential of the sustainability concept in the business processes is not fully understood yet (Negri, 2018). Some insurers have announced divestment programs from fossil fuels, whilst some perform Corporate Social Responsibility (CSR) practices. It is a positive signal. However, the insurance sector needs to comprehensively implement the sustainability concept into all aspects of its risk management, on the liability side and the asset side (Belozyorov & Xie, 2021; Nogueira et al., 2018).

On the liability side, risk management occurs in underwriting preceding the risk transfer that takes place through the stipulation of an insurance policy. For this very reason, the core risk management activities of the insurance business model are executed in underwriting, therefore, sustainability implementation in underwriting is indispensable.

Contractors' All Risks (CAR) policy, as the subject matter of this research, is an insurance policy that provides cover for losses or damages that happen during construction projects. Considering the direct environmental and social impacts caused by construction activities, there is a dire need to implement the sustainability concept and integrate the environmental and social risks into Contractors' All Risks (CAR) policy underwriting.

There are a few studies which assess the sustainability implementation into insurance risk management (Negri, 2018; Nogueira et al., 2018), but there is hardly any one addressing the sustainability implementation in underwriting. In order to fill this gap in literature, we aim to explore this issue. The focus of this study is two-fold; the first is to define the risk criteria to be assessed against the environmental and social risks; and the second is to propose a conceptual model of sustainable Contractors' All Risks (CAR) policy underwriting for Indonesia non-life insurance.

2. Literature Review

Environmental and social issues can create risks to financial institutions such as insurers (OECD, 2001). On that account, risk management experts demanded that the sustainability implementation in the insurance industry should be carried out by integrating those risks into all business activities, including interactions with stakeholders (Linnenluecke & Griffiths, 2010; Sato & Seki, 2010; Lozano, 2012; Allais et al., 2017; Dubey et al., 2017; Gillan et al., 2021). Nevertheless, experts expected that this integration would not only be implemented into day-to-day office operations, but into underwriting activities as well (United Nations Environment Programme Finance Initiative Principles for Sustainable Insurance, 2019). As an addition to improved financial performance and reputation, the integration of these environmental and social risks into underwriting activities are intrinsically anticipated to be able to stimulate

* Corresponding author e-mail: maria.agnes@ui.ac.id

the sustainability implementation into all other business activities (OECD, 2001; Negri, 2018; Nogueira et al., 2018).

The result of a review, conducted to the contents of sustainability reports published by Indonesia non-life insurers for the period of 2020 and 2021, showed that Corporate Social Responsibility (CSR) practices and eco-friendly business operations as the top 2 most prevalent sustainability strategies, and only 1 non-life insurer reported about the environmental and social risks integration in underwriting (Agnes et al., 2023). This factual condition is, of course, somewhat peculiar, given the fact that environmental and social risks have been repeatedly identified as the most severe risks over the last few years and are still predicted to be predominant for the next 10 years (World Economic Forum, 2022). In all good conscience, sustainability implementation certainly will have a greater impact and strengthen the non-life insurance industry's contribution to building a sustainable society if such implementation is executed by integrating environmental and social risks into underwriting, instead of merely focusing on Corporate Social Responsibility (CSR) practices and eco-friendly business operations.

Contractors' All Risks (CAR) policy, as the subject matter of this research, is an insurance policy that provides cover for losses or damages that happen during construction projects. There are various versions of Contractors' All Risks (CAR) policy. However, the one that is generally issued by Indonesian non-life insurers consists of material damage and third-party liability sections. The material damage section provides indemnification to any unforeseen and sudden physical loss or damage of the contract works due to any cause, other than those specifically excluded in the policy, whilst the third-party liability section covers accidental bodily injury or property damage of third parties in connection with the performance of the contract works.

Compared to the other lines of business in the non-life insurance industry, the construction & engineering line, under which Contractors' All Risks (CAR) policy is classified, had been indicated to contain the largest number of environmental and social high risks. According to the United Nations Environment Programme Finance Initiative Principles for Sustainable Insurance (UNEP FI PSI) assessment, the construction & engineering line is depicted to possess environmental high risks to climate-related emissions, deforestation, controversial site clearance, soil pollution, water pollution, impacts on world heritage sites, impacts on threatened species, and unconventional energy practices, whereas it has social high risks in terms of forced resettlement, poor worker safety, violation of worker rights, and misconduct of security personnel (United Nations Environment Programme Finance Initiative Principles for Sustainable Insurance, 2019). Please refer to Table 1 to obtain a detail indication of potential environmental and social risks levels associated with the construction & engineering line.

In conjunction with the UNEP FI PSI assessment, previous research similarly suggested the extensive range of environmental high risks carried by the construction industry since it generates the consumption for 40% of total energy production and 16% of the entire sum of water volume available, as well as discharging 25% of greenhouse gas emissions and 30–40% of solid wastes (Berardi, 2013; Darko et al., 2017; Shan et al., 2017; Susanti et al., 2019; Jingke Hong et al., 2019; Klufallah et al., 2019; Q. He et al., 2020).

Currently, there are no specific regulatory guidelines and manuals regarding sustainable construction or finance. Thus, this study intends to propose a conceptual model of sustainable Contractors' All Risks (CAR) policy underwriting for Indonesian non-life insurance based on the summarization of the UNEP FI PSI guide, the Institute for Sustainable Infrastructure guide, and other related sources.

3. Methods

The data collected in this study is a combination of primary and secondary qualitative data. The primary data was gathered through interviews with non-life insurance underwriting experts and complemented by the secondary data which was obtained from published literature, government documents, and related sources. Qualitative data analysis occurred simultaneously during the research, included in data collection activities.

The study is structured in four phases: First, undertake a literature review to acquire insights on negative environmental and social impacts attributable to the construction industry, second, to define the risk criteria to be assessed against the environmental and social risks in the proposed conceptual model. These risk criteria were determined as a result of the initial literature review, and third, to gather data from the expert interviews. At this phase, the chief and head of the underwriting department from 5 (five) non-life insurance companies were selected as experts and requested to assess of the selected risk criteria. Two were selected as representatives from national companies with total assets below 2 trillion rupiahs and one representative for each of these categories: national company with total assets above 2 trillion rupiahs, joint venture company with total assets below 2 trillion rupiahs, and joint venture with total assets above 2 trillion rupiahs. The Delphi method was chosen for the expert interview phase because it allows informants to respond to other informants' opinions and even to make revisions against their initial opinions. In this way, the method would greatly benefit the designing process of the proposed conceptual model. The fourth phase is to formulate the proposed conceptual model of sustainable Contractors' All Risks (CAR) policy underwriting.

4. Results and Discussion

The process of underwriting a risk consists of the following stages: risk selection, establishing appropriate terms and conditions for the risk, and deciding the appropriate price for the risk. The risk selection process in Contractors' All Risks (CAR) policy underwriting must be guided by risk appetite. It begins with the physical risks identification which afterward assessed against economic risks. The risk identification and assessment process will be based on the construction type, location, Estimated Total Contract Value (ETCV), contractor(s)/subcontractor(s) reputation, etc.

Table 1. Line of Business Construction & Engineering Heat Map

Criteria	Theme	Risk Criteria	Risk Mitigation Examples & Good Practice	Risk Level
Environmental	Climate change	Air pollution, greenhouse gas emissions, and transition risks	Disclosure of climate-related emissions in operations and/or products	
			Breakdown of fuel/material/carbon intensity mix relevant to the client or transaction	
			Environmental & social impact assessment (ESIA) covering negative health impacts, mitigation, and decommissioning where relevant	
			Decarbonisation transition plan/targets, customers fitting new emission mitigation technology, TCFD disclosures	
		Physical risks (e.g. heat, wildfire, extreme precipitation, flood, windstorm, tropical cyclones, sea level rise, water stress)	Nature-based solutions	
	Environmental degradation	Exposure to unconventional mining practices (e.g. mountain top removal, riverine tailings dumping, deep sea mining)	Involvement in initiatives: Extractive Industries Transparency Initiative, International Council on Mining & Metals, Kimberley Process	
		Deforestation or controversial site clearance (e.g. palm oil on peatlands or fragile slopes, illegal fire clearance/logging, biodiversity loss, dam construction)	Certification for palm oil, paper, etc. Dam construction standards: IHA Hydropower Sustainability Assessment Protocol, UNEP Dams & Development, Equator Principles	
		Soil pollution	ESIA covering possible negative health impacts, mitigation measures, and decommissioning plans where relevant	
		Water pollution	Water management practices	
	Protected sites/species	Impacts on World Heritage Sites or other protected areas	ESIA covers impacts on endangered species and sites, including mitigation	
		Impacts on species on IUCN Red List of Threatened Species	ESIA that covers impacts on endangered species and sites, including necessary mitigation measures	
	Unsustainable practices	Exposure to unconventional energy practices (e.g. Arctic oil, hydraulic fracturing, tar sands, deep sea drilling)	Various energy initiatives	
		Illegal fishing vessels, controversial fishing practices or aquaculture techniques	PSI-Oceana guide on illegal, unreported & unregulated (IUU) fishing, IUU fishing lists, Aquaculture/Marine Stewardship Council certification	
		Plastic pollution	PSI guide on the risks of plastic pollution, marine plastic litter, and microplastics to the insurance industry	
	Animal welfare/testing	Live transport over 8 hours or poor conditions or illegal/exotic animals (dead or alive)	Live transport over 8 hours must hold a certificate including training on ventilation/temperature. Good conditions on food, water, spacing, lighting, etc.	
		Controversial living conditions or use of chemicals/medicines	Relevant certification for farming or ethical animal treatment during clinical treatments	
		Lack of anaesthetic or distress-reducing techniques	Compliance with Guiding Principles on Replacement, Reduction & Refinement	
		Use of wild subjects or Great Apes in testing	Compliance with Guiding Principles on Replacement, Reduction & Refinement	
Social	Human rights	Child labour	Policy/statement on protecting and promoting human rights, prohibits child labour, shared with suppliers, regular audits and public findings (e.g. ILO, UNDHR)	
		Human trafficking	Human rights policy that includes a statement on protecting and promoting human rights and prohibits human trafficking	
		Forced labour	Human rights policy that includes a statement on protecting and promoting human rights and prohibits forced labour	
		Forced resettlement (including land/water rights for native people, land grabbing)	Free, prior & informed consent (FPIC) achieved. Effective environmental & social impact assessment (ESIA) process covering consultation, resettlement, compensation aspects	
		Poor worker safety record	Effective occupational health & safety policy that defines safety responsibilities and prevention measures to minimise fatalities, injuries, and health impacts	
		Violation of worker rights	Code of conduct that outlines company's commitment to respect workers' rights	
		Misconduct of security personnel (e.g. physical harm to people, human rights abuses)	Whistle-blower channel to report such violations	
	Controversial weapons	Controversial weapons exposure	Anti-Personnel Mine Ban Convention, Convention on Cluster Munitions	

(Source: UNEP FI PSI, 2019)

Bearing in mind that sustainable underwriting aims to reduce risk and contribute to economic, environmental, and social sustainability, thus the Contractors' All Risks (CAR) policy underwriting should be transformed by way of integrating environmental and social risks into the process (United Nations Environment Programme Finance Initiative Principles for Sustainable Insurance, 2019; Urban & Wójcik, 2019).

4.1. Defining the Risk Criteria

Based on the summarization of risk levels, identified in Table 1, the Institute for Sustainable Infrastructure guide and the Regulation of the Minister of Public Works and Housing of

the Republic of Indonesia No. 9/2021, concerning guidelines for Sustainable Construction Implementation, the selected risk criteria, to be assessed against the environmental and social risks in the proposed sustainable Contractors' All Risks (CAR) policy underwriting model, are listed in Tables 2 and 3. All these criteria were selected based on their extent of impact against the environmental and social risks as well as operationalities, that is why nearly all the selected risk criteria are already adopted in the Regulation of the Minister of Public Works and Housing. Nonetheless, risk criteria E1, E7, S1, and S3 were still selected because the operationalities of the assessment process can still be accomplished properly by examining project documents (e.g. Detail Engineering Design (DED), contracts, etc.) and conducting further investigation (e.g. via news websites, direct interviews with contractors, etc.). A concise summary of the literature review, conducted as the basis for determining the extent of impact from the selected risk criteria, will be briefly explained in the following paragraphs.

Table 2. Risk Criteria for Environmental Risk Assessment

Risk Criteria	Risk Criteria Code	Regulation Reference Code
Impacts on Greenfields	E1	N/A
Impacts on wetlands, shorelines, and waterbodies	E2	KL-7.4.1
Pollutants and wastes	E3	KL-7.1.1
Recycled materials	E4	KL-5.4.1
Prefabricated materials	E5	KL-5.5.1
Regional materials	E6	KL-5.2.1
Useful life	E7	N/A

(Source: Authors, 2022)

Table 3. Risk Criteria for Social Risk Assessment

Risk Criteria	Risk Criteria Code	Regulation Reference Code
Social conflict	S1	N/A
Workplace safety and health	S2	KL-1.1.1
Local employment ratio	S3	N/A

(Source: Authors, 2022)

Impacts on Greenfields (E1)

Land-use and land-cover change has been recognized as one of the factors that causes major effects to the environment and the climate (Brovkin et al., 2013; Prestele et al., 2016). Anthropogenic land-use and land-cover changes are estimated to contribute substantially to the increased amount and concentration of world's greenhouse gas emissions which ultimately leads to global warming and climate change (Wulan et al., 2015). In consideration of the construction industry's share in discharging 25% of the total greenhouse gas emissions (Q. He et al., 2020) and Indonesia's status as the second largest emitter of greenhouses gases from deforestation (Zarin et al., 2016; Tacconi & Muttaqin, 2019), we find that it is significantly important to include this risk criterion into the proposed model.

Impacts on wetlands, shorelines, and waterbodies (E2)

As a consequence of population growth and urbanization, a large number of construction megaprojects have emerged in Southeast Asia, including Indonesia (Hawken et al., 2021). Despite the many benefits presented by these construction megaprojects, disruptions to the environment are also sparked off, including changes in urban water flows, riparian deposition, and flood regimes (Douglass & Miller, 2018). Most major cities and populated areas in Indonesia are located in coastal or riparian environments, on that ground, we then considered to include this risk criterion into the proposed model.

Pollutants and wastes (E3)

Due to its substantial waste generation which takes part approximately 30–40% of solid wastes volume across the world (Berardi, 2013; Darko et al., 2017; Q. He et al., 2020), the waste management issues of the construction industry demand our full attention (Bao et al., 2020). With that being said and the waste crisis which Indonesia is trying to tackle nowadays, we decided to include this risk criterion into the proposed model.

Recycled materials (E4)

The construction industry is not only generating a large number of wastes, but it is also consuming massive amounts of natural resources (Hossain et al., 2020). Minimizing the usage of raw materials will reduce natural resources extraction, the embodied carbon emissions, the energy required to produce and transport those materials, and volume of wastes sent off to landfills (Institute for Sustainable Infrastructure, 2015). This risk criterion is undoubtedly correlated with risk criteria E3 and must be included in the proposed model.

Prefabricated materials (E5)

The advantages of prefabricated materials are manifested by high production efficiency, energy conservation, environmental protection, waste reduction, and guaranteed quality (Ma et al., 2020; Jie & Nan, 2020; Hu & Chong, 2021). This risk criterion is still closely interconnected with risk criteria E3 and E4, hence it is included in the proposed model.

Regional materials (E6)

Transportation is a significant consumer of fossil fuels and the source of greenhouse gas emissions and other pollutants. At the same time, its process also reduces the lifespan of infrastructure due to wear and tear, pollute waters, and damage marine environments. Regional materials, even materials sourced or processed on site, will reduce the impact of long transportation and support the local economies (Institute for Sustainable Infrastructure, 2015). For these reasons, we concluded that this risk criterion should also be included in the proposed model.

Useful life (E7)

Impeccable design and high quality materials will extend useful life of the completed construction projects. The longer the useful life, the less it will need to be replaced, and eventually will reduce the energy, water, and materials, required for refurbishment and rebuilding (Institute for Sustainable Infrastructure, 2015). In this context, we selected this risk criterion to be included in the proposed model.

Social conflict (S1)

Construction projects, primarily the megaprojects, often provoking social conflicts among stakeholders. These

conflicts are normally incited because disparities of interests among stakeholders result in prominent social contradictions that affect social stability. Social conflicts can be caused by various reasons, ranging from land acquisition, demolition, forced resettlement, labor disputes, environmental degradation, wellbeing of the local populations, etc. (Z. He et al., 2020; Singto et al., 2021; Magsi et al., 2022). Genuinely aware of the importance of this risk criterion, we made the decision to include it into the proposed model.

Workplace safety and health (S2)

A construction environment is extremely dynamic and deeply focused on the deadlines which make it very likely to have a high risks of workplace safety and health. Fatigue, due to overexertion, is named to be the leading cause of work-related injuries in the construction environment (Fang et al., 2015). Mismanagement of workplace safety and health will exacerbate and increase the number of work-related accidents and injuries (Lette et al., 2018; Ismail, 2019). In that regard, we included this risk criterion into the proposed model.

Local employment ratio (S3)

In most of the cases, a fair proportion of local employment will be able to prevent social conflicts related with the projects. An emphasis on employment of minority and/or disadvantaged groups members will help to develop local skills and capabilities (Institute for Sustainable Infrastructure, 2015). From that perspective, we selected this risk criterion to be included in the proposed model.

4.2. Expert Interviews

Referring to Tables 2 and 3, expert interviews are subsequently performed to capture experts' perception on the selected environmental and social risk criteria. In these interviews, experts were requested to make assessment towards the selected risk criteria and discussions were held for each of the selected risk criteria. Current implementation, challenges, and prospects of sustainable underwriting were addressed in these discussions. Later, experts were requested to rate the selected risk criteria from a scale of 1 to 10 with the following conditions: 10 should be awarded to any most important risk criteria and 1 to any least important. The results of the rating are summarized in Table 4, while the risk criterion ranking is shown in Table 5.

Table 4. Results of the Experts' Rating

Risk Criteria Code	Experts					Total Score
	A	B	C	D	E	
E1	10	6	10	7	10	43
E2	10	10	10	7	10	47
E3	10	6	8	10	10	44
E4	5	8	6	8	5	32
E5	5	8	6	8	5	32
E6	5	8	6	8	7	34
E7	8	10	6	10	7	41
S1	10	10	10	10	10	50
S2	10	8	10	10	10	48
S3	8	10	8	10	9	45

(Source: Authors, 2022)

Table 5. Risk Criteria Ranking

Risk Criteria Code	Risk Criteria
S1	Social conflict
S2	Workplace safety and health
E2	Impacts on wetlands, shorelines, and waterbodies
S3	Local employment ratio
E3	Pollutants and wastes
E1	Impacts on greenfields
E7	Useful life
E6	Regional materials
E4	Recycled materials
E5	Prefabricated materials

(Source: Authors, 2022)

4.3. Formulation of the Sustainable Contractors' All Risks (CAR) Policy Underwriting Model

The overview of the entirety process flow of the proposed sustainable Contractors' All Risks (CAR) policy underwriting model is outlined in Figure 1, while the environmental and social risks assessment process is then detailed in Figure 2. Any risk assessment process portrayed by either Figure 1 or 2 will be resulted as underwriting decision. It could be an immediate rejection or a decision to proceed to the next step of the risk assessment process, whether it is with or without precondition. A precondition could be in the form of exclusion, warranty, subjectivity, additional clauses, premium loading rate, higher deductible, policy limit reduction, etc.

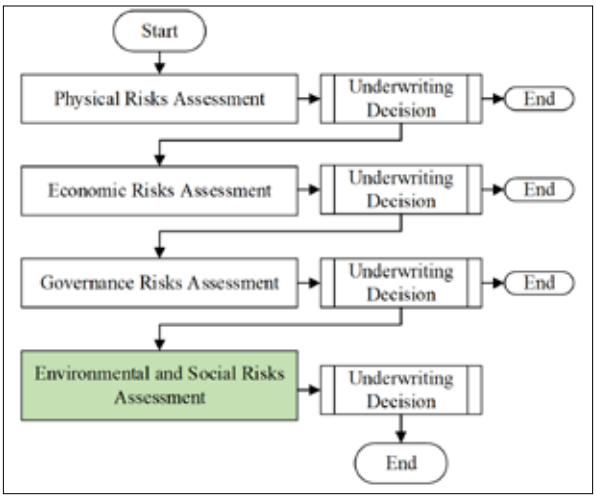

Figure 1. Sustainable Contractors' All Risks (CAR) Policy Underwriting Model

(Source: Authors, 2022)

5. Conclusions

The aim of sustainable underwriting is to reduce risk and contribute to economic, environmental, and social sustainability, thus, the Contractors' All Risks (CAR) policy underwriting should be transformed by way of integrating environmental and social risks into the process. Based on previous study, the process of integrating those risks needs to be in alignment with non-life insurance company's targets, vision, and mission. On that account, this study intends to not only promote the concept of sustainable underwriting or alarm the Indonesia non-life insurance sector about its

significance, but to propose conceptual model for sustainable Contractors' All Risks (CAR) policy underwriting as well. This study aspires for the proposed conceptual model to be of any use for those insurers to eventually able of establishing their internal sustainable underwriting guidelines. Last of all, the proposed conceptual model may be adapted elsewhere with customized risk criteria by following the same method and assessment made towards local applicable regulations.

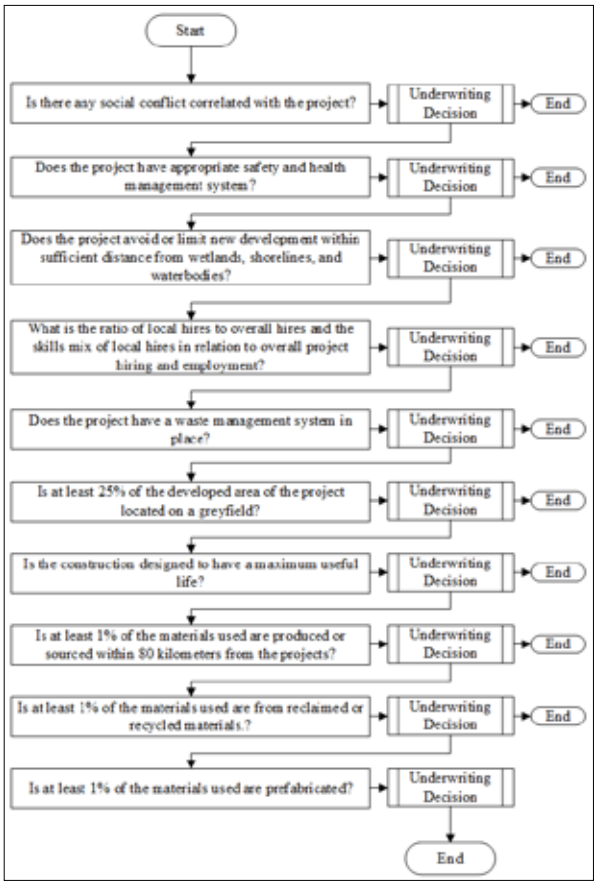

Figure 2. Environmental and Social Risks Assessment

(Source: Authors, 2022)

References

Agnes, M., Koestoer, R. H., & Sodri, A. (2023). Social and Environmental Risks Integration into Underwriting of Non-Life Insurance: A Review of Sustainable Finance in Indonesia. Jurnal Ilmu Lingkungan. 21(1), 125-131. doi: 10.14710/jil.21.1.125-131

Allais, R., Roucoules, L., & Reyes, T. (2017). Governance maturity grid: a transition method for integrating sustainability into companies? Journal of Cleaner Production, 140, 213–226. https://doi.org/10.1016/j.jclepro.2016.02.069

Bao, Z., Lee, W. M. W., & Lu, W. (2020). Implementing on-site construction waste recycling in Hong Kong: Barriers and facilitators. Science of the Total Environment, 747. https://doi.org/10.1016/j.scitotenv.2020.141091

Belozyorov, S. A., & Xie, X. (2021). China's green insurance system and functions. E3S Web of Conferences, 311, 03001. https://doi.org/10.1051/e3sconf/202131103001

Berardi, U. (2013). Clarifying the new interpretations of the concept of sustainable building. Sustainable Cities and Society, 8. https://doi.org/10.1016/j.scs.2013.01.008

Brovkin, V. ;, Boysen, L. ;, Arora, V. K. ;, Boisier, J. P. ;, Cadule, P. ;, Chini, L. ;, Claussen, M. ;, Friedlingstein, P. ;, & Gayler, V. ; (2013). Effect of Anthropogenic Land-Use and Land-Cover Changes on Climate and Land Carbon Storage in CMIP5 Projections for the Twenty-First Century. In M. Journal of Climate ; Boston (Vol. 26).

Chiaramonte, L., Dreassi, A., Paltrinieri, A., & Piserà, S. 2020. Sustainability Practices and Stability in the Insurance Industry. Sustainability 12, 5530.

Darko, A., Zhang, C., & Chan, A. P. C. (2017). Drivers for green building: A review of empirical studies. Habitat International, 60. https://doi.org/10.1016/j.habitatint.2016.12.007

Douglass, M., & Miller, M. A. (2018). Disaster justice in Asia's urbanising Anthropocene. Environment and Planning E: Nature and Space, 1(3), 271–287. https://doi.org/10.1177/2514848618797333

Dubey, R., Gunasekaran, A., Childe, S. J., Papadopoulos, T., Hazen, B., Giannakis, M., & Roubaud, D. (2017). Examining the effect of external pressures and organizational culture on shaping performance measurement systems (PMS) for sustainability benchmarking: Some empirical findings. International Journal of Production Economics, 193, 63–76. https://doi.org/10.1016/j.ijpe.2017.06.029

Fang, D., Jiang, Z., Zhang, M., & Wang, H. (2015). An experimental method to study the effect of fatigue on construction workers' safety performance. Safety Science, 73, 80–91. https://doi.org/10.1016/j.ssci.2014.11.019

Gillan, S. L., Koch, A., & Starks, L. T. (2021). Firms and social responsibility: A review of ESG and CSR research in corporate finance. Journal of Corporate Finance, 66. https://doi.org/10.1016/j.jcorpfin.2021.101889

Hawken, S., Avazpour, B., Harris, M. S., Marzban, A., & Munro, P. G. (2021). Urban megaprojects and water justice in Southeast Asia: Between global economies and community transitions. Cities, 113. https://doi.org/10.1016/j.cities.2020.103068

He, Q., Wang, Z., Wang, G., Zuo, J., Wu, G., & Liu, B. (2020). To be green or not to be: How environmental regulations shape contractor greenwashing behaviors in construction projects. Sustainable Cities and Society, 63. https://doi.org/10.1016/j.scs.2020.102462

He, Z., Huang, D., Fang, J., & Wang, B. (2020). Stakeholder Conflict Amplification of Large-Scale Engineering Projects in China: An Evolutionary Game Model on Complex Networks. Complexity, 2020. https://doi.org/10.1155/2020/9243427

Hong, Jingke, Zhong, X., Guo, S., Liu, G., Shen, G. Q., & Yu, T. (2019). Water-energy nexus and its efficiency in China's construction industry: Evidence from province-level data. Sustainable Cities and Society, 48. https://doi.org/10.1016/j.scs.2019.101557

Hossain, M. U., Ng, S. T., Antwi-Afari, P., & Amor, B. (2020). Circular economy and the construction industry: Existing trends, challenges and prospective framework for sustainable construction. In Renewable and Sustainable Energy Reviews (Vol. 130). Elsevier Ltd. https://doi.org/10.1016/j.rser.2020.109948

Hu, X., & Chong, H. Y. (2021). Environmental sustainability of off-site manufacturing: a literature review. In Engineering, Construction and Architectural Management (Vol. 28, Issue 1, pp. 332–350). Emerald Group Holdings Ltd. https://doi.org/10.1108/ECAM-06-2019-0288

Institute for Sustainable Infrastructure. (2015). ENVISION Rating System for Sustainable Infrastructure.

Ismail, Z. A. (2019). Optimising the safety of road transport workers on IBS building construction projects: a review. Social Responsibility Journal, 15(6), 837–851. https://doi.org/10.1108/SRJ-09-2018-0240

Jie, Z., & Nan, C. (2020). Concrete Construction Waste Pollution and Relevant Prefabricated Recycling Measures. Nature Environment and Pollution Technology, 19(1), 367–372. www.neptjournal.com

Johannsdottir, L. 2014. Transforming the linear insurance business model to a closed-loop insurance model: A case study of Nordic non-life insurers. Journal of Cleaner Production 83, 341–355.

Klufallah, M., Ibrahim, I. S., & Moayedi, F. (2019). Sustainable practices barriers towards green projects in Malaysia. IOP Conference Series: Earth and Environmental Science, 220(1). https://doi.org/10.1088/1755-1315/220/1/012053

Lette, A., Ambelu, A., Getahun, T., & Mekonen, S. (2018). A survey of work-related injuries among building construction workers in southwestern Ethiopia. International Journal of Industrial Ergonomics, 68, 57–64. https://doi.org/10.1016/j.ergon.2018.06.010

Linnenluecke, M. K., & Griffiths, A. (2010). Corporate sustainability and organizational culture. Journal of World Business, 45(4), 357–366. https://doi.org/10.1016/j.jwb.2009.08.006

Lozano, R. (2012). Towards better embedding sustainability into companies' systems: An analysis of voluntary corporate initiatives. Journal of Cleaner Production, 25, 14–26. https://doi.org/10.1016/j.jclepro.2011.11.06

Magsi, H., Sabir, M., Torre, A., & Chandio, A. A. (2022). Management practices to minimize land use conflicts on large infrastructure projects: examples of dams construction in Pakistan. GeoJournal, 87(6), 4851–4861. https://doi.org/10.1007/s10708-021-10532-0

Negri, P. 2018. Sustainable Finance and Non-Financial Disclosure: The Impact for the Insurance Industry. Symphonya. Emerging Issues in Management 1, 110.

Nogueira, F. G., Lucena, A. F. P., & Nogueira, R. 2018. Sustainable Insurance Assessment: Towards an Integrative Model. Geneva Papers on Risk and Insurance: Issues and Practice 43(2), 275–299.

OECD. 2001. OECD Annual Report 2001. OECD Publishing.

Prestele, R., Alexander, P., Rounsevell, M. D. A., Arneth, A., Calvin, K., Doelman, J., Eitelberg, D. A., Engström, K., Fujimori, S., Hasegawa, T., Havlik, P., Humpenöder, F., Jain, A. K., Krisztin, T., Kyle, P., Meiyappan, P., Popp, A., Sands, R. D., Schaldach, R., … Verburg, P. H. (2016). Hotspots of uncertainty in land-use and land-cover change projections: a global-scale model comparison. Global Change Biology, 22(12), 3967–3983. https://doi.org/10.1111/gcb.13337

Sato, M., & Seki, M. (2010). Sustainable business, sustainable planet a Japanese insurance perspective. Geneva Papers on Risk and Insurance: Issues and Practice, 35(2), 325–335. https://doi.org/10.1057/gpp.2010.7

Shan, M., Hwang, B. G., & Zhu, L. (2017). A global review of sustainable construction project financing: Policies, practices, and research efforts. Sustainability (Switzerland), 9(12). https://doi.org/10.3390/su9122347

Singto, C., de Vries, M., Hofstede, G. J., & Fleskens, L. (2021). Ex Ante Impact Assessment of Reservoir Construction Projects for Different Stakeholders Using Agent-Based Modeling. Water Resources Management, 35(3), 1047–1064. https://doi.org/10.1007/s11269-021-02771-0

Susanti, B., Filestre, S. F. H., & Juliantina, I. (2019). The Analysis of Barriers for Implementation of Sustainable Construction in Indonesia. IOP Conference Series: Earth and Environmental Science, 396(1). https://doi.org/10.1088/1755-1315/396/1/012033

Tacconi, L., & Muttaqin, M. Z. (2019). Reducing emissions from land use change in Indonesia: An overview. In Forest Policy and Economics (Vol. 108). Elsevier B.V. https://doi.org/10.1016/j.forpol.2019.101979

United Nations Environment Programme Finance Initiative Principles for Sustainable Insurance. (2019). Underwriting environmental, social and governance risks in non-life insurance business

Urban, M. A., & Wójcik, D. (2019). Dirty banking: Probing the gap in sustainable finance. Sustainability (Switzerland), 11(6). https://doi.org/10.3390/su11061745

World Economic Forum. (2022). The Global Risks Report 2022, 17th Edition.

Wulan, S., Kusnoputranto, H., Supriatna, J., Bintoro Djoefrie, H. M. H., Musthafa, H., & Hakim, A. L. (2015). Life Cycle Assessment of Sago Palm, Oil Palm, and Paddy Cultivated on Peat Land. Journal of Wetlands Environmental Management, 3(1), 14–21. http://ijwem.unlam.ac.id/index.php/ijwem

Zarin, D. J., Harris, N. L., Baccini, A., Aksenov, D., Hansen, M. C., Azevedo-Ramos, C., Azevedo, T., Margono, B. A., Alencar, A. C., Gabris, C., Allegretti, A., Potapov, P., Farina, M., Walker, W. S., Shevade, V. S., Loboda, T. V., Turubanova, S., & Tyukavina, A. (2016). Can carbon emissions from tropical deforestation drop by 50% in 5 years? Global Change Biology, 22(4), 1336–1347. https://doi.org/10.1111/gcb.13153

JJEES

JJEES (2025) 16 (2): 220-226
ISSN 1995-6681

Jordan Journal of Earth and Environmental Sciences

Surface Runoff Estimation Using GIS Data under HEC HMS: Wadi Laussif Subbasin, Algeria

Cheddad S.[1*], Haouchine A.[1], Benmerabet N. [2]

[1] Geo-Environment Laboratory, Houari Boumedian University of Science and Technology, PO Box 32, Bab Ezzouar, 16111, Algiers, Algeria
[2] Water Resources and Sustainable Development Laboratory, Badji Mokhtar University, PO Box 12, Annaba, Algeria

Received on 25 November 2023, Accepted on 2 February 2025

Abstract

This study is a part of the Kherzet Youcef deposit's hydrogeological investigation. Calculating hydrological balance requires knowing the magnitudes of infiltration and flow. One important consideration in hydrogeological research is the rate of infiltration. In this case, the hydrogeological model will make use of it.

In some watersheds, the lack of hydrological measurements, their insufficient or questionable quality, and their reliability limit the precision of hydrologists' forecasts of hydrologic quantities, such as runoff, sediment, and nutrients. This issue is especially serious in developing countries like Algeria, especially, in the Wadi Laussif subbasin's undetected watershed (sub-catchment) area. Furthermore, approaches that allow for accurate watershed estimations of these variables are needed. Because the HEC-HMS model is widely used in hydrology studies to simulate the volume of surface runoff and determine flood peaks, many researchers have used it in flood forecasting. To predict the discharge in the Wadi Laussif subbasin, an attempt has been made to combine a geographic information system (GIS) and the semi-distributed hydrological model HEC-HMS. First, a digital elevation model and the GIS icon on the model were used to determine the basin's characteristics.

Information on daily precipitation was gathered from 1986 to 2020. The hydrological model employs the SCS-CN method to calculate the direct volume of runoff, the SCS unit hydrograph method to convert enough precipitation to a runoff hydrograph, and the lag time approach to determine the channel flow routing. The runoff simulation in the Wadi Laussif subbasin is executed by utilizing rainfall data, basin features, and soil conservation services curve numbers (SCS CN).

In conclusion, the estimation of direct surface runoff at the watershed outflow was conducted using the HEC-HMS model. The result obtained is deemed satisfactory. The approximate value of the estimated correlation coefficient is 0.79. This study contributes to improved water resource management in Algeria by providing a reliable methodology for estimating surface runoff in ungauged basins, crucial for informed decision-making, related to flood control, irrigation planning, and drought mitigation.

Keywords: *Surface runoff, Ungauged subbasin, HEC-HMS, Hydrological model, SCS CN, Kherzet Youcef deposit, Wadi Laussif subbasin.*

1. Introduction

Water resource availability in Algeria, like many regions, is increasingly threatened by climate change, manifested in fluctuating precipitation patterns, rising sea levels, and shifting temperature averages (Asokan and Dutta, 2008). Accurate runoff estimation is crucial for effective water resource management, encompassing flood control, irrigation planning, and the design of drainage networks. However, the scarcity and unreliability of hydrological data in many Algerian watersheds pose significant challenges for hydrologists and water resource managers. This is particularly true in ungauged basins, where limited data hinders the accurate prediction of runoff, sediment transport, and nutrient loads.

This study addresses this critical challenge by developing a reliable methodology for estimating surface runoff in the ungauged Wadi Laussif subbasin, Algeria. Specifically, we aim to:

1. Demonstrate the applicability of the HEC-HMS model in simulating runoff in ungauged basins within the Algerian context.
2. Provide a practical approach for estimating runoff in data-scarce regions to contribute to improved water resource management in Algeria.
3. The findings of this study are highly relevant to Algeria, where a significant portion of the country's watersheds lack adequate hydrological data. By successfully applying the HEC-HMS model to the Wadi Laussif subbasin, this research provides valuable insights into:
   - Improving flood forecasting and early warning systems.
   - Optimizing water resource allocation for irrigation and other uses.
   - Developing sustainable water management strategies in the face of climate change.
   - Supporting informed decision-making related to water resources planning and development in Algeria.

* Corresponding author e-mail: cheddadsouha@gmail.com

This research contributes to a growing body of literature on the application of hydrological models in data-limited environments, particularly in developing countries. It provides a valuable case study for other ungauged basins in Algeria and can inform future research on improving hydrological modeling techniques in data-scarce regions.

The ability to depict landscape elements spatially has been made possible by recent developments in rainfall-based runoff models. The integration of precipitation data with these models, such as the widely used HEC-HMS model (El Hussein et al., 2022; Hamdan et al., 2021; Barik et al., 2017; Dariane et al., 2019; Thameemul Hajaj et al., 2019; Sai et al., 2017), provides a viable method for improving the accuracy of runoff estimation. While distributed models offer the advantage of simulating spatial variability, their implementation can be resource-intensive, particularly in data-scarce environments like Algeria (Piman and Babel, 2013).

The HEC-HMS model is specifically designed to simulate rainfall-runoff processes and predict streamflow within branched basin networks, encompassing diverse geographical regions from small watersheds to large river basins (Abushandi and Merkel, 2013; Verma et al., 2010). The model provides a range of options for hydrological modeling, with key components focusing on the computation of subbasin runoff hydrographs and their routing through channels to the basin outlet (Nag et al, 2024). Given the complexity of hydrological systems and data limitations, the use of rainfall-based runoff simulation models is essential. The combination of HEC-HMS with GIS and remote sensing techniques (Ibrahim-Bathis and Ahmed, 2016) offer a powerful approach to addressing these challenges. Consequently, this research focuses on assessing surface runoff in the Wadi Laussif subbasin utilizing the HEC-HMS model.

2. Material and methods

2.1 Presentation of the Chott Beida Watershed

The Ain Azel depression is part of a vast hydrological basin, Highlands Constantine, which spreads over more than 9580 km² from the region of Ain Beida in the east to that of El Eulma in the west. The National Agency of Water Resources of Algeria assigned it the number 07 under the name of the Constantine Highlands (Figure 1). The Ain Azel plain occupies the western subwatershed (s/BV), coded 07-01, Chott El Beida.

The Wadi Laussif subbasin is a small basin with an area of approximately 74 km².

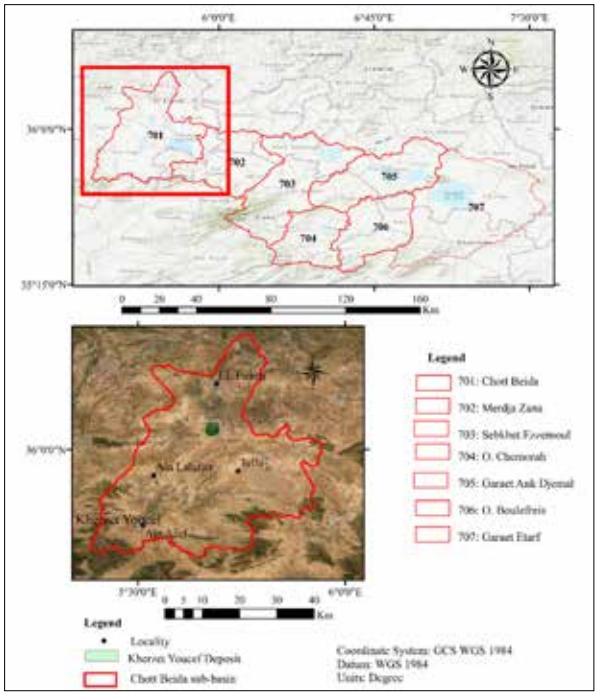

Figure 1. Geographic location of the Wadi Laussif subbasin

The slope is calculated using the slope module of GIS to present the topographic area of the subbasin. Then, the obtained slope is reclassified into categories, as shown in Table 1. The slope categories are chosen according to the classification proposed by Hagerty and Kingston (1992). The obtained result is presented in Figure 2.

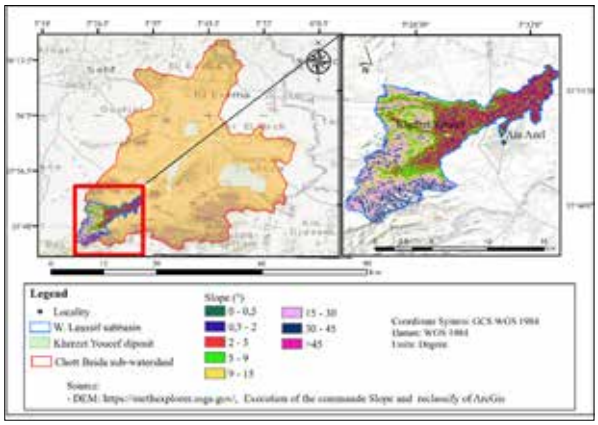

Figure 2. Slope map

Each category's area, expressed in km² and percentage, is shown in Table 1. There is a minor slope (less than 15%) over 41% of the Wadi Laussif subbasin.

Table 1. Slope category (Hagerty and Kingston, 1992)

Category	Slope percentage (%)	Description	Occupied area			
			(km²)	(%)	(km²)	(%)
			Chott Beida		W. Laussif subbasin	
A	0 – 0.5	Plat	100	6.25	0.75	1.018
B	0.5 - 2	Almost plat	255	15.93	8.45	11.424
C	2 – 5	Very slight slope	568	35.48	19.12	25.834
D	5 – 9	slight slope	326	20.36	12.55	16.953
E	9 – 15	Medium slope	149	9.31	10.13	13.689
F	15 – 30	Steep slope	140	8.77	16.13	21.802
G	30 – 45	Very steep slope	63	3.90	6.87	9.279

One aspect that can be incorporated into the subbasin element is the canopy, which can symbolise the existence of plants in the landscape. The amount of precipitation that reaches the ground surface is decreased by plants' ability to intercept it. Water that has been intercepted evaporates in between storms. Transpiration is another way that plants draw water from the earth. Evapotranspiration is the term used to describe the combination of transpiration and evaporation.

Selecting a canopy method is optional but should be used for continuous simulation applications.

Table 2 shows the area occupied by each theme, and Figure 3 displays the land use/land cover map.

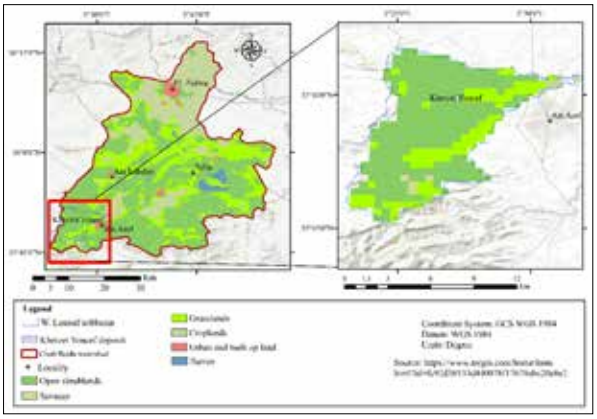

Figure 3. Land use/land cover, Chott Beida watershed

Table 2. Land use/land cover

Theme	Area occupied. (km²)	Area occupied. (%)
Open shrublands: Dominated by perennials (1 – 2 height), 10 – 60% cover	791	49.40
Savannas: Tree cover, 10 -30%, canopies >1Km	5	0.28
Grasslands: Dominate by herbaceous annuals	404	25.24
Croplands: At least 60% of the area is cultured croplands	358	22.36
Urban and built-up land: At least 30% impervious surface area, including building materials, asphalt, and vehicles.	22	1.38
Barren: At least 60% of the area is covered by permanent water bodies.	21	1.33

Infiltration rates vary with rainfall intensity, runoff, and vegetation conditions (Luo et al., 2020). In Chott El Beida watershed, according to Table 3, the land is covered by open shrublands, grasslands, and croplands, representing 49%, 25%, and 22%, respectively. Overall, the cropland effect drove in the same direction as climate change, increasing crop water requirements (3%) and actual evapotranspiration (11%), while decreasing net primary productivity-based water intensity (−15%), according to Vila-Traver et al. (2022).

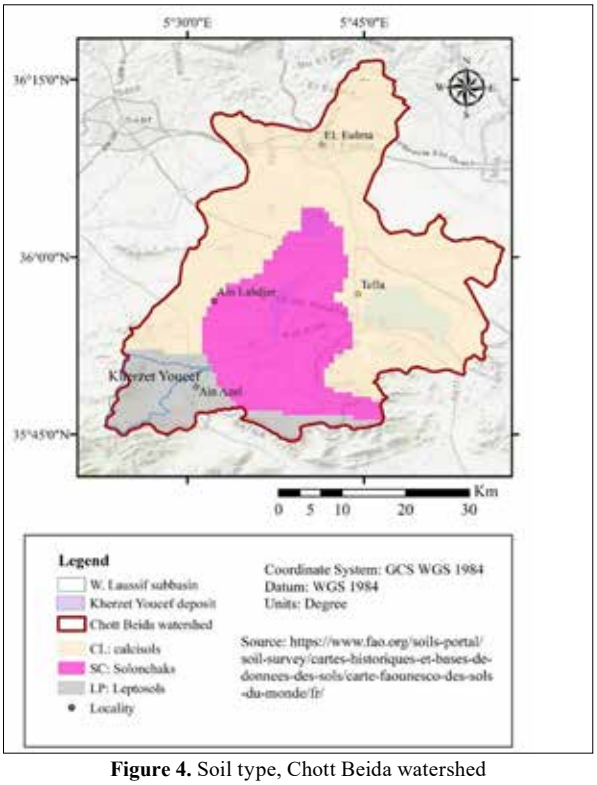

Figure 4. Soil type, Chott Beida watershed

Grasslands and open shrublands cover the Wadi Laussif subbasin; however, the soil is represented by leptosols (Figure 4).

2.2 Hydrological model

The rainfall-runoff model was generated using the HEC-HMS model. It is a semi-distributed, event-based model that divides the catchment into subbasins, computes the runoff response in each subbasin, and routes the river flow to the outlet. HEC-HMS has been extensively used in runoff estimation and land use change impacts on run-off (Yahia et al., 2018; Al-Samawi et al., 2021; Chanchala et al., 2022).

HEC-HMS uses separate models to represent each component of the runoff process, including models that compute runoff volume, direct runoff, and models of base flow (Mokhtari et al., 2016). The SCS-CN method was chosen to estimate the rainfall-runoff model for the loss methods. Channel flow was calculated using the lag time method.

2.2.1 SCS curve number

Assuming that the ratio of actual direct runoff to maximum possible runoff is equal to the ratio of actual infiltration to potential maximum retention and that the amount of initial abstraction is a fraction of the potential maximum retention, the SCS-CN method (NRCS, 2008) is a popular rainfall-runoff model that is based on the water balance calculation.

This method is given by Equations (1), (2), and (3). (In Dahdouh et al., 2018)

$$Q = \frac{(P-I_a)^2}{(P-I_a)+S} \quad (1)$$

$$S = \frac{25400}{CN} - 254 \quad (2)$$

$$I_a = \lambda S \quad (3)$$

Where Q is the runoff depth (mm); P is the gross rainfall depth (mm); I_a is the initial abstraction (mm); and S is the potential retention (mm); λ is the initial abstraction coefficient.

The only parameter, curve number (CN), relates to land cover, soil type, and antecedent moisture condition. At the same time, the constant λ value should be fixed to 0.2, as found in documentation.

2.2.2 Lag time

Hydrometeorological factors (such as rainfall and runoff), watershed features (such as slope, land cover, soils, drainage density, and storage), and stream channel geomorphology all have a direct impact on concentration time (TC) and lag time (TL). In practice, TC and TL are most estimated from those variables using empirical approaches. According to Gericke and Smithers (2014), practically every technique created globally is empirically grounded and represents a constant trait for a particular watershed.

To calculate the TC, the Kirpich equation (in Dagnenet et al., 2022). This equation is used for channel flow and developed for small drainage basins.

$$Tc=0.0663\times L\times S^{-0.385} \quad (4)$$

Where:

Tc is a time of concentration (h),

L is the primary channel length (Km),

S is the primary channel slope (m/m).

For the lag time, the next equation is used:

$$TL=0.6\times Tc \quad (5)$$

2.3 Method

This study employed HEC-HMS integrated with GIS techniques to estimate surface runoff within the ungauged Wadi Laussif subbasin, Algeria. Data acquisition included a 30-meter resolution Digital Elevation Model (DEM) from the SRTM 1 Arc-Second Global data, LULC and soil maps for CN estimation using the SCS-CN method, and 34 years of daily rainfall data (1986-2020). The 34-year rainfall dataset, sourced from the Algerian Ministry of Water Resources, was complete and of high quality. The SCS-CN method was selected due to its established reliability and widespread use in hydrological modeling. A hypothetical storm approach was utilized to provide consistent input for runoff simulations. The HEC-HMS model was then used to process the DEM, delineate the basin, and simulate surface runoff. Recognizing the data limitations in ungauged basins, the study addressed data quality concerns, implemented gap-filling techniques, and conducted sensitivity analyses to assess the impact of data uncertainties on model predictions. While rigorous calibration was not feasible, model parameters were adjusted within reasonable ranges based on expert judgment and literature values. The results of this analysis provide valuable insights into surface runoff characteristics within the Wadi Laussif subbasin and contribute to improved water resource management in data-scarce regions of Algeria.

Figure 5 presents the method used in this work.

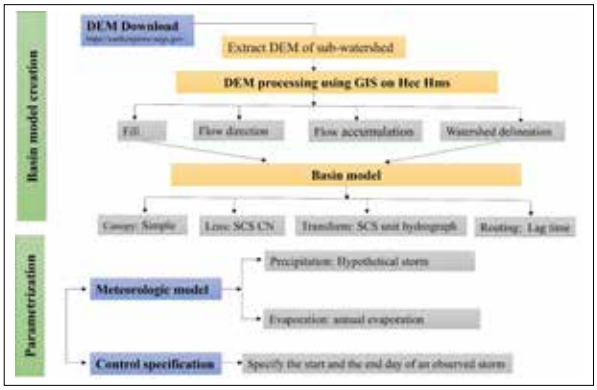

Figure 5. Chart of methodology

3 Results and discussion

3.1 Sub watersheds creation

A digital elevation model (DEM), downloaded from the United States Geological Survey site (USGS), with a 30 m resolution, was processed and used to generate the stream network and to define the sub-catchments with the GIS tools available under the GIS menu. First, we use the tool "Preprocess Sinks" after creating a basin model and adding the terrain (DEM). This tool will run a pit removal algorithm on the terrain data assigned to the selected basin model and produce a new, hydrologically corrected DEM and a raster indicating the location of sinks and the depth at which they were filled. These two new rasters are added to the map layer list as "sink fill" and "sink locations."

The Preprocess drainage tool is then used, which will use an algorithm to ascertain the accumulation and flow direction of each grid cell in the terrain data raster. The hydrologically corrected DEM will be used in this method if the Preprocess Sinks command is executed first. Otherwise, the terrain data component's default elevation dataset or, if available, the reconditioned elevation dataset will be used. The Map Layers list now includes both generated rasters under the names "Flow Direction" and "Flow Accumulation."

Finally, we use the delineate element tool to delineate basins (Figure 6).

Hydrologic and topographic parameters were calculated as the model inputs.

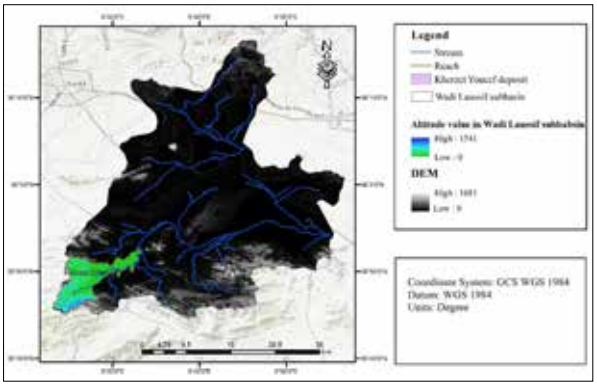

Figure 6. Wadi Laussif subbasin delineation

We compared the area of the subbasin with the area of the subbasin delineated on a topographic map, and the results are shown in Table 3.

The subbasin area, obtained from HEC-HMS, is near the natural area by approximately 3%. This discrepancy primarily stems from the use of different geodetic systems: a local system for the map and the global WGS84 system for the DEM.

Table 3. Wadi Laussif subbasin area

Parameter	From HEC HMS (km²)	From topographic map (km²)	Difference (km²)	Difference (%)
Area	78.50	73.77	4.73	3.10

3.2 Climate data analyses

The fitting of the time series of maximum daily rainfall for the station of Ain Azel shows that the lognormal distribution is the most appropriate (Figure 7). This is given by the following formula of equation 6:

$$F(x) = \frac{1}{\sigma\sqrt{2\pi}} \int_{-\infty}^{x} e^{-\frac{z^2}{2}} dx; z = aLog(x - x_0) + b. \quad (6)$$

The maximum daily rainfall values calculated, using HYFRANPLUS software, for the return periods of 5, 10, 50, 100, and 200 years at the station (Table 4), correspond well to the precipitation recorded during the historical floods observed in the region of Ain Azel.

These results show the reliability of the statistical fit to the lognormal distribution. For the return period of 5 years, a rainfall of 44 mm is calculated.

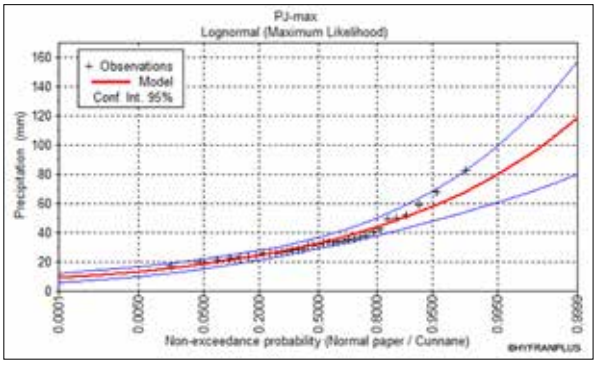

Figure 7. Adjustment of lognormal to the maximum daily rainfall (period 1986-2020)

Table 4. The maximum daily rainfall values calculated for different return periods.

Return period (year)	Maximum daily rainfall (mm)
5	44
10	51.2
20	58
50	66.8
100	73.4

3.3 The unit hydrograph

After preparing all the required parameters for the loss method (Soil Conservation Service – curve number – SCS-CN), the method obtains the subbasin's direct runoff and peak discharge. Figure 8 illustrates the simulated unit hydrographs for return period of 5 years.

For this return period, the peak discharge is estimated to be 85.6 m^3/s; the loss volume is approximately 23.09 mm, the direct runoff volume is 20.91 mm, and the baseflow is approximately 9 mm (Figure 9).

Bibliographical research was carried out, and previous works on the area estimated the runoff value starting by applying empirical formulas based on monthly data averages (Djenba, 2015). The runoff value was estimated at 15.15 mm, and the infiltration was estimated at 8.4 mm.

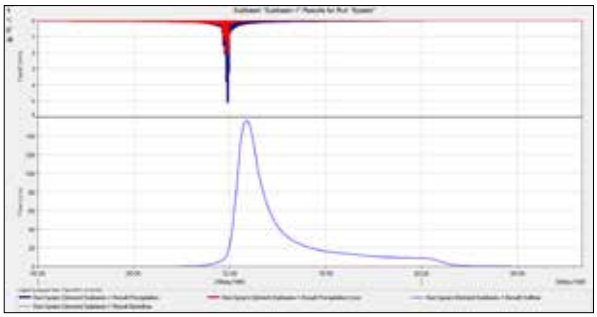

Figure 8. Flood hygrograph for a return period of 5 years

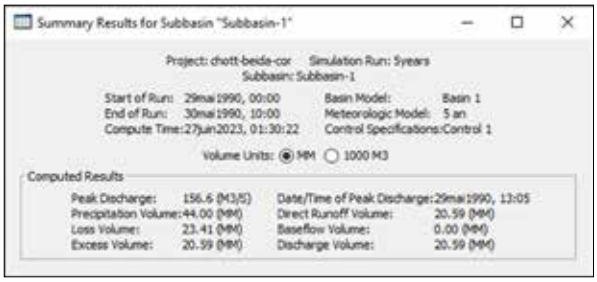

Figure 9. Summary results for a return period of 5 years

3.4 Statistical analysis

This section aims to analyze the model's sensitivity toward the values of the parameters implied in the simulations. To evaluate the flexibility of the rainfall-runoff model in this study case, we used the correlation coefficient (R) (In Dahdouh et al., 2018). It is calculated using the following formula in Equation 7:

$$R = \frac{\sum_{i=1}^{n}(Q_{i,obs} - \bar{Q}_{obs})(Q_{i,sim} - \bar{Q}_{sim})}{\sqrt{\sum_{i=1}^{n}(Q_{i,obs} - \bar{Q}_{obs})^2 (Q_{i,sim} - \bar{Q}_{sim})^2}} \quad (7)$$

where:

$Q_{i,sim}$ is the simulated value at time t=i,

$Q_{i,obs}$ is the observed value at time t=i,

Q_{obs} is the average value,

n is the number of observations.

The correlations between simulated and observed runoff (Figure 10) give linear relationships but with acceptable correlation coefficients ranging from 0.79. This can be explained by the fact that the observed runoff on 29th May 1990 does not necessarily correspond to the rain falling during the same period and that the underground flows can indeed support the surface runoff due to the rain of that day or the previous day.

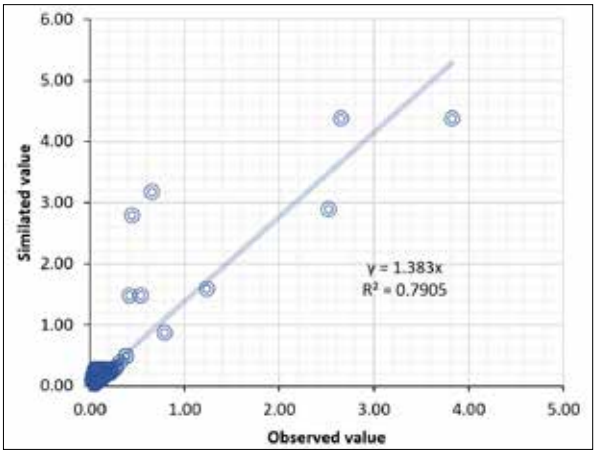

Figure 10. Comparison of simulated discharge and observed runoff in the Wadi Laussif subbasin

Another validation method is used. It visually compares simulated and observed runoff (Figure 11).

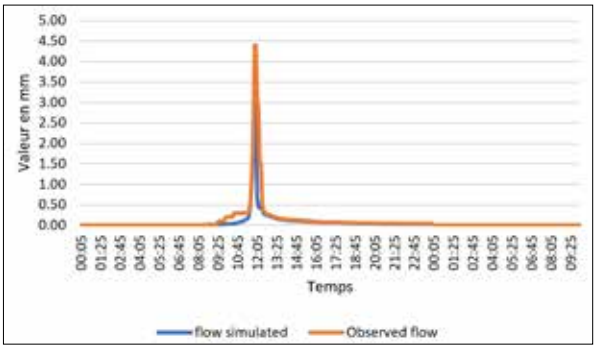

Figure 11. Comparison between observed and simulated runoff

An explicit assumption should be noted.

5. Conclusion

This study successfully applied the HEC-HMS model to simulate surface runoff in the ungauged Wadi Laussif subbasin, a crucial component of the Kherzet Youcef deposit hydrogeological study. By integrating a 30-meter resolution SRTM DEM with the HEC-HMS model and utilizing the SCS-CN method for loss estimation, this research demonstrates a viable approach for runoff estimation in data-scarce environments. Key findings include a satisfactory correlation coefficient of 0.79 between simulated and observed runoff values, demonstration of the model's ability to capture specific hydrological events, e.g., peak flows, time to peak. These results align with previous studies in the region while providing a more robust and spatially distributed assessment of the runoff generation. This study significantly contributes to improved water resource management in the region by providing a reliable methodology for runoff estimation in ungauged basins, supporting the development of a comprehensive hydrogeological model for the Kherzet Youcef deposit, and informing decision-making related to water resource planning, flood control, and drought mitigation in the Wadi Laussif subbasin and potentially other ungauged basins in Algeria. This research emphasizes the importance of integrating GIS and hydrological modeling techniques for effective water resource management in data-limited environments.

Acknowledgments

The authors thank the national non-ferrous company's technical and administrative staff, Kherzet Youcef's unit. Also, our gratitude goes to the administrative staff of the Algerian Water Resource Ministry.

References

Abushandi, E., and Merkel B. (2013). Modelling rainfall runoff relations using HEC-HMS and IHACRES for a single rain event in an arid region of Jordan. Water Resource Management, Vol. 27, pp 2391–2409. https://doi.org/10.1007/s11269-013-0293-4

Al-Hussein, A.A.A., Khan, S., Ncibi, K., Hamdi, N., Hamed, Y. (2022). Flood analysis using HEC-RAS and HEC-HMS: A case study of Khazir River (Middle East- Northern Iraq). Water 2022, Vol. 14, Issue 3779, 19 pages.

https://doi.org/10.3390/w14223779

Al-Samawi, I., Noman, A., Khanbari, K., Quriaa, H., Al-Areeq, N., Aklan, M. (2021). The Impacts of Land-Use Change on the Runoff Characteristics Using HEC-HMS Model: A Case Study in Wadi Al-Mulaikhy Sub-Watershed in Sana'a Basin, Yemen. Water Resources in Arid Lands: Management and Sustainability. Advances in Science, Technology and Innovation, Springer, pp 121 – 130. https://doi.org/10.1007/978-3-030-67028-3_10

Asokan, S.M., and Dutta, D. (2008). Analysis of Water resources in the Mahanadi River basin, India, under projected climate conditions. Hydrological Process, Hydrology Journal, Vol. 22, Issue 18, pp 3589–3603.

Bargaoui, Z., Dakhlaoui, H. and Houcine, A. (2008). Rainfall-runoff modeling and hydroclimatic classification. Journal of Water Science, Vol. 21, Issue 2, pp 233–245. https://doi.org/10.7202/018468ar (In French)

Barik, D.K., Singh, A.D., Sra, M.S. (2017). Estimation of runoff and sediment yield from a small ungauged watershed using GIS and HEC-HMS. International Journal of Civil Engineering and Technology, Vol. 8, Issue 6, pp 517–527.

Chanchala, Padhi, J., and Das, B. (2022). Surface Runoff Estimation of Rana Watershed in Mahanadi River Basin Using HEC-HMS. In: Das, B.B., Hettiarachchi, H., Sahu, P.K., Nanda, S. (eds) Recent Developments in Sustainable Infrastructure (ICRDSI-2020)—GEO-TRA-ENV-WRM. Lecture Notes in Civil Engineering, vol. 207. Springer, Singapore. https://doi.org/10.1007/978-981-16-7509-6_54

Dahdouhi, Y., and Ourdachi, L. (2018). Assessment of two-loss methods for estimation of surface runoff in Zaafrania urban catchment, North-East of Algeria. Journal of water and land development, Vol. 36 (I-II), pp 37-43. DOI: 10.2478/jwld-2018-0004.

Dagnanet, S., Atsushi, T., Mitsuru, T., Nigussie, H., Enyew, A., Derege, T.M., Ayele, A.F., Kindiye, E., Mulatu, L.B., Tadesual, A.S. (2022). Evaluation of lag time and time of concentration estimation methods in small tropical watersheds in Ethiopia. Journal of Hydrology, Vol. 40, Issue 101025.

https://doi.org/10.1016/j.ejrh.2022.101025

Dariane, A.B., Bagheri, R., Karami, F., Javadianzadeh, M.M. (2019). Developing heuristic multi-criteria auto-calibration method for continuous HEC-HMS in snow-affected catchment. International Journal of River Basin Management, Vol. 18, pp 69–80.

Djenba, S. (2015). Influence of parameters: geological, geomorphological, and hydrogeological on the mechanical behavior of soils in the Wilaya of Sétif (Algeria). Thesis, Mohamed Kheider University, Biskra, Algeria. (In French)

Gericke, O.J., and Smithers, J.C. (2014). Review of methods used to estimate catchment response time for the purpose of peak discharge estimation. Hydrological Sciences Journal, Vol.

59, Issue 11, pp. 1935-1971.

Hamdan, A.N.A., Almuktar, S., Scholz, M. (2021). Rainfall-Runoff Modeling Using the HEC-HMS Model for the Al-Adhaim River Catchment, Northern Iraq. Hydrology, Vol. 8, Issue 58, 17 pages. https://doi.org/10.3390/hydrology8020058

Ibrahim-Bathis, K., and Ahmed S.A. (2016). Rainfall-runoff modeling of Doddahalla watershed—an application of HEC-HMS and SCN-CN in an ungauged agricultural watershed. Arabian Journal of Geosciences, Vol. 9, Article number 170.

Luo, J., Zhou, X., Rubinato, M., Li, G., Tian, Y., Zhou, J. (2020). Impact of Multiple Vegetation Covers on Surface Runoff and Sediment Yield in the Small Basin of Nverzhai, Hunan Province, China, Forests, Vol. 11, Issue 3, Article 329. https://doi.org/10.3390/f11030329

Mokhtari, E.H., Remini, B., Hamoudi, S.A. (2016). Modeling of the rain–flow by hydrological modeling software system HEC-HMS – watershed's case of Wadi Cheliff Ghrib, Algeria. Journal of Water and Land Development, Vol. 30, pp 87–100. https://doi.org/10.1515/jwld-2016-0025

Nag, S., Roy, M. B., Roy, P. K. (2024). Integrated hydrological modeling and water resource assessment in the Mayurakshi River Basin: A comprehensive study from historical data to future predictions. Geosystems and Geo-environment, 3(4), 100308. https://doi.org/10.1016/j.geogeo.2024.100308

Piman, T., and Babel, M.S. (2013). Prediction of rainfall-runoff in an Ungauged basin: a case study in the mountainous region of Northern Thailand. Journal of Hydrologic Engineering, Vol. 18, pp 285–296.

Sai, M., Rahul, K.S., Mohanty, B., Asadi, S.S. (2017). Estimation analysis of runoff for Udaygiri Mandal using a potential method: a model study, International Journal of Civil Engineering and Technology, Vol. 8, Issue 4, pp 2062–2068.

Thameemul Hajaj, P.M., Yarrakula, K., Durga Rao, K.H.V., Singh, A. (2019). A semi-distributed flood forecasting model for the Nagavali River using space inputs, Journal of the Indian Society of Remote Sensing, Vol. 47, pp 1683–1692.

Verma, A.K., Jha, M.K., Mahana, R.K. (2010). Evaluation of HEC-HMS and WEPP for simulating watershed runoff using remote sensing and geographical information system, Paddy Water Environment, Vol. 8, pp 131–144.

Vila-Traver, J., De Molina, M.G., Infante-Amate, J., Aguilera, E. (2022). Disentangling the effect of climate and cropland changes on the water performance of agroecosystems (Spain 1922-2016). Journal of Cleaner Production, Vol. 344. https://doi.org/10.1016/j.jclepro.2022.130811.

Yahia, B., Lame, B., Boutkhil, M. (2018). Estimation of Runoff and Sediment Transport: Case of the Mounts of Beni Chougrane, Mascara, Algeria, International Journal of Innovative Approaches in Agricultural Research, Vol. 2, issue 3, pp 153-166. https://doi.org/10.29329/ijiaar.2018.151.2

المملكة الأردنية الهاشمية

صندوق دعم البحث العلمي

الجامعة الهاشمية

المجلة الأردنية
لعلوم الأرض والبيئة

JJEES

مجلة علمية عالمية محكمة

المجلد (١٦) العدد (٢)

http:// jjees.hu.edu.jo/

ISSN 1995-6681

المجلة الأردنية لعلوم الأرض والبيئة

مجلة علمية عالمية محكمة

المجلة الأردنية لعلوم الأرض والبيئة: مجلة علمية عالمية محكمة ومفهرسة ومصنفة، تصدر عن عمادة البحث العلمي في الجامعة الهاشمية وبدعم من صندوق البحث العلمي - وزارة التعليم العالي والبحث العلمي، الأردن.

ترسل البحوث إلكترونيا إلى البريد الإلكتروني التالي:

رئيس تحرير المجلة الأردنية لعلوم الأرض والبيئة

jjees@hu.edu.jo

لمزيد من المعلومات والأعداد السابقة يرجى زيارة موقع المجلة على شبكة الانترنت على الرابط التالي:

www.jjees.hu.edu.jo

المملكة الأردنية الهاشمية صندوق دعم البحث العلمي الجامعة الهاشمية

JJEES

المجلة الأردنية لعلوم الأرض والبيئة

المجلد (16) العدد (2)

مجلة علمية عالمية محكمة تصدر بدعم من صندوق دعم البحث العلمي

ISSN 1995-6681 jjees.hu.edu.jo حزيران 2025